X-ray Diffraction for Residual Stress and Cold Work Measurements of Shot Peened Materials

by

Dorian DELBERGUE

THESIS PRESENTED TO ÉCOLE DE TECHNOLOGIE SUPÉRIEURE
IN PARTIAL FULFILLMENT FOR THE DEGREE OF
DOCTOR OF PHILOSOPHY
Ph.D.

MONTREAL, JULY 20, 2020

ÉCOLE DE TECHNOLOGIE SUPÉRIEURE
UNIVERSITÉ DU QUÉBEC

Dorian Delbergue, 2020

This Creative Commons license allows readers to download this work and share it with others as long as the author is credited. The content of this work cannot be modified in any way or used commercially.

BOARD OF EXAMINERS

THIS THESIS HAS BEEN EVALUATED

BY THE FOLLOWING BOARD OF EXAMINERS

Mr. Philippe Bocher, Ph.D., Thesis Supervisor
Department of Mechanical Engineering at École de technologie supérieure

Mr. Martin Lévesque, Ph.D., Co-supervisor
Department of Mechanical Engineering at École Polytechnique de Montréal

Ms. Ruxandra Botez, Ph.D., President of the Board of Examiners
Department of Automated Manufacturing Engineering at l'École de technologie supérieure

Mr. Mohammad Jahazi, Ph.D., Member of the jury
Department of Mechanical Engineering at École de technologie supérieure

Mr. Manuel François, Ph.D., External Independent Examiner
ICD-LASMIS at Université de Technologie de Troyes

THIS THESIS WAS PRESENTED AND DEFENDED

IN THE PRESENCE OF A BOARD OF EXAMINERS AND THE PUBLIC

ON JUNE 19, 2020

AT ÉCOLE DE TECHNOLOGIE SUPÉRIEURE

To my wife Delphine
and our daughter Sophie.

ACKNOWLEDGEMENTS

First of all, I would like to acknowledge my deepest gratitude to thank Prof. Philippe Bocher and Prof. Martin Lévesque for providing me this wonderful opportunity of pursuing a Ph.D.. I gained in scientific maturity thanks to your guidance, advice, and constructive criticism.

I would like to thank the wonderful group of people that composed the CRIAQ MANU508 project with whom I had the privilege to work with throughout the course of my Ph.D., particularly Thierry Klotz, Rémy Bretin, Charles Bianchetti, Amrita Bag, Antonio Castro Moreno, Fubin Tu, and Hongyan Miao.

I would also like to particularly thank the associate professor and post-doctoral fellows at École de technologie supérieure: Nicolas Vanderesse, Damien Texier, Sébastien Le Corre, and Benjamin Tressou, and also my Ph.D. coworkers Marc Novelli, Pierre Maurel, and Hamid Javadi for your advice, help, and the numerous conversations which helped me, day after day, to enhance my work and stay positive. The technical support of Radu Romanica, Serge Plamondon, and Michel Drouin is also gratefully acknowledged.

I would like to thank the Consortium of Research and Innovation in Aerospace in Québec (CRIAQ), Bell Helicopter, Héroux-Devtek, L3 Communications MAS, and Pratt & Whitney Canada who financially supported the project. I would also like to thank the Natural Sciences and Engineering Research Council of Canada (NSERC) and the Mathematics of Information Technology and Complex Systems (MITACS) for the scholarships I obtained during my Ph.D..

Furthermore, I would like to acknowledge the jury members of this thesis. You provided very useful hints for improving this thesis manuscript, which I have gladly embraced.

Finally, I would like to thank my friends and family for providing an unconditional support during this long chapter of my life. I would like to express a very special thank to my beloved Delphine who endured my day-to-day mood and always encouraged me for the past 5 years. I could not have done it without you all.

Diffraction des rayons X pour la mesure des contraintes résiduelles et des déformations plastiques de matériaux grenaillés

Dorian DELBERGUE

RÉSUMÉ

Les performances en fatigue des pièces aéronautiques peuvent être améliorées dans une certaine mesure via des traitements de surface tel que le grenaillage de précontrainte. Le grenaillage est un procédé de déformation à froid consistant à déformer plastiquement la surface de pièces métalliques en y impactant à grande vitesse des micro-billes, afin d'y introduire des contraintes résiduelles. Ainsi, le grenaillage est souvent considéré comme bénéfique pour l'amélioration des performances en fatigue mais est rarement pris en compte dans les étapes de conception. Pour que ce soit le cas, une mesure précise des contraintes résiduelles et des déformations plastiques introduites est nécessaire. Un grand nombre de techniques (méthode du trou, diffraction des rayons X (DRX), méthode du contour, etc.) existent pour la mesure des contraintes résiduelles, mais seule la DRX permet de la coupler avec la mesure de la déformation plastique.

Cette étude fait partie d'un plus large projet de recherche visant à perfectionner la compréhension du procédé de grenaillage utilisé pour l'amélioration des performances en fatigue de la nuance 300M d'acier, de l'alliage d'aluminium 7050, et du superalliage de nickel IN718 et au développement de modèles de simulation du procédé et de fatigue. Cette étude vise principalement à identifier les problèmes expérimentaux liés à la mesure des contraintes résiduelles. Ce travail de recherche implique la comparaison de la méthode bien connu du $\sin^2\psi$ et la méthode alternative du $\cos\alpha$, deux techniques de DRX basées sur deux géométries de détecteurs et deux méthodes de calcul des contraintes résiduelles différentes. De plus, ce travail montre les possibilités liées à l'utilisation de la largeur du pic de diffraction pour la mesure de la déformation plastique introduite par le grenaillage. Les deux méthodes de DRX ont été comparées, de manière innovante, via l'identification des grains diffractants à partir de cartes EBSD en considérant la géométrie des détecteurs ainsi que la méthode de calcul de chacune des méthodes de DRX. La texture artificiellement produite par la mesure de DRX a été tracée pour la première fois sous forme de figures de pôles. La constante radiographique $1/2S_2$ a été calculée et comparée pour chacun des cas. Il apparaît que les deux techniques présentent des textures artificielles différentes et des constantes radiographiques légèrement différentes ont été trouvées pour les différents ensembles de grains diffractants considérés au cours de cette étude. De plus, la déformation plastique a été évaluée via l'utilisation de courbes de calibration reliant les pics de diffraction à la déformation plastique pour chacun des trois matériaux et différentes conditions de grenaillage. Les profils mesurés de contraintes résiduelles et de déformations plastiques ont été utilisés dans le projet de recherche pour la prédiction des performances de vie en fatigue de pièces grenaillées.

Mots-clés: Diffraction des rayons X, Contraintes résiduelles, Déformation plastique, Grenaillage

X-ray Diffraction for Residual Stress and Cold Work Measurements of Shot Peened Materials

Dorian DELBERGUE

ABSTRACT

Fatigue performance of aerospace components can be improved to some extend by surface treatment like shot peening. Shot peening is a cold work process consisting in impinging particles at high velocity onto the surface of metallic parts. The process induces a surface layer of compressive residual stresses and cold work. Shot peening is often considered as a beneficial surface treatment for fatigue life performance but is rarely taken into account at design stages. To this end, a precise measurement of the induced residual stress and cold work is needed. Numerous techniques (hole drilling, X-ray diffraction, contour, etc.) exist to measure the residual stresses but only the X-ray diffraction (XRD) allows coupling the residual stress measurement with the cold work measurement.

This study is part of larger research project aiming at a better understanding of the shot peening process for the improvement of the fatigue life performance of 300M steel, aluminum alloy 7050, and nickel-based superalloy IN718 components, and at the development of process and fatigue simulation models of the shot peening process. This study primarily aims at identifying the experimental issues related to residual stress measurements. In particular, the research work involved comparing the well-known $\sin^2\psi$ method and the alternative $\cos\alpha$ method, two XRD techniques for residual stress measurements based on two different geometries of detectors and calculation methods. Furthermore, the work shows the possibilities related to the use of the diffraction peak width for the measurement of cold work. The two XRD methods were compared, in an innovative way, through the identification of the diffracting grains from electron backscattered diffraction (EBSD) maps by considering the detector geometry and the calculation method of each method. The artificial textures produced by the XRD measurements were plotted for the first time as pole figures and X-ray elastic constant (XEC) $1/2S_2$ was computed and compared for each case. It results that the two XRD techniques exhibit different artificial textures and slightly different XECs were found for the different sets of diffracting grains considered during this study. Furthermore, the cold work was evaluated through the use of calibration curves relating the diffraction peaks width to the true plastic deformation for the three materials and different shot peening conditions. The measured residual stress and cold work profiles were used in the research project to predict fatigue life performance of shot peened parts.

Keywords: X-ray diffraction, Residual stress, Cold work, Shot peening

TABLE OF CONTENTS

Page

INTRODUCTION 1

CHAPTER 1 LITERATURE REVIEW 5
1.1 General considerations 5
1.2 Materials 7
  1.2.1 300M 7
  1.2.2 IN718 8
  1.2.3 AA7050-T7451 9
1.3 Shot peening 10
  1.3.1 Shot peening mechanics 10
  1.3.2 Shot peening induced residual stresses 10
  1.3.3 Shot peening induced cold work 11
  1.3.4 Shot peening treatment characterization 12
  1.3.5 Shot peening effects 14
    1.3.5.1 Shot peening effects on 300M 14
    1.3.5.2 Shot peening effects on IN718 16
    1.3.5.3 Shot peening effects on AA7050-T7451 16
1.4 Residual stress measurement techniques 17
  1.4.1 Relaxation technique 18
    1.4.1.1 Hole-drilling and ring core methods 18
    1.4.1.2 Slitting method 19
    1.4.1.3 Contour method 19
    1.4.1.4 Layer removal method 19
  1.4.2 Diffraction technique 20
    1.4.2.1 X-ray diffraction method 20
    1.4.2.2 Synchrotron X-ray diffraction method 21
    1.4.2.3 Neutron diffraction method 21
  1.4.3 Other techniques 21
    1.4.3.1 Ultrasonic method 22
    1.4.3.2 Magnetic methods 22
    1.4.3.3 Indentation methods 22
  1.4.4 Measurement methods: penetration and spatial resolution 23
1.5 X-ray diffraction for residual stress measurement 24
  1.5.1 Properties of the emitted X-rays 24
  1.5.2 Crystal structure 27
  1.5.3 X-ray diffraction from planes of atoms 29
  1.5.4 Diffraction peak characterization 31
    1.5.4.1 Peak fitting 31
    1.5.4.2 Peak localization and peak width 31
  1.5.5 Depth of X-rays penetration 33

1.5.6 Effect of residual stresses and cold work on X-ray line 35
1.5.7 Measurement of residual strain 37
1.5.8 Determination of residual stresses 37
1.5.8.1 The $\sin^2\psi$ method 37
1.5.8.2 The $\cos\alpha$ method 38
1.5.8.3 Other residual stress evaluation methods 39
1.5.8.4 Effect of crystallographic texture on the residual stress determination 39
1.6 Residual stress correction due to the layer removal process 40
1.6.1 Moore & Evans correction method 41
1.6.2 FEA matrix relaxation correction method 42
1.7 Chapter conclusions 44

CHAPTER 2 METHODOLOGY 47
2.1 Materials mechanical and microstructural initial conditions 47
2.1.1 300M initial conditions 47
2.1.2 IN718 initial conditions 48
2.1.3 AA7050 initial conditions 50
2.2 Shot peening treatment 51
2.3 Microstructural characterization techniques 52
2.3.1 Scanning electron microscopy 52
2.3.2 Electron backscatter diffraction (EBSD) mapping 54
2.4 Microhardness measurement 55
2.4.1 Vickers microhardness test 56
2.4.2 Knoop microhardness test 57
2.4.3 Microhardness profile: precision and bias 58
2.5 Residual stress measurement 59
2.5.1 Residual stress computation 59
2.5.1.1 $\sin^2\psi$ method 61
2.5.1.2 $\cos\alpha$ method 64
2.5.2 XECs computation 67
2.5.2.1 Theoretical determination of the XECs 68
2.5.2.2 Experimental determination of the second XEC 71
2.5.3 XRD equipment description and measurement conditions 71
2.5.3.1 Proto iXRD apparatus description 71
2.5.3.2 Pulstec μ-X360n apparatus description 73
2.5.3.3 XRD measurement conditions 73
2.5.4 Electropolishing for residual stress profile measurement 74
2.5.4.1 Electropolishing conditions 74
2.5.4.2 Electropolishing depth measurements 75
2.6 Micro-tensile tests for XEC measurement and cold work calibration 77
2.6.1 Micro-tensile specimen geometry and preparation 77
2.6.2 Micro-tensile machine 78

2.6.3 XEC measurements and cold work calibration tests conditions 79

CHAPTER 3 COMPARISON OF THE SIN$^2\psi$ AND COS α METHODS 81
3.1 Examples of shot peening residual stress profile measurement and XEC measurements 81
3.1.1 Estimation of the residual stress profile for a shot peened inhomogeneous microstructure IN718 sample 82
3.1.2 Correction of the shot peening residual stress profiles using measured XECs for an inhomogeneous microstructure IN718 sample 83
3.1.3 XEC measurements via in-situ micro-tensile tests for an homogeneous microstructure IN718 sample 86
3.1.4 Discussion on the shot peening residual stress profile measurement and XEC experimental determination 88
3.2 Implementation of the comparison based on EBSD mapping of IN718 samples 89
3.2.1 Microstructural characterization and analysis of the homogeneous and inhomogeneous IN718 samples 89
3.2.1.1 EBSD maps characterization details 89
3.2.1.2 Microstructure analyses 90
3.2.2 Validation of the 2D EBSD maps use for the identification of the diffracting grains 95
3.2.2.1 Determination of the linear absorption coefficient 95
3.2.2.2 Computation of the maximum effective depth of X-ray penetration 97
3.2.3 Method for identification of the diffracting grains 101
3.3 Identification of the diffracting grains and effect of the angle variations on their number 103
3.3.1 Identification of the diffracting grains 103
3.3.2 Simulation of the diffracting grains from detectors windows 104
3.3.3 Effect of the angle variations on the identified diffracting grains 106
3.3.3.1 Linear detectors: effect of the number of used tilt angles 106
3.3.3.2 2D detector: effect of tilt angle 108
3.3.3.3 2D detector: variation along the α values 109
3.4 XRD measurement induced texture 110
3.5 Computation of the XEC values for the homogenous IN718 sample 113
3.5.1 XEC calculation method 113
3.5.2 XEC computation for the diffracting grains 115
3.5.3 Effect of grain size on the XEC values 118
3.5.4 Effect of diffractometer oscillation 121
3.6 Computation of XRD-induced texture and the XEC values for the inhomogenous IN718 sample 123
3.6.1 XRD measurement induced texture 123

3.6.2 XEC computed for the inhomogeneous microstructure 124
3.7 Chapter conclusions 126

CHAPTER 4 USE OF THE DIFFRACTION PEAK WIDTH FOR COLD WORK ASSESSMENT 131
4.1 Determination of cold work profiles for shot peened IN718 specimens 131
4.1.1 Implementation of the study 131
4.1.2 Residual stress and FWHM profiles for two shot peened IN718 specimens 133
4.1.2.1 Determination of the residual stress and FWHM profiles 133
4.1.2.2 Example of a $FWHM$ value 134
4.1.3 Estimation of cold work profiles 135
4.1.3.1 Determining cold work from XRD peak width 135
4.1.3.2 Calibration curve of IN718: $FWHM$ vs. ε_p 137
4.1.3.3 Cold work profiles of shot peened IN718 138
4.1.3.4 Potential use of the cold work profiles 139
4.1.4 Microhardness profiles 141
4.1.5 Discussion on the cold work affected zone and its measurement 143
4.2 Determination of cold work profiles for the AA7050 specimens 144
4.2.1 Implementation of the study 145
4.2.2 Residual stress and FWHM profiles for two shot peened AA7050 specimens 145
4.2.3 Estimation of cold work profiles 147
4.2.3.1 Calibration curve of AA7050: $FWHM$ vs. ε_p 147
4.2.3.2 Cold work profiles of shot peened AA7050 148
4.2.4 Microhardness profiles 148
4.2.5 Discussion on the cold work affected zone and its measurement 150
4.3 Determination of cold work profiles for the 300M steel specimens 150
4.3.1 Implementation of the study 151
4.3.2 Residual stress and FWHM profiles for two shot peened 300M specimens 151
4.3.3 Estimation of cold work profiles 152
4.3.3.1 Calibration curve of 300M: $FWHM$ vs. ε_p 153
4.3.3.2 Cold work profiles of shot peened 300M 153
4.3.4 Microhardness profiles 155
4.3.5 Evolution of the microstructure below the shot peened surface 156
4.3.6 Discussion on the cold work affected zone and its measurement 160
4.4 Chapter conclusions 163

CONCLUSIONS AND RECOMMENDATIONS 165

APPENDIX I LIST OF PUBLISHED ARTICLES 171

APPENDIX II MATHEMATICAL PROOF I: COS α METHOD 175
APPENDIX III MATHEMATICAL PROOF II 183
APPENDIX IV FIRST XEC ASSESSMENT WITH THE SIN$^2\psi$ METHOD 185
APPENDIX V DIFFRACTING GRAINS IDENTIFICATION: SCRIPT VALIDATION 187
APPENDIX VI ODF EXAMPLE 189
APPENDIX VII SURFACE CHARACTERISTICS AND FATIGUE BEHAVIOR OF SHOT PEENED INCONEL 718 191
APPENDIX VIII EXAMPLE OF $FWHM$ VALUES FOR AA7050 AND 300M 205
APPENDIX IX IN718 - CALIBRATION CURVE OBTAINED AT 700 MPA TRUE ISOSTRESS 207
APPENDIX X EBSD CENTER MAP OF 300M STEEL 209
BIBLIOGRAPHY 211

LIST OF TABLES

Page

Table 1.1 300M steel chemical composition (weight %) (AMS 6257F, 2016). Bal.: balance 7

Table 1.2 Minimal tensile properties required for 300M steel (AMS 6257F, 2016) 8

Table 1.3 IN718 chemical composition (weight %) (AMS 5663M, 2009). Bal.: balance 8

Table 1.4 Minimal tensile properties required for IN718 at room temperature (AMS 5663M, 2009) 9

Table 1.5 AA7050 chemical composition (weight %) (AMS 4050J, 2014). Bal.: balance 9

Table 1.6 Minimal tensile properties required for a 6 mm to 51 mm thick AA7050-T7451 plate (AMS 4050J, 2014) 9

Table 2.1 Average mechanical properties of the studied 300M steel. Reproduced from Bag *et al.* (2019) 47

Table 2.2 Average mechanical properties of the studied IN718 for the 25 mm and 89 mm diameters (∅) bars. Reproduced with permission from Klotz *et al.* (2018a) and Klotz *et al.* (2017a), respectively 49

Table 2.3 Average mechanical properties of the studied AA7050 for the rolling (RD) and transverse (TD) directions. Reproduced from Bianchetti *et al.* (2018) with permission 50

Table 2.4 Shot peening conditions for the treatment of the 300M, IN718, and AA7050 specimens 51

Table 2.5 Shot range diameter and hardness for the S230, CW14, and Z425 media (AMS 2431/2E, 2010; AMS 2431/3D, 2007; AMS 2431/7B, 2013) 52

Table 2.6 XRD measurement conditions for measurements on 300M, IN718, and AA7050 74

Table 2.7 Typical angular positions (β positions) used for the XRD measurement with the Proto iXRD and the Pulstec μ-X360n, for measurements on 300M, IN718, and AA7050 74

Table 2.8 Chemical composition of the electrolytic solutions used for electropolishing. Perchloric acid: $HClO_4$. Solution designation can be found on Struers (2019) website 75

Table 3.1 EBSD subset map size and total map area for the ∅25 mm (homogeneous) and ∅89 mm (inhomogeneous) samples 90

Table 3.2 Grain equivalent diameter $\varnothing_{eq}$ and grain density for the ∅25 mm (homogeneous) and ∅89 mm (inhomogeneous) samples 93

Table 3.3 IN718 chemical composition obtained by optical spectrometry (weight %). Bal.: balance. Reproduced from Klotz *et al.* (2018a) 97

Table 3.4 Number of grains participating to the XRD when data is captured by two linear detectors (for the nine inclinations) or a 2D detector (for one inclination) for the ∅25 mm sample, as depicted in Figure 3.15 103

Table 4.1 Fitting coefficients of Equation (4.3). Reproduced from Klotz *et al.* (2018b) with permission 140

Table 4.2 Microhardness and $FWHM$ values for the base material and the three heat treated conditions: T1: 4 h at 306°C, T2: 2 h at 405°C, and Q: quenched. Measurements were repeated five times, the SD values are presented in parentheses along with the averages 162

LIST OF FIGURES

Page

Figure 1.1 Illustration of type I residual stresses (macrostress), σ^{I}, and the type II and III residual stresses over a few grains, σ^{II} and σ^{III}, respectively 6

Figure 1.2 Typical residual stress profile $\sigma(z)$ below the surface after shot peening. The maximum compressive residual stress σ_{max} is usually found below the surface and is higher than the surface residual stress $\sigma_{\mathrm{surface}}$ 11

Figure 1.3 Typical cold work profile $\varepsilon_p(z)$ below the surface after shot peening. The maximum cold work is often found below the surface or at the sruface. The residual stress profile $\sigma(z)$ is also presented as it is resulting from the plastic defromation........ 12

Figure 1.4 Determination of the shot peening intensity using Almen intensity. (a) Almen strip held on an Almen holder during a shot peening treatmant for a given exposure time. (b) The arc height of the shot peened strip is then measured using an Almen gage. (c) The saturation curve is fitted from the arc height measurements of strips shot peened at different exposure times. The Almen intensity corresponds to the arc height of the saturation point. Reprinted from Gariépy (2012) 13

Figure 1.5 Penetration versus spatial resolution for various residual stress measurements methods. Reprinted from Schajer & Ruud (2013) with permission........ 23

Figure 1.6 Schematic of an X-ray tube showing the production of X-rays 25

Figure 1.7 Schematic comparison of hypothetical X-ray spectra formed of Kα and Kβ lines a) before and b) after the use of a filter. The dashed line is the mass absorption of the adequate filter, having its K absorption edge between the Kα and Kβ lines........ 26

Figure 1.8 Illustration of the Kα doublet, with Kα_1 and Kα_2 components. I_{α_1} and θ_{α_1} are the intensity and the Bragg angle corresponding to the Kα_1 line, respectively, whereas I_{α_2} and θ_{α_2} are the ones for the Kα_2 line........ 27

Figure 1.9 Schematic representation of a unit cell, where $\boldsymbol{a}$, $\boldsymbol{b}$, and $\boldsymbol{c}$ are the unit cell vectors and α, β, and γ are the angles between these vectors 28

Figure 1.10 Schematic representations of a) a body-centered cubic (BCC) structure and b) a face-centered cubic (FCC) structure 28

Figure 1.11 Schematic representation of a cubic unit cell. [100], [0$\bar{1}$0], and [001] directions are presented as vectors. (100) and (23$\bar{1}$) planes are presented in grey 29

Figure 1.12 Diffraction of X-rays by the $\{hkl\}$ planes of a single crystal. Bragg's law is satisfy when the incident X-rays (having a β angle with the surface normal) have a $\theta^{\{hkl\}}$ angle the $\{hkl\}$ planes of atoms (having themself a ψ angle with the surface normal). Other symbols: $\mathbf{V^{\{hkl\}}}$, vector normal to the $\{hkl\}$ planes; $d^{\{hkl\}}$, interplanar spacing; $\mathbf{V_{Scat}}$, scattering vector; λ, X-rays wavelegnth 30

Figure 1.13 Illustration of full width at half the maximum ($FWHM$) value. θ_1 and θ_2, found for $\frac{1}{2}I_{max}$, are used to find the peak position 32

Figure 1.14 Illustration of full width at half the maximum ($FWHM$) value. θ_1 and θ_2, found for $\frac{1}{2}I_{max}$, are used to find the peak position 33

Figure 1.15 The fraction G_x of the total diffracted intensity contributed by a surface layer of depth x, for $\mu = 473$ cm^{-1} (brass), $2\theta = 136.7°$, and normal incidence (Note: 0.001 in. = 25.4 µm). Reprinted from Cullity (1956d) 35

Figure 1.16 Illustration of the lattice strain effects on the diffraction peak. Reprinted from Cullity (1956d) 36

Figure 1.17 Schematic representation of the layer removal process and residual stress redistribution. Reprinted from Savaria *et al.* (2012) with permission 43

Figure 2.1 300M optical micrographs showing a) the tempered martensite, the insert presents a closeup of the martensite laths and plates, and b) the prior austenite grain boundaries. Reprinted from Bag *et al.* (2019) 48

Figure 2.2 IN718 optical micrographs presenting the microstructure of a) the ∅25 mm and b) the ∅89 mm samples. Niobium (NbC) carbides, titanium carbo-nitride (TiCN), and δ phase along the grain boundaries can be observed. Reprinted with permission from Klotz *et al.* (2018a) and Klotz *et al.* (2017a), respectively 49

Figure 2.3 AA7050 optical micrograph presenting in the RD-TD plane the bimodal microstructure composed of small and large grains 50

Figure 2.4 Interaction volume in the case of electron-matter interactions for a scanning electron microscope 53

Figure 2.5 Illustration of electron interaction with crystalline material and Kikuchi diagram (EBSD pattern: EBSP). Reprinted from Maitland & Sitzman (2007) with permission 54

Figure 2.6 Illustration of a Vickers hardness test on a sample surface. The diagonals d_{HV1} and d_{HV2} are measured after indentation with a force F_{HV} 56

Figure 2.7 Illustration of a Knoop hardness test on a sample surface. The diagonal d_{HK} is measured after indentation with a force F_{HK} 57

Figure 2.8 Illustration of the minium recommended spacings for the Knoop and Vickers indentations. Reprinted from ASTM E384-17 (2017) with permission 58

Figure 2.9 Definition of the sample (**S**) and laboratory (**L**) coordinate systems via the azimuth φ and tilt ψ angles. The scattering vector $\mathbf{V_{Scat}}$ is aligned with $\mathbf{L_3}$ 60

Figure 2.10 Illustration of the diffraction cone and the two linear detectors used in the case of the $\sin^2\psi$ method. The stress σ_φ is measured in the direction defined by the detectors plane (φ plane) 62

Figure 2.11 Example of $\varepsilon_{\varphi\psi}^{\{hkl\}}$ vs. $\sin^2\psi$ plot for a measurement on 300M with two linear detectors at nine β-tilts 64

Figure 2.12 Illustration of the diffraction cone and the 2D detector used in the case of the $\cos\alpha$ method. The stress σ_φ is computed for a variation of α from 0° to 90° and the measurement of the corresponding strains $\varepsilon_{\alpha}^{\{hkl\}}$, $\varepsilon_{\pi+\alpha}^{\{hkl\}}$, $\varepsilon_{-\alpha}^{\{hkl\}}$, and $\varepsilon_{\pi-\alpha}^{\{hkl\}}$ 65

Figure 2.13 Example of $\overline{\varepsilon}_{\alpha}^{\{hkl\}}$ vs. $\cos\alpha$ plot for a measurement on 300M with a 2D detector in a single exposure 67

Figure 2.14 Theoretical determination of the $\frac{1}{2}S_2^{\{hkl\}}$ constant using Voigt, Reuss, and Hill models for IN718 and $C_{11}^{\mathrm{C}} = 251.0$ GPa, $C_{12}^{\mathrm{C}} = 135.5$ GPa, and $C_{44}^{\mathrm{C}} = 98$ GPa single crystal elastic constant. Examples of Γ values for different hkl values: $\Gamma(100) = 0$, $\Gamma(311) = 0.157$, $\Gamma(211) = 0.250$, and $\Gamma(111) = 0.333$ 70

Figure 2.15 Proto iXRD apparatus equipped with an interchangeable Cr-tube and two linear detectors (L1 and R2) 72

Figure 2.16 Pulstec μ-X360n apparatus equipped with a Cr-tube and a 2D detector 73

Figure 2.17 Electropolishing depth function of the time for the three materials 76

Figure 2.18 Example of the evolution of the depth profile, measured by the contact profilometer, for a shot peened IN718 specimen after several electropolishing steps 76

Figure 2.19 Drawings of the machined micro-tensile specimens used for a) 300M and IN718, b) AA7050 (dimensions in mm) 78

Figure 2.20 Experimental setups: micro-tensile machine and laser extensometer paired up with the Proto iXRD and Pulstec μ-X360n apparatuses 79

Figure 2.21 Nominal stress and strain evolution during the measurement of the IN718 XEC with the Pulstec μ-X360n 80

Figure 3.1 Residual stress profile assessement of a flat IN718 sample shot peened at 8 A by the $\sin^2\psi$ (Proto iXRD) and the $\cos\alpha$ (Pulstec μ-X360n) methods using Hill model to compute the XEC 83

Figure 3.2 XRD measured stresses vs. applied stresses for determination of the XEC value using a) the $\sin^2\psi$ method (Proto iXRD apparatus) and b) the $\cos\alpha$ method (Pulstec μ-X360n), for an inhomogeneous microstructure IN718 sample 84

Figure 3.3 Corrected residual stress profiles, for a IN718 sample shot peened at 8 A, as if XRD measurements were performed using the XEC values measured via the $\sin^2\psi$ (Proto iXRD) and the $\cos\alpha$ (Pulstec μ-X360n) methods 86

Figure 3.4 XRD measured stresses vs. applied stresses for determination of the XEC value using a) the $\sin^2\psi$ method (Proto iXRD apparatus) and b) the $\cos\alpha$ method (Pulstec μ-X360n), for an homogeneous microstructure IN718 sample 87

Figure 3.5 Orientation distribution maps for a) ∅25 mm (homogeneous microstructure) and b) ∅89 mm (inhomogeneous microstructure) samples represented as inverse pole figure (IPF) maps with respect to the rolling direction (RD) 91

Figure 3.6 Grain size distribution in percent of area ratio for a) ∅25 mm and b) ∅89 mm samples. The equivalent diameter, $\varnothing_{eq}$, is calculated as $\varnothing_{eq} = 2\sqrt{A_g/\pi}$ where A_g is the grain area. In the inset, the large grains designate the grains having a diameter of at least the average diameter plus 4 times the diameter standard deviation ($\varnothing_{eq} > 42$ µm) 92

Figure 3.7 Inverse pole figures for a) ∅25 mm and b) ∅89 mm samples texture analysis with respect to the rolling direction. Note that the <311> directions are shown, as they represent the diffraction direction 93

Figure 3.8 Inverse pole figures for the a) small and b) large ($\varnothing_{eq} > 42$ µm) grains of the ∅89 mm sample texture analysis with respect to the rolling direction. Note that the <311> directions are shown, as they represent the diffraction direction 94

Figure 3.9 Grain orientation spread (GOS) map for the ∅89 mm sample 95

Figure 3.10 Variations of the linear absorption coefficient for nickel (Ni, Z=28), μ_{Ni}, wih the X-ray energy, $E_{photons}$. Note that both axes have a logarithmic scale. Data from Chantler *et al.* (2005) 96

Figure 3.11 Fraction of the total diffracted intensity G_x function of the depth of penetration below the sample surface for different β incident angle and for a) the Mn-Kα radiation and b) the Cr-Kβ radiation. Curves for 0° to 40° β inclinations, with a 10° step size, are represented in grayscale. The average grain sizes of the ∅25 mm and ∅89 mm samples are plotted for comparison 98

Figure 3.12 Variations of the effective penetration depth for different incident beam angles β and for the left and right detectors used in the $\sin^2\psi$ method 100

Figure 3.13 Effect of α angle on the effective penetration depth computed for the Cr radiation in the case of the 2D detector used in the $\cos\alpha$ method and for different incident beam angles β 100

Figure 3.14 Illustration of X-rays diffracted by $\{hkl\}$ planes of an unstressed grain in the Bragg's condition. In this condition, the normal vector of the $\{hkl\}$ planes $\mathbf{V^{\{hkl\}}}$ is coincident with the scattering vector $\mathbf{V_{Scat}}$ and bisects the incident X-rays $\mathbf{V_{IXR}}$ and the diffracted X-rays $\mathbf{V_{DXR}}$, such as they make a $\theta_0^{\{hkl\}}$ angle with the $\{hkl\}$ planes having a lattice spacing $d_0^{\{hkl\}}$ 102

Figure 3.15 Orientation distribution maps of the ∅25 mm sample presenting the diffracting grains identified by a) the two linear detectors for nine inclinations (Proto iXRD) and b) the 2D detector for a single exposure (Pulstec μ-X360n). The IPF representation with respect to the RD has been kept 104

Figure 3.16 Simulated images seen by a) the two linear detectors for $\beta = 25°$ and b) the 2D detector for $\beta = 30°$ for the ∅25 mm sample. Diffracting grains are represented by the circular symbols and IPF-coloring with respect to the RD is used to show their mean orientations 105

Figure 3.17 Total number of unique diffracting grains versus the number of β angles taken by the two linear detectors in a ±25° range. The number of unique diffracting grains identified by the 2D detector at $\beta = 30°$ is plotted as dash-dot line for comparison 107

Figure 3.18 Total number of unique diffracting grains identified by the two linear detectors for different ranges and different number of β angles in a given range. The number of unique diffracting grains identified by the 2D detector at $\beta = 30°$ is plotted as dash-dot line for comparison 107

Figure 3.19 Total number of unique diffracting grains seen by the 2D detector versus the detector β angle 108

Figure 3.20 Simulated Debye ring on the 2D detector for $\beta = 30°$. Each circle represents a diffracting grain. The diffracting grains used for the calculation of $\overline{\varepsilon}_{\alpha}^{\{hkl\}}$ at $\alpha = 45.36°$ are plotted in red as an example 109

Figure 3.21 Pole figure of the (100), (110), (111), and (311) sets of planes for a) the whole ∅25 mm sample EBSD map and for the diffracting grains detected by b) the linear detectors and c) the 2D detector. Note that the (311) set of planes is the strain measurement set of planes used for residual stresses computation 111

Figure 3.22 Pole figure of the (311) diffracting planes for the two linear detectors at a) $\beta = -25°$, b) $\beta = 0°$, and c) $\beta = 25°$ 112

Figure 3.23 Pole figure of the (311) diffracting planes for the 2D detector for the the 125 α angles maximum and minimum texture indexes at a) $\alpha = 0.72°$ and b) $\alpha = 25.20°$, respectively, as well as c) the $\alpha = 45.36°$ example 112

Figure 3.24 Number of diffracting grains detected by the two linear detectors for nine β angles and their corresponding XEC $\frac{1}{2}S_2^{\{311\}}$ values calculated for the {311} planes 115

Figure 3.25 a) XEC $\frac{1}{2}S_2^{\{311\}}$ values calculated for the diffracting grains detected by the 2D detector at $\beta = 30°$ for 125 α angles (from 0° to 90°). b)

Mean and confidence interval ($CI_{95\%}$) of the XEC $\frac{1}{2}S_2^{\{311\}}$ values calculated for different α-step sizes. The corresponding number of α angles is presented below or above the error bar 116

Figure 3.26 Number of diffracting grains detected by the 2D detector for different β angles and corresponding XEC $\frac{1}{2}S_2^{\{311\}}$ values calculated for a 0.72° α-step size (125 α angles) 117

Figure 3.27 Orientation distribution maps of ∅25 mm sample for the following reduction factor: a) R=1 (initial map), b) R=1/2, c) R=1/5, d) R=1/10, e) R=1/15, and f) R=1/20. Information on map maximum texture index and grain density (in grains/mm^2) are also provided 119

Figure 3.28 Histogram of the number of grains for the different reduced maps and the corresponding diffracting grains number for the linear and 2D detectors. The percentage of diffracting grains is also plotted for both detectors geometry 120

Figure 3.29 Mean values and confidence interval on the standard deviation ($CI_{95\%}$) of the XEC $\frac{1}{2}S_2^{\{311\}}$ determined for the diffracting grains detected by the linear and 2D detectors in the case of five resized maps. Results for the 2D detector are presented for 0.72° and 1.2° α-step sizes 121

Figure 3.30 Total number of unique diffracting grains and XEC $\frac{1}{2}S_2^{\{311\}}$ mean values calculated for two different reduction factors a) R=1/15 and b) R=1/20 and for measurements with both techniques in the case of oscillations in the φ-plane. The calculations for the 2D detector were performed using a 1.2° α-step sizes. The error bars represent the confidence interval on the standard deviation ($CI_{95\%}$) 122

Figure 3.31 Pole figure of the (100), (110), (111), and (311) sets of planes for a) the whole inhomogeneous sample (∅89 mm) EBSD map and for the diffracting grains detected by b) the linear detectors and c) the 2D detector. Note that the (311) set of planes is the strain measurement set of planes used for residual stresses computation 124

Figure 3.32 Comparison of the XEC $\frac{1}{2}S_2^{\{311\}}$ calculated for the ∅25 mm and ∅89 mm samples for a) nine β angles in the case of measurements with two linear detectors and b) 125 α angles for the 2D detector at β = 30° 125

Figure 3.33 Mean and confidence interval ($CI_{95\%}$) of the XEC $\frac{1}{2}S_2^{\{311\}}$ calculated for different α step sizes for the ∅89 mm sample. The corresponding number of α angles is presented below or above the error bar 126

Figure 4.1 Geometry of the fatigue IN718 specimen. All dimensions are in mm. The longitudinal direction corresponds to the RD. Reprinted from Klotz *et al.* (2018a) 132

Figure 4.2 Final surface of the 8 A specimen's electropolished pocket 133

Figure 4.3 Residual stress (top) and FWHM (bottom) profiles for fatigue IN718 specimens shot peened with CW14 media at an intensity of 4 A and 8 A 134

Figure 4.4 Example of the $FWHM$-values variation for the α angle describing the Debye ring, for one of the three surface measurements of the CW14 8 A specimen 135

Figure 4.5 a) Empirical curve relating the (420) diffraction peak width to the cold work percentage for Rene95 samples deformed by various means. b) Dependence of (220) peak width on cold work expressed as true plastic strain. Reprinted from Prevéy (1987) and Prevéy (2000), respectively 136

Figure 4.6 Calibration curve for the cold work estimation of IN718 138

Figure 4.7 In-depth cold work profiles for the 4 A and 8 A specimens 139

Figure 4.8 Experimental true stress vs. plastic strain curve and its fitting. Eq. (20) corresponds to Equation (4.3) in the present document. Reprinted from Klotz *et al.* (2018b) with permission 140

Figure 4.9 In-depth yield strength profiles for the 4 A and 8 A specimens 141

Figure 4.10 In-depth microhardness profiles for the IN718 specimens shot peened at an intensity of a) 4 A and b) 8 A. Five measurement profiles are presented per specimen, along with the corresponding fitting curve 142

Figure 4.11 Geometry of the rectangular AA7050 specimen used for the residual stress relaxation measurements. All dimensions are in mm. Reprinted from Bianchetti *et al.* (2018) with permission 145

Figure 4.12 Residual stress (top) and FWHM (bottom) profiles for AA7050 specimens shot peened at an intensity of 8 A with Z425 and S230 media 146

Figure 4.13 Calibration curve for the cold work estimation of AA7050 at 0 MPa true isostress 147

Figure 4.14 In-depth cold work profiles for the AA7050 specimens shot peened at an intensity of 8 A with Z425 and S230 media 148

Figure 4.15 In-depth microhardness profiles for the AA7050 specimens shot peened at a) Z425 8 A and b) S230 8 A. Ten measurement profiles are presented per specimen 149

Figure 4.16 Geometry of the fatigue 300M specimen. All dimensions are in mm. Reprinted from Bag *et al.* (2019) 151

Figure 4.17 Residual stress (top) and FWHM (bottom) profiles for fatigue 300M specimens shot peened at an intensity of 8 A with CW14 and S230 media 152

Figure 4.18 Calibration curve for the cold work estimation of 300M at 0 MPa true isostress 153

Figure 4.19 In-depth cold work profiles for the 300M specimens shot peened at an intensity of 8 A with CW14 and S230 media 154

Figure 4.20 In-depth microhardness profiles for the 300M specimens shot peened at a) CW14 8 A and b) S230 8 A. Ten measurement profiles are presented per specimen 156

Figure 4.21 Optical micrograph of the CW14 specimen cross-section. Microstructure is revealed using Vilella's reagent. The RD is perpendicular to the micrograph 157

Figure 4.22 Orientation map of the subsurface of the CW14 specimen represented as IPF map with respect to the RD 158

Figure 4.23 Evolution of the average grain size from the shot peened surface. The equivalent diameter is computed from the grain's area, whereas the longest diameter corresponds to the longest distance between any two vertices of the grain boundary 158

Figure 4.24 Kernel average misorientation (KAM) map computed for the 1st neighbor order and a 10° threshold angle and evolution of the average KAM values for a given depth 160

LIST OF ABREVIATIONS

2D, 3D	Two Dimensional, Three Dimensional
AA	Aluminum Alloy
AISI	American Iron and Steel Institute
AMS	Aerospace Material Specification
AR	Area Reduction
ASTM	American Society for Testing and Materials
ASM	American Society for Metals
Bal.	Balance
BCC	Body-Centered Cubic (structure)
CW	Cut Wire
DE	Discrete Element
EBSD	Electron BackScattered Diffraction
EDM	Electric Discharge Machining
ETS	École de Technologie Supérieure
El.	Elongation
FE	Finite Element
FEA	Finite Element Analysis
FCC	Face-Centered Cubic (structure)
FWHM	Full Width at Half the Maximum

GOS	Grain Orientation Spread
HK_{xgf}	Knoop Hardness measured for *x* gram-force
HRC	Rockwell Hardness of type C
HV_{xgf}	Vickers Hardness measured for *x* gram-force
IN718	Inconel 718
KAM	Kernel Average Misorientation
LIBAD	Low-Incident-Beam-Angle-Diffraction
MBN	Magnetic Barkhausen Noise
ODF	Orientation Distribution Function
PF	Peak Fitting
SAE	Societe of Automotive Engineers
SD	Standard Deviation
SEM	Scanning Electron Microscope
UTS	Ultimate Tensile Strength
XEC	X-ray Elastic Constant
XRD	X-Ray Diffraction

LIST OF SYMBOLS

Latin symbols

a	Cubic lattice constant
A_g	Grain area
A_{PF}	Variable in the peak fitting function (ratio of intensities)
b	X-ray aperture size of the entrance
B_{PF}	Variable in the peak fitting function (linear background slope)
c	X-ray aperture size of the exit
C_{PF}	Variable in the peak fitting function (linear background intercept)
C_L	Sample-to-2D-detector distance
d	Interplanar spacing
$d^{\{hkl\}}$	Interplanar spacing of the $\{hkl\}$ family of planes
$d_0^{\{hkl\}}$	Interplanar spacing of the unstressed $\{hkl\}$ family of planes
d_{HK}	Diagonal of Knoop indentation
d_{HV}	Diagonal of Vickers indentation
E	Macroscopic Young's modulus
$E^{\{hkl\}}$	Young's modulus of the $\{hkl\}$ planes
E_k	Kinetic energy
$E_{photons}$	Energy of photons
f	Orientation distribution function (ODF)

F_{HK}	Applied force for a Knoop hardness test
F_{HV}	Applied force for a Vickers hardness test
$FWHM$	Breadth of the diffraction peak at half the peak maximum intensity
g_m	Crystallographic orientation of the set of diffracting grains m
hkl	Miller indices
HK	Knoop hardness value
HRC	Rockwell hardness value (type C)
HV	Vickers hardness value
I_0	Intensity of incident X-rays
I_D	Intensity of diffracted X-rays
I_{max}	Maximum intensity of the diffraction peak
$I_{\alpha_1}, I_{\alpha_2}$	Intensity of the $\mathrm{K}\alpha_1$ and $\mathrm{K}\alpha_2$ peaks
$K_{P_{VII}}$	Variable in Pearson VII distribution function (Peak width parameter)
$\mathrm{K}\alpha$	$\mathrm{K}\alpha$ radiation
$\mathrm{K}\alpha_1, \mathrm{K}\alpha_2$	$\mathrm{K}\alpha$ doublet
$\mathrm{K}\beta$	$\mathrm{K}\beta$ radiation
$\mathbf{L}$	Laboratory coordinate system
m	Set of diffracting grains
$m_{P_{VII}}$	Variable in Pearson VII distribution function
n	Integer

R	Reduction ratio
R	Fatigue stress ratio
$\mathrm{R_a}$	Arithmetical mean roughness
R_α	Debye ring radius for a given α angle
R^2	Coefficient of determination
$\mathbf{S}$	Sample coordinate system
$S_1^{\{hkl\}}$, $\frac{1}{2}S_2^{\{hkl\}}$	X-ray elastic constants for the $\{hkl\}$ planes
U_{AC}	X-ray tube voltage
$\mathbf{V}^{\{hkl\}}$	Vector normal to the $\{hkl\}$ planes
$\mathbf{V_{Scat}}$	Scattering vector, bisector of the incident and diffracted X-rays
Z	Atomic number of a chemical element

Greek symbols

α	Localization angle on the 2D detector
β	Angle between incident X-rays and the surface normal
ε_p	Cold work value
$\varepsilon^{\{hkl\}}$	Strain measured on the $\{hkl\}$ planes
$\varepsilon_{\varphi\psi}^{\{hkl\}}$	Strain measured on the $\{hkl\}$ planes in the direction defined by φ and ψ
$\varepsilon_{\alpha}^{\{hkl\}}$	Strain measured on the $\{hkl\}$ planes in the direction defined by α angle on the 2D detector
$\overline{\varepsilon}_{\alpha}^{\{hkl\}}$	Strain parameter computed for the $\cos\alpha$ method

2η	Diffraction cone semi-apex angle
θ	Bragg angle
θ_{Peak}	Bragg angle determined from the diffraction peak position
$\theta^{\{hkl\}}$	Scattering angle (Bragg angle) for the $\{hkl\}$ planes
$\theta_0^{\{hkl\}}$	Scattering angle (Bragg angle) for the unstressed $\{hkl\}$ planes
$\theta_{\alpha_1}, \theta_{\alpha_2}$	Bragg angle of the Kα_1 and Kα_2 peaks
λ	Wavelength of the electromagnetic radiation
$\lambda_{\mathrm{K}\alpha}$	Wavelength of the Kα radiation
$\lambda_{\mathrm{K}\beta}$	Wavelength of the Kβ radiation
μ	Linear absorption coefficient of a material
ν	Poisson's ratio
$\nu^{\{hkl\}}$	Poisson's ratio of the $\{hkl\}$ planes
ρ	Volumetric mass density
$\sigma^{\mathrm{I}}, \sigma^{\mathrm{II}}, \sigma^{\mathrm{III}}$	Types of residual stresses (I: macrostress; II, III: microstresses)
σ_c	Corrected stress
σ_{fmax}	Maximum stress during a fatigue cycle
σ_m	Measured stress
σ_{max}	Maximum compressive residual stress
$\sigma_{\mathrm{surface}}$	Surface residual stress
σ_{true}	True stress

σ_u	Ultimate tensile strength
$\sigma_{y0.05\%}$	0.05% offset yield strength
$\sigma_{y0.2\%}$	0.2% offset yield strength
σ_φ	Stress measured by XRD in the φ direction
ψ	Angle between the $\{hkl\}$ planes normal and the surface normal
τ	Effective penetration depth
ω_I	Angle between the specimen surface and the incident X-rays
ω_D	Angle between the specimen surface and the diffracted X-rays
ω_m	Weight of the set of diffracting grains m

Other symbols

$\varnothing$	Diameter
$\varnothing_{eq}$	Equivalent diameter

LIST OF MEASUREMENT UNITS

	Units of measurements
A	Ampere
mA	Milliampere
V	Volt
kV	Kilovolt
J	Joule
keV	Kiloelectronvolt ($\approx 1.602\ 10^{-16}$ J)
°	Degree
°C	Degree Celsius
in.	Inch
mm	Millimeter
μm	Micrometer
nm	Nanometer
Å	Ångström (10^{-10} m)
ml	Milliliter
s	Second
min	Minute
Hz	Hertz
g	Gram

kg	Kilogram
N	Newton
MPa	Megapascal
GPa	Gigapascal
gf	Gram-force (1 gf ≈ 9.80665 μN)

Physical constants

c	Speed of light in a vacuum (≈ 299.792 10^6 $m.s^{-1}$)
e	Elementary charge (≈ 1.602 10^{-19} A.s)
h	Planck's constant (≈ 6.626 10^{-34} $m^2.kg.s^{-1}$)

INTRODUCTION

Aerospace, automotive and power industries are constantly looking for means to improve the performance of the produced parts, and in particular their fatigue performances. Many processes, such as chemical surface treatments, cold-rolling or shot peening, are known to improve fatigue performances. Shot peening is a cold work process consisting in propelling small particles, also named shots, at high velocity on metallic parts to introduce a surface layer of plastic strain and residual stresses. It has commonly been used as a surface treatment since the 1930's. However, shot peening also increases surface roughness and may introduce surface damages such as material folds and rolled edges, which are detrimental to the component fatigue life (Wagner, 1999; He *et al.*, 2013). Finally, even if shot peening is often considered as a beneficial treatment for fatigue life improvement, its effects are rarely taken into account at design stages, as it necessitates a precise assessment of the introduced residual stress and cold work profiles besides the development of simulation methods and fatigue life prediction models.

Residual stresses are stresses that remain in materials and components when no external loads are applied (Totten *et al.*, 2002). They can either be tensile or compressive, and are self-equilibrated within the whole volume of the material or component. They appears in parts due to differential deformations from one region to the next. They are important drivers for fatigue life improvement. Indeed, a crack nucleation and propagation may be delayed thanks to a compressive residual stress field or, on the contrary, advanced in a tensile residual stress field.

Many techniques exist to measure the residual stresses and the X-ray diffraction (XRD) technique is one among them. The XRD technique has the advantage of providing information on the induced cold work. The XRD technique is widely used in the industry and has been studied by numerous authors over the past decades. Different residual stress determination methods compose this technique, with the so-called $\sin^2\psi$ method, using linear detectors, being the most commonly used. An alternative method called the $\cos\alpha$ method, developed by Taira *et al.*

(1978), starts to reemerge in 2013 thanks to the technological improvements and commercialization of XRD apparatuses equipped with a two-dimensional (2D) detector. This method was initially published in Japanese, limiting its use. The $\cos\alpha$ method offers a faster residual stress determination than the $\sin^2\psi$ method, thanks to the 2D approach.

The residual stress profile induced by shot peening being deeper than the XRD-measurement penetration, a layer removal procedure, such as electropolishing, must be paired-up with the XRD measurement to assess it. During the layer removal process residual stresses may redistribute and an analytical or numerical correction is necessary to adjust the measured values.

In that context, four leading aerospace companies (Héroux-Devtek, Pratt & Whitney Canada, L3-Communications MAS, and Bell Helicopter Textron Canada) regularly using shot peening have joined forces on a common project about the development of predictive tools for shot peening effects on fatigue life for three materials (300M steel, nickel-based superalloy IN718, and aluminum alloy 7050-T7451). The research project involved one M.Sc. student, five Ph.D. candidates, four post-doctoral fellows, and one research associate enrolled in three universities (École de technologie supérieure, École Polytechnique de Montréal, and McGill University). This Ph.D. thesis is part of the research project and covers the aspects related to the residual stresses measurements, in particular, the effect of the XRD method, the cold work quantification, and the effects of the layer removal process.

During this Ph.D. thesis, an extensive work was realized to overcome the research project requirements: determination of the X-ray elastic constant for the three materials to improve the residual stress measurement accuracy, measurements of the residual stress and cold work profiles induced by different shot peening conditions, comparison with finite element simulation of the shot peening process, or for fatigue life prediction model via a modified Navarro and de los Rios model (Navarro & de los Rios, 1988; Navarro & de Los Rios, 1988). These collaborative activities resulted in six peer-reviewed articles and five conference proceedings, listed in Appendix I, in which the present author has the second or third position.

The thesis is organized as follows: A literature review is conduced in Chapter 1, followed in Chapter 2 by a methodology section detailing the implementations for the samples shot peening, the microstructural characterization, the determination of the residual stresses and the X-ray elastic constant, and the calibration of the cold work measurements. Chapter 3 presents a comparison between the $\sin^2\psi$ and $\cos\alpha$ methods based on the identification of the diffracting grains from an EBSD map. Chapter 4 shows the use of the XRD peak width to determine the cold work profile introduced by shot peening for the three materials. Finally, the conclusions of this work as well as the recommendations for future work are provided.

CHAPTER 1

LITERATURE REVIEW

This chapter first introduces the general concepts related to shot peening and its effects on the materials. A review of the residual stress measurement techniques is then presented. Finally, specific information on the X-ray diffraction technique is further provided.

1.1 General considerations

Some definitions are provided in this section to allow describing in the next sections the shot peening process, the residual stress measurement techniques, and the X-ray diffraction for residual stress measurement.

Residual stresses can be classified in three different types. The macrostresses, stresses that vary over large distances compared to the microstructure, are described as type I, σ^{I}. The residual stress variations at the grain scale correspond to a type II, σ^{II}, and are mostly due to the accommodation to the various elastic properties of each grain. Type II stresses are the adaptation of the grains to the type I field. Finally, the type III, σ^{III}, describes the stress variations at the atomic scale, which are typically due to dislocation stress fields or incoherent interfaces (Withers & Bhadeshia, 2001). σ^{II} and σ^{III} are often called microstresses. Figure 1.1 illustrates the three different types of residual stresses with the variation of σ^{I} over a larger distance than σ^{II} and σ^{III}, which varies from grain to grain and within a grain, respectively. It is worth noting that the type II residual stresses are nearly always present in polycrystalline materials that have undergone plastic deformations as the elastic and plastic properties are function of the grains orientation. For a residual stress measurement using the XRD technique, σ^{I} affects the diffraction peak position, whereas σ^{II} and σ^{III} affect the diffraction peak width. Further details are provided in Section 1.5.

When a material is plastically deformed by cold working the mechanical energy which is not converted into heat is stored, raising the material's internal energy. The lattice distortion and

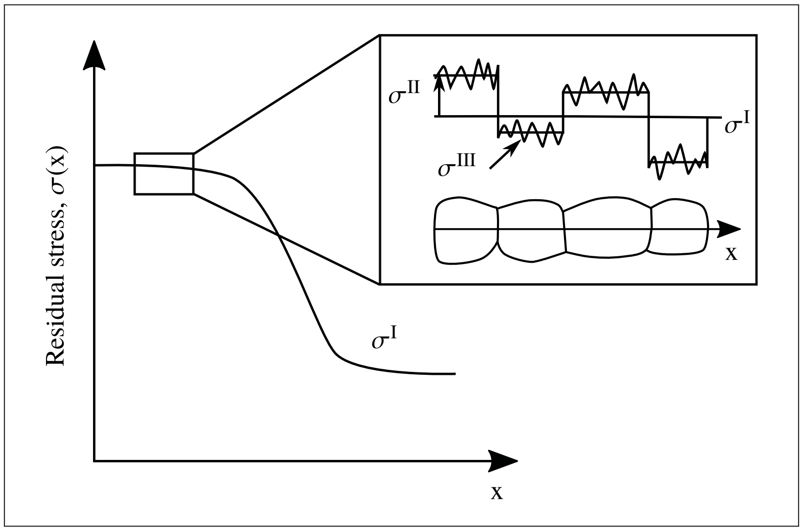

Figure 1.1 Illustration of type I residual stresses (macrostress), σ^{I}, and the type II and III residual stresses over a few grains, σ^{II} and σ^{III}, respectively

disorder are essential characteristics of cold work (Bever *et al.*, 1973). The plastic deformation resistance of the material increases as strain increases and is called strain-hardening (Hertzberg *et al.*, 2012). The plastic deformation in materials of cubic lattice structures takes place by dislocation movements (Kocks, 1976). A dislocation is a linear lattice defect corresponding to an irregularity in the lattice pattern which may results in atoms with missing neighbors (Read, 1953). Thus, strain-hardening is a consequence of the stored dislocations generated by previous plastic deformation and that did not exit the material by reaching the surface, annihilate each other, or being absorbed by grain boundaries (Kocks, 1976).

On the contrary, work softening is when less stress is needed to continue deformation and it is characterized by a decrease of the mechanical properties. The mechanism responsible for work softening is the change in dislocation structure due to the temperature and/or the applied stress (Seeger *et al.*, 1956).

Finally, residual stress relaxation can happen in fatigue as complex interactions occur between the macro residual stress state (type I) and the cycling loading stresses, as well as between the micro residual stresses (type II and III) and the strain-hardening and/or work softening processes of the material under multiple loadings (Löhe *et al.*, 2002). Residual stresses relaxation is hence the response to an applied strain or stress resulting in a decrease in residual stress (in absolute value) (Meyers & Chawla, 2009). For instance, micro residual stresses can relaxed if the dislocations rearrange with a lower distortion energy due to further microplastic deformation. On the other hand they can increase if new dislocations are produced (Löhe & Vöhringer, 2002).

1.2 Materials

Three different materials, having very different mechanical properties, are studied in the research project and are presented in this section.

1.2.1 300M

The medium-carbon (0.4% C) high strength 300M steel is a body-centered cubic (BCC) material manufactured by vacuum arc remelting (VAR). 300M steel is essentially an AISI 4340 steel, widely used in the industry, with a higher silicon concentration (1.6% Si) and slightly higher quantities of carbon and molybdenum (Chandler, 1995a). The minimum and maximum chemical composition required by the AMS 6257F (2016) standard are listed in Table 1.1. For aerospace applications, 300M steel is heat treated as follows (Chandler, 1995a; AMS 6257F, 2016):

- **Normalizing.** Heat at 925°C for 1 h followed by air cooling.
- **Hardening.** Austenitize at 870°C for 1 h followed by oil quenching.
- **Double tempering.** Hold 2 h at 300°C followed by air cooling (×2).

Table 1.1 300M steel chemical composition (weight %) (AMS 6257F, 2016). Bal.: balance

	Ni	Si	Cr	Mn	C	Mo	Cu	V	P	S	Fe
Minimum	1.65	1.45	0.7	0.65	0.4	0.35	-	0.05	-	-	Bal.
Maximum	1.92	1.61	0.8	0.77	0.4	0.37	0.1	0.08	0.006	0.001	-

Youngblood & Raghavan (1977) showed that the microstructure resulting from these heat treatments consists in tempered martensitic laths and plates. The autors reported the presence of carbide precipitates, as well as a very low amount of retained austenite located at the grain boundaries. The minimal tensile properties for 300M steel as specified by AMS 6257F (2016) are presented in Table 1.2. Thanks to its excellent mechanical properties 300M steel is, for instance, widely used for aircraft landing gears and rotor shafts.

Table 1.2 Minimal tensile properties required for 300M steel (AMS 6257F, 2016)

σ_u (MPa)	$\sigma_{y0.2\%}$ (MPa)	El.(%)	AR(%)
1931	1586	8	30

1.2.2 IN718

The nickel-based superalloy Inconel 718 (IN718) is an austenitic face-centered cubic (FCC) matrix material. IN718 exhibits excellent creep and fatigue properties in a various range of temperatures. These properties are conferred by the matrix strengthening thanks to two types of γ precipitates: the metastable γ''-Ni_3Nb and γ'-$Ni_3(Ti,Al)$ precipitates (Oblak *et al.*, 1974; Fournier & Pineau, 1977). IN718 also contains a second phase δ-Ni_3Nb. These particles can be found at the grain boundaries or within the grains (Sundararaman *et al.*, 1988). The minimum and maximum chemical composition required by the AMS 5663M (2009) standard are presented in Table 1.3.

Table 1.3 IN718 chemical composition (weight %) (AMS 5663M, 2009). Bal.: balance

	Ni	Cr	Nb	Mo	Ti	Al	Co	Mn	Si	Cu	C	Fe
Minimum	50.0	17.0	4.75	2.8	0.65	0.2	-	-	-	-	-	Bal.
Maximum	55.0	21.0	5.5	3.3	1.15	0.8	1.0	0.35	0.35	0.3	0.08	-

The minimal tensile properties at room temperature for IN718 (AMS 5663M, 2009) are presented in Table 1.4. Due to its excellent mechanical properties at high temperature IN718 is extensively used for aerospace components such as turbine disks or blades.

Table 1.4 Minimal tensile properties required for IN718 at room temperature (AMS 5663M, 2009)

σ_u (MPa)	$\sigma_{y0.2\%}$ (MPa)	El.(%)	AR(%)
1276	1034	12	15

1.2.3 AA7050-T7451

The aluminum alloy (AA) 7xxx serie is also a FCC metal, mainly alloyed with zinc, and including magnesium and copper. The minimum and maximum chemical composition required by the AMS 4050J (2014) standard for AA7050-T7451 are presented in Table 1.5. T7451 designation stands for the heat treatments that the AA7050 has been given. The T74 designation indicates that the alloy has been solution heat treated and overaged to increase the alloy strength and maintain good corrosion properties. The additional digits (i.e., 51) are assigned to a stress-relieved process, consisting on stretching the material by few percents (Kaufman, 2000).

Table 1.5 AA7050 chemical composition (weight %) (AMS 4050J, 2014). Bal.: balance

	Zn	Cu	Mg	Zr	Fe	Si	Mn	Ti	Cr	Al
Minimum	5.7	2.0	1.9	0.08	-	-	-	-	-	Bal.
Maximum	6.7	2.6	2.6	0.15	0.15	0.12	0.1	0.06	0.04	-

The minimal tensile properties for AA7050-T7451 (AMS 4050J, 2014) are presented in Table 1.6. Thanks to its high ratio of strength to density, AA7050 is often used as part of an aircraft's fuselage.

Table 1.6 Minimal tensile properties required for a 6 mm to 51 mm thick AA7050-T7451 plate (AMS 4050J, 2014)

σ_u (MPa)	$\sigma_{y0.2\%}$ (MPa)	El.(%)	AR(%)
510	441	10	-

1.3 Shot peening

Shot peening treatment is a cold working surface treatment that consists in propelling hard shots at high velocity on a ductile metallic surface. The repeated impacts, by compressing the surface layer, create a tensile plastic deformation zone. Given that the surrounding material is not permanently deformed, it opposes the plastic stretching, which results in a compressive residual stress field (Kirk, 1999).

1.3.1 Shot peening mechanics

Al-Hassani (1981) and Wohlfahrt (1984) have described the mechanical aspect leading to different residual stress profile shapes and have proposed two mechanisms. The maximum plastic strain and consequently residual stress observed beneath the surface was explained by Al-Hassani (1981) as a consequence of the Hertz theory, which implies that when a load is statically applied by a spherical indenter to a softer material, the maximum shear stress is located beneath the surface. On the other hand, Wohlfahrt (1984) used the idea of a hammering process, which leads to an elastic-plastic elongation of the surface, resulting in a maximum compressive residual stress located at the surface.

1.3.2 Shot peening induced residual stresses

A typical shot peening residual stress profile is presented in Figure 1.2. The maximum compressive residual stress σ_{max} is usually found below the surface and is higher than the surface residual stress σ_{surface}. Nonetheless, some authors (Farrahi *et al.*, 1995; Nobre *et al.*, 1999; Cammett *et al.*, 2005; Zinn & Scholtes, 2005; Benedetti *et al.*, 2010) have reported a maximum compressive residual stress located at the surface under various shot peening conditions. The compressive residual stresses are then balanced by the presence of tensile residual stress. Zinn *et al.* (2002) showed that the residual stress profile is mostly affected by the shot energy, which is mainly controlled by shot size and velocity: the bigger the shots and/or the higher the velocity, the higher is the surface compressive residual stress and the deeper are the compressive residual stresses. Zinn *et al.* (2002) also observed that a higher shot flow rate creates a deeper residual stress affected zone. Finally, the residual stress field introduced by shot peening a flat surface is often found and considered as equi-biaxial due to the nature of the treatment (Al-Obaid, 1995; Kim *et al.*, 2012).

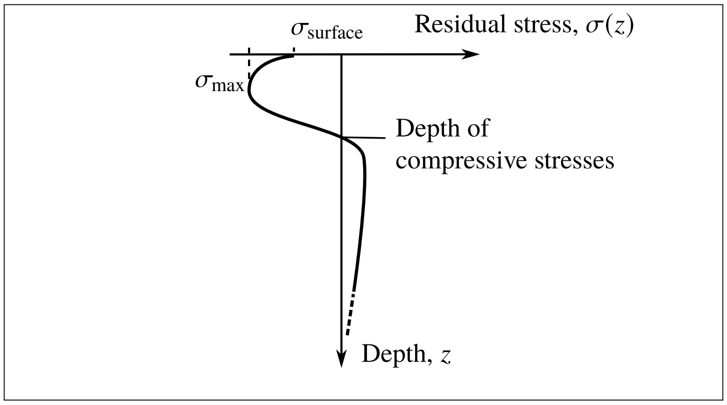

Figure 1.2 Typical residual stress profile $\sigma(z)$ below the surface after shot peening. The maximum compressive residual stress σ_{max} is usually found below the surface and is higher than the surface residual stress σ_{surface}

1.3.3 Shot peening induced cold work

A typical cold work profile, $\varepsilon_p(z)$, induced by shot peening and following the Hertz theory is presented in Figure 1.3 along with the typical residual stress previously presented. Korsunsky (2005) showed that the maximum of plastic deformation is also found under the surface, as the plastic deformation gives rise to the residual stresses (Jun & Korsunsky, 2010), by modeling the residual stress profile induced by shot peening using the concept of eigenstrain (inelastic strain). The cold work is presented instead of the eigenstrain because the only source of eigenstrains in shot peening is plastic strains (Faucheux *et al.*, 2018).

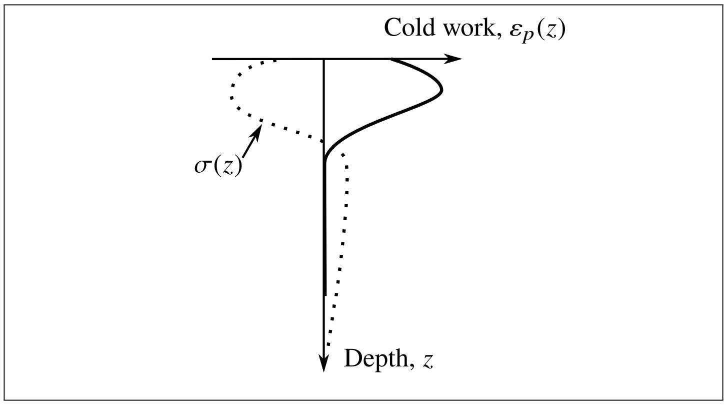

Figure 1.3 Typical cold work profile $\varepsilon_p(z)$ below the surface after shot peening. The maximum cold work is often found below the surface or at the sruface. The residual stress profile $\sigma(z)$ is also presented as it is resulting from the plastic defromation

1.3.4 Shot peening treatment characterization

The shot peening treatment is often characterized by the peening intensity and the surface coverage. The peening intensity is defined as the arc height of a specific point on a saturation curve. It should not be confused with the shot stream energy, which increases with the shot stream flow rate (Kirk, 2016). The term shot energy is often used in academy, especially for numerical researches, whereas the industry prefers the peening intensity to describe a treatment.

The Almen intensity is a measure of the peening intensity commonly used in the industry (SAE J442, 2008). A saturation curve is obtained by shot peening flat steel strips (AISI 1070), called Almen strips (held in a strip holder as shown in Figure 1.4(a)), for different periods of time while keeping the other process parameters constant. When the Almen strip is released from the holder, the strip bends due to the plastic strain accumulated at the peened surface. The free deflection, called arc height, is measured using an Almen gage and converted into Almen units (Figure 1.4(b)). The arc height value increases when increasing the exposure time and reaches saturation. The saturation point is defined as the point where doubling the exposure increases the arc height by only 10% (SAE J443, 2017). The Almen intensity of the treatment is the arc height value a_h^S at the saturation time t_{sat}, as presented in Figure 1.4(c). In the metric system, Almen intensities are evaluated in mm, whereas in the imperial system, Almen intensities are evaluated in thousandths of an inch. The strip designation is always specified after the arc height value. For instance, in the imperial system a 8 A intensity corresponds to a 0.008 in. arc height at saturation for measurements with an A strip type. Three strip types, having different thicknesses, are available to determine the peening intensity: N, A, and C strips (0.79 mm, 1.30 mm, and 2.39 mm thick, respectively). N, A, and C intensities can approximately be related by: 1 A ≈ 0.3 C ≈ 3 N (Champaigne, 1993). The industrial treatments are often performed for intensities measured with an A strip type and 100% coverage. It is worth noting that different combinations of the shot peening parameters can yield the same intensity.

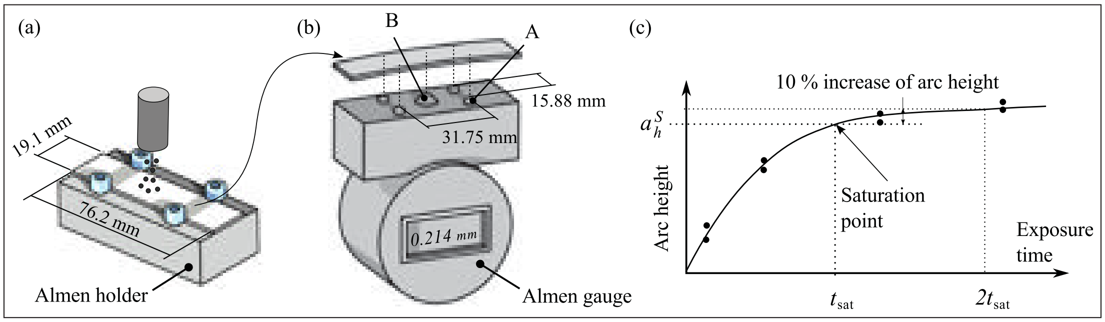

Figure 1.4 Determination of the shot peening intensity using Almen intensity. (a) Almen strip held on an Almen holder during a shot peening treatmant for a given exposure time. (b) The arc height of the shot peened strip is then measured using an Almen gage. (c) The saturation curve is fitted from the arc height measurements of strips shot peened at different exposure times. The Almen intensity corresponds to the arc height of the saturation point. Reprinted from Gariépy (2012)

Coverage is also an important parameter of the treatment. It is an optical measure of the dented surface percentage on the targeted surface (surface of the component and not Almen strip) and allows characterizing the treatment homogeneity. Full coverage is considered when the peened surface is covered by dimples at 98% to 100% (SAE J2277, 2013). Coverage greater than 100% are defined as multiples of the peening time required to reach full coverage.

1.3.5 Shot peening effects

The shot peening process is widely used in industry to improve component's fatigue life. Indeed, de Los Rios *et al.* (1995) have showed that shot peening affects the crack behavior by delaying both crack initiation and crack propagation in A316 stainless steel thanks to the residual stresses and strain-hardening which increase the resistance to plastic deformation at the crack tip. Improvement of the fatigue life also occurs with the grain refinement as grain boundaries act as microstructural barriers that a crack must overcome to propagate, decreasing the crack growth rate (De Los Rios *et al.*, 1999). Different authors (Wang *et al.*, 2003; Sato *et al.*, 2004; Liu *et al.*, 2007; Gariépy, 2012) have observed a grain refinement after shot peening for different materials, such as steels and aluminum alloys.

However, the shot peening treatment also tends to increase the surface roughness, which is known to decrease fatigue life (Maiya & Busch, 1975). Llaneza & Belzunce (2015) showed, in the case of different heat treatments of AISI 4340, that the surface roughness after shot peening increases linearly with the material hardness (the lower the hardness the higher the roughness). The authors also observed an increase of surface roughness with the shot peening intensity.

Finally, the fatigue performance can decrease with the presence of surface defects. Surface defects, such as material overlaps or micro-cracks, have been observed by Fathallah *et al.* (2004) at the shot peened surface of a traditional treatment. Overlapping dimples or craters, decreasing the fatigue performance, have been also observed by Bagherifard & Guagliano (2012) for a more severe shot peening treatment of low-alloy steel (high Almen intensity: 15 C and 1500% coverage).

1.3.5.1 Shot peening effects on 300M

Prevéy *et al.* (2005) studied the effects of shot peening and low plasticity burnishing on corrosion fatigue and stress corrosion cracking performances of 300M steel. The authors performed shot peening with cut wire CW14 media ($\varnothing = 0.35$ mm) for 150% coverage at 8 A and 10 A intensities on a 55 HRC heat-treated material. They reported higher maximum compressive residual stress and surface residual stress for the 8 A specimen with -1033 MPa and -800 MPa, respectively. The residual stress affected layer is deeper for the 10 A specimen (with 160 μm) than for the 8 A (with 125 μm). Torres & Voorwald (2002) observed similar residual stress results after shot peening at 6.3 A for a quenched and tempered AISI 4340 steel having a hardness of 50-53 HRC.

Zinn & Scholtes (2005) studied the influence of shot velocity and shot size on the Almen intensity for a AISI 4140 steel and two heat treatment conditions. Shot peening treatments were performed with steel shot of different sizes: S110 ($\varnothing$ = 0.28 mm), S170 ($\varnothing$ = 0.43 mm), and S230 ($\varnothing$ = 0.58 mm), and for velocities ranging from 20 $m.s^{-1}$ to 40 $m.s^{-1}$, yielding intensities ranging from ~ 4.3 A to ~ 17.5 A. AISI 4140 steel has similar chemical composition than AISI 4340 steel (same carbon amount), but does not contain nickel (Chandler, 1995b,c). Using XRD for residual stress measurements, on an annealed condition Zinn & Scholtes (2005) reported higher peak width values for the surface than for the bulk material. But on a quenched and tempered condition, they have shown that the diffraction peak widths were narrower for the surface and subsurface measurements than for the bulk material values and this for all shot peening conditions (shot sizes and shot velocities). The narrowest width values were found subsurface and the values were decreasing as the shot size and shot velocity were increased. When comparing the peak widths of the bulk materials, the annealed condition exhibit narrower values than the quenched and tempered condition. Zinn & Scholtes (2005) attribute the lower surface and subsurface peak widths of the quenched and tempered condition to microstructural alterations.

Bag *et al.* (2019), members of this research project, observed similar residual stress profiles for shot peening at 8 A with two types of media: S230 and CW14 and a compressive residual stress layer of about 140 μm. They measured in average an higher roughness for the samples shot peened with CW14 media than S230 media, even though CW14 media as a smaller diameter than the S230 media, which can be explained by the more angular geometry of the CW14 media.

1.3.5.2 Shot peening effects on IN718

Prevéy (2000) showed, via XRD measurements, that the depth of compressive residual stresses is roughly 200 μm and than the maximum compressive residual stress can reach -1000 MPa for IN718 shot peened with S110 at an intensity of 10 A and for a coverage of 200%. Using a calibration curve relating peak width to cold work, Prevéy (2000) found that the measured cold work can be as high as 30%, with a cold work affected layer of roughly 120 μm. Hoffmeister *et al.* (2008) found similar cold work affected depth for an identical shot peening intensity.

Cammett *et al.* (2005) studied the effect of the coverage on the induced residual stresses and cold work in IN718 for a shot peening with cut wire CW14 media at a 9 A intensity. For a coverage varying from 61% to 400%, the authors found similar surface residual stresses, about -1100 MPa, for all tested conditions. They also found no significant changes in terms of maximum compressive residual stresses (-1200 MPa) for coverage higher than 85%. Finally, they observed similar cold work profiles for coverage higher than 100%, with a surface value ranging from 25% to 32% and an affected depth of about 125 μm. Similarly, Klotz *et al.* (2018a), members of this research project, found a maximum compressive residual stress of -1020 MPa for shot peening with CW14 at 8 A and 100% coverage and observed a cold work affected layer of 195 μm. Shot peening at 4 A with CW14 and S230, they found a noticeably higher maximum compressive residual stress for the CW14 condition, but similar compressive residual stress and cold work affected layers for the two conditions, about 120 μm.

Zaleski *et al.* (2017) studied the effect of shot peening energy on the surface roughness of IN718. The authors reported a reduction of the roughness after shot peening with respect to the prior milling condition (corresponding to a $R_a = 0.67$ μm).

1.3.5.3 Shot peening effects on AA7050-T7451

Carvalho & Voorwald (2007) worked on the shot peening influence on the fatigue strength of AA7050-T7451 for 120% coverage. Two different media were used glass ($\varnothing$ = 0.4 mm) and ceramic ($\varnothing$ = 0.4 mm) with two different intensities: 13 N ($\approx$ 4.3 A) and 22 N ($\approx$ 7.3 A), respectively. They found that glass shots with a lower intensity introduce more compressive residual stresses than ceramic shots. They reported a -280 MPa surface residual stress and a -450 MPa maximum residual stress for the glass shots versus -110 MPa and -300 MPa, respectively, for the ceramic shots. They observed the same residual stress affected depth, about 350 μm, for both conditions and reported a lower roughness for the glass shots than for the ceramic shots (R_a = 2.09 μm and R_a = 5.54 μm, respectively).

Benedetti *et al.* (2009) showed for AA7075-T651 that shot peening with ceramic shots Z425 for 100% coverage at 4.5 A significantly increases the surface roughness (R_a = 3.39 μm) compared to the as-received material (R_a = 0.25 μm) and creates a hardened layer of 300 μm, with a 190 $HV_{0.1}$ peak of hardness at 150 μm below the surface (bulk hardness: 178 $HV_{0.1}$). The author reported no grain refinement below the surface from optic micrographs. Nonetheless, grain refinement was reported by Gariépy *et al.* (2013) from EBSD maps for AA2024-T351 shot peened with ceramic shots at 7.4 A and for 98% coverage.

Bianchetti *et al.* (2019), members of this research project, found a higher maximum compressive residual stress for ceramic shot Z425 ($\varnothing = [0.43, 0.6]$ mm) than for steel shot S230 when shot peening at an intensity of 8 A and for 100% coverage, but a similar compressive residual stress affected layers of 240 μm. The authors reported the difficulties to determine the cold work profiles introduced by shot peening via microhardness measurements with the acquisition of constant hardnesses through the thickness. Instead, they estimated the cold work profiles using a calibration curve relating peak width to cold work, as Prevéy (2000) for IN718. They found a 150 μm affected layer for both shot peening conditions. In a previous study, Bianchetti *et al.* (2018) observed for a 8 A shot peening intensity a higher roughness for Z425 than for S230 and also showed that shot peening with CW14 increases further the roughness.

1.4 Residual stress measurement techniques

Numerous techniques exist to measure residual stresses. Two main categories stand out: the relaxation and the diffraction techniques, even if unconventional techniques have emerged during the past decades. It is worth noting that residual stresses are never measured directly, but it is rather strains that are recorded, no matter the measurement method. Several factors, such as the residual stress affected depth or the expected maximum residual stress, are to take into consideration to choose the appropriate technique for a given application.

1.4.1 Relaxation technique

Relaxation-based methods use the stress redistribution due to cutting or material removal and therefore they are destructive methods. The relaxations that occur are elastic deformations and can be related to the released residual stresses (Schajer & Ruud, 2013).

1.4.1.1 Hole-drilling and ring core methods

The hole-drilling method (Mathar, 1934; ASTM E837-13a, 2013) is the most commonly used relaxation method. The method consists in drilling step by step a small hole at the center of a standardized hole-drilling strain gage rosette placed at the specimen surface. Beaney (1976) and Beaney & Procter (1974) showed that the bias should not exceed ±10% for uniform residual stresses within the hole depth. The ASTM E837-13a (2013) suggests to use the method for residual stresses that do not exceed 80% of the material yield stress for a thick material and 50% of the material yield stress for a thin material due to the possible occurrence of local yielding at the drilled-hole stress concentration points. Beghini *et al.* (2010) suggested the use of finite element analysis (FEA) to correct the effects of plasticity in the evaluation of high residual stresses.

The ring core method (Milbradt, 1951) is a variant of the hole-drilling method which allows measuring residual stresses close to the material yield stress with a lower risk of introducing plastic deformations due to stress concentration. Indeed, a ring of 15 mm to 150 mm diameter is made around a strain gage rosette instead of drilling a hole (Lu, 1996). Both methods do not allow measuring the surface residual stresses as some material has to be removed before any measurement.

1.4.1.2 Slitting method

The slitting method (Cheng & Finnie, 1985; Prime, 1999; Cheng & Finnie, 2007) consists in cutting a slit using milling cutters or wire electric discharge machining (wire EDM) and measuring the deformation of the specimen surface using strain gage. The depth of the slit is incrementally increased in order to capture the residual stress profile in the direction perpendicular to the slit. Stress profile measurements made with the slitting method are consistent with those of other methods, but the slitting method introduces errors near the surface and some significant divergences with diffraction methods are found, this is due to the higher elastic deformation near the free surface. In fact, differences up to 20% in stress values can mostly be noted 0.2 mm below the surface (Hill, 2013).

1.4.1.3 Contour method

Prime (2001) developed the contour method, a variant of the slitting method, which involves cutting a part into two pieces using a wire EDM. The deformations of the two new surfaces are measured and FEA is used to compute the normal residual stresses released during the cut. The contour method has the advantage to provide a 2D map of the normal residual stress distribution through the part cross-section. As for the slitting method, large deformation are observed near the edges, leading to inaccurate residual stress measurements near them. Therefore, the contour method is not recommended for near-surface residual stress measurements, neither for small parts and/or small magnitude and localized stress field (Prime & DeWald, 2013).

1.4.1.4 Layer removal method

The layer removal method (Lu, 1996) consists in removing material via acid-bath or electropolishing. As the chemical-attack-based methods do not introduce additional residual stresses, the material deformation due to residual stresses release can be documented. The deformation may be measured using strain gages, optical measurement methods, or coordinate-measuring machine. The layer removal method is limited to flat or cylindrical geometries and is time consuming.

1.4.2 Diffraction technique

The X-ray diffraction (XRD) techniques use the crystal lattice of single crystal or polycrystalline materials as a strain gage to determine the residual stresses. These techniques take advantage of the capability of electromagnetic radiation to measure the inter-atomic lattice spacing in crystalline materials and are non-destructive procedures. X-rays or neutrons interact with the atoms of crystals that are arranged in a regular array and the angle of the scattered radiations can be related to the lattice spacing d such as

$$n\lambda = 2d \sin\theta, \tag{1.1}$$

where n is the order of reflection (integer), λ is the wavelength of the electromagnetic radiation used for the residual stress measurement, and θ is the angle of scattered radiations, also called Bragg angle. The presence of residual stresses, or applied stresses, introduces small variations in the d-spacing which changed the measured Bragg angle (Schajer & Ruud, 2013).

1.4.2.1 X-ray diffraction method

The XRD method is capable of measuring the d-spacing which is indicative of the average strain of the irradiated volume (Ruud, 2002). The measurements are usually performed for X-ray wavelengths ranging from 0.7 Å to 3 Å (energy: 18 keV to 4 keV) and for high Bragg angles. High Bragg angles, 2θ, are preferred for residual stress measurement, as small changes in the d-spacing result in measurable changes in 2θ (Fitzpatrick *et al.*, 2005). Such wavelengths allow obtaining diffraction information from only a few microns below the material surface (up to few tens of microns depending on the material absorption coefficient and the considered signal intensity), which makes the XRD technique a surface residual stress measurements technique.

1.4.2.2 Synchrotron X-ray diffraction method

The synchrotron X-ray diffraction method uses X-rays as the traditional XRD methods but with wavelengths shorter than 0.25 Å (energies higher than 50 keV). These shorter wavelengths (or higher energies) allow the X-rays to penetrate much deeper in the material (17 cm for Al at 100 keV (Withers, 2013)). Because of the shorter wavelengths, the synchrotron XRD method employs lower Bragg angles than the XRD methods. Such high X-ray energies are only produced in synchrotron facilities (particule accelerator), where access to beamtime is limited. The synchrotron XRD allows mapping of large elastic strain fields in 2D (Withers, 2013) and mapping of grain-size strain fields. Using this technique, Spolenak *et al.* (2003) have shown that, in a thin film, the interactions between neighboring grains may lead to highly non-uniform stresses in an individual grain (corresponding to σ^{III} stress in Figure 1.1).

1.4.2.3 Neutron diffraction method

The neutron diffraction method (Hutchings *et al.*, 2005) uses penetrating radiations composed of neutrons generated by nuclear fission or spallation (neutrons are generated by the impact onto a target of a high energetic proton beam, such as the one found in a synchrotron). Compared to the two previous diffraction methods, where the X-rays interact with the electrons of the atom, the neutrons interact with the nucleus of the atom, thus making neutrons penetrating several centimeters into the material (Schajer & Ruud, 2013). Therefore, the neutron diffraction method is a bulk residual stress measurement method allowing the measurement of 3D stresses. Similarly to the synchrotron X-ray sources, neutron sources are specific facilities where access is peer-reviewed and limited.

1.4.3 Other techniques

Most of the “other techniques” are non-destructive methods and use the fact that strain or residual stresses may affect the material behaviors, such as sound propagation-speed or magnetic properties.

1.4.3.1 Ultrasonic method

The ultrasonic method (Crecraft, 1967) is based on the measurement of small changes in travel time of an acoustic wave through a material due to stresses. This phenomenon is called acoustoelastic effect (Egle & Bray, 1976). Acoustoelastic constants are needed for the computation of stresses. This method provides low cost comparative measurements (Belassel *et al.*, 2006), but it suffers from the important effects of grain size, crystallographic texture (preferred grain orientation), and surface roughness (Bray, 2013).

1.4.3.2 Magnetic methods

Different magnetic methods exist to measure the residual stresses, the most commonly used being the magnetic Barkhausen noise (MBN) (Jiles, 1988). The MBN method is only applicable on ferromagnetic materials and is based on the response of the material to an applied magnetic field. Pulses, similar to noise, are observed via piezoelectric transducer, when exposing the material to the applied magnetic field, due to the magnetic domain wall movements under stress. The measurement penetration is controlled by the frequency and penetration up to 40 mm for high strength steel at 1 Hz can be observed. A calibration curve obtained for the specific material of interest, relating the stress to the MBN signal response for a given voltage and frequency, is essential for residual stress measurements (Buttle, 2013). The MBN method offers a quick quantitative stress measurement if calibration is already performed but the measurements are highly affected by microstructure. Furthermore, the material response to the applied magnetic field greatly decreases for compressive stresses, making them more difficult to quantify (Garikepati *et al.*, 1988; Gauthier *et al.*, 1998; Yelbay *et al.*, 2010).

1.4.3.3 Indentation methods

The indentation technique consists to indent the tested material with a known indenter geometry and applied force. Material properties, like hardness or elastic modulus, can then be computed from the measurement of the indentation diagonals (ASTM E384-17, 2017). Different methods exist for this purpose such as the microindentation and the nanoindentation, for measurements at the micro and nano scales, respectively. The nanoindentation requires documenting the applies force and the indenter displacement, whereas the microindentation uses a known applied force. Some studies, summarized by Fischer-Cripps (2011), have shown the residual stress measurement feasibility via nanoindentation. However, the accuracy of indentation methods for residual stress measurements is relatively low for general applications, when compared to hole-drilling and XRD (Ruud, 2002). Therefore, the nanoindentation method is usually employed for comparison with other methods, especially when dealing with local stress measurements at the grain level.

1.4.4 Measurement methods: penetration and spatial resolution

Figure 1.5 summarizes the penetration and the spatial resolution for most of the methods previously presented. One can observe that the synchrotron X-ray diffraction has the largest range of spatial resolution for the deepest penetration, but is one of the most expensive methods

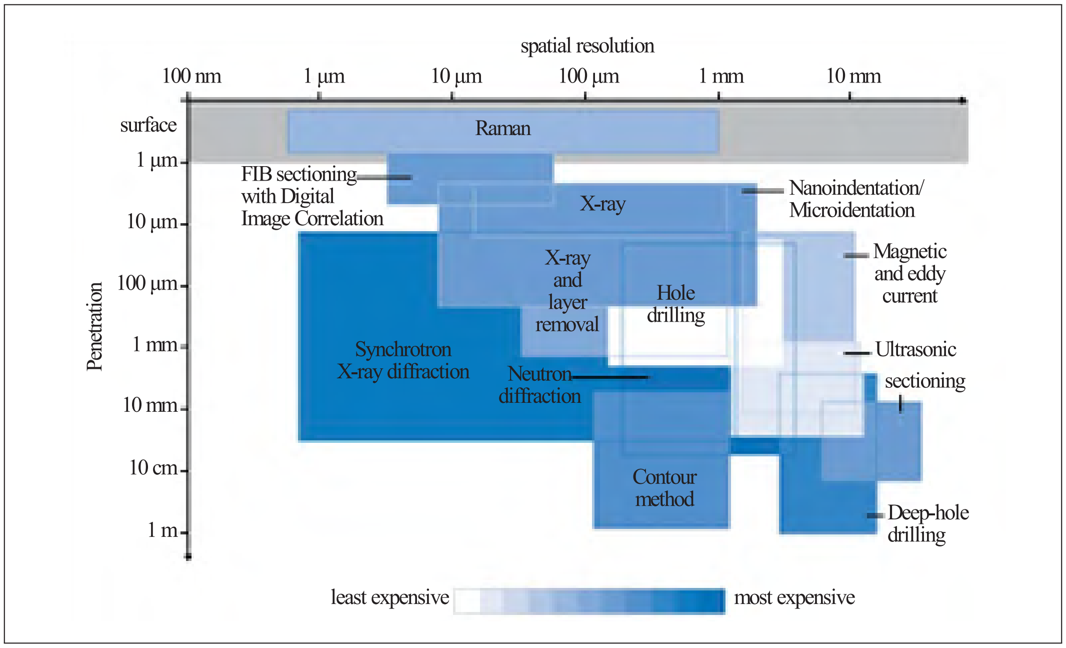

Figure 1.5 Penetration versus spatial resolution for various residual stress measurements methods. Reprinted from Schajer & Ruud (2013) with permission

and, furthermore, synchrotron facilities access is very limited. A compromise, for surface and near surface residual stress measurements, is the conventional X-ray diffraction method paired up with the layer removal method.

1.5 X-ray diffraction for residual stress measurement

Section 1.3 showed that a typical depth affected by shot peening is in the range of 150 μm to 300 μm, for the three materials, when considering the compressive residual stresses and the cold work. Section 1.4 provided an overview of the different techniques available to measure the residual stress. The XRD method paired up with a layer removal method using electropolishing appears to be the most suitable technique to measure the residual stresses introduced by the shot peening process. Consequently, the present section introduces the X-rays properties, as well as the effects of the residual stresses and the cold work on the diffraction peaks leading to their measurements.

1.5.1 Properties of the emitted X-rays

X-rays were discovered in 1895 by the German physicist Roentgen. X-rays are electromagnetic radiations, as light rays but with a much shorter wavelength. When used for diffraction purposes, X-rays have wavelengths lying in the range 0.5-2.5 Å (Cullity, 1956a), whereas the visible light wavelength is in the range 4000-7000 Å (NASA, 2010). X-rays can also be considered as a stream of particles called quanta or photons (Cullity, 1956a).

For residual stress measurements, the radiations are typically produced in an X-ray tube containing two metal electrodes. The high voltage maintained across the two electrodes (also called tube voltage) pulls electrons off the filament (cathode). X-rays are produced when the electrons strike with high velocity the target component (anode), as shown in Figure 1.6. The tube voltage (order of magnitude: kilovolt (kV)) allows accelerating the electrons, whereas the tube current (order of magnitude: milliampere (mA)) controls the flow of electrons pulled off the filament. The spectrum of the emitted X-rays is function of the target metal and the tube voltage.

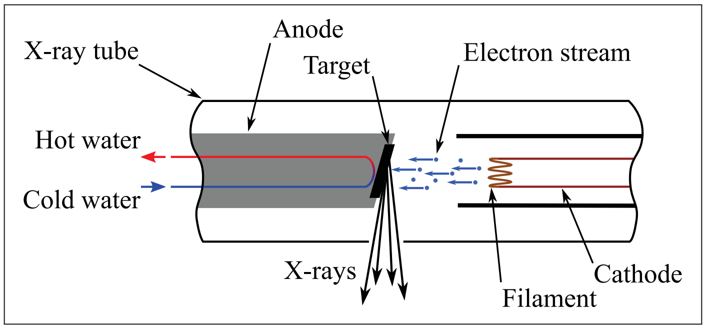

Figure 1.6 Schematic of an X-ray tube showing the production of X-rays

When the tube voltage is raised above a critical value (characteristic of the target material), sharp intensity maxima appear for certain wavelengths, superimposed on a background spectrum. These intensity maxima are called radiations or lines and are characteristic to the eletrons movements of the target. When a bombarding electron knocks out an electron from the K shell of a target metal's atom, a vacancy is created living the atom in an unstable state. If the vacancy is filled out by an electron from the L shell (an higher orbit), the electron movement is accompanied by the emission of a photon having an energy equal to the energy difference between the two orbits. This corresponds to the Kα radiation and the associated energy $E_{photons}$ is equal to

$$E_{photons} = \frac{\mathrm{hc}}{\lambda_{\mathrm{K}\alpha}}, \tag{1.2}$$

where h is the Planck's constant, c is the speed of light in a vacuum, and $\lambda_{\mathrm{K}\alpha}$ is the Kα-radiation wavelength. In this case, the photons energy is also equal to the kinetic energy of bombarding electrons, $E_k = \mathrm{e}U_{AC}$, where e is the elementary charge and U_{AC} is the tube voltage. Therefore, $E_{photons}$ can be expressed as

$$E_{photons} = \frac{\mathrm{hc}}{\lambda_{\mathrm{K}\alpha}} = \mathrm{e}U_{AC}. \tag{1.3}$$

From Equation (1.3), one can express the Kα-radiation wavelength $\lambda_{\mathrm{K}\alpha}$ in function of the tube voltage. Similarly, the Kβ radiation is emitted when an electron from the M shell (higher orbit than the L shell) fills out the vacancy. The Kβ line is of lower intensity than the Kα line because it is more probable that the vacancy is filled out by a L electron than a M electron (Cullity, 1956a). An example of spectrum is presented Figure 1.7a.

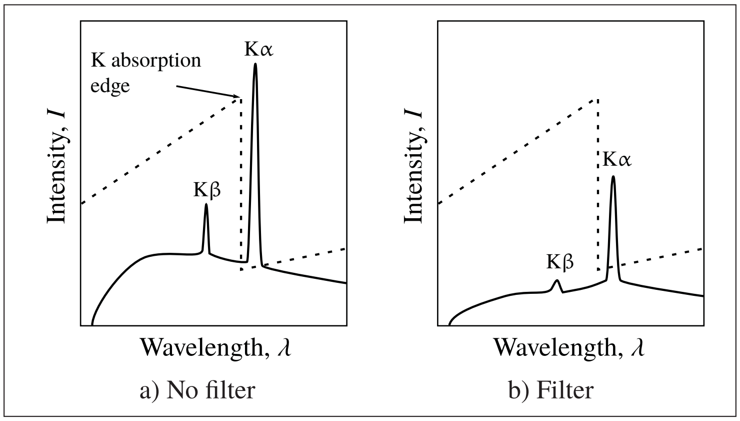

a) No filter

b) Filter

Figure 1.7 Schematic comparison of hypothetical X-ray spectra formed of Kα and Kβ lines a) before and b) after the use of a filter. The dashed line is the mass absorption of the adequate filter, having its K absorption edge between the Kα and Kβ lines

Many X-ray diffraction experiments, such as residual stress measurements, require monochromatic radiation to only deal with a single diffraction peak. The Kα line is more often used than the Kβ line due to its higher intensity. The intensity of the Kβ line is greatly reduced using a thin film of metal having its K absorption edge between the Kα and Kβ wavelengths (as presented in Figure 1.7b). The filter material has typically 1 or 2 atomic number less than the target metal (Cullity, 1956a).

The Kα radiation is composed of two components, called Kα doublet and named Kα_1 and Kα_2 components. An illustration of the Kα doublet is presented in Figure 1.8. Kα_1 intensity is always about twice as strong as Kα_2 intensity. However, Kα_1 and Kα_2 components can have wavelengths so close together that they are not dissociable (Cullity, 1956a).

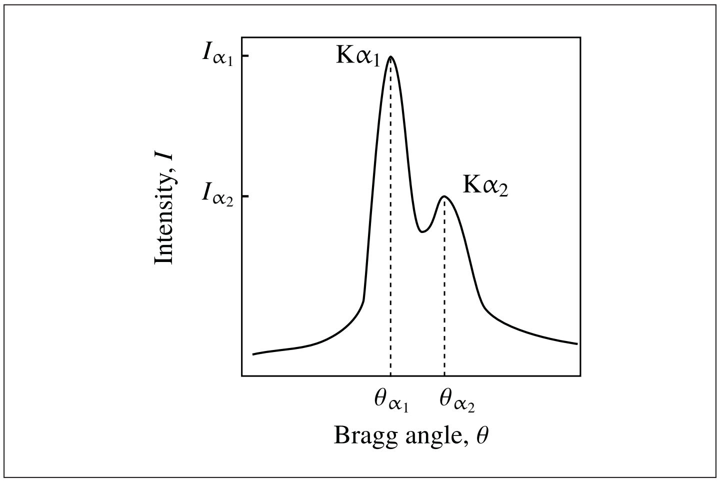

Figure 1.8 Illustration of the Kα doublet, with Kα_1 and Kα_2 components. I_{α_1} and θ_{α_1} are the intensity and the Bragg angle corresponding to the Kα_1 line, respectively, whereas I_{α_2} and θ_{α_2} are the ones for the Kα_2 line

1.5.2 Crystal structure

Unit cell can have various shapes, depending on how the unit vectors $\boldsymbol{a}$, $\boldsymbol{b}$, and $\boldsymbol{c}$ are arranged. Figure 1.9 presents a unit cell and the different vectors and angles. Seven crystal systems can be defined, such as the cubic system ($\|\boldsymbol{a}\| = \|\boldsymbol{b}\| = \|\boldsymbol{c}\|$ and $\alpha = \beta = \gamma = 90°$) or the hexagonal system ($\|\boldsymbol{a}\| = \|\boldsymbol{b}\| \neq \|\boldsymbol{c}\|$, $\alpha = \beta = 90°$, and $\gamma = 120°$). In 1848, Bravais (1848) demonstrated that, when considering the fact that each point lattice have identical surroundings, there are only fourteen point lattices possible to arrange atoms in space. They are now called Bravais lattices. Body-centered cubic (BCC) lattice and face-centered cubic (FCC) lattice are two examples of these fourteen Bravais lattices often found in metals and are presented in Figure 1.10a and 1.10b, respectively.

As the three materials of this study have a cubic structure, only the cubic system is further detailed. Any plane can be described by the reciprocals of the intercepts which the plane makes with the unit axes. As for a cubic unit cell the lattice parameter $a = \|\boldsymbol{a}\|$ is equal to 1, the plane intercepts with the unit axes are fractions: $\frac{1}{h}$, $\frac{1}{k}$, and $\frac{1}{l}$. h, k, and l are the Miller indices, and

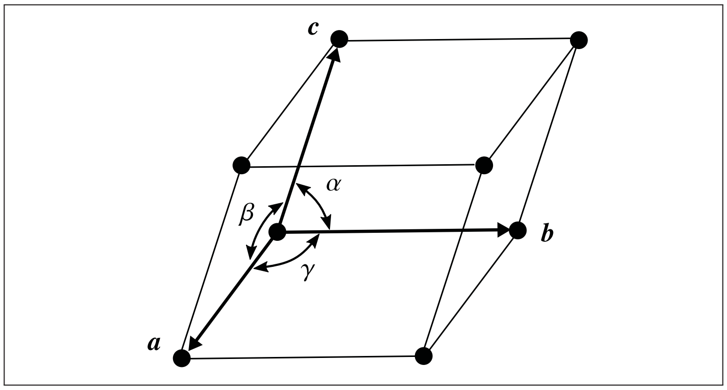

Figure 1.9 Schematic representation of a unit cell, where $\boldsymbol{a}$, $\boldsymbol{b}$, and $\boldsymbol{c}$ are the unit cell vectors and α, β, and γ are the angles between these vectors

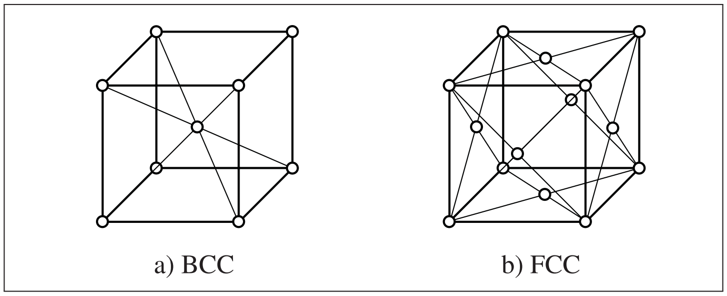
a) BCC

b) FCC

Figure 1.10 Schematic representations of a) a body-centered cubic (BCC) structure and b) a face-centered cubic (FCC) structure

the plane can then be defined as (hkl). The Miller indice of a negative intercept is denoted by an overline, such as -1 is denoted as $\overline{1}$. It is convenient to note that in a cubic system a line direction $[hkl]$ is always perpendicular to a plane (hkl) of the same Miller indices (Cullity, 1956b). Figure 1.11 provides an example of the [100], [010], and [001] directions, as well as the (100) and $(23\overline{1})$ planes of a cubic unit cell.

A crystal is composed by sets of equivalent lattice planes related by symmetry. These sets of planes are often called family of planes and are denoted as $\{hkl\}$. For instance, the six faces of a cube: (100), (010), (001), $(\overline{1}00)$, $(0\overline{1}0)$, and $(00\overline{1})$ are planes of the same family $\{100\}$. The

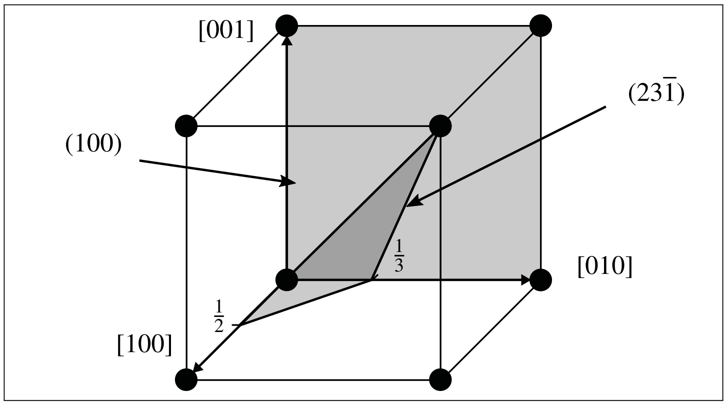

Figure 1.11 Schematic representation of a cubic unit cell. [100], [010], and [001] directions are presented as vectors. (100) and (23$\bar{1}$) planes are presented in grey

interplanar spacing $d^{\{hkl\}}$ is computed from the cubic lattice parameter a as

$$d^{\{hkl\}} = \frac{a}{\sqrt{h^2 + k^2 + l^2}}. \tag{1.4}$$

The cubic lattice parameter a is function of the material composition.

1.5.3 X-ray diffraction from planes of atoms

The diffraction of X-rays by planes of atoms only takes place if the incident X-ray beam satisfies Bragg's law (Equation (1.1)). Thus, if an X-ray beam had to be projected on a single crystal, the $\{hkl\}$ planes would scatter the X-ray beam only for a specific single-crystal direction, when the incident beam and the diffracting planes make a $\theta^{\{hkl\}}$ angle, also called Bragg angle, as shown in Figure 1.12. In this condition (also called condition for diffraction), the vector normal to the $\{hkl\}$ planes, $\mathbf{V}^{\{hkl\}}$, is aligned with the scattering vector, $\mathbf{V}_{\mathbf{Scat}}$, which is the bisector of the incident and diffracted X-rays. Figure 1.12 also defines the X-ray incident angle, β, and the angle between the sample surface and the normal of the $\{hkl\}$ planes, ψ. It is worth noting that Bragg's law is still satisfied if the single crystal is rotated around the incident beam axis. Therefore, there is a multitude of orientations for which the single crystal satisfies Bragg's law. That is why in a polycrystalline material a large number of crystallites may be oriented so they scatter the incident X-rays. Furthermore, if the polycrystalline material is composed of fine grains, the resulting scattered rays form a cone, called the diffraction cone. Finally, Bragg's law can be written taking into account the $\{hkl\}$ planes in the notation as

$$\lambda = 2d^{\{hkl\}} \sin \theta^{\{hkl\}}. \tag{1.5}$$

By convention, the integer n presents in Equation (1.1) is set to 1, as in general the n^{th}-order of reflection from (hkl) planes of lattice spacing $d^{(hkl)}$ can be seen as a first-order of reflection from the $(nh\ nk\ nl)$ planes having a lattice spacing of $d^{(nh\ nk\ nl)} = d^{(hkl)}/n$ (Cullity, 1956c). For instance, the (200) planes, which are the second-order of reflection from the (100) planes and have a lattice spacing of $d^{(200)} = d^{(100)}/2$, can be seen as a first-order of reflection of themselves.

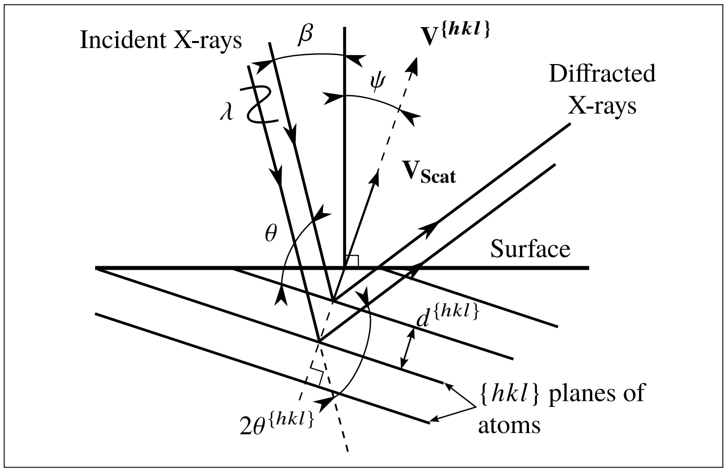
Incident X-rays
β
$\mathbf{V}^{\{hkl\}}$
ψ
Diffracted X-rays
λ
$\mathbf{V}_{\mathbf{Scat}}$
θ
Surface
$d^{\{hkl\}}$
$\{hkl\}$ planes of atoms
$2\theta^{\{hkl\}}$

Figure 1.12 Diffraction of X-rays by the $\{hkl\}$ planes of a single crystal. Bragg's law is satisfy when the incident X-rays (having a β angle with the surface normal) have a $\theta^{\{hkl\}}$ angle the $\{hkl\}$ planes of atoms (having themself a ψ angle with the surface normal). Other symbols: $\mathbf{V}^{\{hkl\}}$, vector normal to the $\{hkl\}$ planes; $d^{\{hkl\}}$, interplanar spacing; $\mathbf{V}_{\mathbf{Scat}}$, scattering vector; λ, X-rays wavelegnth

1.5.4 Diffraction peak characterization

The diffraction peak formed on a detector has to be fitted to be used for further analysis such as residual stress and cold work measurements. Indeed, the peak position (determination of θ) and the peak width can be related to the residual stresses and the material cold work, respectively.

1.5.4.1 Peak fitting

The intensity I of the measured diffraction peak can be expressed as a function of the Bragg angle θ. In presence of the Kα doublet (as presented in Figure 1.8), I is expressed as (Prevéy, 1986; Prevéy, 1987)

$$I(\theta) = I_{\alpha_1} f(\theta - \theta_{\alpha_1}) + A_{PF} I_{\alpha_1} f(\theta - \theta_{\alpha_2}) + B_{PF}\theta + C_{PF} \tag{1.6}$$

where $f(\theta)$ is the Pearson VII distribution function (Prevéy, 1986), I_{α_1} and θ_{α_1} are the intensity and the Bragg angle of the Kα_1 peak, respectively, θ_{α_2} is the Bragg angle of the Kα_2 peak, A_{PF} is a fixed ratio relating the Kα_1 and Kα_2 peaks intensities (often taken as 0.5), and B_{PF} and C_{PF} are the assumed linear background slope and intercept, respectively. The different variables are presented in Figure 1.8. The Pearson VII distribution function in its general form is expressed as (Prevéy, 1986)

$$f(\theta) = \left[1 + K_{P_{VII}}^2 \frac{\theta^2}{m_{P_{VII}}}\right]^{-m_{P_{VII}}} \tag{1.7}$$

where $K_{P_{VII}}$ controls the width of the peak profile and $m_{P_{VII}}$ the decay rate parameter. Hall *et al.* (1977) showed that the Pearson VII distribution can also be used to approximate symmetric diffraction peaks.

1.5.4.2 Peak localization and peak width

If the diffraction peak is adequately fitted, then the peak localization and peak width can be directly determined from the fitting function. However, different methods exist to characterize the peak (Hauk, 1997). Simpler methods are presented in this section for their ease of visualiza-

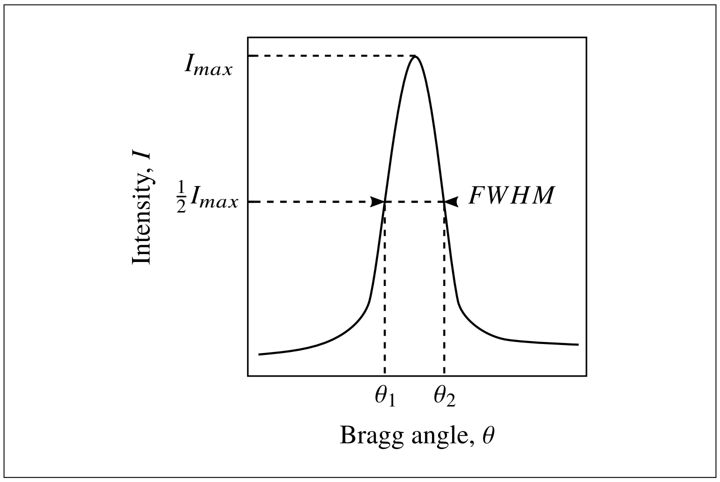

Figure 1.13 Illustration of full width at half the maximum ($FWHM$) value. θ_1 and θ_2, found for $\frac{1}{2}I_{max}$, are used to find the peak position

tion. The simplest method to determine the peak localization makes use of the peak breadth at half the maximum intensity, which implies finding the θ angle corresponding to the maximum intensity of the peak. Figure 1.13 presents a symmetric diffraction peak (ideal case) of maximum intensity I_{max}. The Bragg angles θ_1 and θ_2, determined at half the maximum intensities $\frac{1}{2}I_{max}$, are used to determine the diffraction peak position θ_{Peak} as

$$\theta_{Peak} = \frac{1}{2}\Big[\theta_1(\tfrac{1}{2}I_{max}) + \theta_2(\tfrac{1}{2}I_{max})\Big]. \tag{1.8}$$

The breadth of the peak is also called full width at half the maximum and is abbreviated in the literature as FWHM. Figure 1.13 presents an illustration of the $FWHM$ value, which can be computed as

$$FWHM = \theta_2(\tfrac{1}{2}I_{max}) - \theta_1(\tfrac{1}{2}I_{max}). \tag{1.9}$$

In the case where the parabola foot is not horizontal after the X-ray background was removed, the $FWHM$ value is determined using a straight line parallel to final background (Noyan & Cohen, 1987). Figure 1.14 presents an inclined parabola foot, where the background is fitted by a dotted straight line. The parallel to this line is plotted for $\frac{1}{2}I_{max}$ and the intersection points with the parabola (θ_1 and θ_2) are noted for $FWHM$ determination using Equation (1.8).

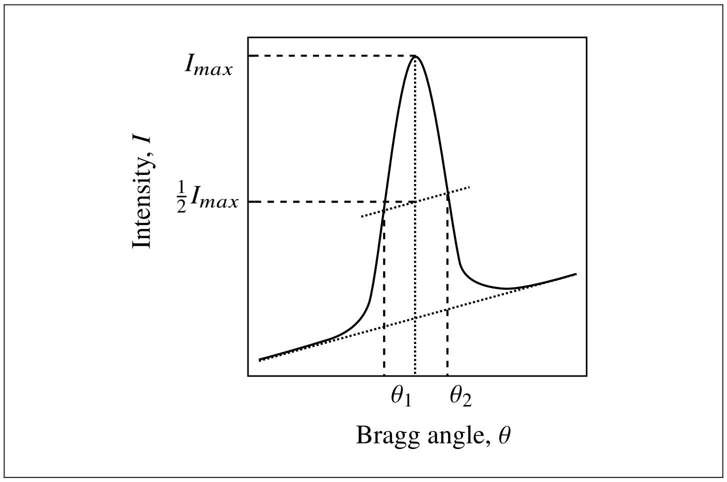

Figure 1.14 Illustration of full width at half the maximum ($FWHM$) value. θ_1 and θ_2, found for $\frac{1}{2}I_{max}$, are used to find the peak position

1.5.5 Depth of X-rays penetration

The effective depth of X-ray penetration is arduously determined as the intensity does not suddenly become zero but rather decreases exponentially (Cullity, 1956d).

X-rays are absorbed by the target material and only a thin surface layer is diffracting the incident X-rays. The absorption depends on the mass absorption coefficient μ/ρ (in cm^{2}g^{-1}) of the material, where μ, which varies with the photons energy $E_{photons}$, is the linear absorption coefficient and ρ is the volumetric mass density for the specific element or material (Maslen, 2006). The linear absorption coefficient μ being important in metals, the irradiated layer is in the order of only few microns to few tens of microns (Noyan & Cohen, 1987).

The following development is only valid for the omega mode (ASTM E2860-12, 2012) which is largely used for residual stress measurement, and corresponds to the $\sin^2\psi$ method presented in Section 1.5.8.1 and developed in Section 2.5.1.1. The diffracted X-rays intensity, dI_D, from an infinitesimally thin layer, dx, located at a depth x below the surface is given by

$$\mathrm{d}I_D = \frac{I_0 bc}{\sin\omega_I}\exp\left\{-\mu x\left[\frac{1}{\sin\omega_I}+\frac{1}{\sin\omega_D}\right]\right\}\mathrm{d}x \tag{1.10}$$

where I_0 is the incident X-ray beam intensity, b and c are the X-ray aperture size entrance and exit, respectively, ω_I and ω_D are the angles between the material surface and the incident and diffracted X-rays, respectively, and can be expressed as

$$\omega_I = \theta + \psi, \tag{1.11a}$$

$$\omega_D = \theta - \psi. \tag{1.11b}$$

Consequently, Equation (1.10) becomes

$$\mathrm{d}I_D = \frac{I_0 bc}{\sin(\theta+\psi)}\exp\left\{-\mu x\left[\frac{1}{\sin(\theta+\psi)}+\frac{1}{\sin(\theta-\psi)}\right]\right\}\mathrm{d}x. \tag{1.12}$$

Integrating Equation (1.12) over a chosen depth gives the intensity of the diffracted X-rays by this specific layer. Furthermore, the total diffracted intensity, I_D, coming out from the total irradiated layer thickness is determined by integrating dI_D for an infinitely thick specimen (practically an "infinite thickness" would only be a few tens or hundreds of microns). Considering the intensity of a layer at a depth x as a fraction G_x of the total diffracted intensity, this fraction can be expressed as (Cullity, 1956d)

$$G_x = \frac{\int_{x=0}^{x=x}\mathrm{d}I_D}{\int_{x=0}^{x=\infty}\mathrm{d}I_D} = 1-\exp\left\{-\mu x\left(\frac{1}{\sin(\theta+\psi)}+\frac{1}{\sin(\theta-\psi)}\right)\right\}, \tag{1.13}$$

canceling the unknown constants I_0, b, and c. It can be noted from Equation (1.13) that the intensity participating to the total diffracted intensity decreases exponentially with the depth.

Finally, in order to have an idea on the thickness of material for which the information of the diffracted beam comes from, an arbitrary decision on the fraction G_x contributing to the total intensity diffracted has to be made. Figure 1.15 presents the variation of the fraction G_x as a

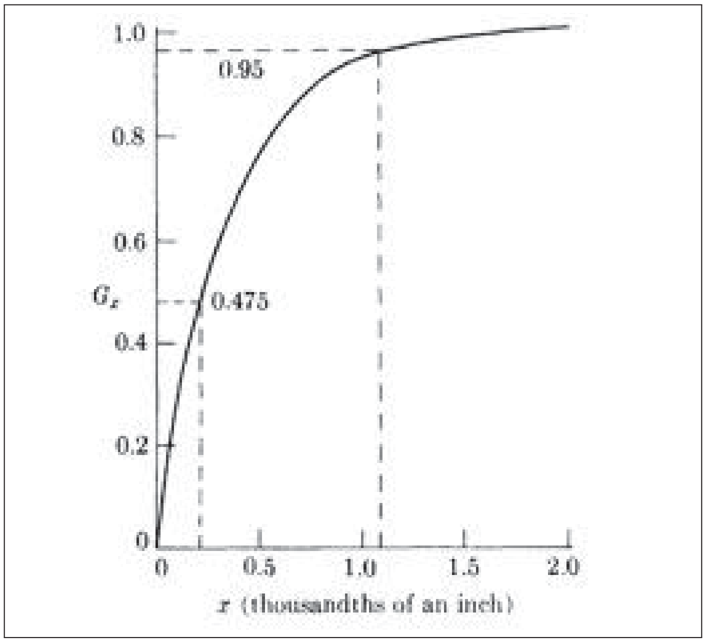

Figure 1.15 The fraction G_x of the total diffracted intensity contributed by a surface layer of depth x, for μ = 473 cm^{-1} (brass), 2θ = 136.7°, and normal incidence (Note: 0.001 in. = 25.4 µm). Reprinted from Cullity (1956d)

function of the depth *x* as obtained by Cullity (1956d) for a brass sample. It can be observed that 95% ($G_x = 0.95$) of the information from the diffraction pattern comes from a layer of about 25 µm (0.0011 in.) thick. To considered 100% of the information from the diffraction pattern, $G_x = 1.0$, the layer thickness has to be doubled. It is worth noting that if the specimen has an ASTM grain-size number of 8 (22 µm) (ASTM E112-13, 2013), then only one grain thick participates to the diffraction pattern. From an experimental standpoint, the effective penetration depth is often determined for $G_x = 63\%$, which corresponds to the center of gravity of the distribution of measured diffracted intensity versus depth (Welzel *et al.*, 2005).

1.5.6 Effect of residual stresses and cold work on X-ray line

A diffraction peak captured for a stress-free polycrystalline is presented in Figure 1.16a, along with the irradiated undeformed crystal lattice having a d_0 lattice spacing. Applying an uniform strain field results in a shift of the diffraction peak, as shown in Figure 1.16b. Figure 1.16c exhibits a nonuniform strain field caused by the crystal lattice bending and resulting in the broadening of the diffraction peak. Microstrains and plastic deformations, leading to type II and III stresses, respectively, also result in a diffraction peak broadening.

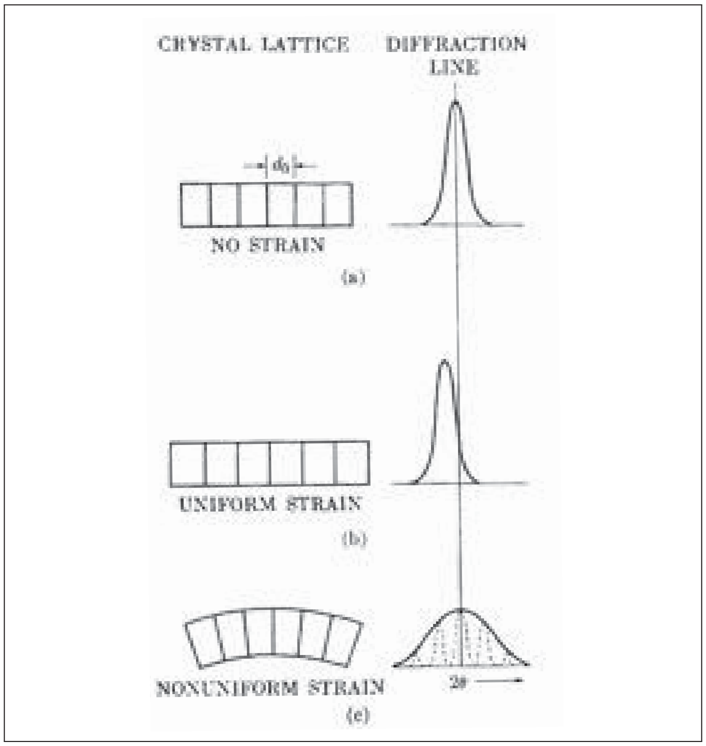

Figure 1.16 Illustration of the lattice strain effects on the diffraction peak. Reprinted from Cullity (1956d)

In most cases X-ray diffraction measurements record the superimposition of the shift and the broadening of the diffraction peak, especially for plastically deformed materials. For a given $\{hkl\}$ family of planes, the interplanar spacing not only varies from grain-to-grain but their mean value also varies from the stress-free value of the undeformed material.

As a consequence, X-ray diffraction can be used not only to measure residual stresses but also to quantify cold work through the use of a calibration curve relating the peak width (FWHM) to the cold work (Prevéy, 1987). Furthermore, the density of dislocations can also be determined from the peak width (Pangborn *et al.*, 1981; Vermeulen *et al.*, 1997; Christien *et al.*, 2013).

1.5.7 Measurement of residual strain

Conventionally, the strain of the irradiated crystallites, $\varepsilon^{\{hkl\}}$, is determined for the $\{hkl\}$ family of planes as (Lu, 1996)

$$\varepsilon^{\{hkl\}} = \frac{d^{\{hkl\}} - d_0^{\{hkl\}}}{d_0^{\{hkl\}}} = \frac{\Delta d^{\{hkl\}}}{d_0^{\{hkl\}}} \tag{1.14}$$

where $d^{\{hkl\}}$ is the interplanar spacing measured using Equation (1.5) and $d_0^{\{hkl\}}$ is the unstressed value of interplanar spacing, often measured on powder material. The measured strain is consequently an average strain of the irradiated crystallites. The strain can also be expressed in terms of Bragg angle as (Lu, 1996)

$$\varepsilon^{\{hkl\}} = -(\theta^{\{hkl\}} - \theta_0^{\{hkl\}}) \cot \theta_0^{\{hkl\}} = \Delta\theta^{\{hkl\}} \cot \theta_0^{\{hkl\}} \tag{1.15}$$

where, similarly, $\theta^{\{hkl\}}$ and $\theta_0^{\{hkl\}}$ are the measured and unstressed Bragg angles.

1.5.8 Determination of residual stresses

Different XRD methods exist to evaluate the residual stresses in polycrystalline materials. A few of them are introduced here. It is worth noting that the stress state in the irradiated layer is often considered as biaxial, due to the very small X-ray penetration. This assumption is well adapted to shot peening, as it is considered to introduce equi-biaxial stresses.

1.5.8.1 The $\sin^2\psi$ method

The $\sin^2\psi$ method is a multi-exposure technique: The X-ray source and the two linear detectors, for most dedicated apparatus, are placed in different β positions, which allow measuring the strain for the given $\{hkl\}$ planes at different ψ orientations. In the case of non-textured material and biaxial stress state, it exists a linear relationship between the strain $\varepsilon^{\{hkl\}}$ and the sine-squared of the ψ position at which it is measured (Noyan & Cohen, 1987). The stress is then computed from the slope of the linear fitting and an X-ray elastic constant (XEC). It is in 1961 that Müller and Macherauch found the procedure to evaluate the stress from the linear dependence of $\varepsilon^{\{hkl\}}$ vs. $\sin^2\psi$ (Müller & Macherauch, 1961). Since then, this method has been the most commonly used one for residual stress evaluation (Fitzpatrick *et al.*, 2005). The $\sin^2\psi$ method is standardized in two American standards: SAE HS784 (2003) and ASTM E2860-12 (2012). The residual stress computation for the $\sin^2\psi$ method is detailed in the methodology section (Chapter 2).

1.5.8.2 The cos α method

Developed by Taira *et al.* (1978), the $\cos\alpha$ method was recently brought up to date with the recent technological improvement of detectors, which allowed the miniaturization of 2D detectors, so called area detectors or imaging plates. Indeed, this detector geometry was formerly dedicated to conventional XRD apparatus, synchrotron or neutron diffraction for texture measurement or phase identification (He, 2009). From 1978 to 2014, only a few papers can be found in the literature relating the use of the $\cos\alpha$ method and 2D detectors for residual stress measurements (Yoshioka & Ohya, 1994; Sasaki *et al.*, 1997; Hiratsuka *et al.*, 2003; Tanaka & Akiniwa, 2004; Sasaki, 2006; Sasaki *et al.*, 2010; Miyazaki & Sasaki, 2014). In 2014, Pulstec Industrial Co. Ltd. obtained a patent (Maruyama, 2014) applicable in a large number of countries allowing it to commercialize diffractometers equipped with small 2D detectors worldwide. Since 2014, a larger number of papers were published. The new apparatus was first described by Miyazaki & Sasaki (2015) and Ling & Lee (2015). The $\cos\alpha$ method was quickly used for experimental work as published by Fujita *et al.* (2016). Analytical (Miyazaki & Sasaki, 2016; Ramirez-Rico *et al.*, 2016) and experimental (Delbergue *et al.*, 2016; Kohri *et al.*, 2016; Ramirez-Rico *et al.*, 2016; Delbergue *et al.*, 2017; Lee *et al.*, 2017; Peterson *et al.*, 2017) comparisons with the $\sin^2\psi$ method were quick to follow.

A 2D detector, when placed perpendicularly to the incoming X-ray beam, allows capturing the entire diffraction data coming from the diffraction cone in a single exposure, i.e., single β position. For a stress-free material, the diffraction data appear as a circle on the detector, also called Debye-Scherrer ring or, shortly, Debye ring. The diffraction data from a stressed material appear as a deformed circle, typical of the presence of a strain field. The obtained circle can be described by an angular position α. The strains $\varepsilon^{\{hkl\}}$, computed for different α-angles, are plotted versus their corresponding $\cos\alpha$ value. In the case of non-textured material and biaxial stress state, it exists a linear dependence of $\varepsilon^{\{hkl\}}$ vs. $\cos\alpha$ from which the residual stress can be evaluated using the material XEC. The residual stress computation for the $\cos\alpha$ method is further detailed in the methodology section (Chapter 2).

1.5.8.3 Other residual stress evaluation methods

Other methods exist for residual stress evaluation such as the two-tilts method or the low-incident-beam-angle diffraction (LIBAD) method.

The two-tilts method (Noyan & Cohen, 1987) is a simplified version of the $\sin^2\psi$ method and is sometimes used for rapid testing. In this method, the linear relationship between $\varepsilon^{\{hkl\}}$ vs. $\sin^2\psi$ is assumed and only two ψ positions are used in the measurement. One of the two ψ positions must be $\psi = 0°$, which corresponds to the undeformed $\{hkl\}$ planes, as they are parallel to the sample surface. The slope is then computed for the residual stress determination, using the XEC.

On an other hand, the low-incident-beam-angle diffraction (LIBAD) method, developed by Van Acker *et al.* (1994) for evaluation of the residual stresses in thin coating. It makes use of a conventional diffractometer equipped with a goniometer. The X-ray source, independent from the linear detector, is set for a constant low X-ray incident beam angle, and consequently a constant X-ray penetration depth, while the detector describes a large range of 2θ-positions to measure different {hkl} planes (i.e., different $2\theta^{\{hkl\}}$ angles). The stress is computed using the XEC for a given depth. By changing the incident beam angle, the stress of different depths can be computed and the stress gradient under the surface estimated.

1.5.8.4 Effect of crystallographic texture on the residual stress determination

The crystallographic texture is the preferred orientation of grains induced by manufacturing process, such as rolling process. Texture, as an essential part of the microstructure, plays an important role in the material properties, especially if the anisotropy of the single crystal properties is large (Kocks *et al.*, 1998).

With the presence of crystallographic texture, the relationships between the measured strain and $\sin^2\psi$ or $\cos\alpha$ values is no longer linear but rather oscillating (Van Houtte, 1993). A 2D detector has the advantage, if the texture is unknown before the XRD measurements, to visually reveal it presence via a strong variation of the diffraction peak intensities along the Debye ring (He *et al.*, 1998).

To overcome the crystallographic texture in the evaluation of the residual stresses (in the case of a material free of σ^{II} stresses originating from plastic strain), the XEC must be computed using the material single-crystal elastic constants, the orientation distribution function (ODF) characterizing the texture, and an micromechanical model like the Voigt model (Voigt, 1928) or the Reuss model (Reuss, 1929), which assume a constant strain and stress, respectively, in the crystallites. In the case of an untextured (isotropic) material the XEC can be computed from the Young's modulus, E, and the Poisson's ratio, ν (Noyan & Cohen, 1987).

1.6 Residual stress correction due to the layer removal process

The shot peening residual stress profile introduced through the treated-sample's depth (hundreds of microns) being larger than the penetration of X-rays (few microns), a process of layer removal by electropolishing is required to determine it. Electropolishing is suitable to remove material, as no additional residual stresses are induced in the material during the process. Nonetheless, the resulting stress redistribution in the material is inevitable and, consequently, the measured stresses must be corrected (Fitzpatrick *et al.*, 2005).

The correction method proposed by Moore & Evans (1958) is still widely used and recommended by the actual standard of residual stress measurement by X-ray diffraction (SAE HS784, 2003), even if it is based on constraining hypotheses. In 1995, Lambda Research's team proposed a new correction method: the so-called FEA correction technique (Hornbach *et al.*, 1995; Lambda Research, 1996). The two methods are presented below.

1.6.1 Moore & Evans correction method

The Moore & Evans correction is an analytical correction relying on four assumptions. First, the equations are only applicable for long tubes or flat plates and far from the edges. Second, the layer removal process is assumed to be homogeneous through the entire surface (cylindrical or flat). Third, the stress must remain elastic during relaxation and redistribution. Fourth, it is assumed that the stress field is either rotationally symmetric or symmetric (Moore & Evans, 1958).

For a flat plate of initial thickness H, Equations 1.16 provide the corrected stresses at a depth z_1 after electropolishing

$$\sigma_{xc}(z_1) = \sigma_{xm}(z_1) + 2\int_{z_1}^{H} \frac{\sigma_{xm}(z)}{z}\mathrm{d}z - 6z_1\int_{z_1}^{H} \frac{\sigma_{xm}(z)}{z^2}\mathrm{d}z \tag{1.16a}$$

$$\sigma_{yc}(z_1) = \sigma_{ym}(z_1) + 2\int_{z_1}^{H} \frac{\sigma_{ym}(z)}{z}\mathrm{d}z - 6z_1\int_{z_1}^{H} \frac{\sigma_{ym}(z)}{z^2}\mathrm{d}z \tag{1.16b}$$

$$\sigma_{zc} = 0 \tag{1.16c}$$

where σ_{xc}, σ_{yc}, and σ_{zc} are the corrected principal stresses in x, y, and z directions with the z axis perpendicular to the flat plate surface, σ_{xm} and σ_{ym} are the stresses measured after electropolishing in x and y directions, respectively.

For a cylindrical bar of initial radius R with rotationally symetric stresses, Equations 1.17 provide the corrected stresses at a radius r_1 after electropolishing

$$\sigma_{rc}(r_1) = -\int_{r_1}^{R} \frac{\sigma_{\theta m}(r)}{r}\mathrm{d}r \tag{1.17a}$$

$$\sigma_{\theta c}(r_1) = \sigma_{\theta m}(r_1) + \sigma_{rc}(r_1) \tag{1.17b}$$

$$\sigma_{zc}(r_1) = \sigma_{zm}(r_1) - 2\int_{r_1}^{R} \frac{\sigma_{zm}(r)}{r}\mathrm{d}r \tag{1.17c}$$

where σ_{rc}, $\sigma_{\theta c}$, and σ_{zc} are the radial, transverse, and longitudinal stresses, respectively, $\sigma_{\theta m}$ and σ_{zm} are the measured transverse and longitudinal stresses, respectively.

1.6.2 FEA matrix relaxation correction method

Electropolishing is a slow process and relatively expensive process. Electropolished pockets are therefore usually preferred over full surface polishing, making the first and second Moore & Evans assumptions potentially invalid. The Lambda Research's team (Hornbach *et al.*, 1995; Lambda Research, 1996) developed a FEA correction method enabling deep measurements in complex geometries using X-ray diffraction, recently improved by Savaria *et al.* (2012).

The FEA matrix relaxation correction also relies on a number of assumptions (Savaria *et al.*, 2012): the stress relaxation is purely elastic; no new residual stresses are introduced during the layer removal process itself; the residual stresses are uniform on the pocket's surface; the thickness of the polishing pocket is small when compared to the in-depth stress gradient; the pocket's geometry must be identical for both numerical calculations and experimentation; and the stresses are uncoupled, i.e., the stress relaxation in one direction is only affected by the stresses previously removed in that same direction.

The FEA matrix relaxation correction method is based on the determination of a correction matrix $\boldsymbol{K}$ such as (Lambda Research, 1996)

$$\boldsymbol{\sigma_c} = [\boldsymbol{I} + \boldsymbol{K}]\boldsymbol{\sigma_m} \tag{1.18}$$

where $\boldsymbol{\sigma_c}$ and $\boldsymbol{\sigma_m}$ are the column vectors containing the corrected and measured stress components, respectively, and $\boldsymbol{I}$ is the identity matrix. For instance, in the case of flate plate, $\boldsymbol{\sigma_c}$ would contain σ_{xc}, σ_{yc}, and σ_{zc} values.

Figure 1.17 describes the layer removal process and the stress relaxation and redistribution in the remaining material. It can be observed that after removing the layer s the relaxation induced a stress variation at point P_d, which is located at a depth d from the top surface. This stress variation at this depth is noted $(\Delta\sigma_d)_s$ and is expressed

$$(\Delta\sigma_d)_s = (\sigma_d)_s - (\sigma_d)_{s-1} = -(K_d)_s(\sigma_{avg})_s \tag{1.19}$$

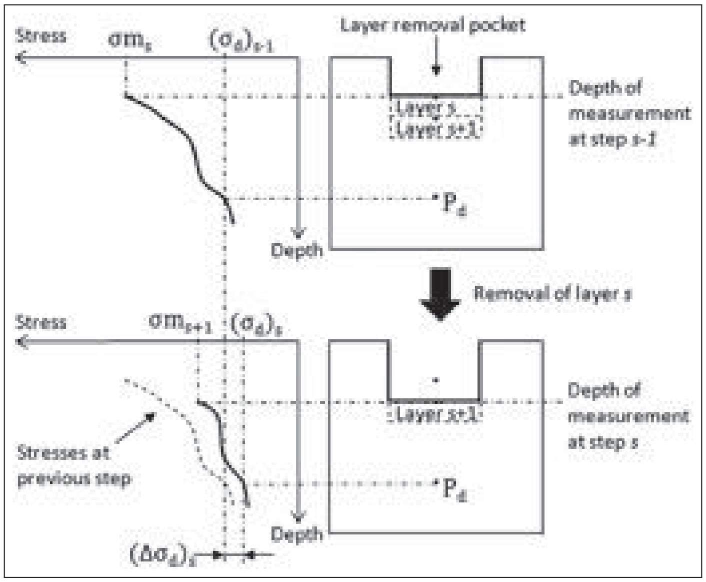
Stress
σm$_s$
$(\sigma_d)_{s-1}$
Layer removal pocket
Layer s
Layer s+1
Depth of measurement at step s-1
P$_d$
Depth
Removal of layer s
Stress
σm$_{s+1}$
$(\sigma_d)_s$
Layer s+1
Depth of measurement at step s
Stresses at previous step
P$_d$
Depth
$(\Delta\sigma_d)_s$

Figure 1.17 Schematic representation of the layer removal process and residual stress redistribution. Reprinted from Savaria *et al.* (2012) with permission

where $(K_d)_s$ is the correction coefficient of the matrix $\boldsymbol{K}$ at a depth d and for a step s, $(\sigma_{avg})_s$ is the average of the stress measured before and after the removal of the layer s, $(\sigma_m)_s$ and $(\sigma_m)_{s+1}$, respectively. Savaria *et al.* (2012) showed that it is more accurate to consider all the stresses along the removed layer thickness rather than using only the surface stress value on the top of the removed layer, as initially proposed by the Lambda Research's team (Hornbach *et al.*, 1995; Lambda Research, 1996). For this purpose, Savaria *et al.* (2012) proposed the use of the averaged stress $(\sigma_{avg})_s$ as

$$(\sigma_{avg})_s = \frac{(\sigma_m)_s + (\sigma_m)_{s+1}}{2}. \tag{1.20}$$

Savaria *et al.* (2012) assume that the $(K_d)_s$ coefficients are independent of the residual stress profile and that they are only affected by the specimen and electropolished pocket geometries. Therefore, they can be determined using a known stress profile virtually introduced in the sample, designed in finite element (FE) software, and after the simulation of the layer removal process. The assessment of the correction relevance is therefore straightforward: Once the $(K_d)_s$ coefficients are determined, the corrected residual stress σ_c can be determined for a given direction and depth d as

$$(\sigma_c)_d = (\sigma_m)_d + \sum_{s=1}^{d-1} \Big((K_d)_s (\sigma_{avg})_s \Big). \tag{1.21}$$

It is worth noting that the FEA correction has been developed and used in the case of induction-induced residual stress profiles, where the affected depth ($\sim$ 2.5 mm) is much larger than the shot peening affected depth ($\sim$ 300 µm). The element size for Savaria *et al.* (2012) was in the order of 50 µm to 100 µm, whereas it has to be in the order of microns to describe a typical shot peening profile. Therefore, for similar electropolished pocket size and sample geometry the number of elements and nodes will be much larger, and consequently the computation time will be longer.

Finally, Lebon *et al.* (2014) showed that the use of a semi-sphere-like pocket geometry, a more realistic pocket geometry, yields more accurate results than a square-parallelogram-like pocket geometry (as used by Savaria *et al.* (2012)) or the Moore & Evans correction, when compared to a known residual stress profile.

1.7 Chapter conclusions

In this chapter, the basics for understanding the scientific developments that followed were presented. The literature review was focused on the residual stresses introduced by the shot peening treatment and their measurement, in the case of three materials with very different mechanical behaviors. Shot peening, characterized by the Almen intensity and the coverage, introduces gradients of residual stresses and cold work. These gradients, with affecting a layer of hundreds of microns, differ from one material to another. It is reported that shot peening introduced a hardened layer for most material, such as IN718 and AA7050. However, the literature on 300M steel being less extensive, only a potential microstructural alteration was reported below the surface of the quenched and tempered condition of the more generic steel version AISI 4340. Furthermore, the most common residual stress measurements techniques were presented. The XRD method appears to be the most suitable method for the evaluation of the residual stress profile introduced by shot peening, when paired up with a layer removal procedure, such as electropolishing, due to the low effective penetration of X-rays. The residual stress computation is generally performed using the $\sin^2\psi$ method, but the $\cos\alpha$ method is being brought up to date with the commercialization of compact 2D detectors. In addition to the residual stress measurement, the XRD method has the advantage of simultaneously providing information on cold work, through the diffraction peak width analysis. Finally, the residual stress redistribution due to the layer removal process has to be considered. Two correction methods exist: an analytical method and a FEA-based method developed to correct larger affected depths than for the shot peening ones. The use of the latter may be limited by the computation time for the description of realistic pocket geometries.

An innovative comparison of the $\sin^2\psi$ and $\cos\alpha$ methods based on the specificities of the computation methods and of the detectors geometries, and on an EBSD map is detailed in the following chapters. The diffraction peak width is used to characterize the cold work profiles induced by different shot peening conditions for the three studied materials, which has never been done for the AA7050 and 300M. Finally, the unusual behavior of the peak width profiles through depth for the shot peened 300M is explained.

CHAPTER 2

METHODOLOGY

This chapter details the means implemented to carry out this study. The first section describes the shot peening treatments. The second section presents the mechanical behavior characterization tools deployed during this study. Finally, the third section provides details on the microstructural characterization techniques. Note that AA7050-T7451 specimens or samples will be referred to as AA7050 specimens or samples for reading convenience.

2.1 Materials mechanical and microstructural initial conditions

The mechanical and microstructural initial conditions of the three materials are detailed below. Part of the presented results were published in several articles as listed in the Introduction. 300M, IN718, and AA7050 materials were tested. The chemical composition of the received materials were in accordance with the AMS 6257F (2016), AMS 5663M (2009), and AMS 4050J (2014) standards presented in Chapter 1, respectively.

2.1.1 300M initial conditions

Three samples, extracted from 86.2 mm diameter bars, were used to determined the mechanical properties of the studied 300M steel. The average mechanical properties are presented in Table 2.1.

Table 2.1 Average mechanical properties of the studied 300M steel. Reproduced from Bag *et al.* (2019)

E (GPa)	$\sigma_{y0.2\%}$ (MPa)	σ_u (MPa)	El. (%)	ν
197	1693	2020	11.7	0.28

The 300M tempered martensite microstructure was revealed by etching using Vilella's reagent (1 g of Picric acid, 5 ml of HCl, and 100 ml of ethanol) for 20 s. The optical micrograph is presented in Figure 2.1a. The insert presents a closeup of the martensite laths and plates mixture. The prior austenite grain boundaries were revealed by Kohn's method of controlled oxidation (heat treating the polished sample in a 1 Pa vacuum following the austenitizing procedure allows revealing the preferential oxidation of the boundaries) (ISO 643, 2003) and are presented in Figure 2.1b. The average grain size of the prior austenite is 23 μm (Bag *et al.*, 2019).

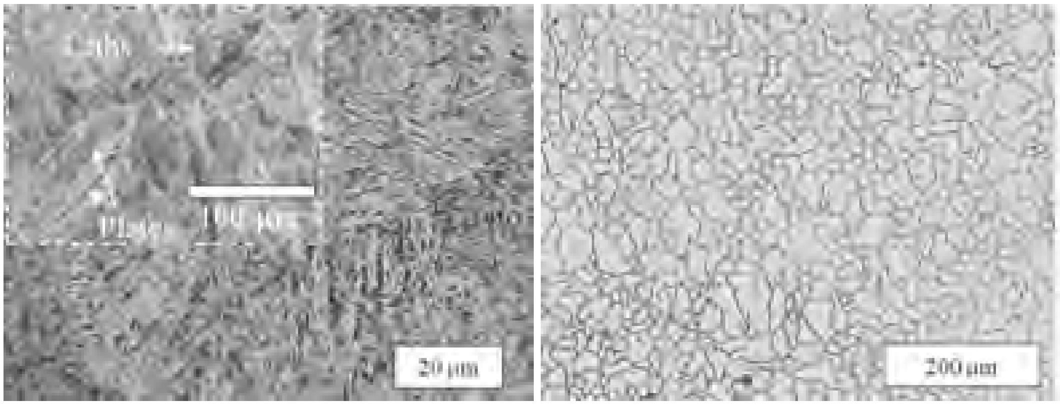

a) Tempered martensite

b) Prior austenite

Figure 2.1 300M optical micrographs showing a) the tempered martensite, the insert presents a closeup of the martensite laths and plates, and b) the prior austenite grain boundaries. Reprinted from Bag *et al.* (2019)

2.1.2 IN718 initial conditions

Two diameters of initial IN718 bars were used for the present study: 25 mm (1 in.) and 89 mm (3.5 in.) bars. The average mechanical properties were determined for three samples of each diameters and are presented in Table 2.2. A 10% difference in elastic limit can be observed between the two types of samples, mainly due to the precipitation state.

The microstructure of the ∅25 mm and ∅89 mm IN718 bars are presented in Figures 2.2a and 2.2b, respectively. An homogeneous austenite FCC matrix microstructure can be observed for the ∅25 mm sample (Figure 2.2a), whereas a bimodal microstructure is found in the ∅89 mm sample (Figure 2.2b). The homogeneous microstructure has a 13 μm average grain size with grains diameters ranging from 5 μm to 30 μm (Klotz *et al.*, 2018a). Whereas the bimodal microstructure has two distinct groups of grain size, having mean diameters of 10 μm and 30 μm. Grains having diameters as large as 100 μm can be found (Klotz *et al.*, 2017a), as shown in Figure 2.2b. Figures 2.2a and 2.2b also show the presence of titanium carbo-nitride (TiCN), δ phase (Ni_3Nb), and Niobium (NbC) carbides. The NbC carbides sizes were ranging from 3 μm to 14 μm with a 9 μm average size for both materials. Some δ phase can be observed along the grain and twin boundaries, revealing them.

Table 2.2 Average mechanical properties of the studied IN718 for the 25 mm and 89 mm diameters (∅) bars. Reproduced with permission from Klotz *et al.* (2018a) and Klotz *et al.* (2017a), respectively

Sample	E (GPa)	$\sigma_{y0.2\%}$ (MPa)	σ_u (MPa)	El. (%)	ν
∅25 mm	205	1156	1415	23	-
∅89 mm	205	1253	1413	24	0.32

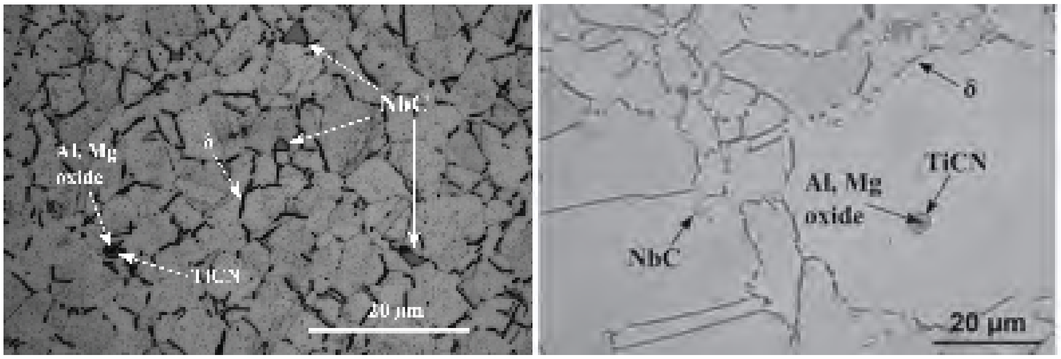

a) ∅25 mm

b) ∅89 mm

Figure 2.2 IN718 optical micrographs presenting the microstructure of a) the ∅25 mm and b) the ∅89 mm samples. Niobium (NbC) carbides, titanium carbo-nitride (TiCN), and δ phase along the grain boundaries can be observed. Reprinted with permission from Klotz *et al.* (2018a) and Klotz *et al.* (2017a), respectively

2.1.3 AA7050 initial conditions

The AA7050 samples were obtained from rolled plates. The mechanical properties of the AA7050 were determined for the rolling (RD) and transverse (TD) directions. Four tests were conducted per directions and the average mechanical properties are presented in Table 2.3. The two directions exhibit similar mechanical properties.

Table 2.3 Average mechanical properties of the studied AA7050 for the rolling (RD) and transverse (TD) directions. Reproduced from Bianchetti *et al.* (2018) with permission

Direction	E (GPa)	$\sigma_{y0.2\%}$ (MPa)	σ_u (MPa)	El. (%)
RD	70.4	463	517	13.5
TD	70.6	464	521	12.0

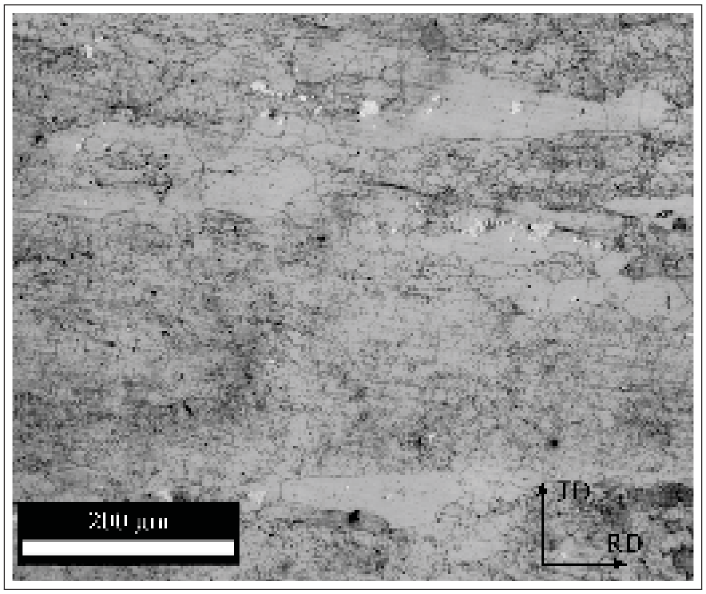

Figure 2.3 AA7050 optical micrograph presenting in the RD-TD plane the bimodal microstructure composed of small and large grains

The microstructure of the rolled AA7050 material, revealed by Weck's reagent (4 g of $KMnO_4$, 1 g of NaOH, and 100 ml of distilled water), is presented for RD-TD plane in Figure 2.3. The microstructure is composed of unrecrystallized (small) and bands of recrystallized (large) grains, having 7 μm and 47 μm average grain sizes, respectively. The larger grains are elongated in the rolling direction and can be up to 189 μm long. Such a microstructure tends to have burns while revealing it, with regions of small grains burning faster than the large grain region, as seen in the bottom right corner.

2.2 Shot peening treatment

The material presented above were shot peened. The shot peening process is a mechanical surface treatment introducing structural modifications, as presented in Chapter 1. This section aims to present the shot peening conditions used for the three materials. It is worth noting that specimen were machined by the industrial partners and shot peening treatments were realized by the Ph.D. co-workers.

Shot peening was performed in agreement with AMS 2430T (2015) standard. The shot peening conditions used for the treatment of 300M, IN718, and AA7050 specimens are summarized in Table 2.4. Two sets of shot peened specimens were produced when two intensities appear in the table. The shot range diameter and hardness of the media are presented in Table 2.5. All shot peening treatments were realized at 100% coverage.

Table 2.4 Shot peening conditions for the treatment of the 300M, IN718, and AA7050 specimens

Shot peening conditions	300M	IN718	AA7050
Media	S230 & CW14	CW14	Z425 & S230
Intensity	4 A & 8 A	4 A & 8 A	8A
Coverage	100%	100%	100%

Table 2.5 Shot range diameter and hardness for the S230, CW14, and Z425 media (AMS 2431/2E, 2010; AMS 2431/3D, 2007; AMS 2431/7B, 2013)

Media	Shot range diameter (mm)	Hardness (HRC)
S230	[0.5 , 0.85]	[55 , 62]
CW14	[0.325 , 0.375]	[45 , 52]
Z425	[0.43 , 0.60]	[58 , 63]

2.3 Microstructural characterization techniques

This section presents the scanning electron microscopy technique and electron backscatter diffraction characterization mapping method. The microstructures, observed using a scanning electron microscope to obtain orientation distribution maps, are presented in Chapter 3.

2.3.1 Scanning electron microscopy

The scanning electron microscopy (SEM) is based on the electron-matter interactions to produce images. Images are produced by scanning the sample surface with a beam of electrons set in motion by an accelerating voltage. High resolution images of the observed surface can be obtained with a larger depth of field than the classical optical microscope, which is limited by the visible light wavelength. SEM imaging can reveal fine microstructures.

When an incident beam of electrons interacts with the matter, a pear-like interaction volume can be observed. The size of the interaction volume varies with the material composition and the beam energy. The electron-matter interaction is schematized in Figure 2.4. The emitted radiations (also presented in Figure 2.4) are:

- **Secondary electrons** with a low energy, they are ejected by the incident electrons. They come from a superficial layer of the material. The secondary electrons are often used to study the sample surface-variations.

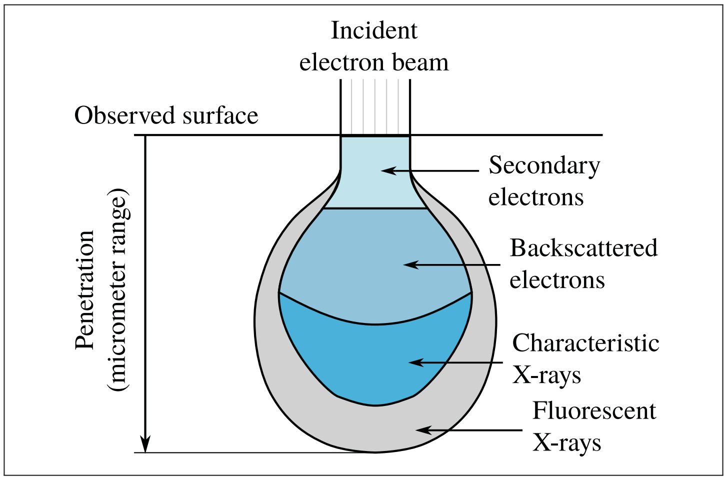
Incident
electron beam
Observed surface
Secondary
electrons
Backscattered
electrons
Characteristic
X-rays
Fluorescent
X-rays
Penetration
(micrometer range)

Figure 2.4 Interaction volume in the case of electron-matter interactions for a scanning electron microscope

• **Backscattered electrons** consisting of high-energy electrons. Electrons from the incident beam are scattered by sample atoms after an elastic scattering interaction. They can be used for chemical composition contrast between areas, as heavier atoms backscattered more electrons. Backscattered electrons can also be used to produce electron backscatter diffraction (EBSD) images, which is detailed in the next section.

• **Characteristic X-rays**, which are emitted when an incident electron removes an electron from the inner-shell, causing a higher-energy electron to fill the shell, which releases a photon (X-ray) with a characteristic energy (or wavelength as seen in Chapter 1). This provides an information on the chemical element types and their proportions. The corresponding analysis techniques are the energy-dispersive X-ray spectroscopy (EDS) and the wavelength-dispersive X-ray spectroscopy (WDS).

• **Fluorescent X-rays**, also emitted under the form of light. They are often seen as noise, when not intentionally produced. Nonetheless, they can still be used for chemical composition characterization in energy dispersive X-ray fluorescence (ED-XRF) spectroscopy.

2.3.2 Electron backscatter diffraction (EBSD) mapping

Particularly developed between 1973 and 1994, and now used as a standard characterization technique, the EBSD mapping uses the backscattered electrons to determine the crystallographic orientation of the grains forming the microstructure (Dingley, 2012). This technique allows accessing information such as local texture or deformation at the grain scale, which is not possible with the classic analyses using secondary or backscattered electrons.

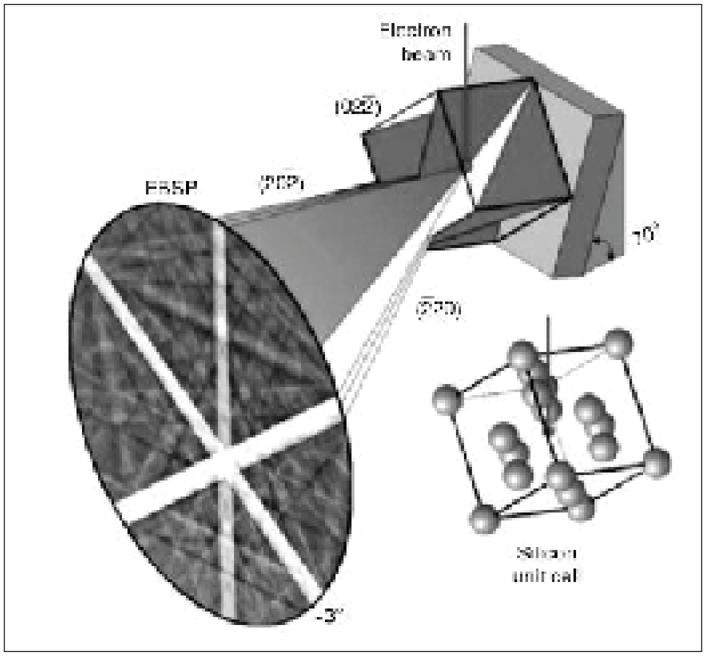

Figure 2.5 Illustration of electron interaction with crystalline material and Kikuchi diagram (EBSD pattern: EBSP). Reprinted from Maitland & Sitzman (2007) with permission

When an electron beam interacts with the grain for which the crystallographic orientation is sought, the electrons are scattered in two diffraction cones for each diffracting plane according to Bragg's law (Equation (1.5)). The intersection of the diffraction cones with the EBSD detector forms some crossing bands, called Kikuchi bands, as shown in Figure 2.5. Knowing the crystalline-structure type of the material, it is possible to determine the crystallographic orientation of the targeting grain, as for a specific crystallographic orientation corresponds an unique pattern of the Kikuchi bands, named Kikushi diagram. The Kikuchi diagram is affected by elastic and plastic strains. Elastic strain shifts the pattern, whereas the plastic strain degrades the pattern (Wright *et al.*, 2011). In practice, the sample surface must be carefully prepared not to introduce plastic strain during polishing, before being placed at 70° in the SEM chamber to increase the size of the sample region from which the incident electrons may backscatter and escape. During this study, the samples were electropolished after manual polishing to ensure that no plastic strains are present at the specimen surface. More details regarding the specimens preparation will be provided in Section 2.6 as the tensile specimens are the ones studied. An Hitachi SU-70, equipped with an Bruker EBSD camera, was used. After parameters adjustment, the electron beam scans the surface with a 0.5 μm step size. The EBSD maps were first analyzed using HKL Channel 5 software and then using MTEX, a MATLAB open source package (Bachmann *et al.*, 2011).

2.4 Microhardness measurement

The material hardness defines the resistance of the material to localized plastic deformation induced by an indenter and a known load. The term "microhardness" is employed for low applied loads and therefore micrometer size indentations. For surface treatment, such as shot peening, hardness is often used to measure variations in surface properties. Hardness profiles are measured on transverse sections at constant load. For a given load, the lower the penetration is, the harder is considered the material. Different loads are used during this study, as the harness variation is large between the softer material, AA7050, and the harder material, 300M.

Different hardness tests exist, which are performed with different types of indenters. Developed in 1900, the Brinell scale allows measuring the hardness through the penetration of a steel-ball indenter (Hill *et al.*, 1989). The Vickers scale has been developed as an alternative to the Brinell scale which suffers from its dependence to the indenter diameter. The Vickers hardness test makes use of a square-based-pyramid diamond indenter and has one of the widest scales, therefore, it can be used for a large variety of materials. The Rockwell scale is used for harder materials through the use of a ball indenter and a preload, establishing the zero-position. One last hardness scale often used for metallic materials is the Knoop hardness test, based on pyramidal it allows measuring near surface hardness.

The next two subsections provide more details on the Vickers and Knoop scales, as they enable near surface measurement of shot peening induced mechanical properties variations.

2.4.1 Vickers microhardness test

The Vickers microhardness test is carried out using a square-based pyramidal-shaped diamond indenter, leaving a square mark on the sample surface, as shown in Figure 2.6. The diamond indenter penetrates the sample surface with a known force, F_{HV}, during a defined dwell time of 10 s. The diagonals are then measured and Vickers hardness is computed as (ASTM E384-17, 2017)

$$HV = 1854.4 \frac{F_{HV}}{d_{HV}^2} \tag{2.1}$$

where $\mathrm{F_{HV}}$ is expressed in grams-force (gf) and d_{HV} is the average of the measured diagonals d_{HV1} and d_{HV2} expressed in micrometers. The gram-force is a unit of force and represents the

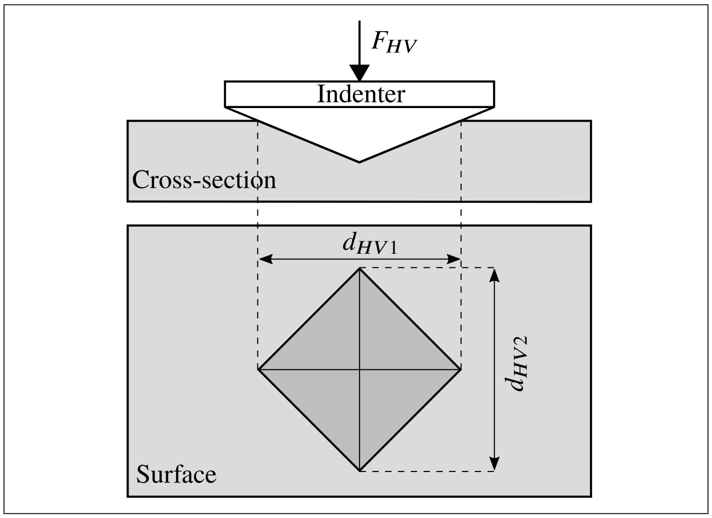

Figure 2.6 Illustration of a Vickers hardness test on a sample surface. The diagonals d_{HV1} and d_{HV2} are measured after indentation with a force F_{HV}

force exerted by a gram of mass. The Vickers hardness scale is reported as $\mathrm{HV}_{F_{HV}gf}$ when Vickers microhardness values are presented. For instance, a hardness value HV measured with a load of 100 gf will be reported as HV $\mathrm{HV}_{100\mathrm{gf}}$.

2.4.2 Knoop microhardness test

The Knoop microhardness test is performed using a rhombic-based pyramidal-shaped diamond indenter, leaving an elongated mark on the sample surface, as shown in Figure 2.7. The long diagonal d_{HK} is measured after applying a known force F_{HK} and the Knoop hardness is determined as (ASTM E384-17, 2017)

$$HK = 14229\frac{F_{HK}}{d_{HK}^2} \tag{2.2}$$

where F_{HK} and d_{HK} are expressed in grams-force and micrometers, respectively. Similarly to the Vickers scale, the Knoop hardness scale is reported as HK $\mathrm{HK}_{F_{HK}\mathrm{gf}}$ when Knoop microhardness values are presented.

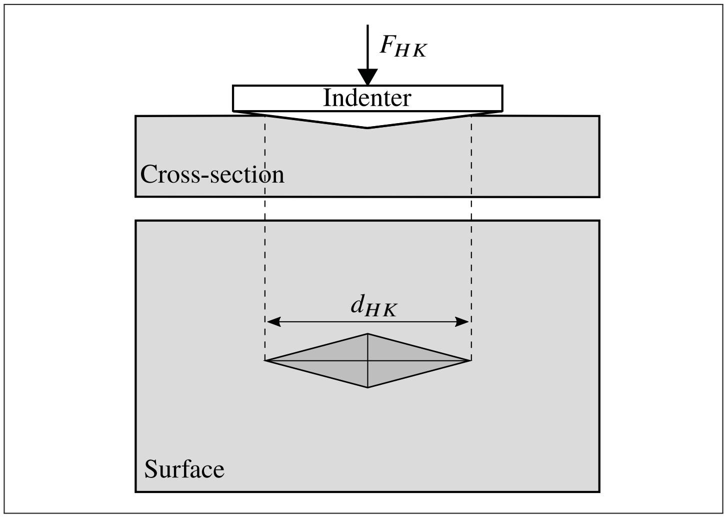

Figure 2.7 Illustration of a Knoop hardness test on a sample surface. The diagonal d_{HK} is measured after indentation with a force F_{HK}

2.4.3 Microhardness profile: precision and bias

Sample preparation is key for precise microhardness measurements. Sample surface should be flat so indenter is perpendicular to it, else incorrect results may emerge from the distortion of the indentation shape. For instance, in the case of Vickers hardness tests, one diagonal may be notably longer than the other. For very low loads ($\leq$ 200 gf), residual deformations from mechanical polishing must be removed (ASTM E384-17, 2017). Furthermore, material homogeneity, orientation and/or texture may affect the measure and, as a micro-characterization, the measurement repeatability.

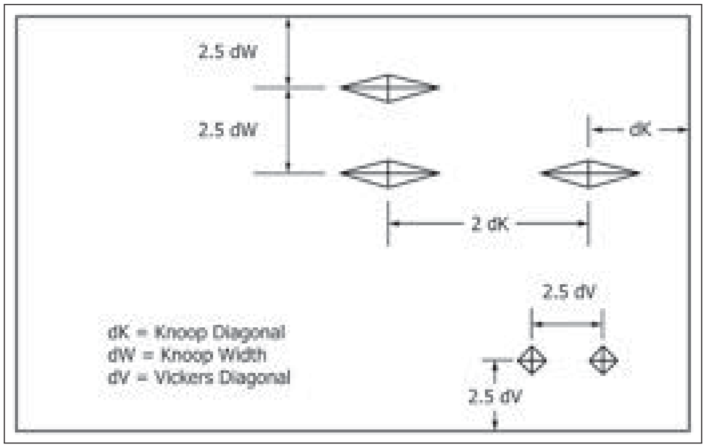

Figure 2.8 Illustration of the minium recommended spacings for the Knoop and Vickers indentations. Reprinted from ASTM E384-17 (2017) with permission

When more than one indentation is made, the ASTM E384-17 (2017) standard recommends a certain spacing between the indentations to ensure measurements repeatability, especially for microhardness profile determination. For Vickers microhardness tests, the minimum recommended indentations spacing is $2.5d_{HV}$. A similar distance from the sample surface has to be respected. For the Knoop microhardness tests, the indentations must be spaced by 2.5 times the indentation width on the width direction and $2d_{HK}$ on the diagonal direction. As for the Vickers measurements test, similar distances from the edges have to be respected. Figure 2.8 illustrates these different spacings. Note that dK and dV correspond to d_{HK} and d_{HV}, respectively, and that the indents are not to scale. Indeed, for a given load the width of the Knoop indent is smaller than the diameters of the Vickers indent, which allows having indents closer to the shot peened surface.

2.5 Residual stress measurement

This section details the $\sin^2\psi$ and $\cos\alpha$ methods along with the determination of the XEC for the residual stress evaluation. The XRD equipment used during this study are presented as well as the electropolishing procedure for the determination of the residual stress profile.

2.5.1 Residual stress computation

As mentioned in Chapter 1, different methods exist to compute the residual stresses from the strain $\varepsilon^{\{hkl\}}$ measured along the normal of $\{hkl\}$ planes, which is aligned with the scattering vector $\mathbf{V_{Scat}}$. In XRD, $\varepsilon^{\{hkl\}}$ is computed from the change in lattice spacing or shift in Bragg angle as

$$\varepsilon^{\{hkl\}} = \frac{d^{\{hkl\}} - d_0^{\{hkl\}}}{d_0^{\{hkl\}}} = -(\theta^{\{hkl\}} - \theta_0^{\{hkl\}}) \cot \theta_0^{\{hkl\}}. \tag{2.3}$$

The measured strain $\varepsilon^{\{hkl\}}$ corresponds to the strain $\varepsilon_{33}^{\mathrm{L}}$ expressed in the laboratory coordinate system (i.e., $\mathbf{L_1}$, $\mathbf{L_2}$, $\mathbf{L_3}$). Figure 2.9 presents the laboratory coordinate system and the sample coordinate system (i.e., $\mathbf{S_1}$, $\mathbf{S_2}$, $\mathbf{S_3}$), which in the case of a rolled material corresponds to the rolling, transverse, and normal directions. The laboratory coordinate system is defined by a rotation by an azimuth angle φ about the $\mathbf{S_3}$-axis and a rotation by an tilt angle ψ about the $\mathbf{L_2}$-axis, so the $\mathbf{L_3}$ axis is aligned with the scattering vector $\mathbf{V_{Scat}}$.

The measured strain $\varepsilon^{\{hkl\}}$ can also be expressed in terms of strain components $\varepsilon_{ij}^{\mathrm{S}}$ in sample coordinate system with respect to the Einstein summation convention by

$$\varepsilon^{\{hkl\}} = \varepsilon_{33}^{\mathrm{L}} = \mathrm{v}_i \mathrm{v}_j \varepsilon_{ij}^{\mathrm{S}} \tag{2.4}$$

where v_i and v_j are the components of the scattering vector $\mathbf{V_{Scat}}$.

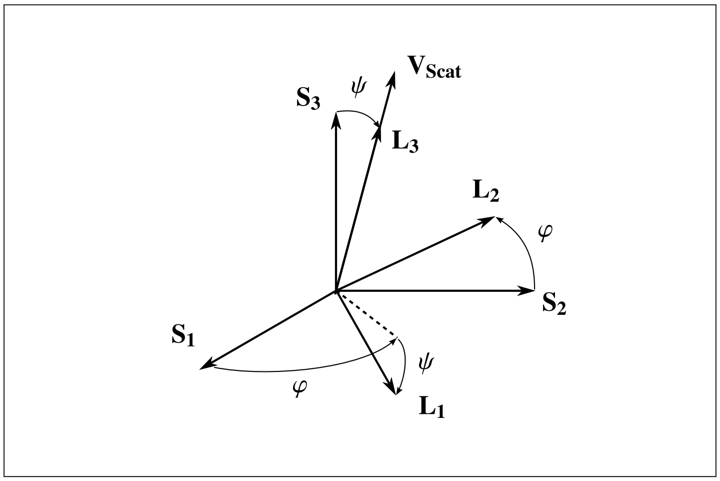

Figure 2.9 Definition of the sample (**S**) and laboratory (**L**) coordinate systems via the azimuth φ and tilt ψ angles. The scattering vector $\mathbf{V_{Scat}}$ is aligned with $\mathbf{L_3}$

If the material under consideration can be consider isotropic and homogeneous, Hooke's law can be used to relate the macroscopic stress, σ^{S}, to the strain as expressed in the sample coordinate system as

$$\varepsilon_{ij}^{S} = \frac{1+\nu}{E}\sigma_{ij}^{S} - \delta_{ij}\frac{\nu}{E}\sigma_{kk}^{S} \tag{2.5}$$

where E and ν are the material's macroscopic Young's modulus and Poisson's ratio values, respectively.

The $\sin^2\psi$ and $\cos\alpha$ methods make use of Equations (2.4) and (2.5) to evaluate the residual stress under the assumption of biaxial stress state (i.e., $\sigma_{33}^{S} = \sigma_{23}^{S} = \sigma_{13}^{S} = 0$) in the irradiated layer and non-textured polycrystalline material. The only differences between the two methods lie in the expression by different angles of the scattering vector $\mathbf{V_{Scat}}$ in the sample coordinate system and in the fact that the $\cos\alpha$ method uses an alternative strain-parameter to take advantage of the 2D detector. The $\sin^2\psi$ and $\cos\alpha$ methods are detailed in the following sections. For reading convenience, the exponent describing the coordinate system is not further displayed, but it is worth noting that the strain ε_{ij} and stress σ_{ij} components are expressed in the sample coordinate system.

2.5.1.1 $\sin^2\psi$ method

The $\sin^2\psi$ method often makes use of diffraction data collected by one or two linear detectors, using only part of the diffraction cone. Therefore, the X-ray head has to take different β-positions to allow the residual stress measurement, making it a multi-exposure technique. In this method, only the scattered X-rays contained in the φ plane, as illustrated in Figure 2.10, are captured by two linear detectors (two detectors are considered here as this configuration equipped most of the XRD apparatuses dedicated to residual stress measurement). The linear detectors are presented by arcs of circles as they are in reality slightly curved. For a given detector position, the strain measurement is performed along the scattering vector $\mathbf{V_{Scat}}$, also contained in the φ plane. $\mathbf{V_{Scat}}$ vector can be expressed in the sample coordinate system ($\mathbf{S_1}$, $\mathbf{S_2}$, $\mathbf{S_3}$ defined in Figure 2.10) as

$$\mathbf{V_{Scat}}(\varphi,\psi) = \begin{bmatrix} \mathrm{v}_1 \\ \mathrm{v}_2 \\ \mathrm{v}_3 \end{bmatrix} = \begin{bmatrix} \sin\psi\ \cos\varphi \\ \sin\psi\ \sin\varphi \\ \cos\psi \end{bmatrix}, \tag{2.6}$$

where φ and ψ are the azimuth and the tilt angles, respectively (the angles are defined in Figure 2.10). ψ corresponds to the angle between the sample surface and the normal to the $\{hkl\}$ planes.

$\varepsilon^{\{hkl\}}$ being function of φ and ψ angles, it is denoted as $\varepsilon^{\{hkl\}}_{\varphi\psi}$ and Equation (2.4) can be developed using Equation (2.6) as

$$\begin{aligned} \varepsilon^{\{hkl\}}_{\varphi\psi} = \frac{d^{\{hkl\}} - d_0^{\{hkl\}}}{d_0^{\{hkl\}}} &= \varepsilon_{11}\cos^2\varphi\ sin^2\psi + \varepsilon_{12}\sin 2\varphi\ sin^2\psi + \varepsilon_{22}\sin^2\varphi\ sin^2\psi \\ &+ \varepsilon_{33}\cos^2\psi + \varepsilon_{13}\cos\varphi\ sin2\psi + \varepsilon_{23}\sin\varphi\ sin2\psi. \end{aligned} \tag{2.7}$$

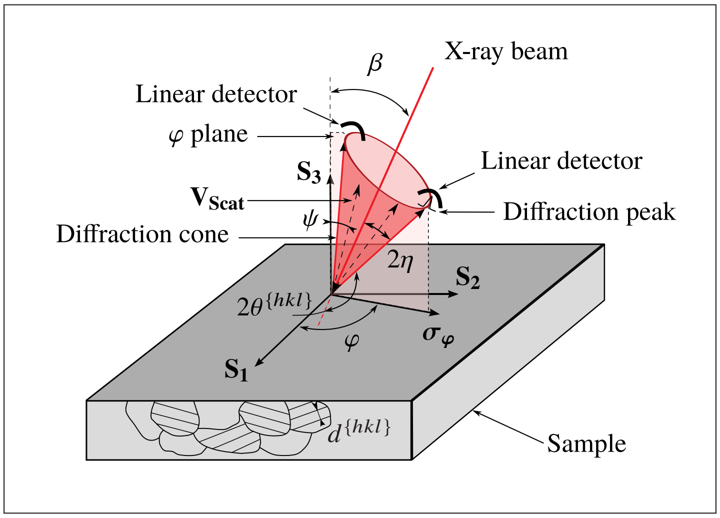
X-ray beam
β
Linear detector
φ plane
S_3
V_{Scat}
ψ
Diffraction cone
Linear detector
Diffraction peak
2η
S_2
$2\theta^{\{hkl\}}$
φ
σ_φ
S_1
$d^{\{hkl\}}$
Sample

Figure 2.10 Illustration of the diffraction cone and the two linear detectors used in the case of the $\sin^2\psi$ method. The stress σ_φ is measured in the direction defined by the detectors plane (φ plane)

By substitution using Equation (2.5), Equation (2.7) becomes

$$\begin{aligned}\varepsilon_{\varphi\psi}^{\{hkl\}} = {} & \frac{1+\nu^{\{hkl\}}}{E^{\{hkl\}}}\left[\sigma_{11}\ \cos^2\varphi + \sigma_{12}\ \sin 2\varphi + \sigma_{22}\ \sin^2\varphi - \sigma_{33}\right]\ \sin^2\psi \\ & + \frac{1+\nu^{\{hkl\}}}{E^{\{hkl\}}}\sigma_{33} - \frac{\nu^{\{hkl\}}}{E^{\{hkl\}}}\left[\sigma_{11}+\sigma_{22}+\sigma_{33}\right] \\ & + \frac{1+\nu^{\{hkl\}}}{E^{\{hkl\}}}\left[\sigma_{13}\ \cos\varphi + \sigma_{23}\ \sin\varphi\right]\ \sin 2\psi\end{aligned} \tag{2.8}$$

where $E^{\{hkl\}}$ and $\nu^{\{hkl\}}$ are the average Young's modulus and Poisson's ratio determined for the $\{hkl\}$ planes over the diffracting grains, respectively. The use of $E^{\{hkl\}}$ and $\nu^{\{hkl\}}$ allows taking into consideration the crystal anisotropy to relate the strain measured on crystallographic planes to the macroscopic stress.

Using the assumption of biaxial stress state ($\sigma_{33} = \sigma_{23} = \sigma_{13} = 0$), such as the residual stress introduced by shot peening, Equation (2.8) can be written as

$$\varepsilon_{\varphi\psi}^{\{hkl\}} = \frac{1+\nu^{\{hkl\}}}{E^{\{hkl\}}}\sigma_\varphi \sin^2\psi - \frac{\nu^{\{hkl\}}}{E^{\{hkl\}}}(\sigma_{11}+\sigma_{22}) \tag{2.9}$$

where $\sigma_\varphi = \sigma_{11}\cos^2\varphi + \sigma_{12}\sin 2\varphi + \sigma_{22}\sin^2\varphi$ is the macroscopic stress to be measured along the direction φ defined by the linear detectors plane (see Figure 2.10).

By defining $S_1^{\{hkl\}}$ and $\frac{1}{2}S_2^{\{hkl\}}$, the XECs of the $\{hkl\}$ planes, as

$$S_1^{\{hkl\}} = \frac{-\nu^{\{hkl\}}}{E^{\{hkl\}}}, \tag{2.10a}$$

$$\frac{1}{2}S_2^{\{hkl\}} = \frac{1+\nu^{\{hkl\}}}{E^{\{hkl\}}}, \tag{2.10b}$$

Equation (2.9) can be rewritten as

$$\varepsilon_{\varphi\psi}^{\{hkl\}} = \frac{1}{2}S_2^{\{hkl\}}\sigma_\varphi \sin^2\psi + S_1^{\{hkl\}}(\sigma_{11}+\sigma_{22}). \tag{2.11}$$

Finally, the stress to be determined σ_φ can be computed by differentiating Equation (2.11) with respect to $\sin^2\psi$ as

$$\sigma_\varphi = \frac{1}{\frac{1}{2}S_2^{\{hkl\}}}\frac{\partial\varepsilon_{\varphi\psi}^{\{hkl\}}}{\partial\sin^2\psi}. \tag{2.12}$$

Equation (2.12) shows that only $\frac{1}{2}S_2^{\{hkl\}}$ has to be known to determine σ_φ. When plotting the measured strain $\varepsilon_{\varphi\psi}^{\{hkl\}}$ as a function of $\sin^2\psi$, and based on the assumptions listed previously, one can determine the stress σ_φ, in the measurement direction φ, if a linear regression between $\varepsilon_{\varphi\psi}^{\{hkl\}}$ and $\sin^2\psi$ is found. Therefore, several ψ angles have to be used to obtain the relationship between $\varepsilon_{\varphi\psi}^{\{hkl\}}$ and $\sin^2\psi$ when the diffracted X-rays are captured with two linear detectors. Practically, the several ψ angles needed, which correspond to different $\mathbf{V_{Scat}}$ vectors, are obtained when changing the incident X-ray beam angle, $\beta = \psi \pm \eta$ (with $2\eta = \pi - 2\theta$ being the diffraction cone semi-apex angle shown in Figure 2.10).

Figure 2.11 provides an example of linear regression for a measurement on 300M where the strain has been determined for the two linear detectors, namely left and right detectors. Knowing the XEC, one can compute the stress from the linear regression slope.

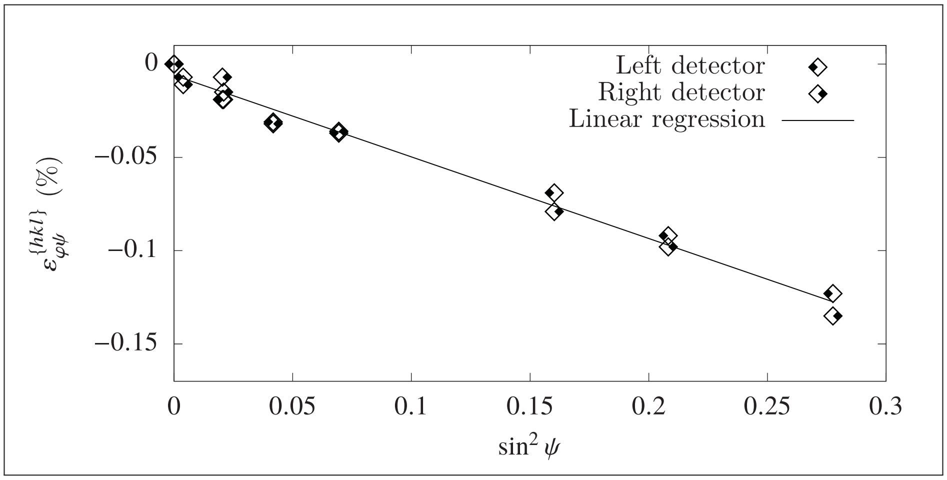

Figure 2.11 Example of $\varepsilon_{\varphi\psi}^{\{hkl\}}$ vs. $\sin^2\psi$ plot for a measurement on 300M with two linear detectors at nine β-tilts

Three points are worth noting. Firstly, it is often assumed that the biaxial stress state of the irradiated layer implies that the lattice spacing of the planes of atoms parallel to the specimen surface ($\psi = 0°$) approximately corresponds to the unstressed lattice spacing $d_0^{\{hkl\}}$. Therefore, the lattice spacing value found for $\psi = 0°$ is substituted by $d_0^{\{hkl\}}$ yielding a $\varepsilon_{\varphi,\psi=0}^{\{hkl\}} = 0$. Such substitution introduces negligible error compared to the error introduced by other sources such as wrong XECs (Noyan & Cohen, 1987), which can lead to a stress error of 20% (Fitzpatrick *et al.*, 2005). Secondly, if the linear regression condition is not met, due to texture for instance, Equation (2.12) can not be used to determined the stress as the points will not be aligned. Finally, each β position provides measurements from different depths.

2.5.1.2 cos α method

For the $\cos\alpha$ method, the stress calculation can be done with a single X-ray exposure when a large enough region of the Debye ring is measured by a 2D detector. The 2D detector allows acquiring diffraction peaks for several ϕ and ψ angles in a single exposure. A stress-free material, such as powder, exhibits a perfectly circular Debye ring, as the lattice spacings $d_0^{\{hkl\}}$ are the same in every direction. A stressed surface will modify the ring radius and its distortion can be described using the α angle defined as the plane angle on the 2D detector plane, as schematized in Figure 2.12.

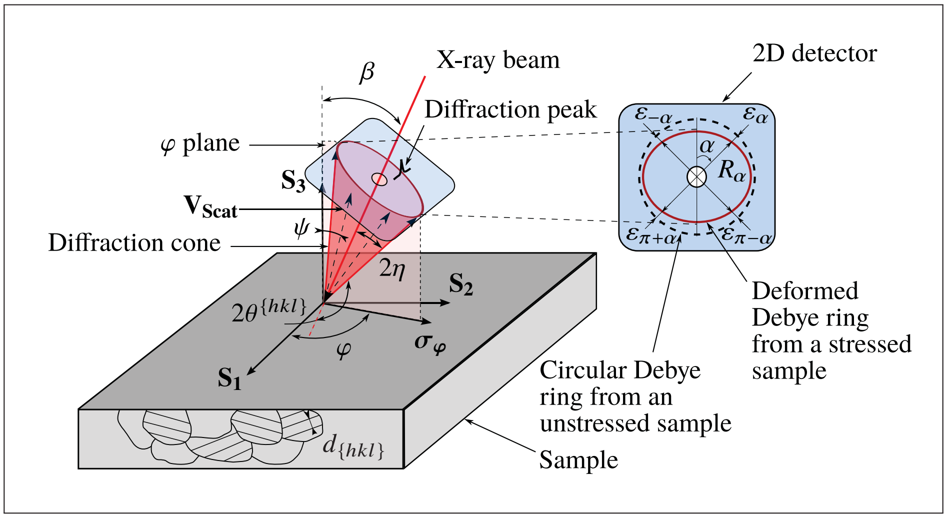
β
X-ray beam
2D detector
Diffraction peak
φ plane
$\varepsilon_{-\alpha}$
ε_{α}
α
R_{α}
$\mathbf{S_3}$
$\mathbf{V_{Scat}}$
ψ
Diffraction cone
$\varepsilon_{\pi+\alpha}$
$\varepsilon_{\pi-\alpha}$
2η
$\mathbf{S_2}$
$2\theta^{\{hkl\}}$
σ_{φ}
φ
$\mathbf{S_1}$
Deformed Debye ring from a stressed sample
Circular Debye ring from an unstressed sample
$d_{\{hkl\}}$
Sample

Figure 2.12 Illustration of the diffraction cone and the 2D detector used in the case of the cos α method. The stress σ_{φ} is computed for a variation of α from 0° to 90° and the measurement of the corresponding strains $\varepsilon_{\alpha}^{\{hkl\}}$, $\varepsilon_{\pi+\alpha}^{\{hkl\}}$, $\varepsilon_{-\alpha}^{\{hkl\}}$, and $\varepsilon_{\pi-\alpha}^{\{hkl\}}$

The strain is measured along the scattering vectors $\mathbf{V_{Scat}}$ for different α angles. Therefore, when the measurement is made with a planar detector, the $\mathbf{V_{Scat}}$ vectors should be defined in the sample coordinate system using the angle α and the diffraction cone's semi-apex angle 2η, which gives

$$\mathbf{V_{Scat}}(\eta,\beta,\varphi,\alpha) = \begin{bmatrix} \cos\eta\ \sin\beta\ \cos\varphi - \sin\eta\ \cos\beta\ \cos\varphi\ \cos\alpha - \sin\eta\ \sin\varphi\ \sin\alpha \\ \cos\eta\ \sin\beta\ \sin\varphi - \sin\eta\ \cos\beta\ \sin\varphi\ \cos\alpha + \sin\eta\ \cos\varphi\ \sin\alpha \\ \cos\eta\ \cos\beta + \sin\eta\ \sin\beta\ \cos\alpha \end{bmatrix}. \tag{2.13}$$

For a given α-angular position on the 2D detector, the measured strain $\varepsilon_{\alpha}^{\{hkl\}}$ can be obtained from the ring radius R_{α} as

$$\varepsilon_{\alpha}^{\{hkl\}} = -\Delta\theta\ \cot\theta_0 = \frac{1}{2}\left(2\theta_0 - \pi + \tan^{-1}\frac{R_{\alpha}}{C_L}\right)\ \cot\theta_0, \tag{2.14}$$

where C_L is the sample-to-detector distance. Similarly to Equation (2.7), the measured strain $\varepsilon_\alpha^{\{hkl\}}$ can be related to the strain components ε_{ij} in sample coordinate system with respect to the Einstein summation convention as

$$\varepsilon_\alpha^{\{hkl\}} = \frac{1}{2}\Big(2\theta_0 - \pi + \tan^{-1}\frac{R_\alpha}{C_L}\Big)\,\cot\theta_0 = \mathrm{v}_i\mathrm{v}_j\varepsilon_{ij}. \tag{2.15}$$

The $\cos\alpha$ method makes use of a parameter $\overline{\varepsilon}_\alpha^{\{hkl\}}$ defined as

$$\overline{\varepsilon}_\alpha^{\{hkl\}} = \frac{1}{2}\Big[(\varepsilon_\alpha^{\{hkl\}} - \varepsilon_{\pi+\alpha}^{\{hkl\}}) + (\varepsilon_{-\alpha}^{\{hkl\}} - \varepsilon_{\pi-\alpha}^{\{hkl\}})\Big], \tag{2.16}$$

where $\varepsilon_\alpha^{\{hkl\}}$, $\varepsilon_{\pi+\alpha}^{\{hkl\}}$, $\varepsilon_{-\alpha}^{\{hkl\}}$, and $\varepsilon_{\pi-\alpha}^{\{hkl\}}$ are strains determined at four points symmetrically located at 90° on the Debye ring for a given α angle (as shown in Figure 2.12) using Equation (2.14).

The parameter $\overline{\varepsilon}_\alpha^{\{hkl\}}$ can be expressed in terms of stresses using trigonometric simplifications and by combining Equation (2.5), Equation (2.13), and Equation (2.15) into Equation (2.16) as

$$\overline{\varepsilon}_\alpha^{\{hkl\}} = -\frac{1+\nu^{\{hkl\}}}{E^{\{hkl\}}}\sin 2\eta\,\sin 2\beta\,\cos\alpha\,\sigma_\varphi, \tag{2.17}$$

where $\sigma_\varphi = 1/2(\sigma_{11}(1+\cos 2\varphi)+\sigma_{22}(1-\cos 2\varphi)+2\sigma_{12}\sin 2\varphi)$. The detailed mathematical development allowing the stress computation (transition from Equation (2.16) to Equation (2.17)) is not presented in the article introducing the $\cos\alpha$ method by Taira *et al.* (1978) and was not available in the limited literature in 2014. Consequently, the mathematical proof has been performed and is presented in Appendix II.

Differentiating Equation (2.17) with respect to $\cos\alpha$ and isolating σ_φ yields

$$\sigma_\varphi = -\frac{E^{\{hkl\}}}{1+\nu^{\{hkl\}}}\frac{1}{\sin 2\eta\,\sin 2\beta}\frac{\partial\overline{\varepsilon}_\alpha^{\{hkl\}}}{\partial\cos\alpha} = -\frac{1}{\frac{1}{2}S_2^{\{hkl\}}}\frac{1}{\sin 2\eta\,\sin 2\beta}\frac{\partial\overline{\varepsilon}_\alpha^{\{hkl\}}}{\partial\cos\alpha}. \tag{2.18}$$

If a linear regression between $\overline{\varepsilon}_\alpha^{\{hkl\}}$ and $\cos\alpha$ is found then the stress σ_φ can be computed. Figure 2.13 provides an example of $\overline{\varepsilon}_\alpha^{\{hkl\}}$ vs. $\cos\alpha$ plot when stress is being measured using

125 $\overline{\varepsilon}_{\alpha}^{\{hkl\}}$ values (dividing the Debye ring into 500 sections). It is worth noting that due to the cosine properties the point density increases the closer the $\cos\alpha$ values reach 1.

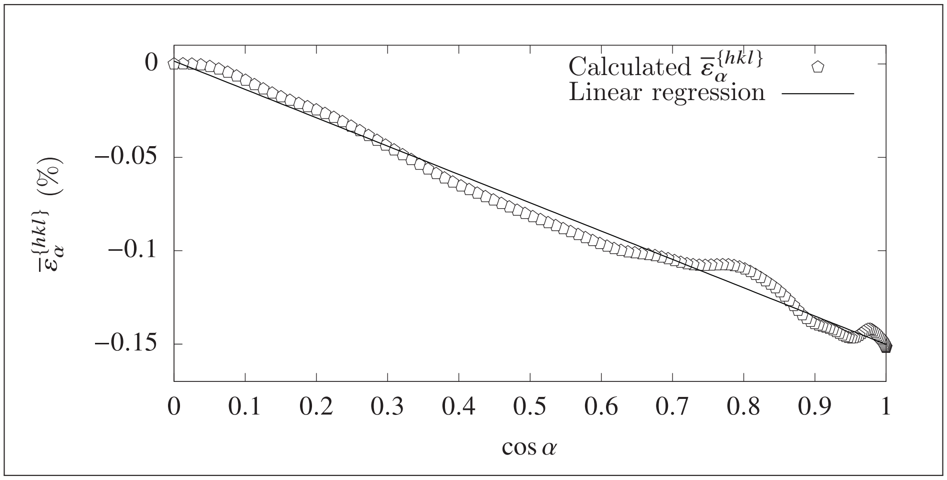

Figure 2.13 Example of $\overline{\varepsilon}_{\alpha}^{\{hkl\}}$ vs. $\cos\alpha$ plot for a measurement on 300M with a 2D detector in a single exposure

Equation (2.18) can also be found in reference books Noyan & Cohen (1987) and Hauk (1997) as

$$\sigma_{\varphi} = \frac{1}{\frac{1}{2}S_2^{\{hkl\}}} \frac{1}{[\sin^2(\beta - \eta) - \sin^2(\beta + \eta)]} \frac{\partial \overline{\varepsilon}_{\alpha}^{\{hkl\}}}{\partial \cos\alpha}. \tag{2.19}$$

The mathematical transition from $(-\sin 2\eta \ \sin 2\beta)$ to $[\sin^2(\beta - \eta) - \sin^2(\beta + \eta)]$ leading to Equation (2.19) is presented in Appendix III.

2.5.2 XECs computation

Different methods can be deployed to determine the XECs of a material. In the case of an isotropic material, the simplest way would be to use the material macroscopic values of the Young's modulus, E, and Poisson's ratio, ν, as elastic constant as

$$S_1 = \frac{-\nu}{E} \text{ and } \frac{1}{2}S_2 = \frac{1+\nu}{E}. \tag{2.20}$$

Nonetheless, because the strain is measured for a specific $\{hkl\}$ crystallographic direction and material single crystal properties can be highly anisotropic, it is more accurate to account for the $\{hkl\}$ direction of the X-ray measurement and to use the $S_1^{\{hkl\}}$ and $\frac{1}{2}S_2^{\{hkl\}}$, presented earlier in Equations (2.10a) and (2.10b). They can be theoretically computed from micromechanical models, such as Voigt and Reuss models, or experimentally measured. The two techniques are described in the two following sections.

2.5.2.1 Theoretical determination of the XECs

The micromechanical models below have been developed for the case of cubic metals and isotropic polycrystals.

For the Voigt model, the strain tensors are assumed to be the same in all the grains and the resulting compliance tensor is averaged over all grain orientations (Murray, 2013), yielding the following XECs expressions (Van Houtte & De Buyser, 1993)

$$\left(S_1^{\{hkl\}}\right)^{\text{Voigt}} = \frac{S_0(S_{1111}^{\text{C}} + 2S_{1122}^{\text{C}}) + 10S_{1122}^{\text{C}}S_{1212}^{\text{C}}}{3S_{1111}^{\text{C}} - 3S_{1122}^{\text{C}} + 4S_{1212}^{\text{C}}}, \tag{2.21a}$$

$$\left(\frac{1}{2}S_2^{\{hkl\}}\right)^{\text{Voigt}} = \frac{10S_{1212}^{\text{C}}(S_{1111}^{\text{C}} - S_{1122}^{\text{C}})}{3S_{1111}^{\text{C}} - 3S_{1122}^{\text{C}} + 4S_{1212}^{\text{C}}}, \tag{2.21b}$$

where S_{1111}^{C}, S_{1122}^{C}, and S_{1212}^{C} are the fourth-rank compliance tensor components of S_{ijkl}, and S_0 is defined as

$$S_0 = S_{1111}^{\text{C}} - S_{1122}^{\text{C}} - 2S_{1212}^{\text{C}}. \tag{2.22}$$

Note that the $ijkl$ indices are not related to the hkl Miller indices (which are display in exponent when referred to) but to the components of the compliance tensor.

For the Reuss model, the stress tensors are assumed to be the same in all the grains and the average over the diffracting grains is performed by integrating the elastic constants over a 2π rotation around $\boldsymbol{L_3}$, as the diffracting grains have their $\mathbf{V}^{\{hkl\}}$ vectors aligned with $\boldsymbol{L_3}$ (Van

Houtte & De Buyser, 1993)

$$\left(S_1^{\{hkl\}}\right)^{\text{Reuss}} = S_{1122}^{\text{C}} + S_0\Gamma, \tag{2.23a}$$

$$\left(\frac{1}{2}S_2^{\{hkl\}}\right)^{\text{Reuss}} = S_{1111}^{\text{C}} - S_{1122}^{\text{C}} - 3S_0\Gamma, \tag{2.23b}$$

where Γ is the orientation parameter, function of the Miller indices for the diffracting planes under investigation, defined as

$$\Gamma = \frac{h^2k^2 + h^2l^2 + k^2l^2}{(h^2 + k^2 + l^2)^2}. \tag{2.24}$$

It is worth noting that the Reuss limits are dependent of the diffracting planes, which is actually not the case for Voigt limits.

Intermediate micromechanical models exist beside the Voigt and Reuss models as it is clear that real material behaviors do not correspond to the Voigt nor the Reuss theory (Van Houtte & De Buyser, 1993). The Hill model (often found as the Neerfeld-Hill model) is one of them and suggests the use of the average between the Voigt and Reuss models as

$$\left(S_1^{\{hkl\}}\right)^{\text{Hill}} = \frac{1}{2}\left[\left(S_1^{\{hkl\}}\right)^{\text{Voigt}} + \left(S_1^{\{hkl\}}\right)^{\text{Reuss}}\right], \tag{2.25a}$$

$$\left(\frac{1}{2}S_2^{\{hkl\}}\right)^{\text{Hill}} = \frac{1}{2}\left[\left(\frac{1}{2}S_2^{\{hkl\}}\right)^{\text{Voigt}} + \left(\frac{1}{2}S_2^{\{hkl\}}\right)^{\text{Reuss}}\right]. \tag{2.25b}$$

The Hill model is often preferred for the calculation of the XECs over more complicated micromechanical models as the self-consistent method develop by Kröner (1958), due to its calculation simplicity and experimental evidence showing a reasonable approximation of the XECs behavior (Murray, 2013).

The use of the micromechanical models require the accurate knowledge of the single crystal elastic constant tensor, which is not easy to obtained, especially for alloyed materials. An example of $\frac{1}{2}S_2^{\{hkl\}}$ theoretical computation with the three models is provided in Figure 2.14

for IN718. The single crystal elastic constants $C_{11}^{\mathrm{C}} = 251.0$ GPa, $C_{12}^{\mathrm{C}} = 135.5$ GPa, and $C_{44}^{\mathrm{C}} = 98$ GPa were averaged from experimental values reported in the literature at room temperature for a certain range of grain sizes and compositions (Ledbetter & Reed, 1973; Margetan *et al.*, 2005; Haldipur, 2006; Aba-Perea *et al.*, 2016). It is worth noting that $\boldsymbol{C}^{\mathbf{C}}$ components are expressed with the matrix notation, not the tensor notation, and that $S_{ij} = (C_{ij})^{-1}$. The components of the compliance tensor are consequently obtained by inverting $\boldsymbol{C}^{\mathbf{C}}$ and using the following identities: $S_{1111} = S_{11}$, $S_{1122} = S_{12}$, and $S_{1212} = \frac{1}{4}S_{66}$. The Voigt limit is constant at $\left(\frac{1}{2}S_2^{\{hkl\}}\right)^{\mathrm{Voigt}} = 6.10 \times 10^{-6}\ \mathrm{MPa}^{-1}$, whereas the Reuss limit and the subsequent Hill values vary with the orientation parameter Γ. The $\{311\}$ planes, often used for the XRD measurements of IN718 residual stresses, yield a Γ value of 0.157 and XECs computed with the Reuss and Hill models of $\left(\frac{1}{2}S_2^{\{311\}}\right)^{\mathrm{Reuss}} = 6.98 \times 10^{-6}\ \mathrm{MPa}^{-1}$ and $\left(\frac{1}{2}S_2^{\{311\}}\right)^{\mathrm{Hill}} = 6.54 \times 10^{-6}\ \mathrm{MPa}^{-1}$ are obtained, respectively.

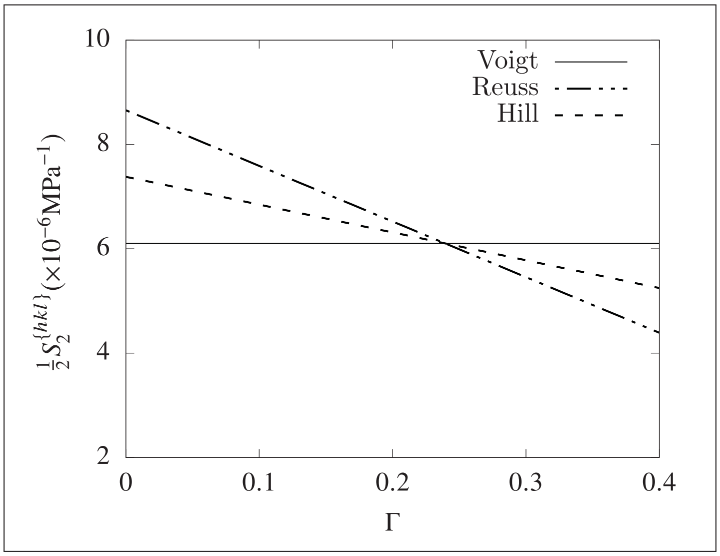

Figure 2.14 Theoretical determination of the $\frac{1}{2}S_2^{\{hkl\}}$ constant using Voigt, Reuss, and Hill models for IN718 and $C_{11}^{\mathrm{C}} = 251.0$ GPa, $C_{12}^{\mathrm{C}} = 135.5$ GPa, and $C_{44}^{\mathrm{C}} = 98$ GPa single crystal elastic constant. Examples of Γ values for different hkl values: $\Gamma(100) = 0$, $\Gamma(311) = 0.157$, $\Gamma(211) = 0.250$, and $\Gamma(111) = 0.333$

2.5.2.2 Experimental determination of the second XEC

The XEC $\frac{1}{2}S_2^{\{hkl\}}$ can also be experimentally determined via in-situ tests. A loading fixture is required to apply known loads while the specimen is being irradiated by X-ray apparatus (ASTM E1426-98, 2009). The use of a tensile machine has been preferred to a four-point bending fixture to obtain a constant applied stress through the entire specimen section. Thus, no variations in applied stresses were expected in the irradiated volume. The tested specimen should be as close as possible in chemical composition and microstructure to the material in which the residual stresses are to be evaluated.

In this method, described by Munsi *et al.* (2003), an initial XEC value, often computed from macroscopic elastic constant values, is chosen to allow a first assessment of the stress values. The correction factor of the XEC can be obtained from the slope of the linear regression when plotting the XRD-measured stresses versus the applied stresses. If the assumed initial XEC value is not the appropriate XEC value then the slope is not equal to 1 and corresponds to the correction factor to be applied. The correction factor may also be dependent on many factors related to the XRD measurement itself. With this experimental determination of the XEC, the obtained value should only be used for the same XRD conditions.

Further details are provided on the specimens geometries and micro-tensile machine used for the determination of the XEC in Section 2.6.

2.5.3 XRD equipment description and measurement conditions

Two XRD diffractometers were used in this study and are presented here, along with the XRD measurement conditions.

2.5.3.1 Proto iXRD apparatus description

A Proto iXRD apparatus was used for the measurements with two linear detectors and is presented in Figure 2.15. The detectors are position sensitive scintillation detectors (PSSD) and are positioned on both side of the X-ray source. The X-ray tube is interchangeable and is often operated at maximum 25 kV and 5 mA. The detectors positions are fixed relative to the X-ray source, but are both mounted on a 4-axis motorized head (three translations: X, Y, Z, and one rotation: β). This configuration is called Omega mode (ASTM E2860-12, 2012). Each detector captures a diffraction peak, therefore the entire head has to tilt several times to allow the linear regression to be described.

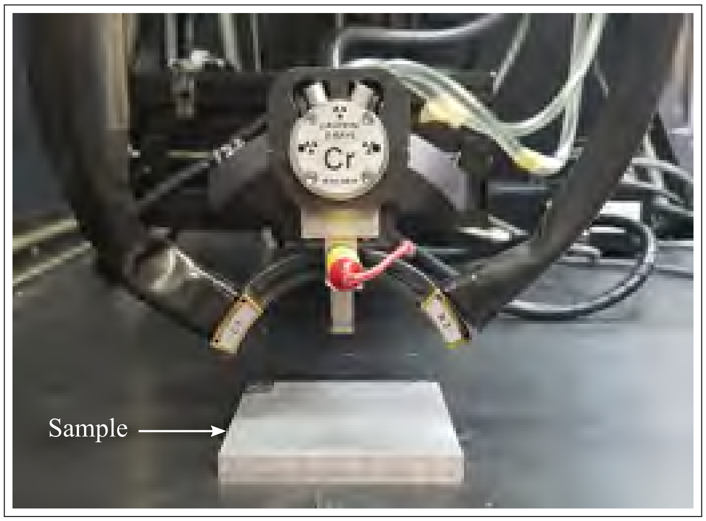

Figure 2.15 Proto iXRD apparatus equipped with an interchangeable Cr-tube and two linear detectors (L1 and R2)

In order to perform the measurements on Kα radiation only, a chromium (Cr) tube ($\lambda_{\mathrm{K}\alpha}$ = 2.291 Å (Cullity, 1956e)) and vanadium (V) filters placed in front of the detectors were used for the measurements on 300M and AA7050, whereas a manganese (Mn) tube ($\lambda_{\mathrm{K}\alpha}$ = 2.103 Å (Cullity, 1956e)) and Cr filters were used for measurements on IN718. The filters are often made of the tube's target previous element in the periodic table ($Z - 1$, with Z the atomic number of tube target) to filter the Kβ radiation as presented in Section 1.5.1. To acquire a diffraction peak at a given β position, a typical exposure time is between 30 s to 1 min. Seven to nine β positions are often used to measure the residual stresses, yielding a total exposure time of 5 min to 9 min.

2.5.3.2 Pulstec μ-X360n apparatus description

A Pulstec μ-X360n apparatus was used for the measurements with a 2D detector and is presented in Figure 2.16. The 2D detector allows measuring the residual stresses with a single exposure, i.e., single tilt angle (β). The apparatus tilt angle has to be manually adjusted in a range of 25° to 35° for most common metals. The Debye ring can be divided by up to 500 times, when a α-step size of 0.72° is used, providing up to 125 $\overline{\varepsilon}_{\alpha}^{\{hkl\}}$ points for the linear regression. This X-ray diffractometer is equipped with a non-interchangeable Cr-tube operated at 30 kV and 1 mA. The diffraction peaks obtained after typically 60 s to 90 s are not-filtered to allow measurements on the Kβ radiation ($\lambda_{\mathrm{K\beta}}$ = 2.085 Å (Cullity, 1956e)) for nickel-based superalloys for example.

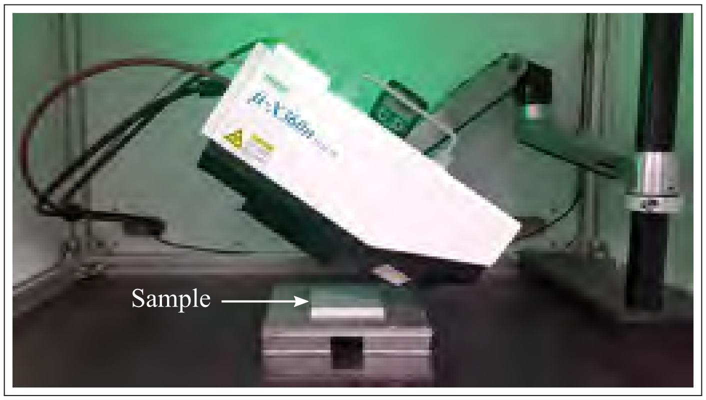

Figure 2.16 Pulstec μ-X360n apparatus equipped with a Cr-tube and a 2D detector

2.5.3.3 XRD measurement conditions

The XRD measurement conditions are listed in Table 2.6: $\{hkl\}$ planes, their d-spacing, and the corresponding Bragg angle (function of the radiation wavelength), for the Proto iXRD and Pulstec μ-X360n. The typical angular positions of the diffractometers' heads are listed in Table 2.7 based on the XRD measurement conditions listed in Table 2.6 and corresponding to the β positions in Figures 2.10 and 2.12. Residual stress measurements were realized using the apparatus dedicated software. The penetration depth of the X-rays varies from one diffractometer to the other, especially in the case of the IN718 where two different targets are used (i.e., two different wavelengths). The computation of the effective penetration depths for the IN718 is detailed in Section 3.2.2.2.

Table 2.6 XRD measurement conditions for measurements on 300M, IN718, and AA7050

			Proto iXRD		Pulstec μ-X360n	
Material	$\{hkl\}$	$d_0^{\{hkl\}}$	Tube - K line	$2\theta_0^{\{hkl\}}$	Tube - K line	$2\theta_0^{\{hkl\}}$
300M	{211}	1.17 Å	Cr - Kα	156.4°	Cr - Kα	156.4°
IN718	{311}	1.08 Å	Mn - Kα	151.8°	Cr - Kβ	148.2°
AA7050	{311}	1.22 Å	Cr - Kα	139.1°	Cr - Kα	139.1°

Table 2.7 Typical angular positions (β positions) used for the XRD measurement with the Proto iXRD and the Pulstec μ-X360n, for measurements on 300M, IN718, and AA7050

Material	Proto iXRD	Pulstec μ-X360n
300M	[±25° ±17.48° ±11.8° 0°]	35°
IN718	[±25° ±14.06° ±7.27° 0°]	30°
AA7050	[±20.5° ±15.12° ±3.82° 0°]	25°

2.5.4 Electropolishing for residual stress profile measurement

The electropolishing conditions for the layer removal process and the thickness of the removed layers are presented in this section.

2.5.4.1 Electropolishing conditions

A layer removal process has to be paired up with the XRD surface measurement to obtain a residual stress profile. The process of choice is the electropolishing, as it does not introduce further residual stresses. Using a Proto electropolisher, local surface electropolishing was performed under the form of a 7×7 mm pocket. Pocket geometry was controlled by the use of a silicone-rubber-mold made for this study. Masks, made of electrical tape and placed on the samples surface, were used to avoid the solution to spread at the sample-mold interface realizing clean pocket shapes. In the electropolishing process the sample is configured as an anode, and with suitable electrolytic solution, voltage and current the surface is dissolved. Two different perchloric-acid-based solutions, prepared in-house, were used. Their chemical compositions are listed in Table 2.8. A2 solution, containing distilled water, was used to electropolish AA7050 samples. This solution can be used for steel materials, nonetheless, as recommended by Struers (2019), A3 solution was preferred for 300M samples, which allows avoiding surface oxidation. The latter was also used for IN718 samples. Voltage and current were set to 60 V and auto ($\sim$ 1 A), respectively, for the three materials. Solution flux was set to $\sim$ 0.75-0.88 ml.min^{-1} (5-6 machine flux settings), which allows having enough solution renewal with low pressures at the different interfaces, avoiding leakages.

Table 2.8 Chemical composition of the electrolytic solutions used for electropolishing. Perchloric acid: $HClO_4$. Solution designation can be found on Struers (2019) website

Solution	Composition	Application
A2	8% Perchloric acid + 10% Butoxyethanol + 73% Ethanol + 9% Distilled water	AA7050
A3	6% Perchloric acid + 35% Butoxyethanol + 59% Methanol	300M & IN718

2.5.4.2 Electropolishing depth measurements

The depths obtained in function of the electropolishing time are presented for the three materials in Figure 2.17. The electropolishing has been performed following the conditions listed in the previous section. Figure 2.17 exhibits the data for the relaxation fatigue specimens, which have been fitted by a linear function of the type $y = ax$. The time corresponds to the cumulative time to reach a given depth (considering the previous steps). The slopes provide the electropolishing speeds. It can be observed that the layer removal process goes much faster for the combination AA7050 and A2 solution than for 300M or IN718 and A3 solution. The electropolishing speeds were roughly determined before the residual stress profile measurements to better target the needed depth as the shape and the approximate affected depths were known either from the literature, or from the in-house shot peening process simulations.

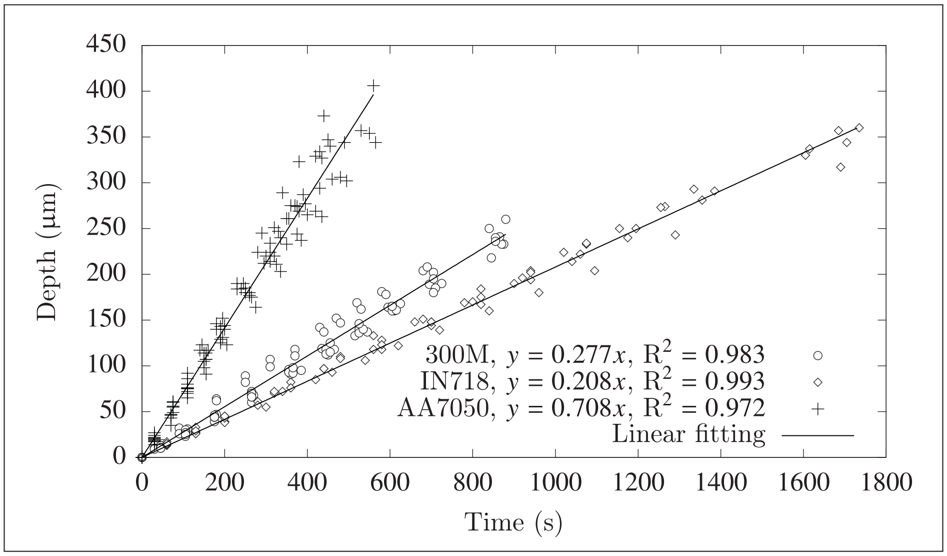

Figure 2.17 Electropolishing depth function of the time for the three materials

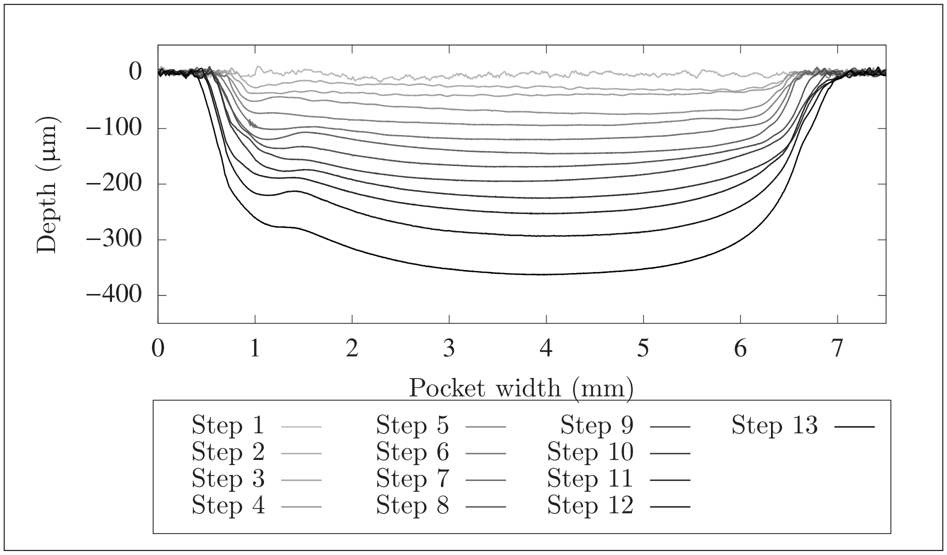

Figure 2.18 Example of the evolution of the depth profile, measured by the contact profilometer, for a shot peened IN718 specimen after several electropolishing steps

The depth of the removed layers were measured using a Mitutoyo SJ-400 profilometer, a contact profilometer using a stylus. Figure 2.18 presents the evolution of the pocket depth after several electropolishing steps. It can be observed that the depth is not constant through the entire pocket width, introducing some errors in the assessment of the depth at which the XRD measurement is done and in the associated values of residual stress. A confocal microscope Olympus LEXT OLS 4100 was used to perform some 3D mapping of the electropolished pocket to better capture the depth variations. A confocal microscope uses a laser beam to measure sample surface heights and can be considered as a non-contact profilometer. The entire pocket geometry acquisition is time consuming at such magnification (×20), but it provides a better signal-to-noise ratio than lower magnification (×5), resulting in a better contrast and resolution. Therefore, the rather technique has systematically been used for the pocket geometry effects on accuracy of residual stress measurements.

2.6 Micro-tensile tests for XEC measurement and cold work calibration

The micro-tensile specimen geometry and preparation for the XEC determination, and cold work calibration are presented in this section. The micro-tensile machine and the measurements conditions are also displayed.

2.6.1 Micro-tensile specimen geometry and preparation

Two types of micro-tensile specimen geometries were used for the XEC measurements and cold work calibration, one for 300M and IN718, and one for AA7050 as presented in Figure 2.19. The two geometries were extracted in the rolling direction (RD) of the bulk material. The design of specimens gage sections is a trade off between reachable thickness, micro-tensile machine loading capacity, and minimum gage section width required for XRD depending on the collimator size (A collimator is a device which narrows the X-ray beam. Changing the collimator size changes the size of the irradiated zone). The specimen contours were first machined from rolled block of material using CNC machine, providing thick specimens ($\sim$ 15 mm), which were then sliced to the thicknesses exhibited in Figure 2.19 using a precision cutting machine Struers Secotom-50.

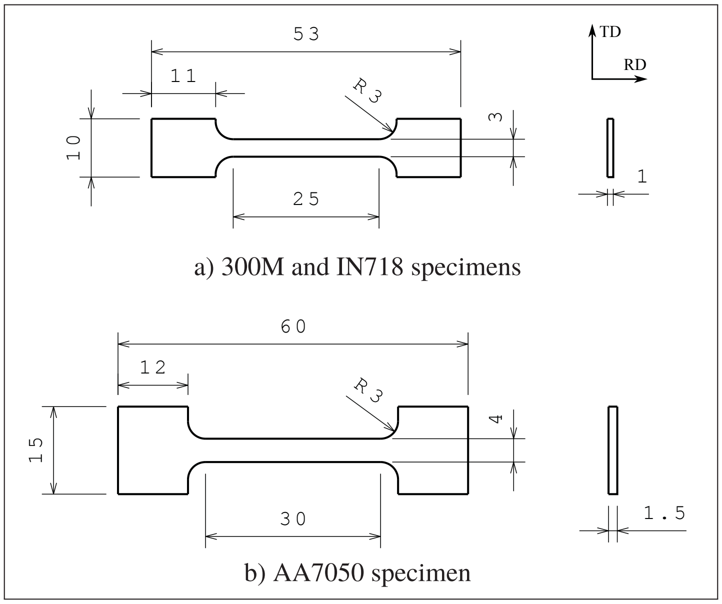

a) 300M and IN718 specimens

b) AA7050 specimen

Figure 2.19 Drawings of the machined micro-tensile specimens used for a) 300M and IN718, b) AA7050 (dimensions in mm)

Specimens were manually polished using SiC papers (up to grade 1200 CAMI grit designation). Care was taken to keep parallelism. Finally, to remove the layer affected by the polishing, the specimens were electropolished as suggested by the ASTM E1426-98 (2009) standard using the respective solutions listed in Table 2.8 and a Struers LectroPol-5 electrolytic polishing machine. The electropolishing was carried out for one side of the specimens, which was then used for the XRD measurements. It allowed removing the residual deformation that polishing may induce, which especially affect the cold work calibration as deformation increases the peak width.

2.6.2 Micro-tensile machine

The micro-tensile machine used for the tests is a 5 kN module manufactured by Kammrath & Weiss GmbH. The machine is equipped with a 5 kN loading cell measuring the applied force.

Displacement rate were set to 3 µm.s^{-1} and specimen elongation/contraction was continuously recorded by a Keyence LS-7030M optical extensometer during the whole experiment to assess the macroscopic strain. Figure 2.20 exhibits the micro-tensile and laser extensometer setup when paired up with the Proto iXRD and Pulstec μ-X360n apparatuses.

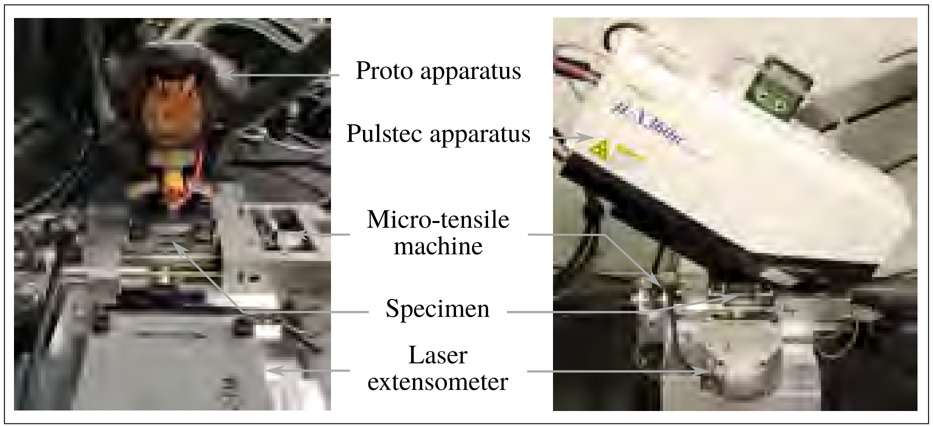

Figure 2.20 Experimental setups: micro-tensile machine and laser extensometer paired up with the Proto iXRD and Pulstec μ-X360n apparatuses

2.6.3 XEC measurements and cold work calibration tests conditions

The XEC measurements and the cold work calibration tests were realized using the micro-tensile machine for both types of experiments. The XRD measurements were performed as close to the middle of the specimens as possible depending on the XRD measurement conditions and the setup footprint.

The XEC $\frac{1}{2}S_2^{\{hkl\}}$ was measured on a single specimen for each material. The XRD measurements were performed for 0%, 5%, 10-70% of the yield strengths (Tables 1.2, 1.4, and 1.6), i.e., nine loads, and were repeated seven times for each loads in the loading and unloading conditions. Figure 2.21 presents the nominal stress-strain applied during the measurement of the IN718 XEC with the Pulstec μ-X360n. The plateaus correspond to the XRD measurement periods, i.e., the seven measurement repetitions. The nominal stress and strain were found to be constant during these measurement periods for all three materials. For the highest loading condition in the case of the 300M, some load decrease (4.3 MPa) was documented between the beginning and the end of the plateau, mostly due to a slightly sliding of the specimen in the grips at this specific loading condition. This is mainly caused by the high surface hardness of the specimen preventing the grips to properly penetrate the specimen and hold the load during the test.

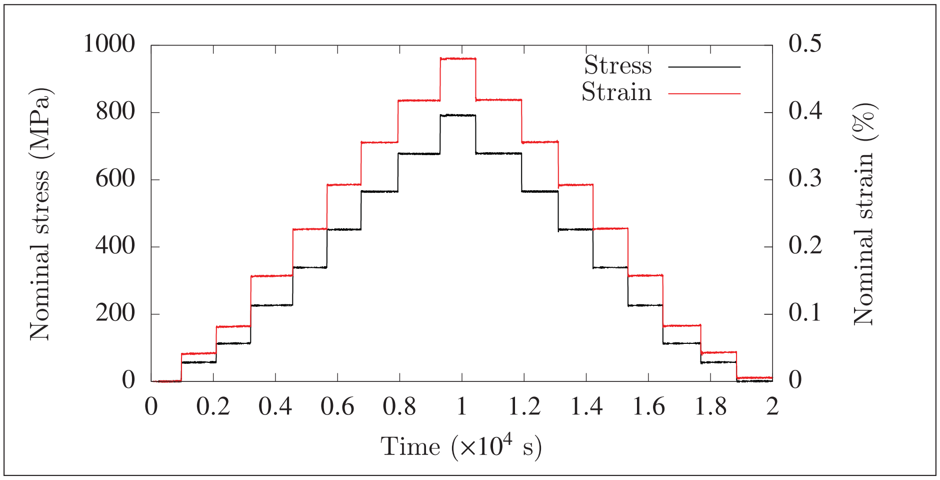

Figure 2.21 Nominal stress and strain evolution during the measurement of the IN718 XEC with the Pulstec μ-X360n

Cold work calibrations were performed on a single specimen for each material to allow the determination of cold work profiles from XRD measurements via the use of the FWHM values. The tests were true-strain-controlled with an increasing step of 0.5% for the 300M and 1% for the IN718 and AA7050. True strains were computed using the elongations measured by the optical extensometer, whereas true stresses were computed from the recorded force.

CHAPTER 3

COMPARISON OF THE SIN$^2\psi$ AND COS α METHODS

This chapter compares the $\sin^2\psi$ and $\cos\alpha$ methods in terms of diffracting-grains number, crystallographic texture, and X-ray elastic constant based on the identification of the diffracting grains from an EBSD map and on the specificities of computation methods, such as detector type. In 2014, after the commercialization worldwide of the first residual stress dedicated diffractometer equipped with a 2D detector, the two methods were quickly compared experimentally on various materials (Delbergue *et al.*, 2016; Kohri *et al.*, 2016; Ramirez-Rico *et al.*, 2016; Delbergue *et al.*, 2017; Lee *et al.*, 2017; Peterson *et al.*, 2017) and analytically (Miyazaki & Sasaki, 2016; Ramirez-Rico *et al.*, 2016).

The first section presents examples of the stress measurements performed with the $\sin^2\psi$ method (Proto iXRD) and the $\cos\alpha$ method (Pulstec μ-X360n) showing some differences in the determination of the $\frac{1}{2}S_2^{\{311\}}$ XEC. The second sections describes the microstructural characterization, the computation of the maximum penetration depth of X-rays, and the identification of the diffracting grains. The diffracting grains as identified from EBSD maps are presented in the third section and the effect of some angles on the number of diffracting grains is systematically documented. The fourth section discuses the “artificial” texture induced by the XRD measurements. Finally, the fifth and sixth sections compare the two residual stress calculation methods based on the computation of the XEC for the respective sets of diffracting grains. Part of the presented results have been published in Delbergue *et al.* (2019).

3.1 Examples of shot peening residual stress profile measurement and XEC measurements

Examples of measured residual stress profiles for a shot peened inhomogeneous IN718 sample are presented in this section to illustrate the differences between the two XRD computation methods and report the encountered difficulties. First, the residual stresses profiles were evaluated using the theoretical value of the XEC. Secondly, the XEC was experimentally determined for the two XRD computation methods. Thirdly, the residual stress profiles were computed using the experimental XEC values. Fourthly, as differences rose, the XEC were also experimentally determined for an homogeneous IN718 sample. Finally, the section is concluded by a discussion.

3.1.1 Estimation of the residual stress profile for a shot peened inhomogeneous microstructure IN718 sample

A flat 76.2 mm × 50.8 mm × 10.2 mm IN718 sample, extracted from the ∅89 mm bar (bimodal microstructure), shot peened with an intensity of 8 A at 100% coverage was used to measure the residual stresses using the two computation methods. Residual stresses were evaluated after XRD measurements of the deformation of the $\{311\}$ crystallographic planes and using the XEC computed via the Hill model $\left(\frac{1}{2}S_2^{\{311\}}\right)^{\text{Hill}} = 6.54 \times 10^{-6}\ \text{MPa}^{-1}$, as shown in Section 2.5.2.1. The Moore & Evans correction was applied to account for the residual stresses redistribution after each material removal by electropolishing as the geometries of the sample and the electropolished pocket were compatible with Moore & Evans assumptions.

The measured profiles are presented in Figure 3.1 for the two methods. The errorbars present the averages of the errors provided by the software and are mainly affected by the error in fitting of $\varepsilon_{\varphi\psi}^{\{hkl\}}$ vs. $\sin^2\psi$ and $\overline{\varepsilon}_{\alpha}^{\{hkl\}}$ vs. $\cos\alpha$ plots for the $\sin^2\psi$ and $\cos\alpha$ methods, respectively. The measured profiles have similar trends with similar plateaus of compressive residual stresses and tensile residual stress peaks of about 200 MPa. Residual stress differences of 5 MPa and 250 MPa are found at the surface and for the plateaus between the two XRD computation methods.

The errorbars for the $\cos\alpha$ method are larger than for the $\sin^2\psi$ method. This is mainly due to the fact that the $\overline{\varepsilon}_{\alpha}^{\{hkl\}}$ vs. $\cos\alpha$ plots exhibit a higher oscillation of the data, yielding an increase of the measurement errors that are computed from the linear regression accuracy. For both methods, it can be observed that the errors increase with the depth, due to the increase of the electropolished pocket's depth gradient (as shown in Figure 2.18, the electropolished pocket presents a gradient of depth which increases the deeper the material is removed).

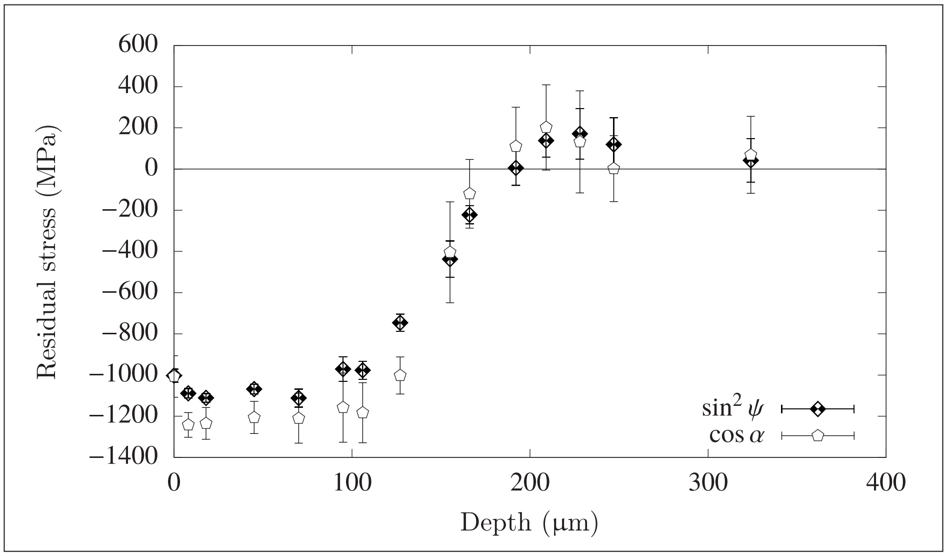

Figure 3.1 Residual stress profile assessement of a flat IN718 sample shot peened at 8 A by the $\sin^2\psi$ (Proto iXRD) and the $\cos\alpha$ (Pulstec μ-X360n) methods using Hill model to compute the XEC

3.1.2 Correction of the shot peening residual stress profiles using measured XECs for an inhomogeneous microstructure IN718 sample

The XEC $\frac{1}{2}S_2^{\{311\}}$ was also experimentally measured for both XRD computation methods using the micro-tensile machine presented in Section 2.6.2 and following the procedure described in Section 2.6.3. The XEC computed via the Hill model was taken as initial XEC value for the XRD measurements. The micro-tensile sample needed for the experiment was machined from a 76.2 mm × 50.8 mm × 10.2 mm block also extracted from the ∅89 mm bar.

The XRD measurement values plotted versus the applied stresses are presented in Figures 3.2a and 3.2b for the experiments using the $\sin^2\psi$ (Proto iXRD) and $\cos\alpha$ (Pulstec μ-X360n) methods, respectively. The seven measurements for the nine applied loads (see Section 2.6.3 for more details) are presented in black and red for the loading and unloading conditions, respectively. The linear fitting is presented as the straight line and the fitting coefficients are exhibited in the legend of the plots. The dashed line presents a reference line in the hypothetical case where the XEC $\frac{1}{2}S_2^{\{311\}}$ value can be estimated with the Hill model ($y = x$). The XRD measurements being more time consuming for the Proto iXRD than for the Pulstec μ-X360n,

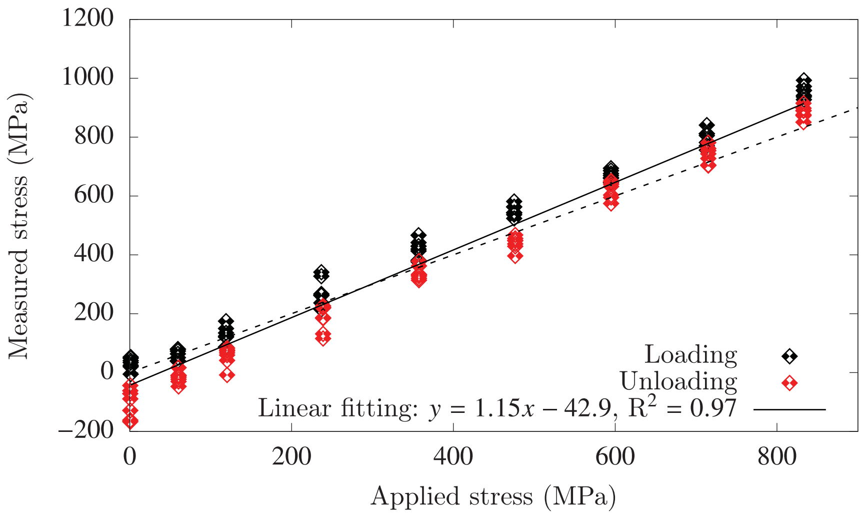

a) $\sin^2\psi$ method

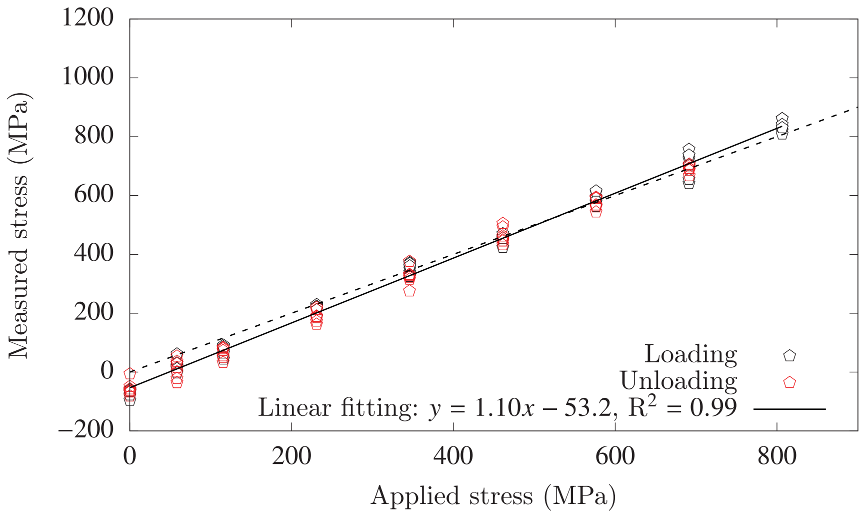

b) $\cos\alpha$ method

Figure 3.2 XRD measured stresses vs. applied stresses for determination of the XEC value using a) the $\sin^2\psi$ method (Proto iXRD apparatus) and b) the $\cos\alpha$ method (Pulstec μ-X360n), for an inhomogeneous microstructure IN718 sample

the measurements for the loading and unloading conditions were realized over two working days, consequently the measurements at 70% of the yield strength ($\sim$ 800 MPa) were repeated the second day as a starting point for the unloading condition. Therefore, at 70% of the yield strength, two sets of measurements are present in Figure 3.2a, whereas Figure 3.2b only presents one set of measurements.

For both measurements with the $\sin^2\psi$ and $\cos\alpha$ methods, the measurements for a given load are moderately scattered with an average standard deviation of 29 MPa and 22 MPa, respectively. Consequently, the linear regressions fit well the data with a coefficient of determination R^2 of 97% and 99%, respectively. A negative y-intercept is observed in both cases, which suggests the presence of compressive residual stresses at the surface despite the careful sample preparation. The two methods provide surface compressive residual stresses of the same order of magnitude. Furthermore, it can be observed in both cases that the slope is higher than 1, meaning that, using the XEC value computed from the Hill model, the measured stresses are over estimated by 15% and 10% for the $\sin^2\psi$ and $\cos\alpha$ methods, respectively (i.e., the XEC is underestimated when using the Hill model for computation). The slopes can be used as correction factors to assess $\frac{1}{2}S_2^{\{311\}}$, yielding two XEC values $\left(\frac{1}{2}S_2^{\{311\}}\right)^{\sin^2\psi} = 7.51 \pm 0.21 \times 10^{-6}$ MPa^{-1} and $\left(\frac{1}{2}S_2^{\{311\}}\right)^{\cos\alpha} = 7.20 \pm 0.11 \times 10^{-6}$ MPa^{-1}. The errors are computed using 95% confidence intervals for the slopes determined from the linear regressions. When computing independently the slopes for the loading and unloading conditions, a maximum difference between the two of 0.06 is found for the $\sin^2\psi$ method , or a 4% difference.

These results raise a problem as the XEC $\frac{1}{2}S_2^{\{311\}}$ for the $\{311\}$ planes is a material constant and should not differ when evaluated using two different XRD apparatuses and residual stress computation methods. Note that a prior XEC assessment with the $\sin^2\psi$ method was performed and is presented in Appendix IV, yielding a higher difference between the two methods. Such a difference between the two methods can be due to the material's inhomogeneous microstructure, the measurement methods, or a combination of both, and assuming that they are the major sources of differences between the two methods (i.e., by neglecting the other sources of errors like instrumental errors).

The computed stress being linearly dependent of the XEC, the already measured residual stress profiles can be corrected using the slope values as correction factors. Results would be identical as if the measurements were made with the experimentally determined XEC values: $\left(\frac{1}{2}S_2^{\{311\}}\right)^{\sin^2\psi}$ and $\left(\frac{1}{2}S_2^{\{311\}}\right)^{\cos\alpha}$. Figure 3.3 presents the corrected profiles of the shot peening residual stress profiles measured using the $\sin^2\psi$ and $\cos\alpha$ methods, presented in Figure 3.1. As expected, the residual stress values decrease, as the XEC calculated via the Hill model was an underestimated value. Differences between the two XRD methods measurements increase, especially at the plateau of compressive residual stresses.

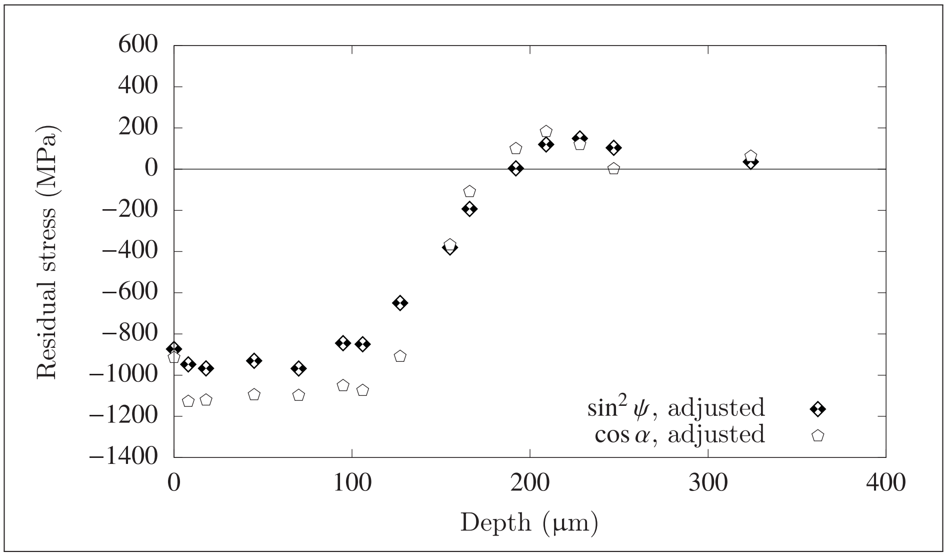

Figure 3.3 Corrected residual stress profiles, for a IN718 sample shot peened at 8 A, as if XRD measurements were performed using the XEC values measured via the $\sin^2\psi$ (Proto iXRD) and the $\cos\alpha$ (Pulstec μ-X360n) methods

3.1.3 XEC measurements via in-situ micro-tensile tests for an homogeneous microstructure IN718 sample

The XEC $\frac{1}{2}S_2^{\{311\}}$ was also experimentally measured for an homogeneous microstructure IN718 sample. The homogeneous and inhomogeneous samples have identical chemical compositions and without the presence of crystallographic texture the XEC $\frac{1}{2}S_2^{\{311\}}$ values should be similar. The micro-tensile sample was machined from the head of a fatigue sample, used in Klotz *et al.*

(2018a), extracted from the ∅25 mm bar. Identical experimental conditions, as presented in Section 3.1.2, were used to determine the XEC using the two XRD computation methods.

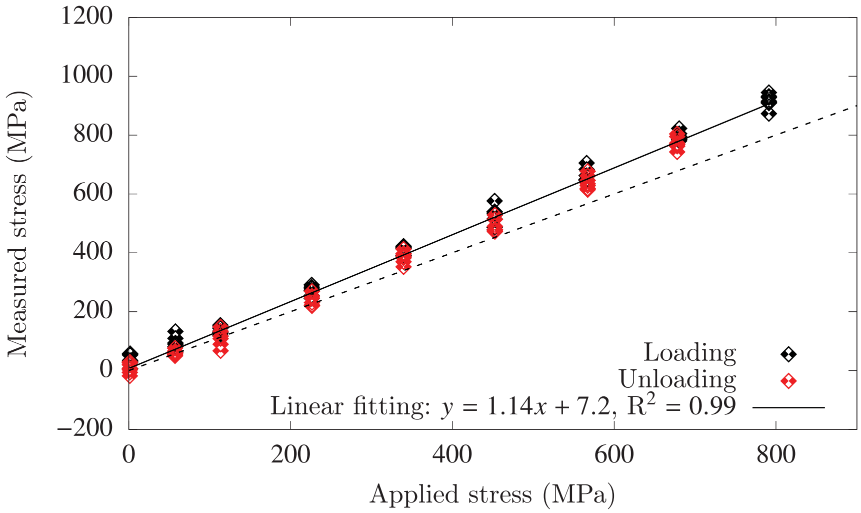

a) $\sin^2\psi$ method

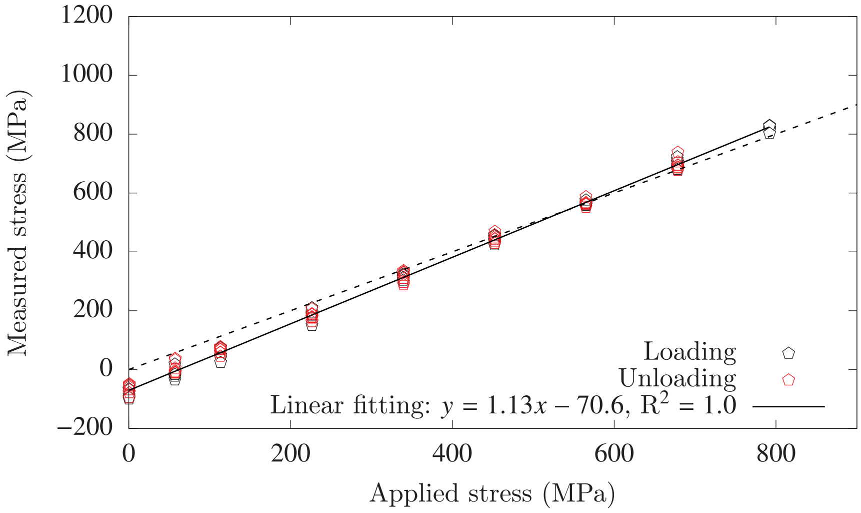

b) $\cos\alpha$ method

Figure 3.4 XRD measured stresses vs. applied stresses for determination of the XEC value using a) the $\sin^2\psi$ method (Proto iXRD apparatus) and b) the $\cos\alpha$ method (Pulstec μ-X360n), for an homogeneous microstructure IN718 sample

Figures 3.4a and 3.4b exhibit the XRD measurement values for the XEC assessment experiments using the $\sin^2\psi$ (Proto iXRD) and $\cos\alpha$ (Pulstec μ-X360n) methods, respectively. The measurement time for the Proto iXRD apparatus being faster for the homogeneous sample than for the inhomogeneous sample, the experiment was performed in one day, thus only seven measurements were realized at 70% of the yield strength, i.e., only seven loading measurements are exhibited at $\sim$ 800 MPa, as for the measurements with the $\cos\alpha$ method. The average of measurements' standard deviations are similar to those obtained for the inhomogeneous sample experiments, with an average standard deviation of 21 MPa and 15 MPa for the $\sin^2\psi$ and $\cos\alpha$ methods, respectively. The linear regressions fit well the data with R^2 values of 99% and 100%. The linear regressions provide different y-intercepts, but in the same order of magnitude than for the inhomogeneous sample. The difference between the slope values is lower with slopes of 1.14 and 1.13 for the $\sin^2\psi$ and $\cos\alpha$ methods, respectively. It results two close XEC values: $\left(\frac{1}{2}S_2^{\{311\}}\right)^{\sin^2\psi} = 7.43 \pm 0.12 \times 10^{-6}$ MPa^{-1} and $\left(\frac{1}{2}S_2^{\{311\}}\right)^{\cos\alpha} = 7.39 \pm 0.07 \times 10^{-6}$ MPa^{-1}.

3.1.4 Discussion on the shot peening residual stress profile measurement and XEC experimental determination

Large differences of the XEC values have been observed between the $\sin^2\psi$ and $\cos\alpha$ computation methods especially for the inhomogeneous microstructure, whereas the XEC is a material constant and should not vary. It is worth noting that the XEC values determined for the homogeneous microstructure sit between the two XEC values determined for the inhomogeneous microstructure. In the practical case of the shot peening residual stress profile, the differences between the two method can reach 16% of the measured value.

The inhomogeneous microstructure of the samples extracted from the ∅89 mm bar to provide the micro-tensile specimen and the shot peened sample could explain the large differences obtained between the $\sin^2\psi$ and $\cos\alpha$ computation methods. However, these differences could also be explained by the differences between the two computation methods, or by a combination of the microstructure and the computation methods, hence the need for a comparison of the two computation methods based on the microstructure of the irradiated samples.

The comparison of the $\sin^2\psi$ and $\cos\alpha$ methods that follows in the next sections is performed in terms of diffracting-grain number and X-ray elastic constant (XEC) of the diffracting-grain set, according to the detector specificities, which was made by identifying the diffracting grains from EBSD maps.

3.2 Implementation of the comparison based on EBSD mapping of IN718 samples

This section first provides further details on the EBSD maps (used for the comparison of the $\sin^2\psi$ and $\cos\alpha$ methods) and their analysis for the ∅25 mm (homogeneous microstructure) and the ∅89 mm (inhomogeneous microstructure) IN718 samples. Secondly, the effective depth of X-ray penetration is computed to establish that the use of 2D EBSD maps is sufficient for the comparison. Finally, the method for identification of the diffracting grains, based on the EBSD maps, is detailed.

3.2.1 Microstructural characterization and analysis of the homogeneous and inhomogeneous IN718 samples

This subsection provides some details on the acquisition and analysis of the EBSD maps. The two types of microstructure are then analyzed.

3.2.1.1 EBSD maps characterization details

Large EBSD scans were performed to characterize the grain size distribution, quantify the degree of crystallographic texture, and investigate the effect of the set of grains participating to the XRD measurements on the XEC values. The scans were carried out on areas having sizes similar to the irradiated areas during XRD measurements (≈ 2 mm^2). Table 3.1 summarizes the subset and total map areas measured with a step size of 0.5 µm for both the homogeneous and inhomogeneous samples.

Grain size distributions and crystallographic texture were determined by post-treatment using MATLAB and the MTEX open source package (Bachmann *et al.*, 2011). Grains were identified

Table 3.1 EBSD subset map size and total map area for the ∅25 mm (homogeneous) and ∅89 mm (inhomogeneous) samples

Sample	Subset map size (μm)	Total map area (mm^2)
∅25 mm	317 × 237.5	1.414
∅89 mm	635 × 476	1.154

using a grain detection angle of 10°. Twins were considered as unique grains to limit the artifacts arising from the determination of the grain's mean orientation, thus increasing the total number of indexed grains. The orientation distribution functions (ODF) were calculated using the de la Vallée Poussin kernel (Hielscher, 2013) and all measurement points to account for grain size effect from surface observation. Samples texture analyses are presented as inverse pole figure (IPF) plots with respect to the RD. Texture analyses associated to XRD measurements are also presented using pole figures.

3.2.1.2 Microstructure analyses

The grains microstructure was characterized by EBSD over regions representative of the X-ray irradiated zones. Large areas (for EBSD mapping, see Table 3.1) in the RD-TD plane were scanned for both ∅25 mm and ∅89 mm samples. The resulting maps were plotted for the RD using inverse pole figure (IPF) and are presented in Figure 3.5. Each color corresponds to a crystal orientation. The ∅25 mm sample presents a fine and homogeneous grain size distribution, while the ∅89 mm sample exhibits a bimodal microstructure composed of small grains and few large grains. The grains equivalent diameter distributions are presented as a function of the area they occupy in Figure 3.6. A 6 μm average grain size was calculated for the 35805 detected grains for the homogeneous sample, whereas the average grain size was 8 μm for the inhomogeneous sample and 10610 grains were detected (corresponding to an ASTM grain size number 12 and 11 (ASTM E112-13, 2013), respectively). Table 3.2 summarizes the grains distribution for the two specimens. The ∅89 mm sample's bimodal microstructure is documented in Figure 3.6b inset, where grains were divided into two families: the "large grains"

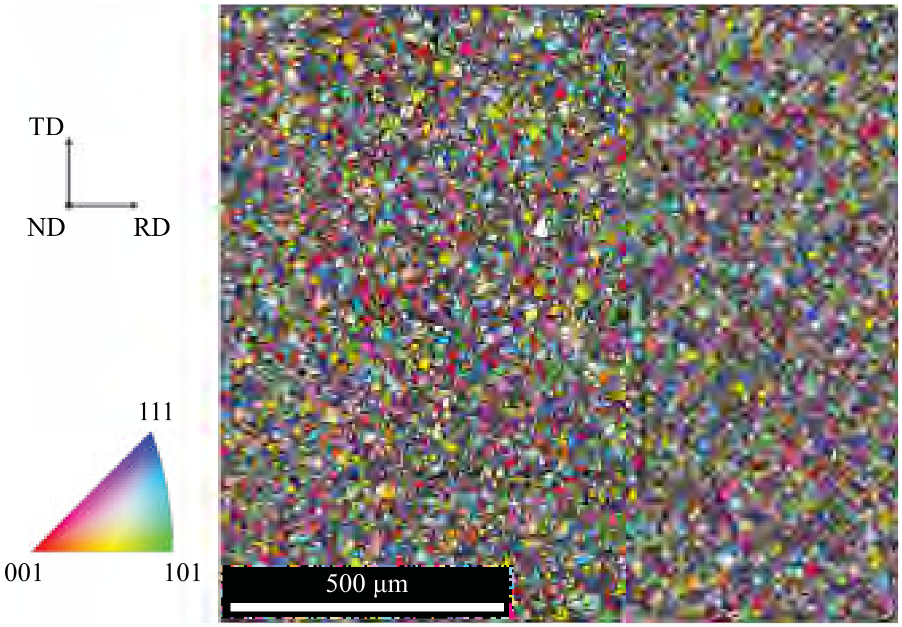
TD
ND
RD
111
001
101
500 µm

a) ∅25 mm sample

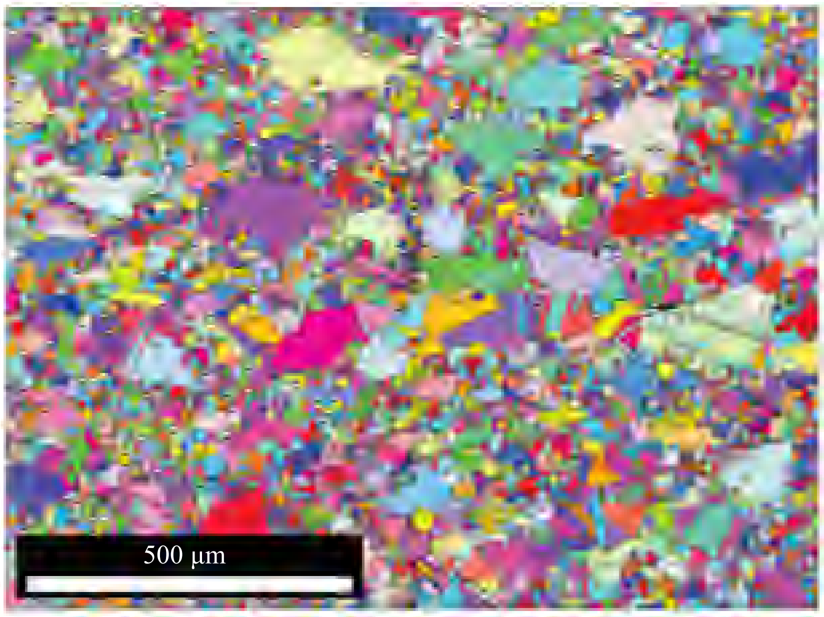

b) ∅89 mm sample

Figure 3.5 Orientation distribution maps for a) ∅25 mm (homogeneous microstructure) and b) ∅89 mm (inhomogeneous microstructure) samples represented as inverse pole figure (IPF) maps with respect to the rolling direction (RD)

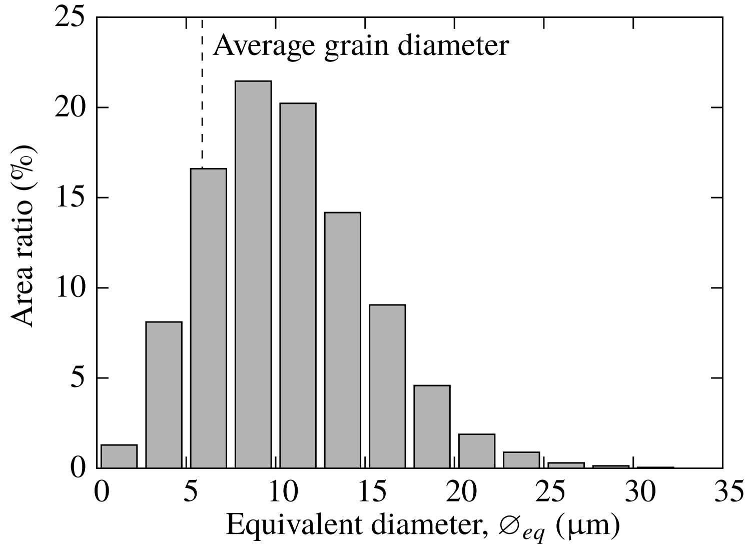

a) ∅25 mm sample

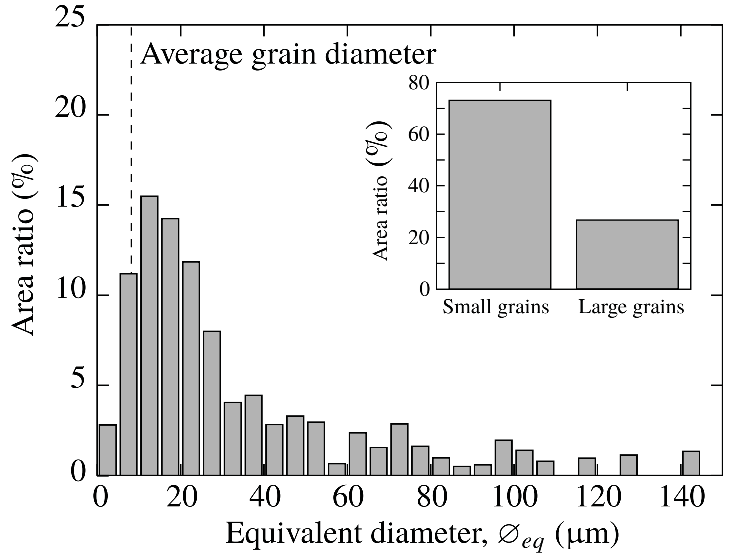

b) ∅89 mm sample

Figure 3.6 Grain size distribution in percent of area ratio for a) ∅25 mm and b) ∅89 mm samples. The equivalent diameter, $\varnothing_{eq}$, is calculated as $\varnothing_{eq} = 2\sqrt{A_g/\pi}$ where A_g is the grain area. In the inset, the large grains designate the grains having a diameter of at least the average diameter plus 4 times the diameter standard deviation ($\varnothing_{eq} > 42$ µm)

were defined as the grains larger than the average grains size plus four times the equivalent diameter standard deviation (SD), i.e., an equivalent diameter higher than 42 μm (the equivalent diameter, $\varnothing_{eq}$, is calculated as $\varnothing_{eq} = 2\sqrt{A_g/\pi}$ where A_g is the grain area). 93 grains (0.87% of the grains population) were found occupying 26% of the map area.

Table 3.2 Grain equivalent diameter $\varnothing_{eq}$ and grain density for the ∅25 mm (homogeneous) and ∅89 mm (inhomogeneous) samples

Sample	Grain equivalent diameter (μm)				Grain density (grains/mm^2)
	Mean	SD	Min.	Max.	
∅25 mm	6	4	1	31	25316
∅89 mm	8	8	1	140	9200

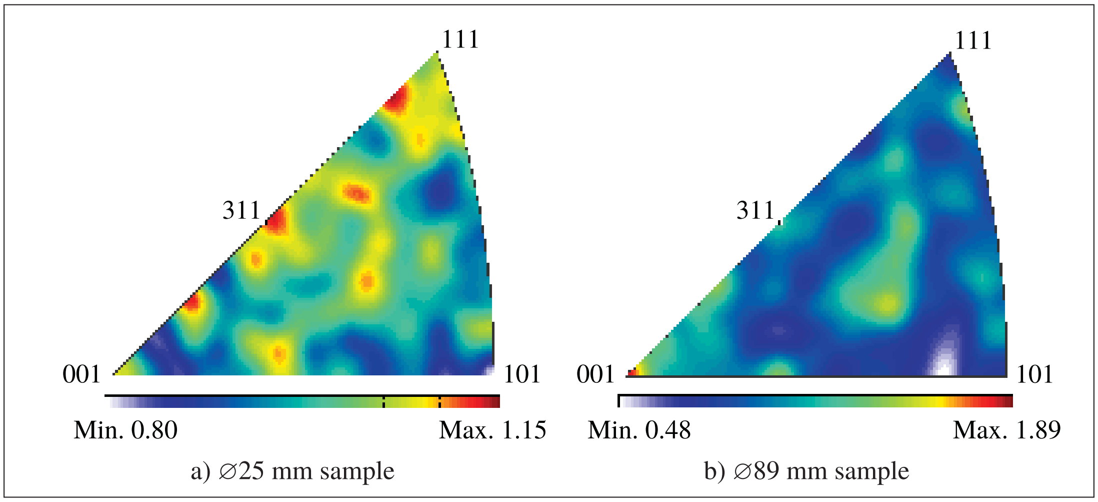

a) ∅25 mm sample

b) ∅89 mm sample

Figure 3.7 Inverse pole figures for a) ∅25 mm and b) ∅89 mm samples texture analysis with respect to the rolling direction. Note that the <311> directions are shown, as they represent the diffraction direction

The crystallographic textures of the ∅25 mm and ∅89 mm samples are presented as IPF plots with respect to the RD in Figures 3.7a and 3.7b, respectively. No preferable orientation is observed for the ∅25 mm sample with a texture index of 1.15, whereas for the ∅89 mm sample, a slightly higher occurrence of the <001> crystallographic orientations is found in the RD, but with a low intensity around 1.9. Such a texture is often observed after recrystallization of rolled

FCC material (Etter & Baudin, 2013). Nevertheless, both samples can not be considered as highly textured. The crystallographic directions of interest <311> are also shown in Figure 3.7.

The crystallographic texture of the ∅89 mm sample can be displayed individually for the two groups of grain size (small and large grains). Figures 3.8a and 3.8b present the texture analysis for the small ($\varnothing_{eq} < 42$ μm) and large ($\varnothing_{eq} > 42$ μm) grains, respectively. No preferable orientation is observed for the group of small grains, whereas the large grains exhibit a higher occurrence of the <001> crystallographic orientations in the RD. The pattern found in Figure 3.8b is very similar to that found in Figure 3.7b, meaning that the slight texture found for the ∅89 mm sample is mainly due to the large grains (unrecrystallized grains).

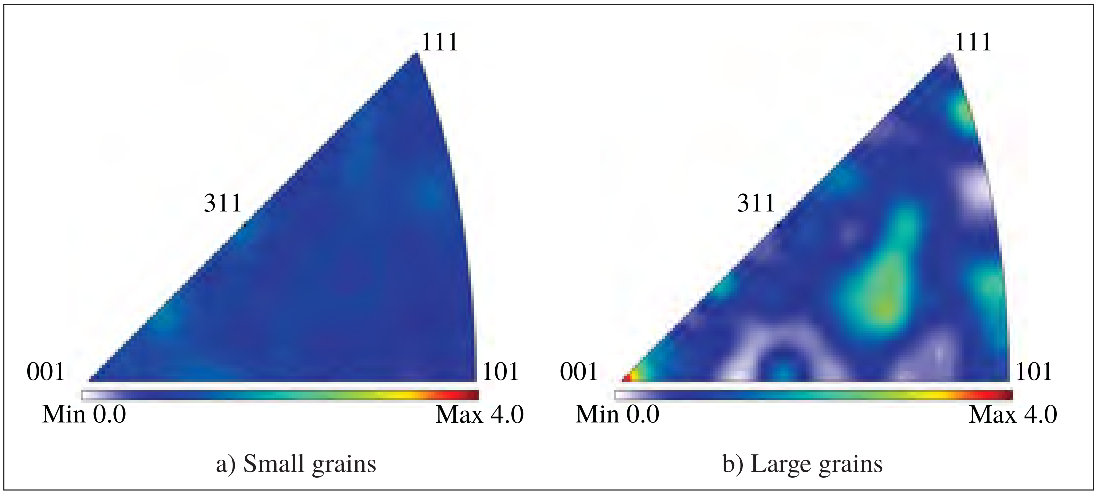

a) Small grains

b) Large grains

Figure 3.8 Inverse pole figures for the a) small and b) large ($\varnothing_{eq} > 42$ μm) grains of the ∅89 mm sample texture analysis with respect to the rolling direction. Note that the <311> directions are shown, as they represent the diffraction direction

Figure 3.9 presents the grain orientation spread (GOS) map for the ∅89 mm sample. The GOS associated to one grain is the mean value of the misorientations between all the pixels of the grain and the mean orientation of the grain (Ayad *et al.*, 2012). This value is sensitive to the state of the material (degree of plastic deformation or recrystallization). The large grains (unrecrystallized grains) of the bimodal sample (∅89 mm sample) exhibit higher GOS values.

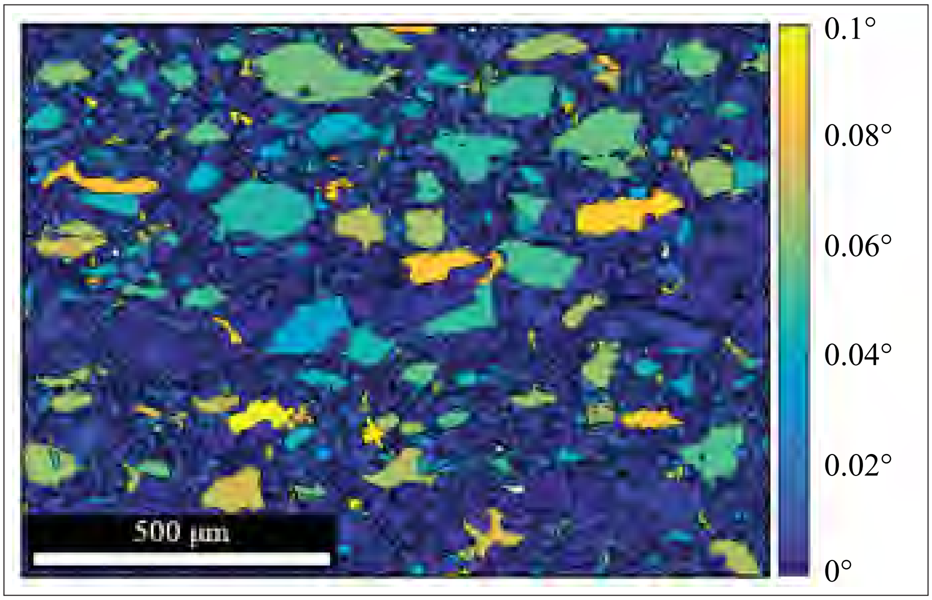

Figure 3.9 Grain orientation spread (GOS) map for the ∅89 mm sample

3.2.2 Validation of the 2D EBSD maps use for the identification of the diffracting grains

This subsection compares the average grain size previously determined from the EBSD maps to the effective depth of X-ray penetration computed for both XRD methods. Showing that the effective depth of X-ray penetration is smaller than the average grain size justifies the use of 2D EBSD maps to identify the diffracting grains for the comparison of the $\sin^2\psi$ and $\cos\alpha$ methods. But first, the determination of the linear absorption coefficient μ_{IN718} for the IN718, needed to compute the effective penetration, is realized.

3.2.2.1 Determination of the linear absorption coefficient

Material's linear absorption coefficient μ depends on the chemical composition and the X-ray energy (i.e., the X-ray wavelength). The variations of linear absorption coefficient for nickel (Ni), μ_{Ni}, with the X-ray energy, $E_{photons}$, is presented as example in Figure 3.10. Two distinct K absorption edges are visible for $\sim$ 0.9 keV and $\sim$ 8 keV. The K absorption edges have a mirror shape when compared to that illustrated in Figure 1.7 because the X-ray energy is inversely related to the wavelength (Equation (1.2)).

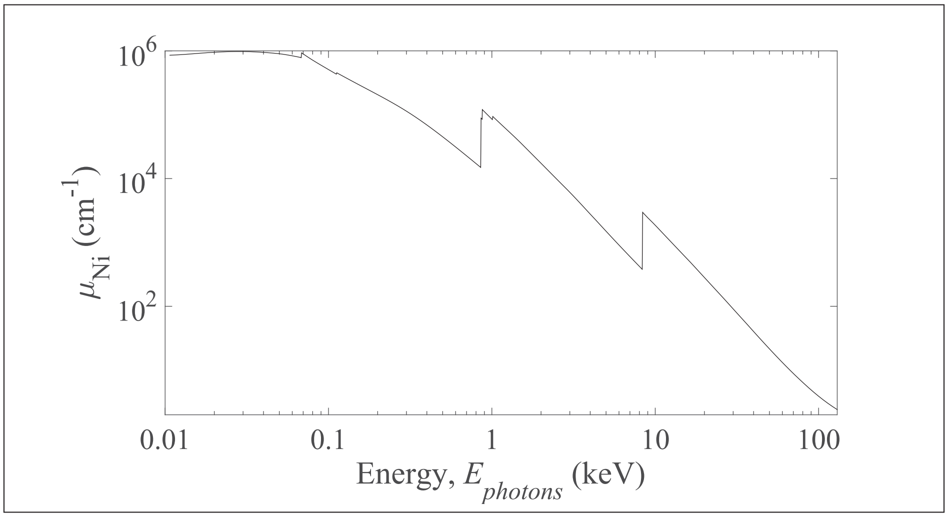

Figure 3.10 Variations of the linear absorption coefficient for nickel (Ni, Z=28), μ_{Ni}, wih the X-ray energy, $E_{photons}$. Note that both axes have a logarithmic scale. Data from Chantler *et al.* (2005)

The total linear absorption coefficient for the IN718, μ_{IN718}, is computed as

$$\mu_{\mathrm{IN718}} = \sum_{i=1}^{n} \mu_i w_i \tag{3.1}$$

where μ_i is the linear absorption coefficient of the i element composing the IN718 and w_i is its weight percent. A measured chemical composition was preferred to the average of the compositions required by the AMS 5663M (2009) standard listed in Table 1.3 to determine μ_{IN718} and is listed in Table 3.3. In the present case, the Kα line of the Mn-spectra and the Kβ line of the Cr-spectra are used for the $\sin^2\psi$ and $\cos\alpha$ methods resulting in two different X-ray energies $E_{photons}(\lambda_{\mathrm{Mn-K\alpha}})$ = 5.895 keV and $E_{photons}(\lambda_{\mathrm{Cr-K\beta}})$ = 5.950 keV, respectively. Consequently, the μ_i values have to be determined for the two levels of energy. For instance, μ_{Ni} can be determined for $E_{photons}(\lambda_{\mathrm{Mn-K\alpha}})$ = 5.895 keV and $E_{photons}(\lambda_{\mathrm{Cr-K\beta}})$ = 5.950 keV, using Figure 3.10, and is equal to 959 cm^{-1} and 934 cm^{-1}, respectively. Finally, μ_{IN718} is found to be equal to 986 cm^{-1} and 961 cm^{-1} for measurements of the IN718 with the Mn-tube using the Kα line ($\sin^2\psi$ method) and the Cr-tube using the Kβ line ($\cos\alpha$ method), respectively.

Table 3.3 IN718 chemical composition obtained by optical spectrometry (weight %). Bal.: balance. Reproduced from Klotz *et al.* (2018a)

Elements	Ni	Fe	Cr	Nb	Mo	Ti	Al	Co	Mn	Si
Composition	Bal.	19.53	17.84	5.02	3.07	1.16	0.64	0.35	0.16	0.06

3.2.2.2 Computation of the maximum effective depth of X-ray penetration

The depth of X-ray penetration is evaluated for different incident X-ray beam angles (i.e., β angles) via the use of the fraction of the total diffracted intensity G_x (Equation (1.13)) computed using the linear absorption coefficients ($\mu_{\text{IN718}}(\lambda_{\text{Mn-K}\alpha})$ and $\mu_{\text{IN718}}(\lambda_{\text{Cr-K}\beta})$) previously determined. It is worth noting that the maximum depth of X-ray penetration is always found for $\psi = 0°$, when the diffracting planes are parallel to the surface, which minimizes the traveled distance of the incident and diffracted X-rays and consequently their absorption, resulting in diffraction information coming from deeper layers below the irradiated surface.

To only study the difference in penetration depth between the Mn and Cr radiations used by the $\sin^2\psi$ and $\cos\alpha$ methods for measurements of IN718 samples, respectively, a fictitious configuration with only one linear detector placed at the right side of an X-ray source is considered. In this configuration, ψ is computed as $\psi = \beta + \pi - 2\theta_0^{\{311\}}$, which allows determining β when $\psi = 0°$ ($\beta = -14.1°$ and $\beta = -15.9°$ for the Mn and Cr radiations, respectively). The {311} planes are considered and the associated $2\theta_0^{\{311\}}$ value for each radiation is listed in Table 2.6. The evolution of G_x with the depth of penetration is presented in Figures 3.11a and 3.11b for β values ranging from $-20°$ to $40°$ for the Mn and Cr radiations, respectively. For the two types of radiations, it can be observed that G_x values increase with the depth and that, for a given G_x value, the affected depth decreases with the incident beam inclination. As expected, the curves $\beta = -14.1°$ and $\beta = -15.9°$, corresponding to $\psi = 0°$, represent the case of the highest penetration depth for the Mn and Cr radiations, respectively, i.e., lowest

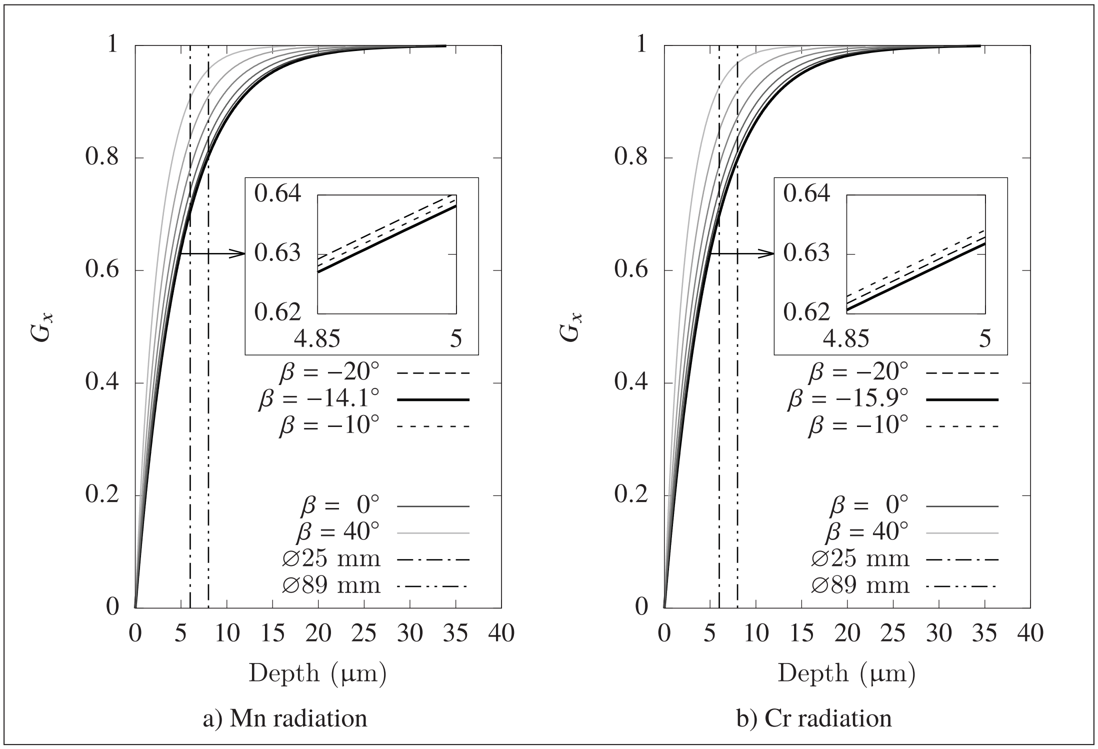

a) Mn radiation

b) Cr radiation

Figure 3.11 Fraction of the total diffracted intensity G_x function of the depth of penetration below the sample surface for different β incident angle and for a) the Mn-Kα radiation and b) the Cr-Kβ radiation. Curves for 0° to 40° β inclinations, with a 10° step size, are represented in grayscale. The average grain sizes of the ∅25 mm and ∅89 mm samples are plotted for comparison

curves represented by thick black lines and visible in Figures 3.11a and 3.11b insets. G_x is often taken equal to 63% to determine the effective penetration depth τ, which corresponds to the center of gravity of the distribution of measured diffracted intensity versus depth (Welzel *et al.*, 2005). For $G_x = 63\%$, the maximum penetration depths are 4.89 µm and 4.98 µm for the Mn ($\beta = -14.1°$ curve) and Cr ($\beta = -15.9°$ curve) radiations, respectively. Thus, when measuring diffraction from the {311} planes, the Cr-Kβ line provides information from a slightly deeper layer (1.6% more) than the Mn-Kα line. However, both values of penetration depth are smaller than the average grain sizes of the ∅25 mm and ∅89 mm samples, which are presented by the dashdotted lines in Figures 3.11a and 3.11b. If a left linear detector was chosen for the study instead of a right one, the curves would be the same for opposite values of β, i.e., for instance for the Mn radiation the maximum penetration depth would be found for $\beta = 14.1°$.

The effective penetration depth can be computed taking into consideration the detector configuration. For the $\sin^2\psi$ method, two linear detectors are used in an Ω goniometer configuration, hence the effective penetration depth τ can be computed as (Noyan & Cohen, 1987)

$$\tau = \frac{\sin^2\theta_0^{\{311\}} - \sin^2\psi}{2\mu_{\mathrm{IN718}}\sin\theta_0^{\{311\}}\cos\psi}, \tag{3.2}$$

with $\psi = \beta-\pi+2\theta_0^{\{311\}}$ and $\psi = \beta+\pi-2\theta_0^{\{311\}}$ for the left and right detectors of the Proto iXRD, respectively, and using $\mu_{\mathrm{IN718}}(\lambda_{\mathrm{Mn-K\alpha}})$ and $2\theta_0^{\{311\}}$ listed in Table 2.6. The effective penetration depth of the diffraction information captured by the two linear detectors is plotted versus the incident X-ray beam angle β in Figure 3.12. β values vary from $-40°$ to $40°$, which includes the experimentally used range of values. The two curves are symmetric with respect to the y-axis at $\beta = 0°$, which represents the position where the incident X-ray beam is perpendicular to the specimen surface. Hence, for a given inclination (except $\beta = 0°$), the two linear detectors capture diffraction data from different depths. For each detector, the maximum effective penetration depth of 4.92 µm is found for $\beta = \pm 14.1°$ (i.e., when $\psi = 0°$ which corresponds to the case where the $\{311\}$ planes are parallel to the specimen surface). The maximum effective penetration depth is slightly higher than the penetration depth previously computed for $G_x = 63\%$ (4.89 µm).

For the $\cos\alpha$ method, which uses a 2D detector, the effective penetration depth τ can be computed by taking into account the α angle as (Tanaka, 2018)

$$\tau = \frac{1}{\mu_{\mathrm{IN718}}}\left(\frac{1}{\cos\beta} + \frac{1}{-\cos 2\theta_0^{\{311\}}\cos\beta + \sin 2\theta_0^{\{311\}}\sin\beta\cos\alpha}\right)^{-1}, \tag{3.3}$$

where α is the localization angle on the 2D detector, as shown in Figure 2.12, and using $\mu_{\mathrm{IN718}}(\lambda_{\mathrm{Cr-K\beta}})$ and $2\theta_0^{\{311\}}$ listed in Table 2.6. Figure 3.13 presents the variations of the effective penetration depth plotted versus the α angle for several β angles using Equation (3.3). β values only range from 0° to 40° with a 5° step size, as the inclination of the Pulstec μ-X360n apparatus is kept in this smaller range during experiments. The $\beta = 15.9°$ curve has been plotted instead of the $\beta = 15°$ curve as it produces the highest penetration depth. Observed at $\alpha = 180°$, the

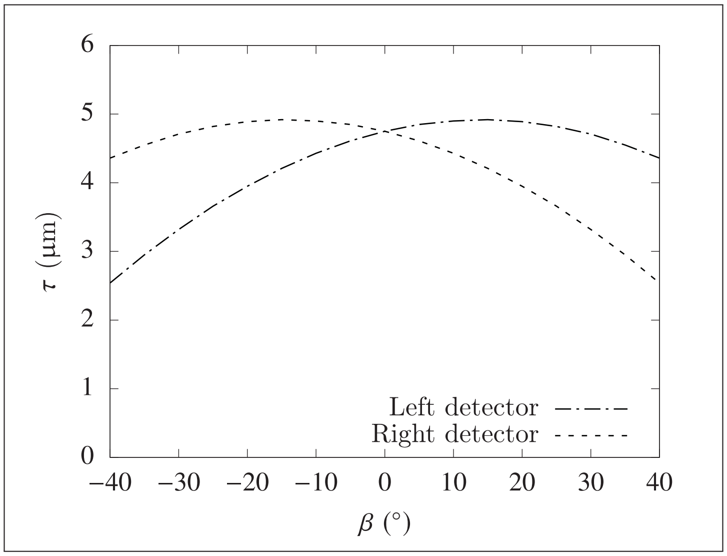

Figure 3.12 Variations of the effective penetration depth for different incident beam angles β and for the left and right detectors used in the $\sin^2\psi$ method

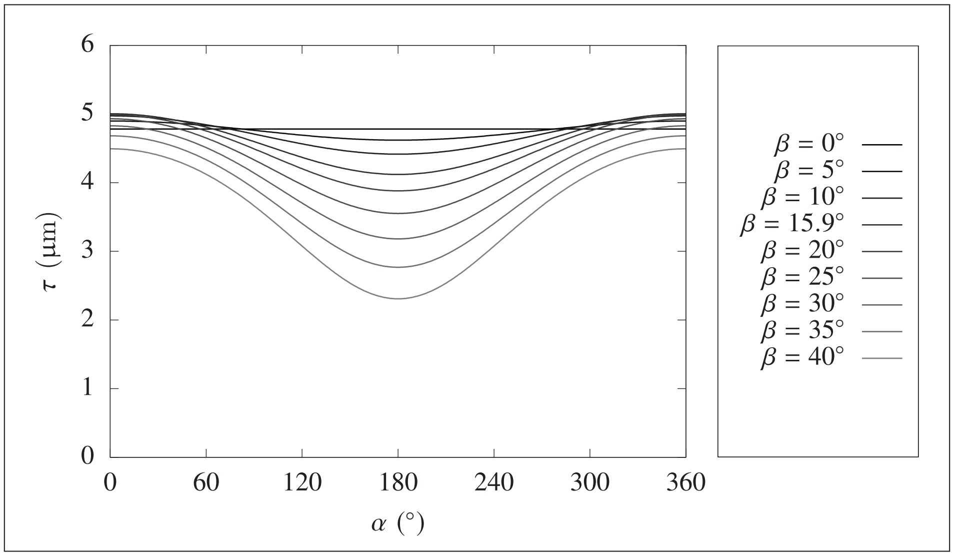

Figure 3.13 Effect of α angle on the effective penetration depth computed for the Cr radiation in the case of the 2D detector used in the $\cos\alpha$ method and for different incident beam angles β

curves are ranged in the same order as in the legend. The effective penetration depth varies with α, i.e., the effective penetration depth of the diffraction data varies along the Debye ring, except for $\beta = 0°$ where it is constant (horizontal line in Figure 3.13) as in this case the 2D detector is parallel to the specimen surface and therefore the diffracted X-rays have an identical inclination for all α angles. For all the curves (except for the $\beta = 0°$ curve), the effective penetration depth is the lowest for $\alpha = 180°$ as it corresponds to the most inclined diffracted X-rays (i.e., the highest ψ values or the $\{311\}$ planes which are the less parallel to the specimen surface). The maximum effective penetration depth of 5.00 μm is found for $\alpha = 0°$ and 360° of $\beta = 15.9°$ curve, which is slightly higher than the penetration depth previously computed for $G_x = 63\%$ (4.98 μm).

For both XRD computation methods, the maximum effective penetration depth of 5 μm is lower than the average grain sizes of the ∅25 mm and ∅89 mm samples (6 μm and 8 μm, respectively). Consequently, the 2D EBSD maps obtained for the ∅25 mm and ∅89 mm samples can be used for the comparison of the $\sin^2\psi$ and $\cos\alpha$ methods, as it is assumed that only the layer of grains obtained by EBSD could diffract.

3.2.3 Method for identification of the diffracting grains

The comparison of the $\sin^2\psi$ and $\cos\alpha$ methods is based on the identification of the diffracting grains. A MATLAB script using MTEX package has then been developed to identify the grains meeting the Bragg's condition for the two types of detectors (linear and 2D detectors). Under this condition and for an unstressed sample, the diffracting planes have to make a $\theta_0^{\{hkl\}}$ angle with the incoming X-rays to scatter the incoming X-ray beam for the particular planes under consideration, as shown in Figure 3.14. In this figure, $\mathbf{V_{IXR}}$, $\mathbf{V_{DXR}}$, and $\mathbf{V}^{\{hkl\}}$ are unit vectors representing the incident X-rays, the diffracted X-rays, and the vector normal to the $\{hkl\}$ planes, respectively. To verify the Bragg's law conditions (Equation (1.5)), $\mathbf{V}^{\{hkl\}}$ has to be the bisector vector of $\mathbf{V_{IXR}}$ and $\mathbf{V_{DXR}}$, providing a geometrical condition for selecting the diffracting grains. The MTEX package was used for calculating each grain's mean orientation. The $\mathbf{V}^{\{hkl\}}$ vector can thus be determined for any (h, k, l) Miller indices and the condition for diffraction can be expressed by the dot product of $\mathbf{V_{IXR}}$ and $\mathbf{V}^{\{hkl\}}$. Diffraction in Bragg's

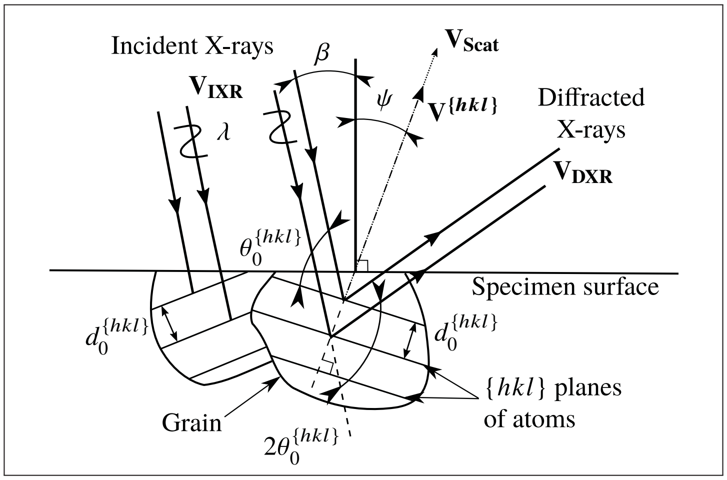
Incident X-rays
β
$\mathbf{V_{Scat}}$
$\mathbf{V_{IXR}}$
ψ
$\mathbf{V^{\{hkl\}}}$
Diffracted X-rays
λ
$\mathbf{V_{DXR}}$
$\theta_0^{\{hkl\}}$
Specimen surface
$d_0^{\{hkl\}}$
$d_0^{\{hkl\}}$
$\{hkl\}$ planes of atoms
Grain
$2\theta_0^{\{hkl\}}$

Figure 3.14 Illustration of X-rays diffracted by $\{hkl\}$ planes of an unstressed grain in the Bragg's condition. In this condition, the normal vector of the $\{hkl\}$ planes $\mathbf{V^{\{hkl\}}}$ is coincident with the scattering vector $\mathbf{V_{Scat}}$ and bisects the incident X-rays $\mathbf{V_{IXR}}$ and the diffracted X-rays $\mathbf{V_{DXR}}$, such as they make a $\theta_0^{\{hkl\}}$ angle with the $\{hkl\}$ planes having a lattice spacing $d_0^{\{hkl\}}$

condition can take place when

$$(90 - \theta_0^{\{hkl\}}) = \cos^{-1}\left(\frac{\mathbf{V_{IXR}} \cdot \mathbf{V^{\{hkl\}}}}{\|\mathbf{V_{IXR}}\|\|\mathbf{V^{\{hkl\}}}\|}\right). \tag{3.4}$$

A tolerance of ±2° was used to replicate the XRD line-broadening effect, allowing some deviation from the exact Bragg condition. The 4° tolerance is close to the diffraction peaks widths experimentally obtained for both techniques in the experiments presented in Section 3.1, or in some published work (Delbergue *et al.*, 2017; Klotz *et al.*, 2018a). It allows focusing the investigation on the diffraction information coming from the highest intensities of potential diffraction peaks. In the present case, the $\{hkl\}$ planes under consideration are the $\{311\}$ planes.

The validation of the identification diffracting grains script is presented in Appendix V.

3.3 Identification of the diffracting grains and effect of the angle variations on their number

Based on the EBSD map of the homogeneous sample (∅25 mm sample), the diffracting grains are identified for the two types of detectors and their respective specificities to reveal the difference in number of unique diffracting grains. The effect of the number of tilt angles on the diffracting grains number is studied for the case of the two linear detector, whereas the effect of the tilt angle value is studied for the 2D detector.

3.3.1 Identification of the diffracting grains

The grains in diffraction condition were first identified using the developed MATLAB script on the ∅25 mm sample as it represents the ideal case of an homogeneous microstructure. The XRD conditions and diffractometers parameters ({311} planes and their corresponding $d_0^{\{311\}}$ and $2\theta_0^{\{311\}}$, tube, K lines, and diffractometer angular position) used in the script are listed in Tables 2.6 and 2.7. Nine β angles ([±25° ±19.01° ±14.06° ±7.27° 0°]) were preferred to the seven β angles listed in Table 2.7 to increase the number of diffracting grains for the $\sin^2\psi$ method in the comparison of the two stress computation methods. Section 3.3.3 details the effects of the number of β angles on the diffracting grains number.

Table 3.4 Number of grains participating to the XRD when data is captured by two linear detectors (for the nine inclinations) or a 2D detector (for one inclination) for the ∅25 mm sample, as depicted in Figure 3.15

Detectors type	Proto iXRD Linear detectors	Pulstec μ-X360n 2D detector
Nb. of diffracting grains	5540	8183
Grains percentage	15.5%	22.9%
Area percentage	15.0%	22.4%

Figures 3.15a and 3.15b present in IPF-coloring the diffracting grains if X-ray diffraction was captured by the two linear detectors of the Proto iXRD and the 2D detector of the Pulstec

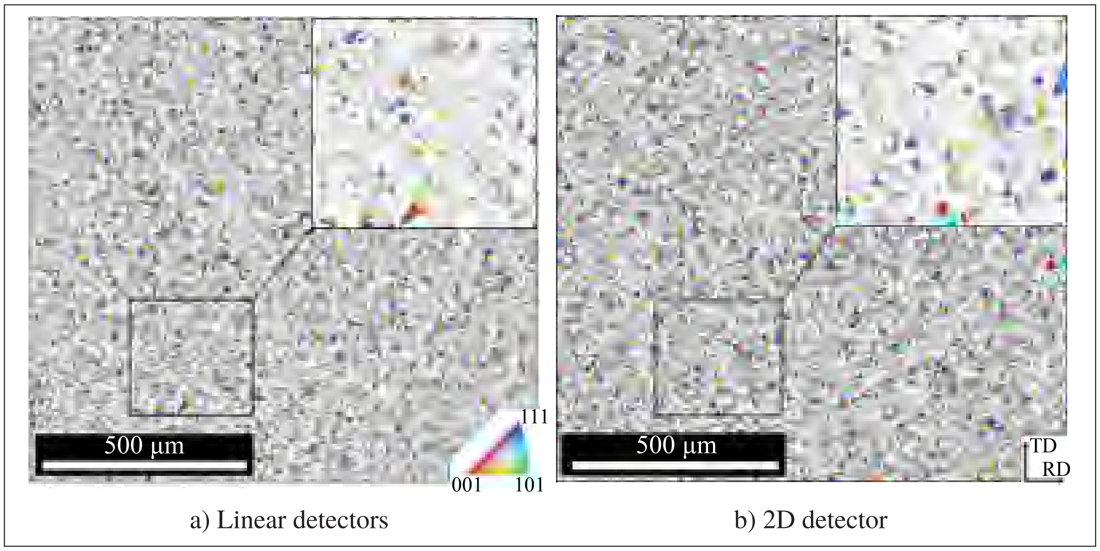

a) Linear detectors

b) 2D detector

Figure 3.15 Orientation distribution maps of the ∅25 mm sample presenting the diffracting grains identified by a) the two linear detectors for nine inclinations (Proto iXRD) and b) the 2D detector for a single exposure (Pulstec μ-X360n). The IPF representation with respect to the RD has been kept

μ-X360n, respectively. Figure 3.15a is the superimposition of the diffracting grains captured by the two linear detectors for nine acquisition positions. Figure 3.15b exhibits the diffracting grains seen by the 2D detector for a single exposure at $\beta = 30°$. The number of diffracting grains was calculated in the two situations and is reported in Table 3.4. The grains participating to the diffraction data represent 15.0% and 22.4% of the EBSD map area for the $\sin^2\psi$ and $\cos\alpha$ methods, respectively. The 2D detector thus samples 32% more unique diffracting grains than the linear detectors swept along 9 β angles. Only 1129 unique grains are shared between the diffracting grains identified by the two linear detectors (5540 identified diffracting grains) and the 2D detector (8183 identified diffracting grains), corresponding to 20% and 14% of them, respectively. Some of these shared diffracting grains can be observed in Figure 3.15.

3.3.2 Simulation of the diffracting grains from detectors windows

The intersections of the diffraction cone with the two linear and 2D detectors were simulated, to better understand how the 2D detector can see 32% more diffracting grains in a single exposure than the two linear detectors in nine exposures. Figures 3.16a and 3.16b present the simulated images seen by the two linear detectors at $\beta = 25°$ and by the 2D detector at $\beta = 30°$, respectively, for a single exposure. The images are formed by simulating the intersection of a plane with a diffraction cone for each type of detectors and considering their physical geometries. Each circular symbol represents the localization of X-rays scattered by a diffracting grain intersecting the detector plane (as illustrated in Figure 2.12). The diffracting grains' mean orientations are presented using IPF-coloring with respect to the RD. The X axis is parallel to the RD while the Y axis is parallel to the TD, and that the incoming X-rays (not represented here) would be at the coordinates (0,0). The two linear detectors can be observed in Figure 3.16a with the presence of two distinct regions. The full Debye ring was captured by the 2D detector as shown in Figure 3.16b. Note that the Y-width of the regions, in Figure 3.16a, is related to the physical width of the linear detectors, whereas the X-width is linked to the 2° tolerance angle used for the identification of the diffracting grains, which also corresponds to the ring width in Figure 3.16b.

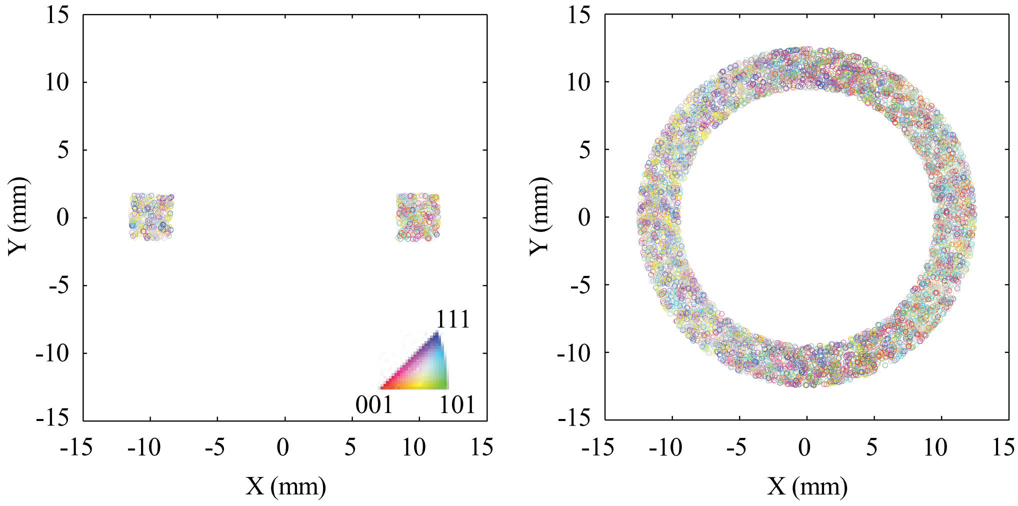

a) Linear detectors

b) 2D detector

Figure 3.16 Simulated images seen by a) the two linear detectors for $\beta = 25°$ and b) the 2D detector for $\beta = 30°$ for the ∅25 mm sample. Diffracting grains are represented by the circular symbols and IPF-coloring with respect to the RD is used to show their mean orientations

3.3.3 Effect of the angle variations on the identified diffracting grains

The effect of the tilt angles number on the number of diffracting grains is presented in this section for the linear detectors, as it is a multi-exposure technique. The effect of the tilt angle on the number of diffracting grains identified by the 2D detector is also presented, along with an example of the identified diffracting grains for a given α position.

3.3.3.1 Linear detectors: effect of the number of used tilt angles

3 to 21 β angles have been simulated for the same range of maximum angles: ±25°. Increasing the number of β angles would not only increase the number of diffracting grains but also the measurement time. Figure 3.17 presents the number of unique diffracting grains versus the number of β angles. The values are compared to the number of unique diffracting grains seen by the 2D detector for a measurement at $\beta = 30°$ (the grains highlighted in Figure 3.15b). The case of nine β angles corresponds to the number of measurements for which the number of additional diffracting grains decreases with increasing the number of β angles. Nine β angles were chosen for the study as they represent a realistic potential-measurement-time with a noticeable increase of the diffracting grains number compared to seven β angles.

The total number of diffracting grains stays below the 8183 unique grains participating to the diffraction captured by the 2D detector, even for a high number of linear-detectors positions (e.g., 21 β angles). Increasing the number of β angles further than 21 does not significantly increase the number of unique diffracting grains due to the superimposition of the β-positions. Indeed, for 21 β angles the angular section per β-position is only 2.4°, consequently a 1.6° overlap is created when considering the ±2° tolerance used to identify the diffracting grains. Hence, at 25 β angles the overlap has increased to the point where the angular section is equal to tolerance, i.e., for two consecutive β positions the detectors capture diffraction from the same diffracting grains.

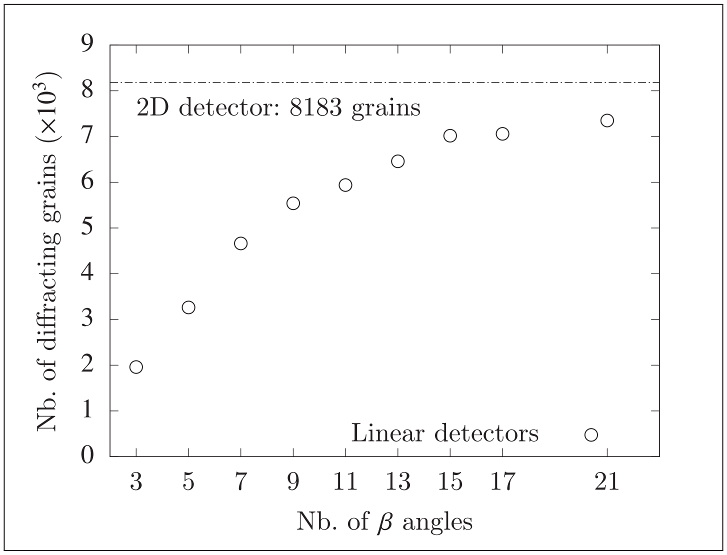

Figure 3.17 Total number of unique diffracting grains versus the number of β angles taken by the two linear detectors in a ±25° range. The number of unique diffracting grains identified by the 2D detector at $\beta = 30°$ is plotted as dash-dot line for comparison

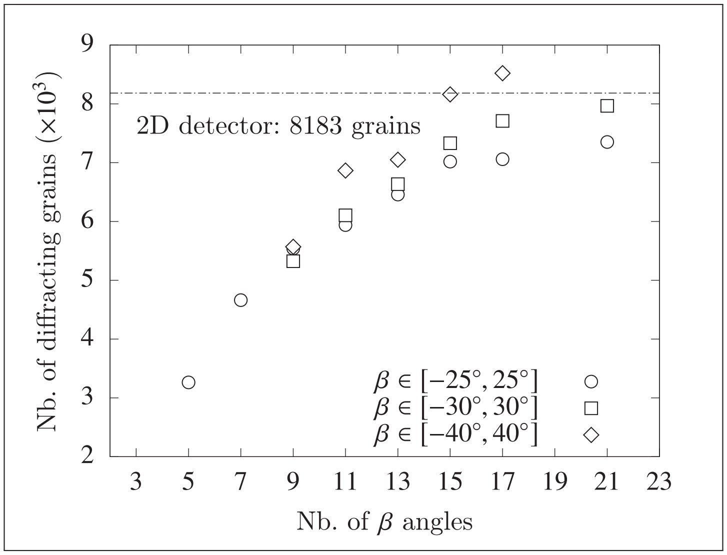

Figure 3.18 Total number of unique diffracting grains identified by the two linear detectors for different ranges and different number of β angles in a given range. The number of unique diffracting grains identified by the 2D detector at $\beta = 30°$ is plotted as dash-dot line for comparison

The effects of the superimposition can be limited by broadening the range of β-positions. Figure 3.18 presents the evolution of the number of unique diffracting grains for different ranges: $\beta \in [-25°, 25°]$, $\beta \in [-30°, 30°]$, and $\beta \in [-40°, 40°]$. In the ±40° range and starting from 15 β angles, the number of unique diffracting grains identified by the two linear detectors is equivalent or higher than that obtained by the 2D detector, while it stays below in the ±30° range, plateauing at 7966. It can be observed that for nine β angles the number of unique diffracting grains is similar for the different ranges (less than 5% difference).

3.3.3.2 2D detector: effect of tilt angle

The influence of the X-ray incident angle on the number of diffracting grains has been studied for the cos α method. β angles ranging from 10° to 45° have been simulated. Figure 3.19 presents the number of unique diffracting grains for the different 2D detector inclinations. The figure shows that the number of unique diffracting grains remains almost constant, regardless of the β angle. This observation might result from the fact that the homogeneous sample exhibits an isotropic distribution of the grains' mean orientations.

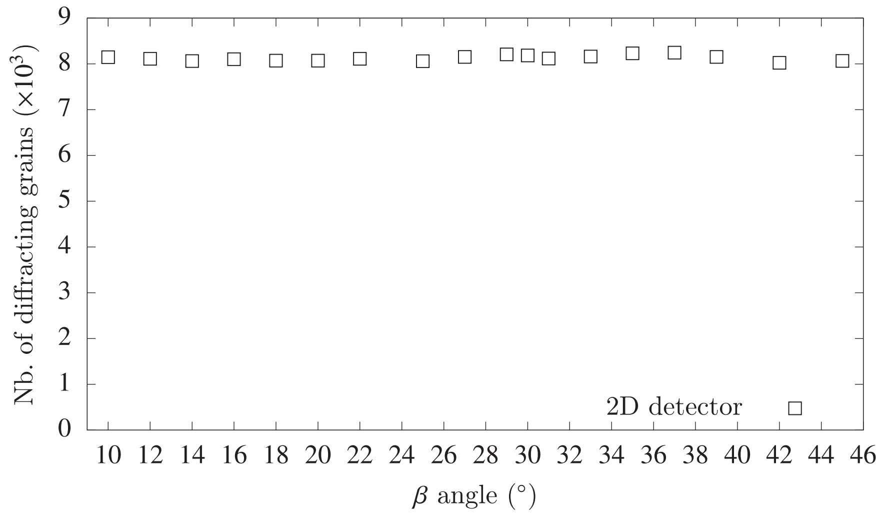

Figure 3.19 Total number of unique diffracting grains seen by the 2D detector versus the detector β angle

3.3.3.3 2D detector: variation along the α values

As mentioned in Section 2.5.1.2, the parameter $\overline{\varepsilon}_{\alpha}^{\{hkl\}}$ is computed, for a given α angle, from the strains measured at four orthogonal positions on the Debye ring. Consequently, the full scan of the Debye ring is carried out for a variation of α from 0° to 90°. Therefore, only a small part of the collected data is used for the strain computation at a given α. Figure 3.20 presents a simulated Debye ring seen on a 2D detector for a single exposure at $\beta = 30°$. Each circle corresponds to a given diffracting grain. The grains used for the calculation of $\overline{\varepsilon}_{\alpha}^{\{hkl\}}$ at $\alpha = 45.36°$ are highlighted in red as an example. The α-step size being set to 0.72°, 125 α angles are used to compute the 125 $\overline{\varepsilon}_{\alpha}^{\{hkl\}}$ values. The $\overline{\varepsilon}_{\alpha}^{\{hkl\}}$ values may then be plotted versus the corresponding $\cos\alpha$ values to determine the residual stress. In the case where no diffracting grains are detected for a given α, the α-step size could be increased to allow computing $\overline{\varepsilon}_{\alpha}^{\{hkl\}}$ values.

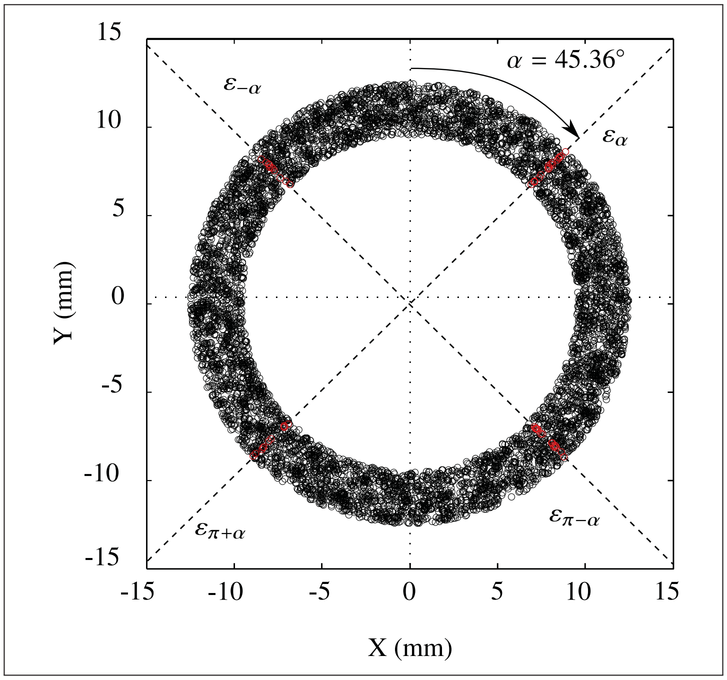

Figure 3.20 Simulated Debye ring on the 2D detector for $\beta = 30°$. Each circle represents a diffracting grain. The diffracting grains used for the calculation of $\overline{\varepsilon}_{\alpha}^{\{hkl\}}$ at $\alpha = 45.36°$ are plotted in red as an example

3.4 XRD measurement induced texture

Different sets of diffracting grains are identified when using the two diffraction techniques, and different crystallographic textures may be obtained via the linear detectors and the 2D detector during XRD measurements. The ∅25 mm sample (homogeneous microstructure) is used to reveal these “artificial" textures created by the detector type and its corresponding method of stress computation ($\sin^2\psi$ or $\cos\alpha$ method). Using the developed script and the MTEX package, pole figures can be plotted for the diffracting grains identified by the two different types of detectors. The pole figures for the (100), (110), (111), and (311) sets of planes are presented in Figures 3.21a, 3.21b, and 3.21c for all the grains of the ∅25 mm sample, and only for the diffracting grains detected by the two linear detectors and the 2D detector, respectively. The (311) pole figure has been plotted in addition to the traditional (100), (110), and (111) pole figures to present the textures introduced by XRD measurements to the planes used for strain measurements.

Figure 3.21a confirms the presence of an isotropic microstructure for the ∅25 mm sample (also observed in Figures 3.5a and 3.7a) with the absence of preferential crystallographic directions in the pole figures. Furthermore, the maximum texture index stays fairly low.

Like Figure 3.15a, Figure 3.21b is the superimposition of the nine different positions taken by the linear detectors. However, Figures 3.22a, 3.22b, and 3.22c show the pole figures for three specific β angles taken by the linear detectors: $\beta = -25°$, $\beta = 0°$, and $\beta = 25°$, respectively. For each pole figure, two hot spots representing the localization of the two linear detectors can be observed. They are the center of concentric circles. The detectors motion during the residual stresses measurements can be observed as a straight line at the center of the (311) pole figure in Figure 3.21b, which results from the displacement of the concentric circles, illustrated in Figure 3.22. The texture index determined for the linear detectors is the highest of the three cases presented in Figure 3.21. For all β angles, the maximum texture index is found to be higher than 20, as illustrated in Figure 3.22 with the three specific β angles.

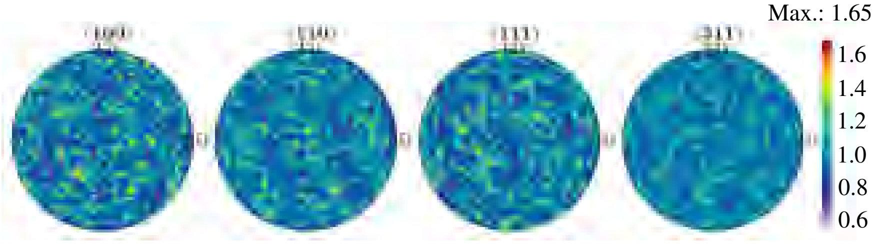

a) ∅25 mm sample

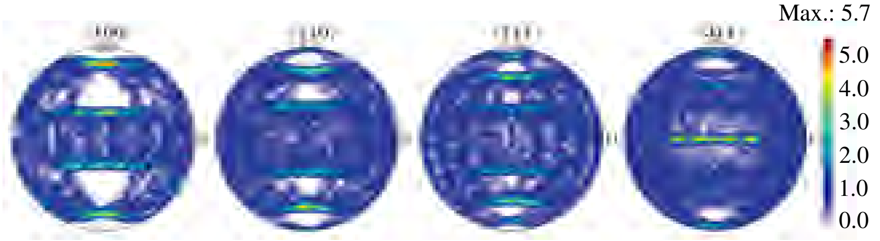

b) Linear detectors

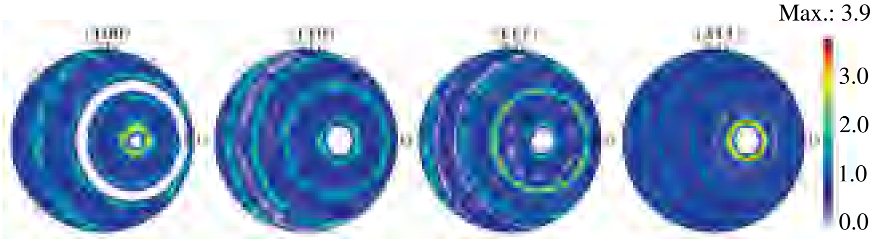

c) 2D detector

Figure 3.21 Pole figure of the (100), (110), (111), and (311) sets of planes for a) the whole ∅25 mm sample EBSD map and for the diffracting grains detected by b) the linear detectors and c) the 2D detector. Note that the (311) set of planes is the strain measurement set of planes used for residual stresses computation

On the other hand, the 2D detector, by its geometry, allows the Debye ring to be captured in its entirety, which results in the circle of high index visible in the (311) pole figure of Figure 3.21c. The concentric circles are not centered because of the incident angle of the X-ray beam ($\beta = 30°$). Nonetheless, the $\cos\alpha$ method implies dividing the Debye ring in 500 sections (α-step size of 0.72°) for the $\overline{\varepsilon}_{\alpha}^{\{hkl\}}$ calculation, as shown in Figure 3.20, which results in the intermediate textures presented in Figure 3.23. The α steps providing the highest ($\alpha = 0.72°$) and the lowest ($\alpha = 25.20°$) texture indexes are presented in Figures 3.23a and

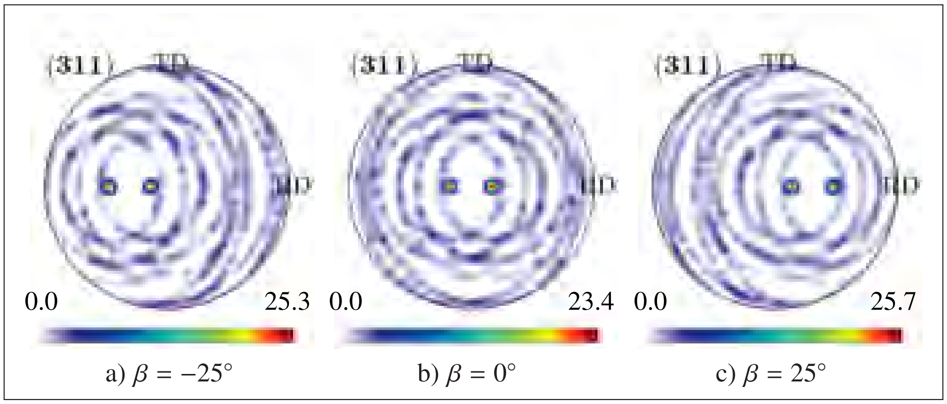

a) $\beta = -25°$ b) $\beta = 0°$ c) $\beta = 25°$

Figure 3.22 Pole figure of the (311) diffracting planes for the two linear detectors at a) $\beta = -25°$, b) $\beta = 0°$, and c) $\beta = 25°$

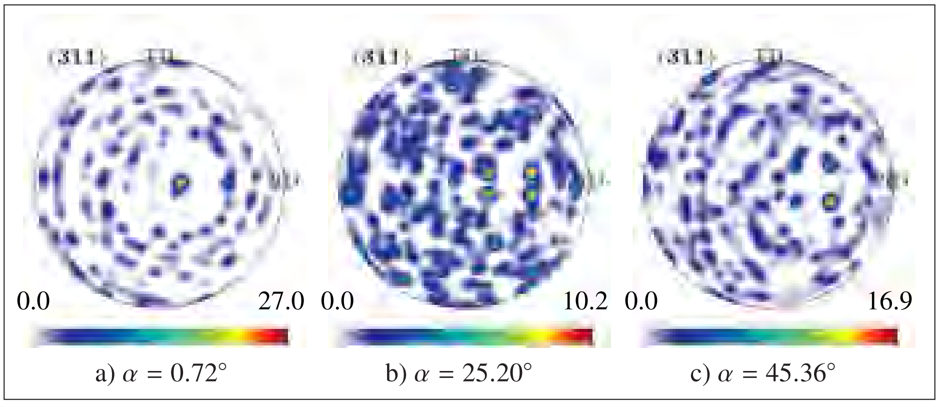

a) $\alpha = 0.72°$ b) $\alpha = 25.20°$ c) $\alpha = 45.36°$

Figure 3.23 Pole figure of the (311) diffracting planes for the 2D detector for the the 125 α angles maximum and minimum texture indexes at a) $\alpha = 0.72°$ and b) $\alpha = 25.20°$, respectively, as well as c) the $\alpha = 45.36°$ example

3.23b, respectively. A large variation of the maximum texture index can be observed between them. The highest indexes are found for the cases where α values are close to 0° or to 90° and only two hot spots can be distinguished. Figure 3.23c corresponds to the pole figure of the highlighted grains given as an example in Figure 3.20. The four strain measurements at α, $\pi + \alpha$, $-\alpha$, and $\pi - \alpha$ imply four hot spots (visible in Figures 3.23b and 3.23c), center of four concentric circles, but because of the low α-step size, the circles are not clearly defined.

Furthermore, for α values close to 0° or to 90°, only two hot spots can be distinguished, which results in higher maximum texture indexes.

The pole figures of the diffracting grains detected by the two types of detectors during the entire XRD measurement (Figures 3.21b and 3.21c) exhibit two distinct textures. These textures are accentuated when only considering the specific angles β and α (Figures 3.22, and 3.23). These “artificial" textures may affect the XEC value of the diffracting grains and therefore the measured stress, as the stress is linearly dependent of the XEC value in both calculation methods.

3.5 Computation of the XEC values for the homogenous IN718 sample

This section presents the XEC $\frac{1}{2}S_2^{\{hkl\}}$ calculation method for the diffracting grains identified from the EBSD of the homogeneous sample. $\frac{1}{2}S_2^{\{hkl\}}$ values were computed for the two types of detectors and different conditions such as different tilt angles or grain size.

3.5.1 XEC calculation method

The XEC $\frac{1}{2}S_2^{\{hkl\}}$ of a given set of diffracting grains was determined for comparison of the $\sin^2\psi$ and $\cos\alpha$ methods using MTEX package (Mainprice *et al.*, 2011) as follows:

- The IN718 single crystal stiffness tensor, $\boldsymbol{C}^{\mathbf{C}}_{\mathbf{IN718}}$, also used in Section 2.5.2.1 (C^{C}_{11} = 251.0 GPa, C^{C}_{12} = 135.5 GPa, and C^{C}_{44} = 98.0 GPa), was assigned to all the grains of the EBSD map.
- An ODF, f, was calculated for the set of diffracting grains to account for the possibility of some anisotropy introduced by the XRD measurement. An example of ODF is provided in Appendix VI.
- The ODF was then used to determine the average stiffness tensor of the set of diffracting grains computed for the Voigt and Reuss bounds (hypothesis of constant elastic strain and stress, respectively, in all crystallites) as (Mainprice *et al.*, 2011)

$$\langle \boldsymbol{C} \rangle^{\mathrm{SVoigt}} = \sum_{m=1}^{M} \boldsymbol{C}^{\mathbf{C}}_{\mathbf{IN718}}(g_m)\omega_m f(g_m) \tag{3.5a}$$

$$\langle \boldsymbol{C} \rangle^{\text{SReuss}} = \left[\sum_{m=1}^{M} \boldsymbol{C}_{\mathbf{IN718}}^{\mathbf{C}}{}^{-1}(g_m)\omega_m f(g_m) \right]^{-1} \tag{3.5b}$$

where $\langle \boldsymbol{C} \rangle^{\text{SVoigt}}$ and $\langle \boldsymbol{C} \rangle^{\text{SReuss}}$ are the average stiffness tensors expressed in the sample reference system (defined in Figure 2.9), S, for the Voigt and Reuss bounds, respectively, and are calculated for the selected set of m diffracting grains having an orientation g_m and a weight ω_m. The brackets refer the average over the grains that satisfy a particular diffraction condition.

- The XEC $\frac{1}{2}S_2^{\{hkl\}}$ was calculated with the quasi-isotropic XEC equation used in the case of biaxial stress state (Van Houtte & De Buyser, 1993):

$$\frac{1}{2}S_2^{\{hkl\}} = \langle S_{3333} \rangle^{\text{L}} - \langle S_{3311} \rangle^{\text{L}} \tag{3.6}$$

where $\langle S_{3333} \rangle^{\text{L}}$ and $\langle S_{3311} \rangle^{\text{L}}$ are the fourth-rank compliance tensor coefficients of $\langle \boldsymbol{S}_{ijkl} \rangle^{\text{L}} = \boldsymbol{a}_{im}\boldsymbol{a}_{jn}\boldsymbol{a}_{ko}\boldsymbol{a}_{lp}\langle \boldsymbol{S}_{\boldsymbol{mnop}} \rangle^{\text{S}}$ expressed in the laboratory system (defined in Figure 2.9), L, with $\langle \boldsymbol{S}_{ijkl} \rangle^{\text{S}} = (\langle \boldsymbol{C}_{ijkl} \rangle^{\text{S}})^{-1}$. The laboratory system is defined as the z axis being coincident to the scattering vector $\mathbf{V}_{\mathbf{Scat}}$ and $\boldsymbol{a}_{\boldsymbol{ij}}$ is the rotation matrix from S-system to L-system. The tensors $\langle \boldsymbol{C} \rangle^{\text{SVoigt}}$ and $\langle \boldsymbol{C} \rangle^{\text{SReuss}}$ were used to compute $\frac{1}{2}S_2^{\{hkl\}}$ for the Voigt and Reuss bounds.

- Finally, as the experimentally measured elastic constants are often close to the average of the Voigt and Reuss bounds (Gnäupel-Herold *et al.*, 1998; Murray, 2013), the Neerfeld-Hill limit (Equation (2.25b)), which is the arithmetic mean of Voigt and Reuss bounds (Hill, 1952), was used during the study and is reminded here

$$\left(\frac{1}{2}S_2^{\{hkl\}}\right)^{\text{Hill}} = \frac{1}{2}\left[\left(\frac{1}{2}S_2^{\{hkl\}}\right)^{\text{Voigt}} + \left(\frac{1}{2}S_2^{\{hkl\}}\right)^{\text{Reuss}}\right]. \tag{3.7}$$

It is worth noting that the <*hkl*> crystallographic direction is taken into consideration in the calculation of $f(g_m)$ as it is computed for the identified diffracting grains. When computed for the {311} planes, the XEC $\left(\frac{1}{2}S_2^{\{hkl\}}\right)^{\text{Hill}}$ is presented in the following sections as $\frac{1}{2}S_2^{\{311\}}$ for convenience.

This procedure for $\frac{1}{2}S_2^{\{311\}}$ computation was carried out for each one of the different β-tilts and linear detectors for the $\sin^2\psi$ method and for each combination of β-tilt and α-angular position for the $\cos\alpha$ method.

3.5.2 XEC computation for the diffracting grains

Figure 3.24 presents the XEC values for the nine β angles used for residual stress measurements using the linear detectors as well as the number of diffracting grains detected for each position. The results are separately given for the two linear detectors, namely the left and right detectors (they correspond in Figure 3.16a to the circles in negative and positive X values, respectively, or to the left and right concentric circles in Figure 3.22, respectively). It can be observed that the number of diffracting grains remains almost constant, around 380 diffracting grains per detector and per inclination. For the nine positions and the two linear detectors, the XEC average and confidence interval, $CI_{95\%}$, are 6.33×10^{-6} MPa^{-1} and 0.23×10^{-6} MPa^{-1}, respectively. The $CI_{95\%}$ value is computed from the lower bound of the 95% confidence interval on the standard deviation of an assumed normal distribution, determined with a χ^2 test (Hines *et al.*, 2008).

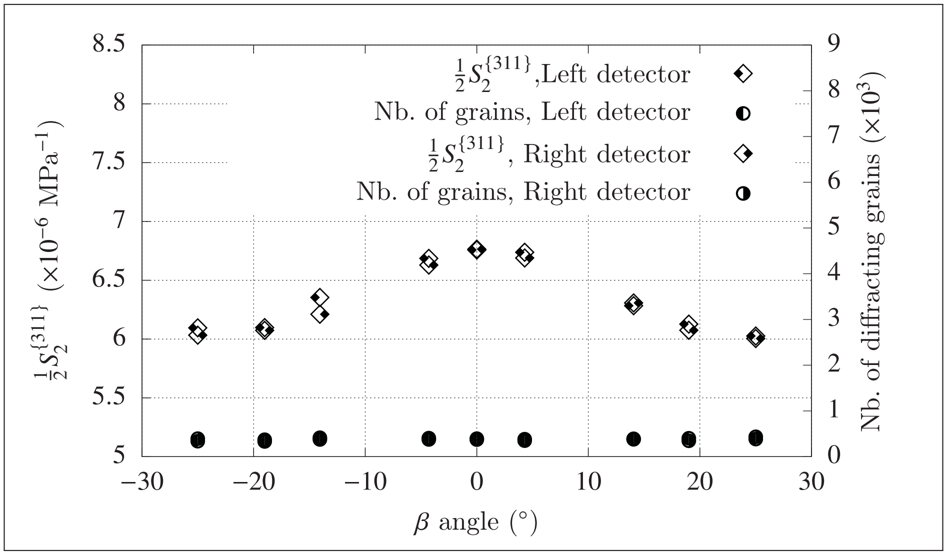

Figure 3.24 Number of diffracting grains detected by the two linear detectors for nine β angles and their corresponding XEC $\frac{1}{2}S_2^{\{311\}}$ values calculated for the {311} planes

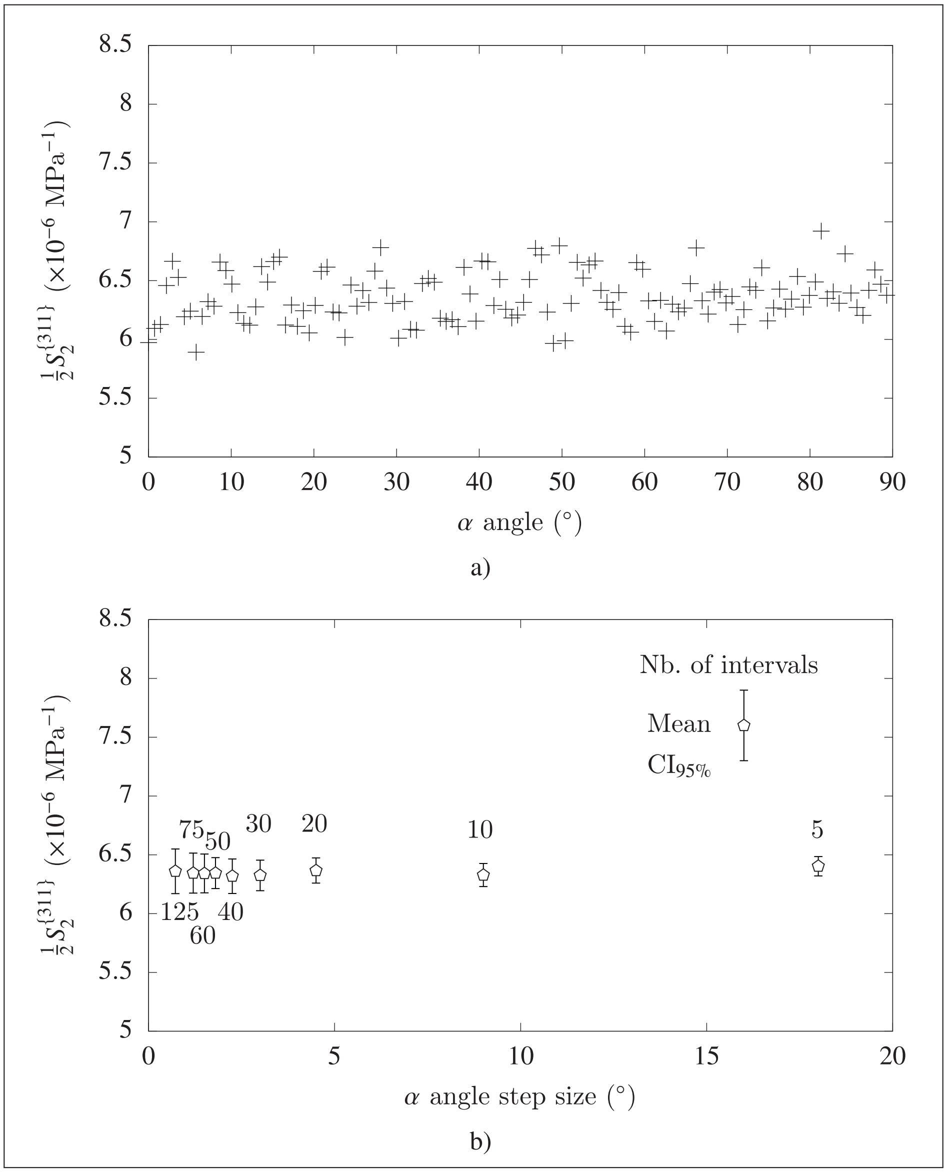

Figure 3.25 a) XEC $\frac{1}{2}S_2^{\{311\}}$ values calculated for the diffracting grains detected by the 2D detector at $\beta = 30°$ for 125 α angles (from 0° to 90°). b) Mean and confidence interval (CI$_{95\%}$) of the XEC $\frac{1}{2}S_2^{\{311\}}$ values calculated for different α-step sizes. The corresponding number of α angles is presented below or above the error bar

For the 2D detector, the $\frac{1}{2}S_2^{\{311\}}$ were calculated for a 0.72° α-step size to characterize the ring geometry. The 125 XEC values determined for $\beta = 30°$ are presented in Figure 3.25a. The values range from 5.89×10^{-6} MPa^{-1} to 6.92×10^{-6} MPa^{-1} and a mean value of 6.36×10^{-6} MPa^{-1} is observed, yielding a CI$_{95\%}$ of 0.19×10^{-6} MPa^{-1}. This low α-step size implies five times less diffracting grains per α value than for a given β-position with the two linear detectors, resulting in a larger range of the computed values but a lower $\mathrm{CI}_{95\%}$ value (as the confidence interval is also based on the population size). Figure 3.25b exhibits the mean and the confidence interval values of the XEC calculated for different α-step sizes. It can be observed that increasing the step size narrows the confidence interval $\mathrm{CI}_{95\%}$, while the mean value remains almost constant. Indeed, decreasing the number of intervals increases the number of orientations accounted for in one interval, which results in better approximation of the XEC.

Different β angles have also been simulated for the 2D detector and 0.72° α-step size. The average XEC value and the number of diffracting grains for the different β angles are shown in Figure 3.26. A quasi-constant number of diffracting grains can be observed throughout the entire range of simulated β angles. The average XEC value slightly decreases for high β angles (a 0° β angle corresponds to a normal incident X-ray beam).

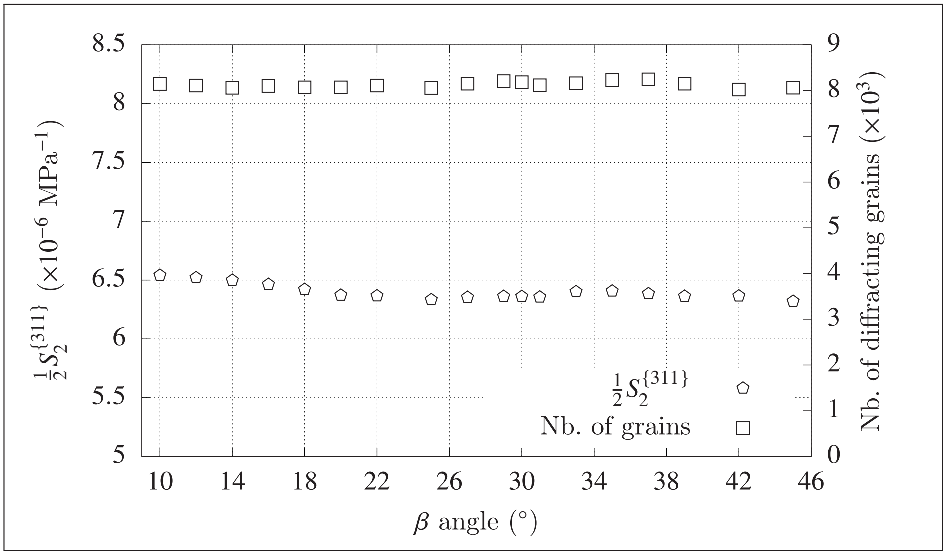

Figure 3.26 Number of diffracting grains detected by the 2D detector for different β angles and corresponding XEC $\frac{1}{2}S_2^{\{311\}}$ values calculated for a 0.72° α-step size (125 α angles)

For the linear detectors, the diffracting grains average XEC value is higher than the random texture XEC value, whereas for the 2D detector is slightly lower. These differences are most likely due to the fact that it is determined on sets of grains having a slight texture. The XEC values computed for the two detector types are not statistically different and seem not to be highly affected by the detector's position, i.e., β angle, in the case of the homogeneous microstructure.

3.5.3 Effect of grain size on the XEC values

XRD measurements quality may suffer when a relatively small number of orientations are diffracting, leading to anisotropy inherent to the used XRD method. The grain size or grain density can therefore affect the XRD measurement. The grains size effect on the XEC was studied by "artificially" reducing the grain density. The initial EBSD map size was reduced while keeping the same irradiated zone area, decreasing the grain density. Five resized EBSD maps, using a reduction ratio of R= 1/2, 1/5, 1/10, 1/15, and 1/20, were thus investigated, providing grains density ranging from 12526 grains/mm^2 to 1232 grains/mm^2. It is worth noting that the initial EBSD map grain density is 25316 grains/mm^2 (Table 3.2), corresponding to an average grains size of 6 µm (ASTM grain size number 12). On a 2D map, a 1/20 reduction ratio corresponds to a twenty times increase of the grain size, giving a 120 µm average equivalent diameter (ASTM grain size number 3) or a grain density of 1232 grains/mm^2.

Figure 3.27 presents the different reduced maps as orientation distribution maps with respect to the RD. The map reduction was set to start from the upper left corner of the initial EBSD map, shown in Figure 3.27a. The grain size was artificially increased by focusing the area of interest on a smaller portion of the initial map and by keeping the same scale. The IPF have also been determined for each map and maximum texture indexes are reported in Figure 3.27. It can be observed that increasing the average grain size slightly increases the maximum texture index without creating a specific texture. Figure 3.28 presents, for the six cases, the total number of grains and the total number of unique diffracting grains for both detectors. The grains number is reduced from 35805 grains (25316 grains/mm^2) to 1743 grains (1232 grains/mm^2). Constant percentages of diffracting grains were found for the linear detectors and the 2D detector, as 15% and 23%, respectively.

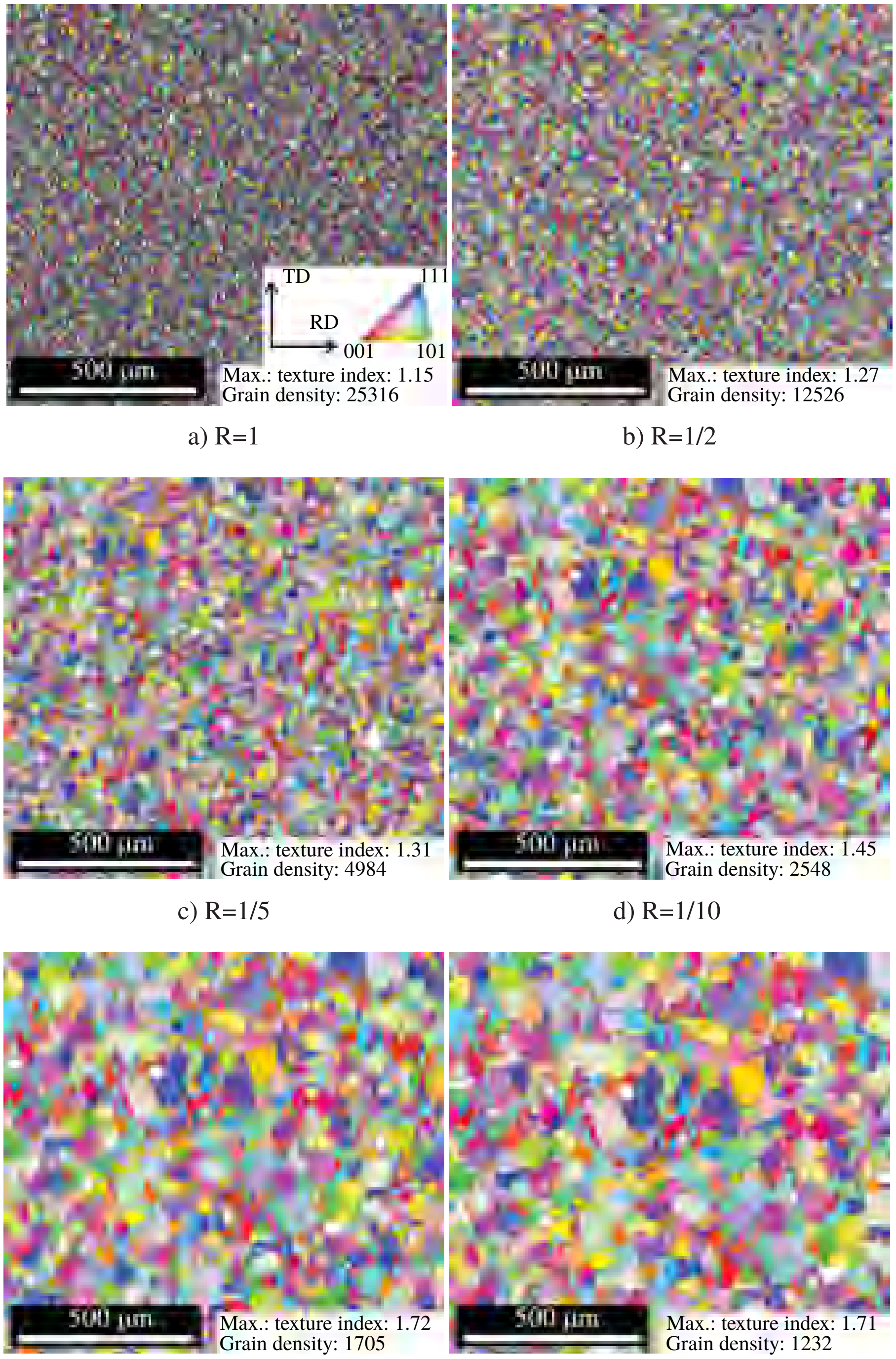
TD
111
RD
001
101
500 µm
Max.: texture index: 1.15
Grain density: 25316
500 µm
Max.: texture index: 1.27
Grain density: 12526
500 µm
Max.: texture index: 1.31
Grain density: 4984
500 µm
Max.: texture index: 1.45
Grain density: 2548
500 µm
Max.: texture index: 1.72
Grain density: 1705
500 µm
Max.: texture index: 1.71
Grain density: 1232

a) R=1 b) R=1/2

c) R=1/5 d) R=1/10

e) R=1/15 f) R=1/20

Figure 3.27 Orientation distribution maps of ∅25 mm sample for the following reduction factor: a) R=1 (initial map), b) R=1/2, c) R=1/5, d) R=1/10, e) R=1/15, and f) R=1/20. Information on map maximum texture index and grain density (in grains/mm^2) are also provided

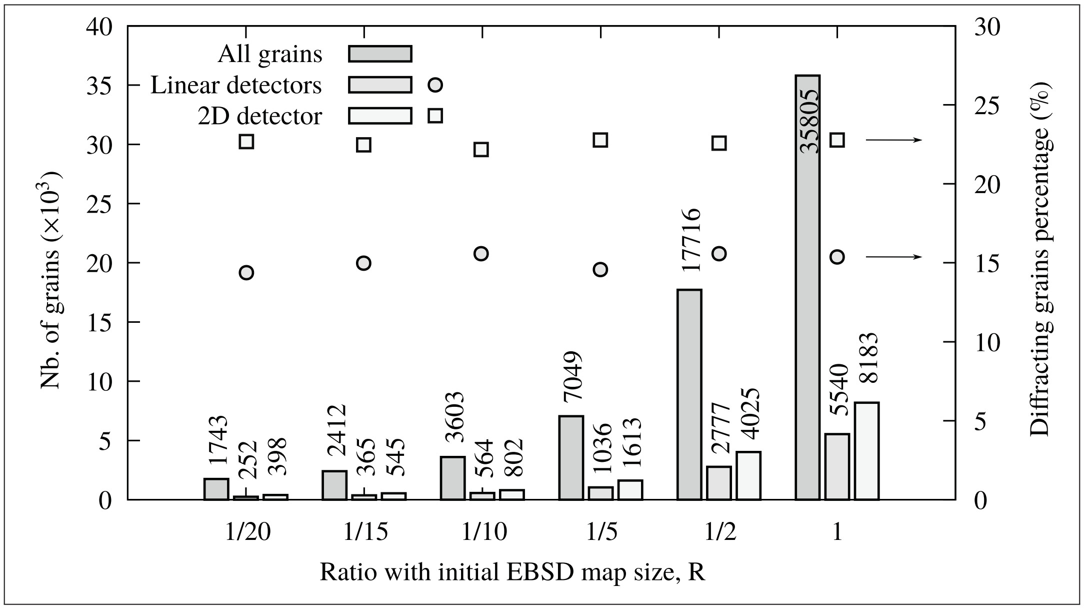

Figure 3.28 Histogram of the number of grains for the different reduced maps and the corresponding diffracting grains number for the linear and 2D detectors. The percentage of diffracting grains is also plotted for both detectors geometry

The calculated XEC was only affected by the change in grain density, due to the homogeneous grain orientation and grain size distributions. For the five resized maps, XEC $\frac{1}{2}S_2^{\{311\}}$ mean and confidence interval values have been calculated for both diffractometer types and were compared with the results of the initial EBSD map (R=1). The results are presented in Figure 3.29. $\frac{1}{2}S_2^{\{311\}}$ values increase by up to 2.1% as the grain density decreases whereas the confidence interval significantly broadens. For the 2D detector, increasing the α-step size increases the number of grains taken into consideration for each XEC computation, broadening the confidence interval $\mathrm{CI}_{95\%}$. When the number of diffracting grains decreases significantly, the α-step size for analysing the Debye ring has to be increased to 1.2° to ensure the presence of diffraction data for all α intervals. For instance, in the case of $\mathrm{R} = 1/20$, the $\frac{1}{2}S_2^{\{311\}}$ values can only be computed for a α-step size of 1.2°, or higher. The values vary from 5.16×10^{-6} MPa^{-1} to 8.40×10^{-6} MPa^{-1}, yielding a 0.58×10^{-6} MPa^{-1} confidence interval. The high $\mathrm{CI}_{95\%}$ values can still be explained by the very low number of diffracting grains participating to each XEC estimation. Therefore, high α-step size should be used when large grains (or low grain density) are found in the material.

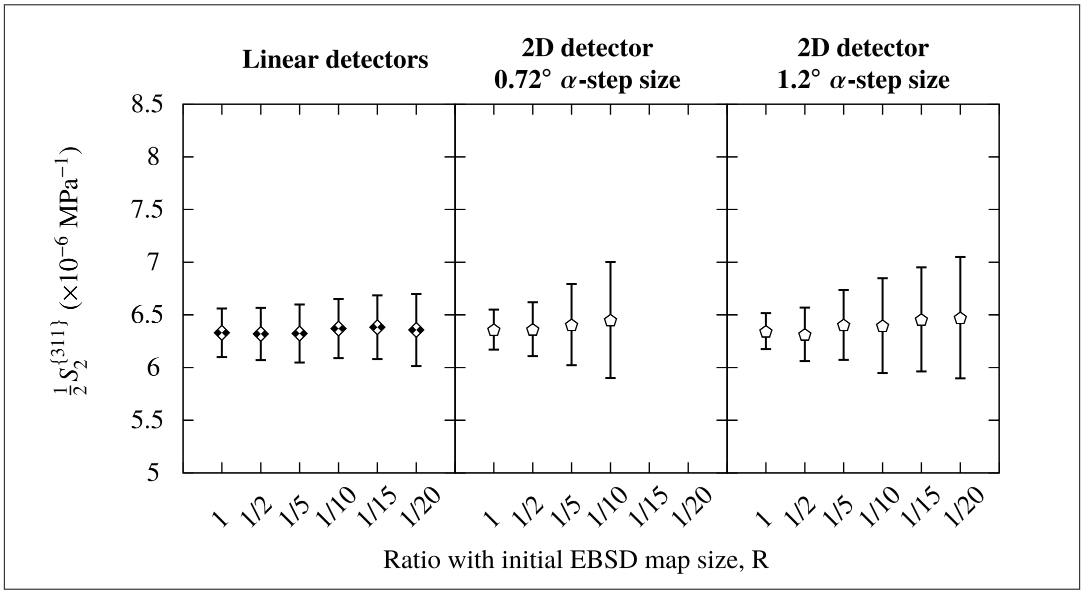

Figure 3.29 Mean values and confidence interval on the standard deviation ($\mathrm{CI}_{95\%}$) of the XEC $\frac{1}{2}S_2^{\{311\}}$ determined for the diffracting grains detected by the linear and 2D detectors in the case of five resized maps. Results for the 2D detector are presented for 0.72° and 1.2° α-step sizes

3.5.4 Effect of diffractometer oscillation

Experimentally, the number of diffracting grains can be increased by oscillating the X-ray beam in the φ-plane. Different oscillation values have been simulated around the β-position for both diffractometers using 1° oscillation-steps, meaning that for a $\beta = 25°$ position and a 2° oscillation the X-ray beam and the detectors were oscillating from 23° to 27°. The simulations were realized for the reduction ratios R = 1/15 and R = 1/20, corresponding to a 90 µm and 120 µm average grain sizes, respectively, where the low grain density allows only a small number of diffracting grains, yielding a broader XEC confidence interval. The results are presented in Figures 3.30a and 3.30b for R = 1/15 and R = 1/20, respectively. The values for the steady positions (presented in Figures 3.28 and 3.29) are reminded as 0° oscillations. For both diffractometers, the oscillations increase the number of diffracting grains detected by the detectors. A 2° oscillation captures up to 55% more diffracting grains for the 2D detector, whereas the linear detectors only capture up to 36% more grains. Increasing the oscillation

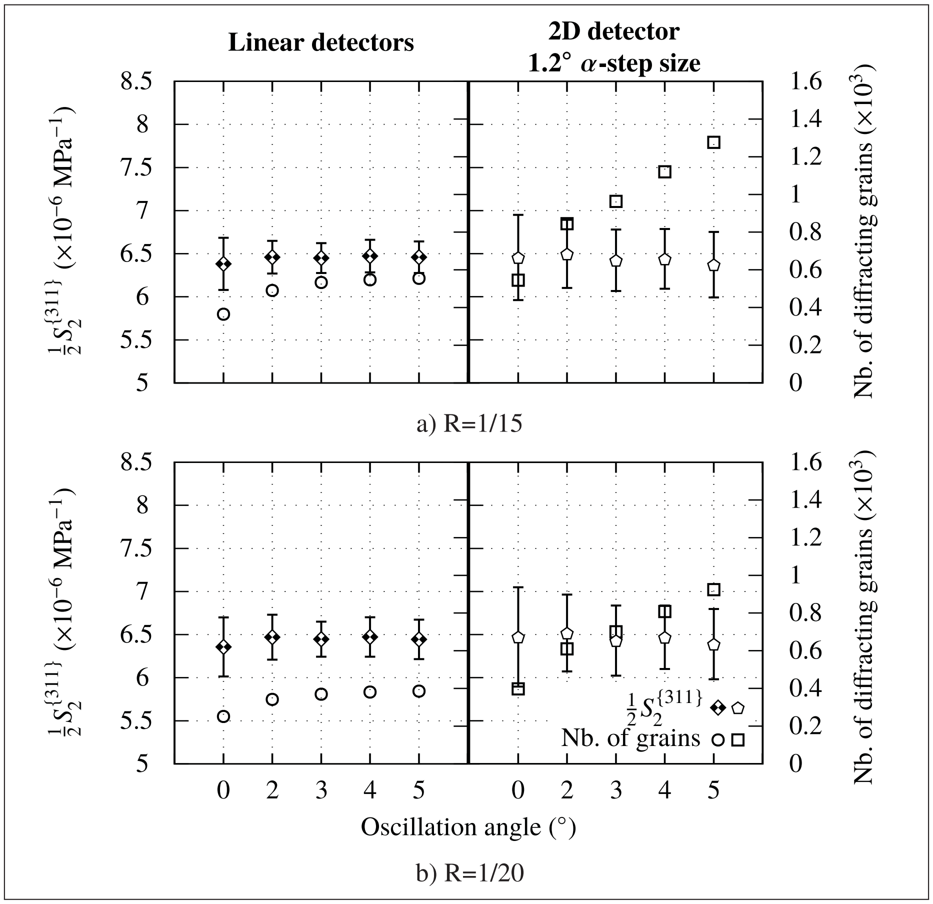

a) R=1/15

b) R=1/20

Figure 3.30 Total number of unique diffracting grains and XEC $\frac{1}{2}S_2^{\{311\}}$ mean values calculated for two different reduction factors a) R=1/15 and b) R=1/20 and for measurements with both techniques in the case of oscillations in the φ-plane. The calculations for the 2D detector were performed using a 1.2° α-step sizes. The error bars represent the confidence interval on the standard deviation ($\mathrm{CI}_{95\%}$)

angle for the linear detectors does not increase significantly the total number of diffracting grains due to the fact that the oscillation for a β-position ends up superimposing the oscillations of the other β-positions, hence the asymptotic curves. The XEC values tend to decrease with the oscillations for the 2D detector, while increasing for the two linear detectors. With oscillations, the confidence interval on the standard deviation is found to be narrower by up to 43% and 36% for the linear detectors and the 2D detector, respectively. For the two reduction ratios, the narrowest confidence intervals are found for 3° and 4° oscillations for the linear detectors and the 2D detector, respectively.

3.6 Computation of XRD-induced texture and the XEC values for the inhomogenous IN718 sample

The “artificial" textures induced by the XRD measurements, as well as the XEC, have been plotted for the inhomogeneous sample. The ∅89 mm sample exhibits a bimodal microstructure composed of a large number of grains having a 6 μm average grain size and very few grains with a grain size higher than 100 μm, as depicted in Figures 3.5b and 3.6b.

3.6.1 XRD measurement induced texture

As for the ∅25 mm sample, the “artificial" texture induced by the XRD measurements was plotted for the ∅89 mm sample (inhomogeneous microstructure). Figure 3.31a presents the pole figures for the (100), (110), (111), and (311) sets of planes for the ∅89 mm sample, whereas Figures 3.31b and 3.31c present the “artificial" textures induced by the XRD measurements with the two linear detectors (nine β angles) and for the 2D detector (one β angle), respectively. When compared to the homogeneous microstructure of the ∅25 mm sample, the bimodal microstructure found for the ∅89 mm sample increases the texture index from 1.65 (Figure 3.21a) to 5.9 (Figure 3.31a), without inducing a specific crystallographic texture.

The “artificial" textures induced by the XRD measurements and visible in Figures 3.31b and 3.31c are similar but less defined than for the ∅25 mm sample (Figures 3.21b and 3.21c), as the bimodal microstructure limits the possibilities of having a grain oriented in the diffraction condition. Consequently, the blue color has partially be replaced by the white color (a lower index) and spots of high texture index have appeared. Furthermore, the maximum indexes have triple when compared to the ones of the homogeneous microstructure, with the maximum index is still found for the $\sin^2\psi$ method and the linear detectors.

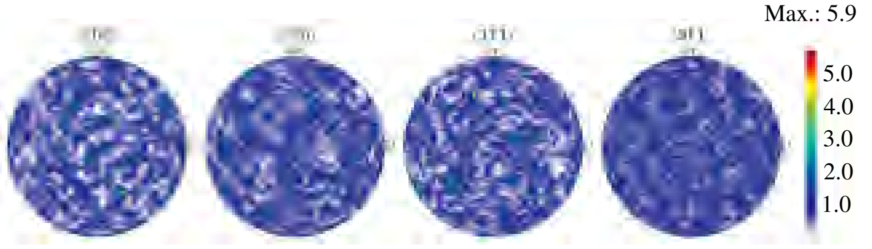

a) ∅89 mm sample

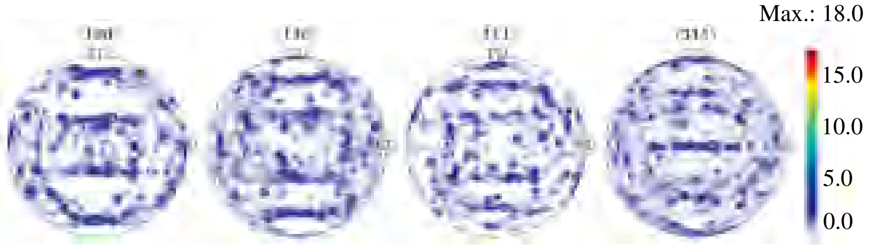

b) Linear detectors

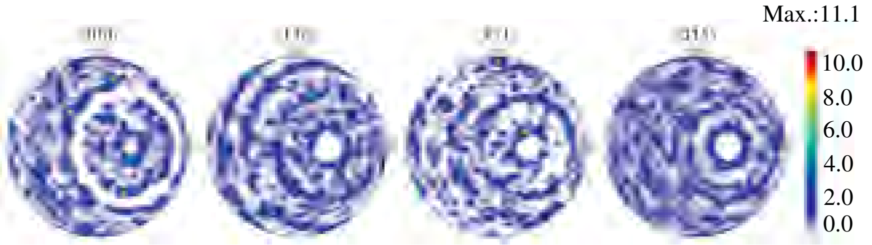

c) 2D detector

Figure 3.31 Pole figure of the (100), (110), (111), and (311) sets of planes for a) the whole inhomogeneous sample (∅89 mm) EBSD map and for the diffracting grains detected by b) the linear detectors and c) the 2D detector. Note that the (311) set of planes is the strain measurement set of planes used for residual stresses computation

3.6.2 XEC computed for the inhomogeneous microstructure

A bimodal microstructure composed of a large number of grains having a 6 μm average grain size and very few grains with a grain size higher than 100 μm were found in the ∅89 mm sample, as depicted in Figures 3.5b and 3.6b. The effect of grain size is considered thanks to the use of weights ω_m in the computation of the Voigt and Reuss bounds (Equations (3.5a) and (3.5b)) for the XEC determination. The XEC calculations for both microstructures are presented in Figure 3.32a for the two linear detectors using nine β angles. The average XEC and confidence interval values of the nine β angles are 6.41×10^{-6} MPa^{-1} and 0.33×10^{-6} MPa^{-1}, respectively for the ∅89 mm sample. The mean value is higher than that found for the ∅25 mm sample and, more importantly, the confidence interval has broadened by 44%.

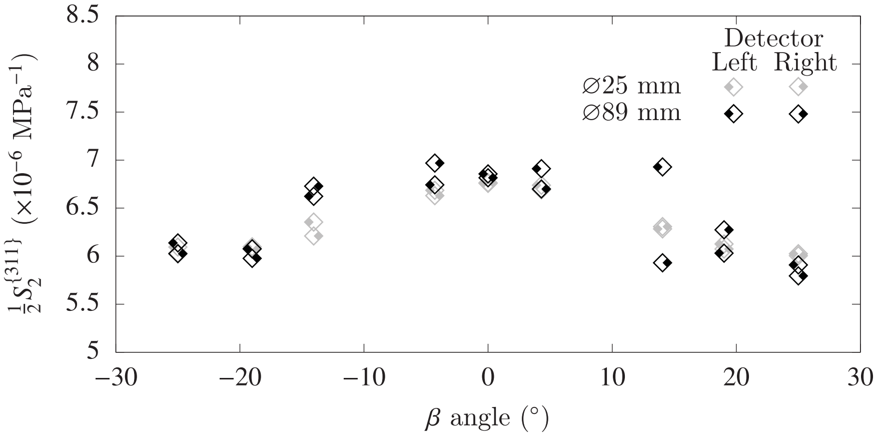

a) Linear detectors

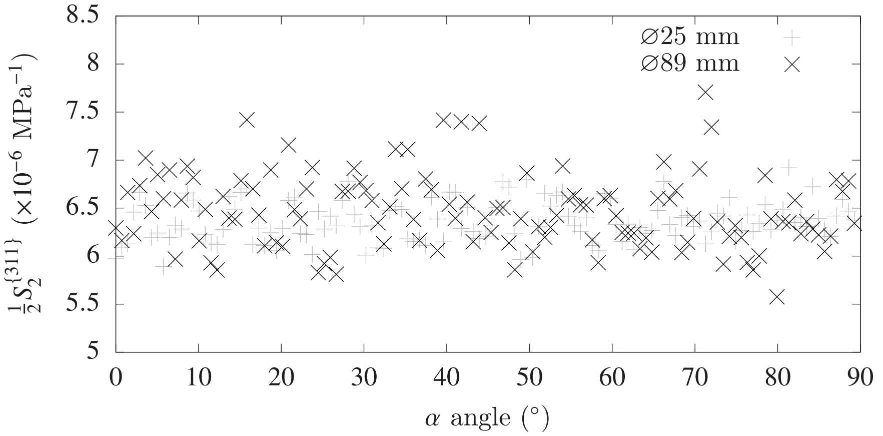

b) 2D detector

Figure 3.32 Comparison of the XEC $\frac{1}{2}S_2^{\{311\}}$ calculated for the ∅25 mm and ∅89 mm samples for a) nine β angles in the case of measurements with two linear detectors and b) 125 α angles for the 2D detector at $\beta = 30°$

The XEC was also calculated for the 2D detector at $\beta = 30°$ and for 125 α angles. The XEC values computed for the ∅89 mm sample, when compared to those obtained for the ∅25 mm sample, are presented in Figure 3.32b. The average value is also found to be higher than the ∅25 mm sample value: $6.47{\times}10^{-6}$ MPa^{-1}, whereas the confidence interval of $0.36{\times}10^{-6}$ MPa^{-1} has nearly doubled. Figure 3.33 exhibits the XEC mean values for different α-step sizes for comparison with Figure 3.25b. As for the ∅25 mm sample, the confidence interval narrows when the step size increases, but remains significantly higher.

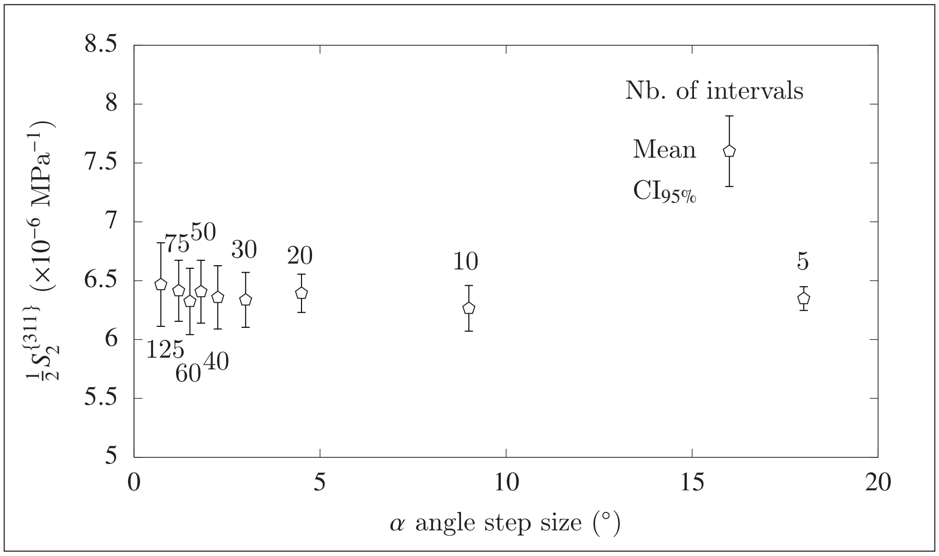

Figure 3.33 Mean and confidence interval (CI$_{95\%}$) of the XEC $\frac{1}{2}S_2^{\{311\}}$ calculated for different α step sizes for the ∅89 mm sample. The corresponding number of α angles is presented below or above the error bar

3.7 Chapter conclusions

In this chapter, the residual stress measurement techniques: the $\sin^2\psi$ method coupled with two linear detectors and the $\cos\alpha$ method coupled with a 2D detector have been compared via the identification of the diffracting grains from an EBSD map for each method and through the computation of the XEC of these diffracting grains, and this for an homogeneous and inhomogeneous (bimodal) microstructure of IN718.

First, an example of experimental determination of the XEC $\frac{1}{2}S_2^{\{311\}}$, using the $\sin^2\psi$ and $\cos\alpha$ methods, was presented for IN718 samples exhibiting a homogeneous and inhomogeneous microstructures. For the inhomogeneous microstructure, a 4% difference was found between the measured XEC values using the $\sin^2\psi$ and $\cos\alpha$ methods. This difference fell to 0.5% for measurements on the homogeneous sample. The measured XEC values are in average 6% higher than the Reuss limit (upper limit), computed in Chapter 2. The fact that the experimentally determined XEC values are higher than the Reuss limit could be due to the use of inappropriate single crystal elastic constants. The single crystal elastic constants were averaged from the literature for a certain range of grain sizes and compositions which do not characterize well enough the composition and grain size of the present IN718. A comparison of the $\sin^2\psi$ and $\cos\alpha$ methods, based on the identification of the diffracting grains from EBSD maps, is then performed to attempt to explain the differences observed between the two methods.

An EBSD map, having a size comparable to the irradiated area, was acquired for each sample. The effective depth of X-ray penetration of each XRD method being smaller than the average grain size determined from the two EBSD maps, it was assumed for the comparison that only the layer of grains obtained by EBSD could diffract and that the layers below were not participating to the diffraction. When taking into account the specificities of each method, it was observed that the 2D detector captures diffraction data from 1.5 times more unique grains in a single exposure (one tilt angle) than the two linear detectors for nine tilt angles. For the 2D detector, the number of unique diffracting grains was found to be quasi-constant for the range of tested tilt angles ([10°,45°]). Whereas for the two linear detectors, it was observed that increasing the number of tilt angle further than 21, in the range of ±25°, does not increase the number of unique diffracting grains due to the superimposition of the tilt positions. Even for 21 different tilt angles, the number of unique diffracting grains is lower than for the 2D detector. By broadening the range of tilts to ±40° and from 15 tilts, the number of unique diffracting grains identified by the two linear detectors reaches the value obtained for the 2D detector. From an experimental point of view, ±40° range and 15 tilts would increase the measurement time by 67% when compared to ±25° range, or ±40° range, and 9 tilts.

For the homogeneous microstructure, the $\frac{1}{2}S_2^{\{311\}}$ values, when computed for a given set a diffracting grains (given β or α), vary by about 7% and 9% from the average value for the linear detectors and 2D detector, respectively. Variations of up to 10% of the XEC value have been observed between the different sets of diffracting grains and the XEC value computed for the Hill bound. These variations reach up to 18% of the XEC value for the inhomogeneous microstructure, which tends to increase the $\frac{1}{2}S_2^{\{311\}}$ average values and to broaden the confidence interval on the standard deviation. It has been shown that increasing the α-step size for the 2D detector narrows the confidence interval.

The effect of the grain size has also been simulated. For both the linear detectors and 2D detector, the percentage of diffracting grains was found to remain quasi-constant for the different grain sizes simulated when compared to the initial case. The $\frac{1}{2}S_2^{\{311\}}$ average values were also found to stay quasi-constant for an increase of the grain size, which only broadened the confidence interval. The initial α-step size was found to be not large enough, for a grain size higher than 60 µm, to have diffraction data for each α-step, which would make impossible the computation of the strain parameter $\overline{\varepsilon}_\alpha^{\{hkl\}}$ for the 125 values of α. The simulation of the diffractometer oscillation, for the cases of the two larger grain sizes, have shown an increase of diffracting grains number and consequently a decrease of the confidence interval width for both types of detectors.

The “artificial” textures induced by the XRD measurements was revealed using the homogeneous microstructure. For the linear detectors, a global texture was plotted for the nine tilts angles and compared to the texture induced by the 2D detector in a single exposure. Each type of detectors induces a specific texture. The different textures were found to be even more pronounced when plotted for a given β angle for the linear detectors and a given β and α angle for the 2D detector. In the case of the inhomogeneous microstructure, the “artificial” textures were found to be further increased.

This chapter allowed to highlight the creation of two different “artificial” textures when measuring the residual stresses with the linear detectors and 2D detector. The low number of shared diffracting grains between the two methods (representing 20% and 14% of the total identified diffracting grains for the $\sin^2\psi$ and $\cos\alpha$ methods, respectively) implies that the strains are measured from different sets of grains, hence the slightly different values of XEC measured and presented in the first section. In the case of the bimodal microstructure, this difference can be increased due to the presence of large grains which exhibit high misorientation, if they are found in diffraction condition.

CHAPTER 4

USE OF THE DIFFRACTION PEAK WIDTH FOR COLD WORK ASSESSMENT

This chapter presents the use of the XRD peak width for the determination of the cold work profile introduced by shot peening. The three materials were studied as they provide a wide range of material's hardness as the shot peening conditions change. The cold work affected depths evaluated by XRD were compared to microhardness profiles. Section 4.1 presents two calibration curves for the IN718 to highlight the effect of a load in the elastic region. The estimated cold work profile is then used in an example of application. Section 4.2 presents the results for the AA7050. Section 4.3 presents the results for the 300M, which exhibit a different trend than the previous materials. The differences are explained by the use of an optical micrograph and an EBSD scan. Finally, Section 4.4 concludes this chapter.

4.1 Determination of cold work profiles for shot peened IN718 specimens

The first part of this chapter determines the cold work profiles of two shot peened IN718 specimens. This section is divided in four subsections: i) the study implementation, the determination of ii) the residual stress and FWHM profiles, iii) the resulting cold work profiles, and iv) the microhardness profiles. This section is concluded by the interpretation and discussion of the results.

4.1.1 Implementation of the study

The residual stresses and the FWHM values were determined using the Pulstec μ-X360n apparatus following the XRD measurement conditions listed in Table 2.6. Two fatigue specimens, made from the $\varnothing$25 mm bars of IN718 (homogeneous microstructure), were used for this study to provide realistic cold work profiles. The two specimens were shot peened with CW14 media (media properties are presented in Table 2.5) at two different Almen intensities: 4 A and 8 A, with a coverage of 100% (shot peening conditions will be further used to describe the specimens). The geometry of the specimens is presented in Figure 4.1. The specimens were initially designed to study the relaxation of the residual stresses when subjected to uniaxial fatigue testing. Results can be found in Klotz *et al.* (2018a) (visible in Appendix VII) and showed a small residual stresses relaxation in high cycle fatigue (σ_{fmax} = 1100 MPa) and a redistribution of the residual stresses in low cycle fatigue (σ_{fmax} = 1370 MPa). This unconventional geometry was used to avoid the curvature effects of cylindrical specimens on the XRD measurements. XRD measurements were performed at the center of the specimen's wider section (top view of Figure 4.1). The in-depth residual stress and FWHM profiles were obtained by electropolishing the surface following the conditions listed in Section 2.5.4.1. Due to the specimen's narrow width, the pocket size was 6×9 mm to leave enough material on each side of the pocket to avoid leakages of the electrolytic solution during the electropolishing process. The width of the pocket was large enough to allow XRD measurements with the use of a 1 mm collimator. The final surface obtained by electropolishing of the 8 A specimen is presented in Figure 4.2.

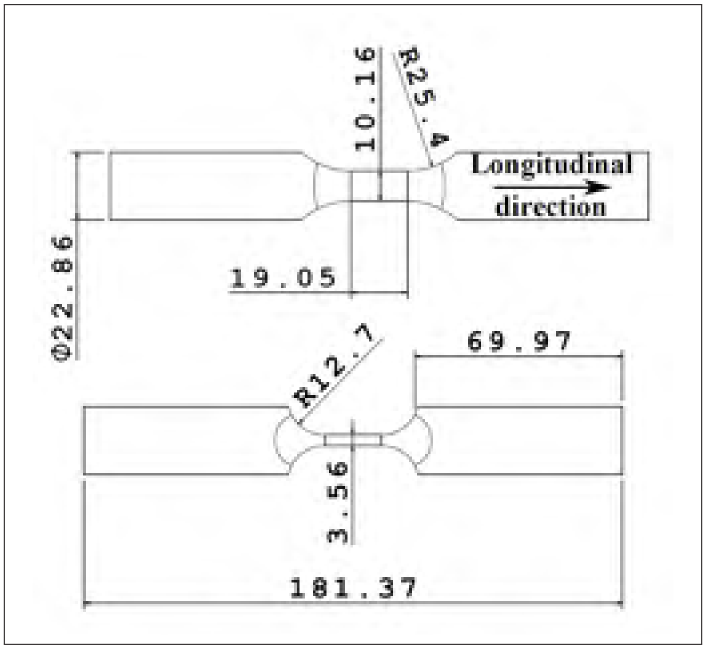

Figure 4.1 Geometry of the fatigue IN718 specimen. All dimensions are in mm. The longitudinal direction corresponds to the RD. Reprinted from Klotz *et al.* (2018a)

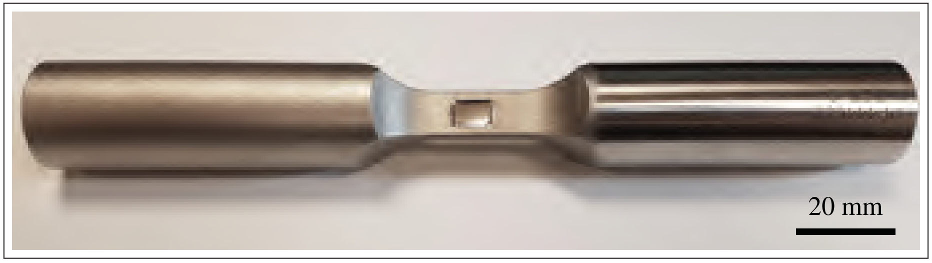

Figure 4.2 Final surface of the 8 A specimen's electropolished pocket

4.1.2 Residual stress and FWHM profiles for two shot peened IN718 specimens

The residual stress and FWHM profiles are presented for two shot peening conditions. An example of the estimated $FWHM$ values is also presented.

4.1.2.1 Determination of the residual stress and FWHM profiles

The residual stress and FWHM profiles obtained for the 4 A and 8 A specimens are presented in Figure 4.3. The residual stress and the $FWHM$ value are obtained in a single XRD measurement. The XRD measurements were repeated three times and their averages are presented in Figure 4.3. For the residual stress graph, the error bars represent the average of the three XRD-measurement errors provided by the diffractometer software. It is worth noting that on average the standard deviation of the three residual stress measurements is relatively low at 18 MPa. For the FWHM graph, the standard deviation of the $FWHM$ values being less than 0.1°, the error bars are not shown as they are too small and would not be visible. A similar surface (about -850 MPa) and maximum (about -1020 MPa at 30 μm) compressive residual stresses are found for the 4 A and 8 A specimens. However, a lower affected depth is found for the 4 A specimen (about 120 μm) than for the 8 A specimen (about 160 μm). Regarding the FWHM profiles, a lower (-8%) $FWHM$ value (i.e., a narrower peak width) is systematically found at the surface for the 4 A specimen than for the 8 A specimen. The $FWHM$ values are found to stop decreasing at about 105 μm and 190 μm for the 4 A and 8 A specimens, respectively.

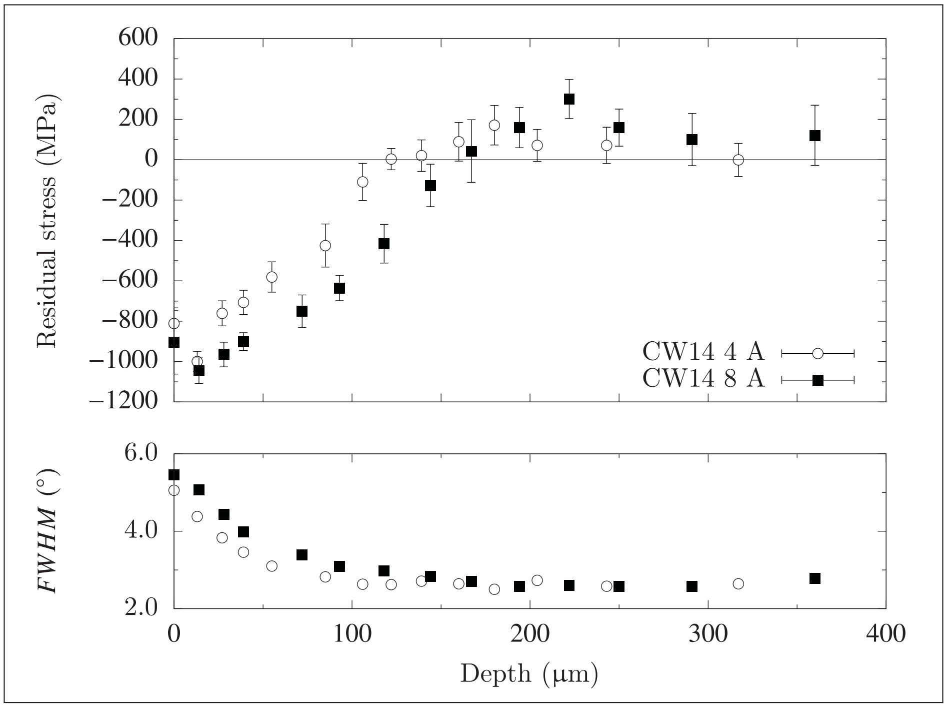

Figure 4.3 Residual stress (top) and FWHM (bottom) profiles for fatigue IN718 specimens shot peened with CW14 media at an intensity of 4 A and 8 A

4.1.2.2 Example of a $FWHM$ value

A $FWHM$ value presented in Figure 4.3 is in fact the average of 500 $FWHM$ values. The Pulstec apparatus provides 500 diffraction peaks in a single exposure when the minimum α-step size (0.72°) is used, as reported in Chapter 3. Figure 4.4 presents, for one of the three surface measurements of the 8 A specimen, the 500 $FWHM$ values obtained when the Debye ring is divided into 500 sections. Large variations of the $FWHM$ values around the α values of 35° and 187° can be observed. They can be due to significant variations of the plastic strain for the specific diffracting grains.

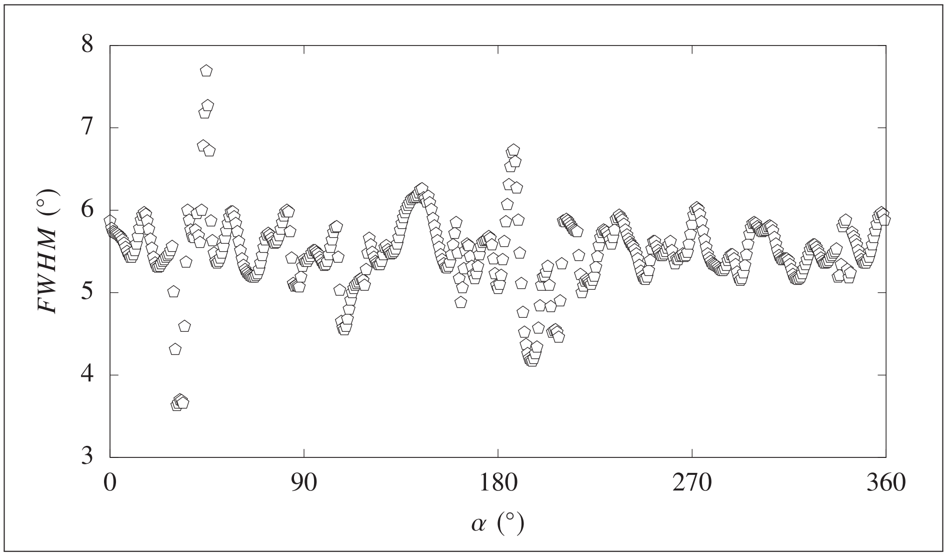

Figure 4.4 Example of the $FWHM$-values variation for the α angle describing the Debye ring, for one of the three surface measurements of the CW14 8 A specimen

4.1.3 Estimation of cold work profiles

The cold work profiles are estimated for the 4 A and 8 A specimens. Firstly, the method for the estimation, which uses a calibration curve to relate $FWHM$ values to cold work (Prevéy, 2000), is detailed. In this method, a specimen is plastically deformed and unloaded before the $FWHM$ value is being measured. This procedure is then repeated for incremental plastic deformations to obtain the calibration curve. Secondly, to show that $FWHM$ values are independent of elastic loadings, the calibration curve obtained for the unloaded specimen is compared to one obtained when the specimen is elastically loaded during XRD measurements. Thirdly, the estimated cold work profiles are exhibited for the two shot peening conditions. Finally, an example of a potential use of the estimated cold work profiles is provided.

4.1.3.1 Determining cold work from XRD peak width

For grains larger than few hundreds of nanometers Averbach & Warren (1949) suggested that the strain introduced by cold work in the grains, as it differs from one grain to another, would account for the major part of the peak broadening. For smaller grains, the peak width can also be related to the crystallite size (Warren, 1990). Consequently, in the case of shot peened IN718, with a grain size in the micrometer range, the peak broadening can be related to the increase of plastic deformation. Prevéy (1987) has shown for IN718 and Rene95 (another nickel-based superalloy) that a given amount of cold work, whether introduced by tension or compression, produced a given peak width. Therefore, a calibration curve can be determined by tensile or compression testing to estimate the cold work introduced by a surface treatment. Figure 4.5a presents the $FWHM$ values obtained by Prevéy (1987) for Rene95 and produced by different amounts of cold work, and this for different modes of deformation. It can be observed that the data fell in the same curve whether they were obtained by tensile or compression testing. Figure 4.5b presents a similar trend of values obtained by Prevéy (2000) for IN718. The evolution of the $FWHM$ values with the amount of cold work was described by Prevéy (2000) as

$$FWHM = H\left[1 - \exp\left(-I\varepsilon_p\right)\right] + J\varepsilon_p + K \tag{4.1}$$

where H, I, J, and K are fitting coefficients.

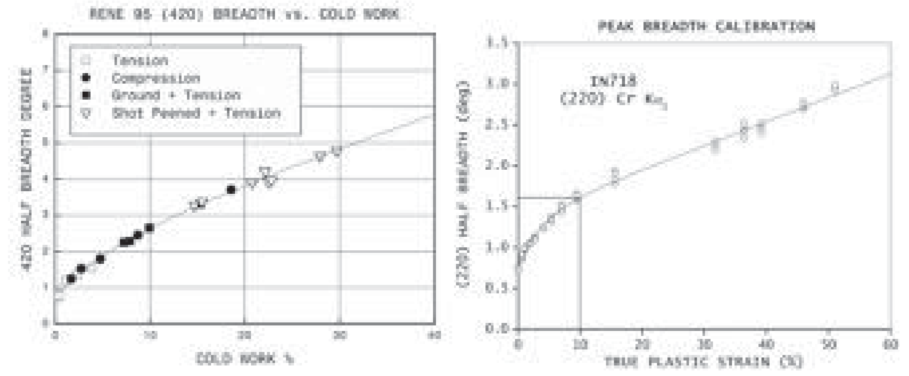

a) b)

Figure 4.5 a) Empirical curve relating the (420) diffraction peak width to the cold work percentage for Rene95 samples deformed by various means. b) Dependence of (220) peak width on cold work expressed as true plastic strain. Reprinted from Prevéy (1987) and Prevéy (2000), respectively

Since the $FWHM$ values are independent of the plastic deformation mode, high cold work values can be determined from calibration curves obtained via tensile testing, even if the tensile testing introduces less plastic deformation than compression testing as necking happens. Once the fitting coefficients of Equation (4.1) are found for the calibration curve, one can easily estimate the cold work introduced by a specific treatment, such as shot peening, from the peak width of an XRD measurement.

4.1.3.2 Calibration curve of IN718: $FWHM$ vs. ε_p

The calibration curve was obtained by increment of plastic deformation and is presented in Figure 4.6. Three XRD measurements, providing the $FWHM$ values, were performed between each increment for an unloaded specimen following the experiment conditions listed in Section 2.6. XRD measurements were stopped once the UTS was reached, i.e., at $\varepsilon_p = 18\%$. Figure 4.6 exhibits a similar trend than that found in Figure 4.5b by Prevéy (2000), i.e., exponential increase followed by a linear portion, allowing the use of Equation (4.1) to extrapolate the $FWHM$ values at higher cold work values ε_p. The fitting coefficients are presented in the figure. The scattering of the $FWHM$ values is found to increase with the increase of true plastic strain, leading to possible errors. The maximum SD of the three measurement is 0.07° at $\varepsilon_p = 18\%$. The calibration curve can then be used to estimate the cold work profiles induced by the two shot peening conditions. The independence of the $FWHM$ values from elastic loadings is shown in Appendix IX, where the XRD measurements were performed while the specimen was under controlled elastic load.

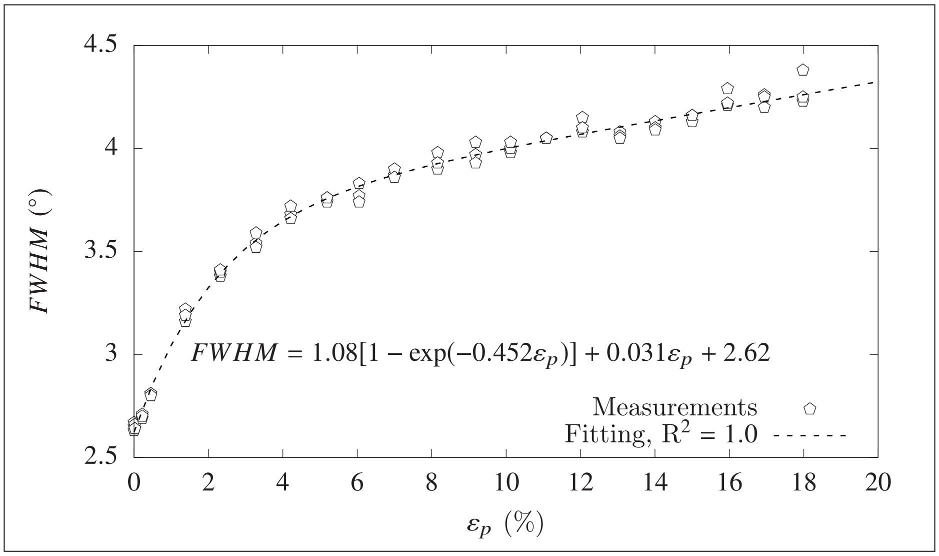

Figure 4.6 Calibration curve for the cold work estimation of IN718

4.1.3.3 Cold work profiles of shot peened IN718

The in-depth cold work profiles are presented for the 4 A and 8 A specimens in Figure 4.7. The estimations were performed using the FWHM profiles (Figure 4.3) and the calibration curve (Figure 4.6). The surface values of cold work are found to be the maximum values: 44% and 56% for the 4 A and 8 A specimens, respectively. The cold work values exhibit an exponential decreasing trend, which can be fitted as

$$\varepsilon_p = a \exp(-bx) \tag{4.2}$$

where x is the depth and a and b are fitting coefficients. From the fittings, it is found that the cold work reach 0.2% plastic deformation at about 95 µm and 150 µm for the 4 A and 8 A specimens, respectively.

The presented cold work values are average values computed from the average $FWHM$ values. However the cold work could be computed for the 500 $FWHM$ values obtained for a given XRD measurement to observe its variations. Using the data set of Figure 4.4, it can be observed that cold work values range from 4% to 128%, for this surface measurement. By excluding the extreme variations of the $FWHM$ values around $\alpha = 35°$ and $\alpha = 187°$, the interval is reduced to 27% to 82%.

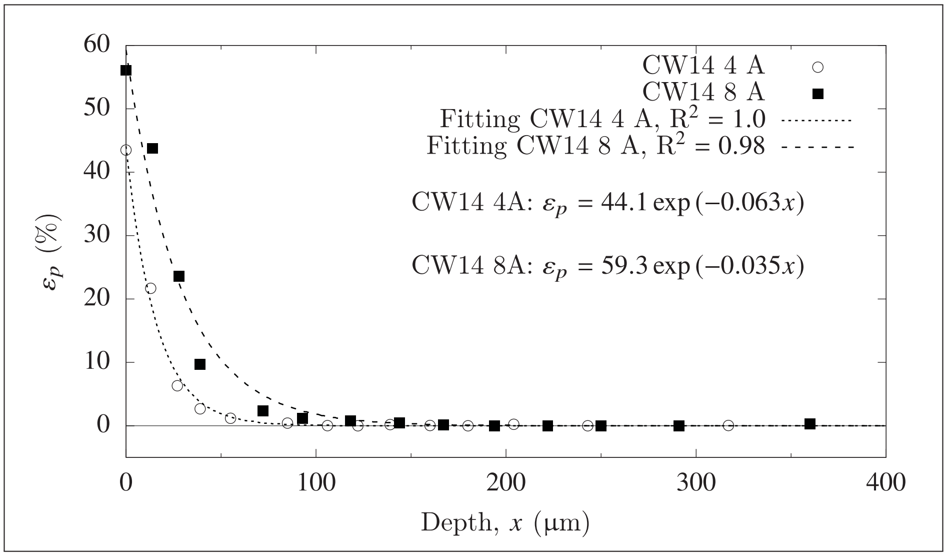

Figure 4.7 In-depth cold work profiles for the 4 A and 8 A specimens

4.1.3.4 Potential use of the cold work profiles

For this research project, the cold work profiles were used in Klotz *et al.* (2018b) to compute the evolution of yield strength as a function of the depth below the shot peened surface using the true stress versus plastic strain curve of the material.

Figure 4.8 presents the experimental true stress versus plastic strain curve obtained for the studied IN718 (Klotz *et al.*, 2018b) and fitted by the Chaboche's constitutive equation (Chaboche & Rousselier, 1983),

$$\sigma_{true}(\varepsilon_p) = a_1 \left[1 - \exp\left(-b_1\varepsilon_p\right)\right] + a_2 \left[1 - \exp\left(-b_2\varepsilon_p\right)\right] + \sigma_{y0.05\%} \tag{4.3}$$

where $\sigma_{y0.05\%}$ is the 0.05% offset yield strength, a_1, a_2, b_1, and b_2 are fitting coefficients. The 0.05% offset yield strength ($\sigma_{y0.05\%}$ = 1074 MPa) was preferred to the commonly used 0.2% offset yield strength ($\sigma_{y0.2\%}$ = 1156 MPa) to better capture the residual stress redistri-

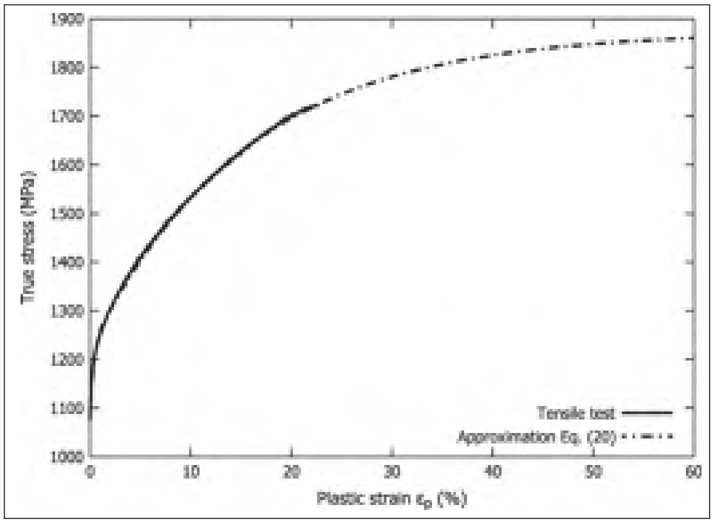

Figure 4.8 Experimental true stress vs. plastic strain curve and its fitting. Eq. (20) corresponds to Equation (4.3) in the present document. Reprinted from Klotz *et al.* (2018b) with permission

bution modeled by Klotz *et al.* (2018b). Equation (4.3) allows extrapolating data for higher deformations than those produced by tensile testing. The fitting coefficients are presented in Table 4.1.

Table 4.1 Fitting coefficients of Equation (4.3). Reproduced from Klotz *et al.* (2018b) with permission

a_1 (MPa)	a_2 (MPa)	b_1	b_2
147.5	652.0	324.28	6.49

Using the cold work profiles determined by XRD (Figure 4.7), the in-depth yield strength profiles can be estimated thanks to Equation (4.3) and the fitting coefficients obtained for the true stress versus plastic strain curve (listed in Table 4.1). The yield strength profiles estimated for the 4 A and 8 A specimens are presented in Figure 4.9. The profiles exhibit similar trends than the cold work profiles, as they are computed from them. It can be observed that the plastic deformation induced by shot peening (Figure 4.7) allows increasing significantly the yield strength of the layers below the shot peened surface. The 0.2% offset yield strength of the initial material ($\sigma_{y0.2\%}$ = 1156 MPa) is reached at 85 µm and 163 µm deep for the 4 A and 8 A specimens, respectively. The yield strength profiles were used in a modified Navarro and de los Rios crack propagation model to predict the propagation of cracks in shot peened specimens by Klotz *et al.* (2018b).

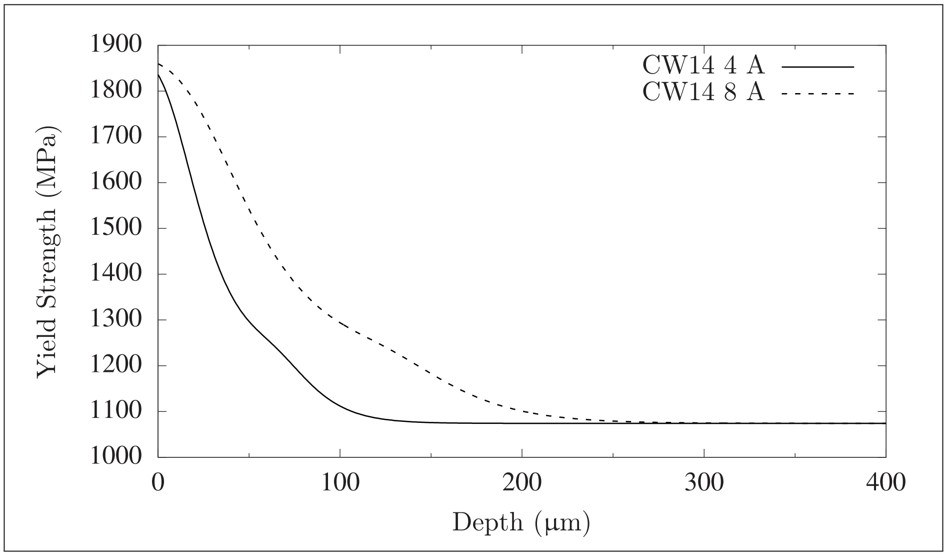

Figure 4.9 In-depth yield strength profiles for the 4 A and 8 A specimens

4.1.4 Microhardness profiles

The microhardness profiles were determined for comparison with the cold work profiles obtained via XRD, as both provide information on the plastic deformation. The microhardness profiles were determined using a Vickers indenter and a 100 gf load on the section of the 4 A and 8 A specimens following the measurements details given in Section 2.4. They are presented in Figures 4.10a and 4.10b, respectively. Each figure is composed of five measurement profiles. The points are not aligned for a given depth because of the difficulties to be exactly at the same depth when starting a profile measurement. This is especially difficult for indented surfaces, such as the ones produced by shot peening. The two shot peening conditions exhibit a noisy exponential decreasing hardness as the depth increases. For both specimens, the microhardness values are scattered, yielding low coefficients of determination R^2. Nonetheless, the fitting curves describe adequately the trend of the profiles. From the fitting, an equivalent microhardness of 481 $\mathrm{HV}_{100\mathrm{gf}}$ is found for the stabilized values. For the first measurements, at about 20 µm below the surface, the average microhardness is found to be 516 $\mathrm{HV}_{100\mathrm{gf}}$ and 548 $\mathrm{HV}_{100\mathrm{gf}}$ for the 4 A and 8 A specimens, respectively. By considering the stabilized hardness value (i.e., 481 $\mathrm{HV}_{100\mathrm{gf}}$) plus the SD of the hardnesses below a depth of 200 µm (i.e., 10 $\mathrm{HV}_{100\mathrm{gf}}$), the affected zones extend to about 70 µm and 150 µm, for the 4 A and 8 A specimens, respectively.

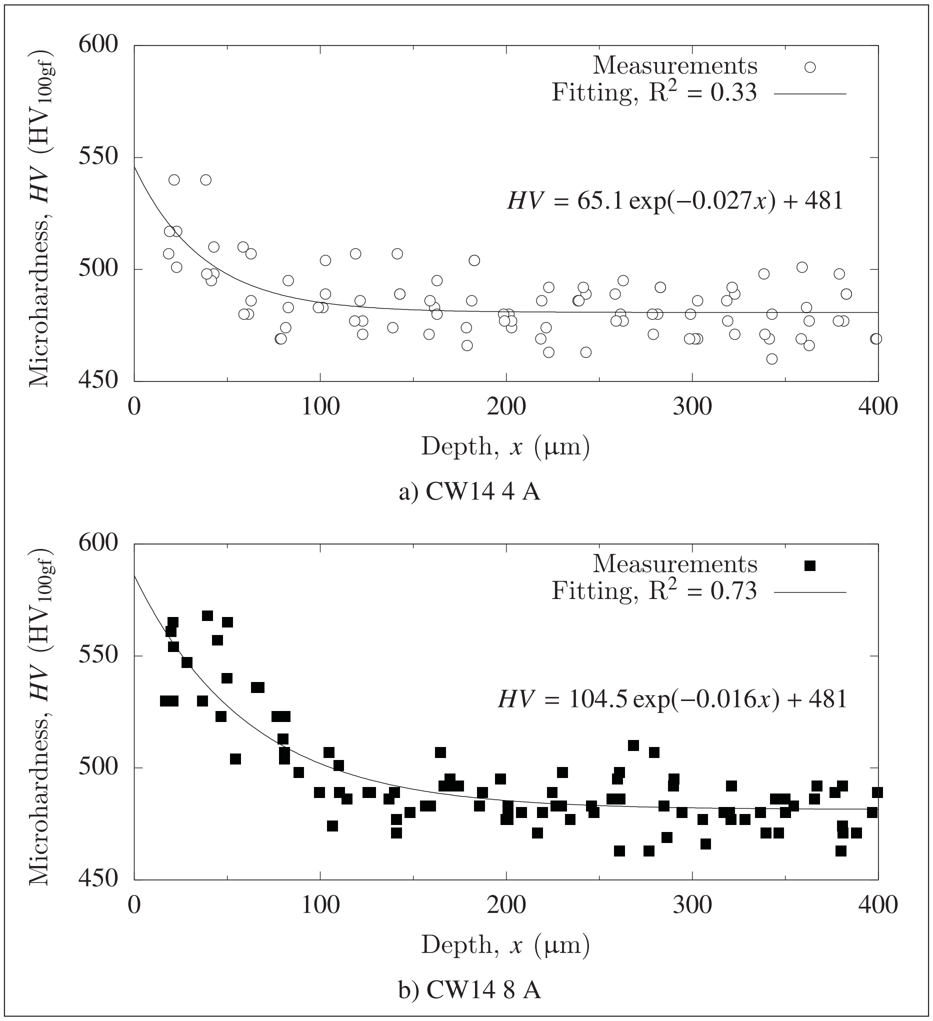

Figure 4.10 In-depth microhardness profiles for the IN718 specimens shot peened at an intensity of a) 4 A and b) 8 A. Five measurement profiles are presented per specimen, along with the corresponding fitting curve

The near surface values were taken at about 20 μm below the surface ($\approx 1.1d_{HV}$), which is lower than the $2.5d_{HV}$ value recommended by the ASTM E384-17 (2017) standard and used to prevent edge effects leading to a smaller microhardness value. However, following the standard would have led to a starting point 50 μm below the shot peened surface and most of the hardness gradient would have been missed. Decreasing the load, leading to a smaller indent and shorter distances, results in high hardness variations and incoherent results. Therefore, the 100 gf load was kept and care was taken to keep only symmetrical indents (no indent with a larger diagonal in the direction perpendicular to the shot peened surface). As it is not the case, it proves that the near surface material was subjected to strain-hardening.

Hardness can empirically be correlated to yield strength (Cahoon *et al.*, 1971; Pawade *et al.*, 2008). However, as the microhardness technique does not allow capturing surface and near surface strain-hardening, the determination of the in-depth yield strength profile, as with XRD measurements, is impossible.

4.1.5 Discussion on the cold work affected zone and its measurement

For a given shot peening intensity, the depth affected by cold work was found to be smaller than the one affected by residual stresses. Furthermore, due to the high sensitivity of the FWHM to low strain, as seen in the shape of the calibration curve in Figure 4.6 (i.e., exponential increase of $FWHM$ at low ε_p values), the depth at which 0% of cold work is reached is over estimated if one consider that it is evaluated by the depth at which the FWHM profile returns to a quasi-constant value (compare Figures 4.3 and 4.7). Consequently, the cold work affected depth should not be evaluated from the FWHM vs. depth graph, as it is often done in the literature (Zinn & Scholtes, 2005; Hoffmeister *et al.*, 2008; Gariépy *et al.*, 2013; Heydari Astaraee *et al.*, 2017).

For the highest shot peening intensity (8 A), the depth affected by cold work (150 μm) was found to be the same for an estimation with the use of the $FWHM$ values and microhardness testing. However, for the lowest intensity (4 A), the affected depth was found to be 95 μm using the $FWHM$ values and 70 μm by microhardness testing. This difference can be explain by a larger variation of the microhardness measurements for the 4 A specimen than for the 8 A specimen, which yields a much lower coefficient of determination ($R^2 = 0.33$).

The cold work affected depth estimated in this project for the 8 A specimen (150 μm) is identical to the one found by Prevéy (2000) for a sample shot peened at 8 A for 200% coverage. However, a higher cold work surface value (56%) than that found by Prevéy (2000) (40%) was estimated. The difference can be due to the use of a different shot peening media (not specified in Prevéy (2000)) or, as mentioned before, to the possible error induced by the calibration curve at high cold work value.

A potential use of the cold work profile, determined using the FWHM profile, is the estimation of yield strength variations below the surface using Chaboche's constitutive equation. The yield strength estimations can then be used in FE model to predict residual stress relaxation which can then be used to better predict fatigue life, as performed by my colleague and published in (Klotz *et al.*, 2018b). The residual stress relaxation was measured for two fatigue loading conditions (σ = 1100 MPa and 1370 MPa) at a stress ratio $R = 0.1$ and for the specimen's geometry presented in Figure 4.1 (the residual stress relaxation profiles are not presented here, but in Appendix VII) to fit the FE model. Fatigue life prediction was performed by coupling Navarro and de los Rios crack propagation model (Navarro & de los Rios, 1988; Navarro & de Los Rios, 1988) with Chan's crack initiation model (Chan, 2003). The crack propagation model was modified to consider residual stress and cold work profiles in the computation of the crack closure. Residual stresses were also added to the initiation model. Predictions were compared to fatigue testing results for cylindrical specimens. Fatigue lives were predicted with a maximum of ±15% error with respect to the average experimental results (Klotz *et al.*, 2018b).

4.2 Determination of cold work profiles for the AA7050 specimens

The second part of this chapter determines and compares the cold work profile of two shot peened AA7050 specimens. This section is divided in four subsections: i) the study implementation, the determination of ii) the residual stress and FWHM profiles, iii) the resulting cold work profiles, and iv) the microhardness profiles. This section is concluded by the interpretation and discussion of the results.

4.2.1 Implementation of the study

The specimen's geometry, used for the determination of the residual stress and FWHM profiles, is presented in Figure 4.11. This specimen's geometry was used for the determination of residual stress relaxation and to observe the emergence of surface crack using the replication technique (Bianchetti *et al.*, 2018). Two shot peening conditions were tested through the use of two media: S230 and Z425 (media properties are presented in Table 2.5). Shot peening was performed at an intensity of 8 A for a 100% coverage. Residual stress were measured using the Pulstec μ-X360n and the measurement conditions listed in Tables 2.6 and 2.7. A 2 mm collimator was used for the XRD measurements because the grains were large (see Figure 2.3) and, thus, not enough were in a favorable orientation for diffraction.

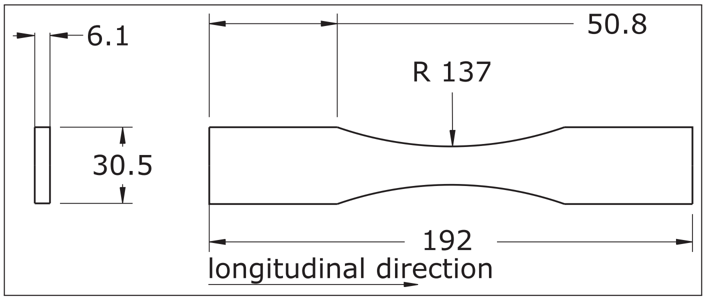

Figure 4.11 Geometry of the rectangular AA7050 specimen used for the residual stress relaxation measurements. All dimensions are in mm. Reprinted from Bianchetti *et al.* (2018) with permission

4.2.2 Residual stress and FWHM profiles for two shot peened AA7050 specimens

The residual stress and FWHM profiles obtained for the Z425 and S230 specimens are presented in Figure 4.12. The presented values are the average of three measurements. The errorbars, representing the average of the three XRD-measurement errors, are presented for the residual stress measurements. The standard deviation of the residual stress and FWHM measurements are found to be on average 8 MPa and 0.02°, respectively. The two specimens exhibit a similar surface residual stress with -228 MPa and -217 MPa for the specimens treated with Z425 and S230 media, respectively. Both specimens exhibit their maximum compressive residual stress at a depth of about 72µm and a similar residual stress affected zone affected zone (230µm). The maximum compressive residual stress of -353 MPa is found for the Z425 specimen, whereas the S230 specimen exhibits a maximum compressive residual stress of -280 MPa. No distinct tensile peak can be observed. Regarding FWHM profiles, an identical peak width is found at the surface of the two specimens and the *FWHM* values decrease gradually toward a constant value of 1.98°. This constant value is first found at about 250 µm. An example of the *FWHM*-variations for a given XRD measurement on the S230 specimen is presented in Appendix VIII.

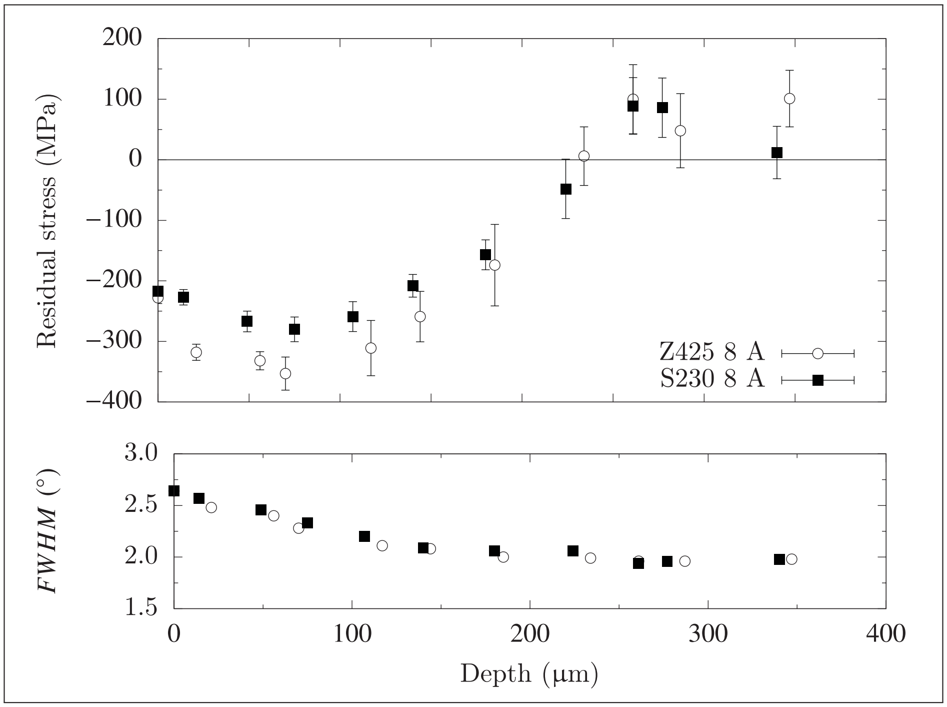

Figure 4.12 Residual stress (top) and FWHM (bottom) profiles for AA7050 specimens shot peened at an intensity of 8 A with Z425 and S230 media

4.2.3 Estimation of cold work profiles

The calibration curve for AA7050 is presented, along with the estimated cold work profiles.

4.2.3.1 Calibration curve of AA7050: $FWHM$ vs. ε_p

The calibration curve for AA7050 was obtained at 0 MPa true isostress (unloaded specimen) and following the experiment conditions listed in Section 2.6. The calibration curve ($FWHM$ vs. ε_p) is presented in Figure 4.13. XRD measurements were performed up to material's UTS ($\varepsilon_p = 5.5\%$). The measurement points are fitted using Equation (4.1) and fitting coefficients are presented in Figure 4.13. The standard deviation of the three measurements do not exceed 0.01°. An exponentially increasing trend followed by a linear trend can be observed and Equation 4.1 fits well the data. It can also be observed that the variations of the $FWHM$ values occur on a much smaller range (less than 1°, i.e., about 25% of its initial value) for the AA7050.

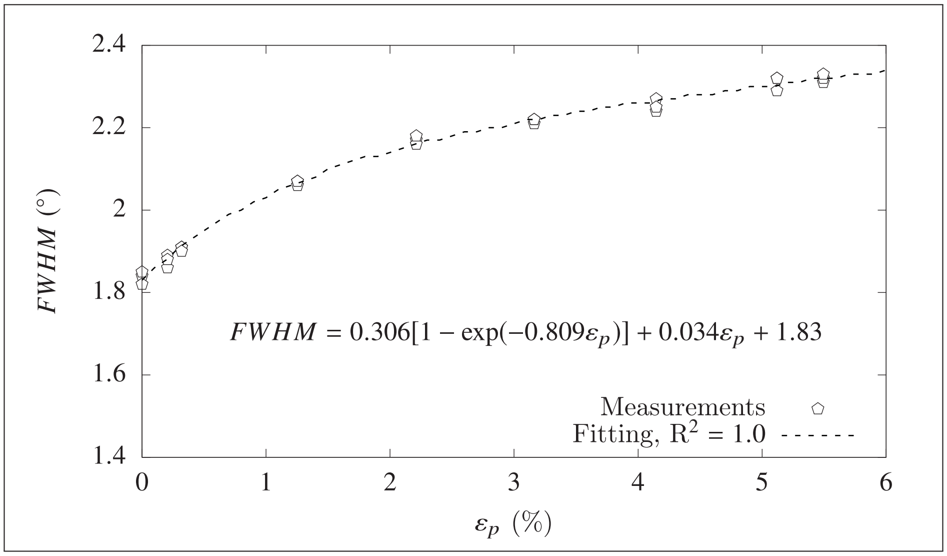

Figure 4.13 Calibration curve for the cold work estimation of AA7050 at 0 MPa true isostress

4.2.3.2 Cold work profiles of shot peened AA7050

Computed from the FWHM profiles (Figure 4.12) and the calibration curve (Figure 4.13), the in-depth cold work profiles are presented in Figure 4.14 for the Z425 and S230 specimens. The errorbars are not presented as the widest 95% confidence interval is ±2% and would not be visible. The two specimens exhibit a similar behavior which can be fitted by an exponential function as shown in Figure 4.14. A maximum cold work value of 15% is found at the surface of both specimens. A stabilized cold work value of 0.6% is found from about 120 μm.

For the deepest cold work measurements, the values do not reach 0%. This could be due to the noise in the measurements or the existence of microstresses σ^{II} and σ^{III}, which are present to accommodate the tensile macrostresses visible in Figure 4.12.

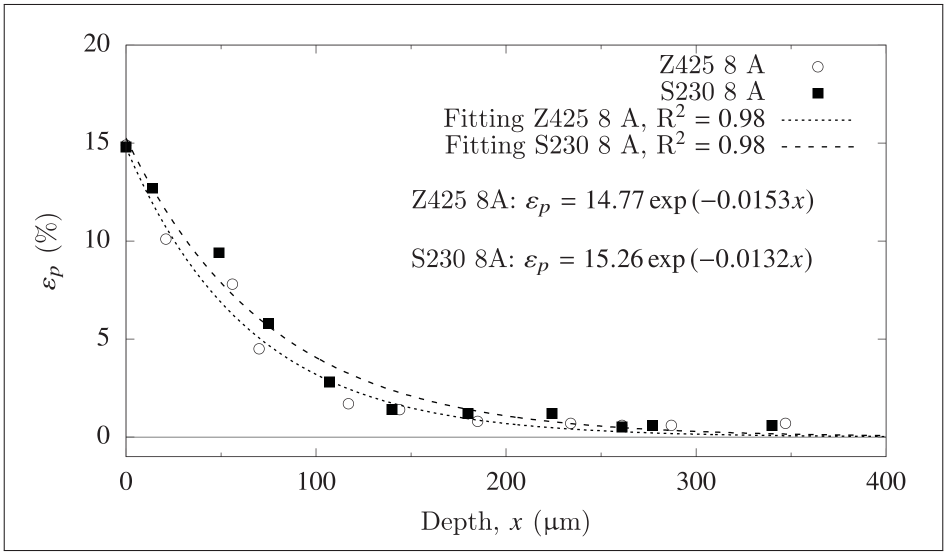

Figure 4.14 In-depth cold work profiles for the AA7050 specimens shot peened at an intensity of 8 A with Z425 and S230 media

4.2.4 Microhardness profiles

The microhardness profiles were determined using a Vickers indenter and a 25 gf load, for comparison with the cold work profiles obtained for the Z425 and S230 specimens. Results are presented in Figure 4.15a and 4.15b, respectively. The samples were cold mounted for the

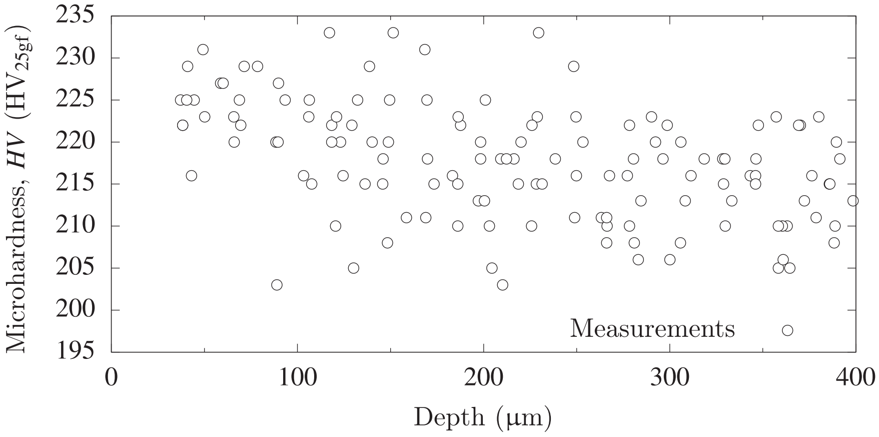

a) Z425 8 A

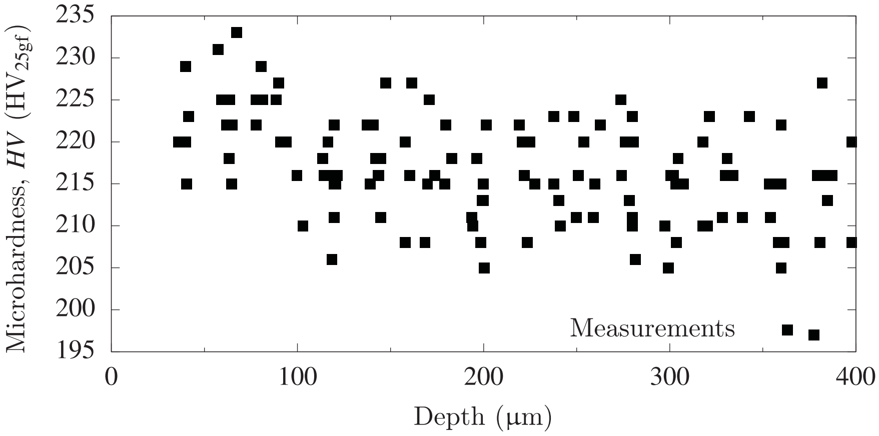

b) S230 8 A

Figure 4.15 In-depth microhardness profiles for the AA7050 specimens shot peened at a) Z425 8 A and b) S230 8 A. Ten measurement profiles are presented per specimen

materialographic preparation because the hot mounting technique led to flat microhardness profiles, even if hot mounting was performed at 150°C only. Ten measurement profiles were performed to describe the trend as the measurements are more spread than for the IN718 due to the larger size of the grains in the base material. Contrary to the IN718 microhardness measurements, only the measurements performed at $2.5d_{HV}$ below the surface were kept, due to the large scattering of the measurements. For both specimens, a slight increase of microhardness can be observed below the surface but this increase is only of the order of 15 HV_{25gf}. The affected depth is estimated to be about 150 μm. The microhardness of the base material (below the non-affected depth) exhibit an 50 HV_{25gf} offset compared to the 160 HV_{25gf} generally found for an AA7050-T7451 (ASM Aerospace Specification Metals, 2019). This offset is most likely due to a calibration issue for low loading values on the microhardness machine.

4.2.5 Discussion on the cold work affected zone and its measurement

The calibration curve obtained for the AA7050 (Figure 4.13) exhibits a trend similar to that obtained for the IN718 (Figure 4.6): Increasing the plastic deformation broadens the diffraction peak. The cold work profiles deduced for the two specimens are very similar and no difference between the two can be observed. Both specimens exhibit a surface cold work value of 15% and a 120 μm affected depth. A comparable affected depth (150 μm) is found with the microhardness measurements. On the contrary, the residual stress profile generated by the Z425 media exhibits a significantly higher maximum compressive residual stress than the S230 media a the same shot peening intensity.

In the case of aluminum, the use of the $FWHM$ values from the XRD measurements is more suitable than the microhardness testing to evaluate the cold work affected depth introduced by shot peening.

4.3 Determination of cold work profiles for the 300M steel specimens

The third part of this chapter aims to determine the cold work profile of two shot peened 300M specimens and explains the unconventional subsurface behavior observed in this particular case. This section is divided in four subsections: i) the study implementation, the determination of ii) the residual stress and FWHM profiles, iii) the resulting cold work profiles, and iv) of the microhardness profiles. This section is concluded by the interpretation and discussion of the results.

4.3.1 Implementation of the study

The residual stresses and FWHM profiles were determined for flat specimens using the Pulstec μ-X360n apparatus. The specimens were shot peened with CW14 and S230 media (media information are presented in Table 2.5) at an intensity of 8 A with a coverage of 100%. The geometry of the specimens, designed to study the residual stress relaxation when subjected to uniaxial fatigue testing, is presented in Figure 4.16. The in-depth profiles were obtained by electropolishing a 7×7 mm pocket at the specimens' surface. Results were also used in Bag *et al.* (2019) to describe the shot peening treatments of fatigue specimens tested at $R = -1$ (tension/compression). It was found that shot peening had no significant effect on the fatigue performances as they were driven by the presence of non-metallic inclusions within the material.

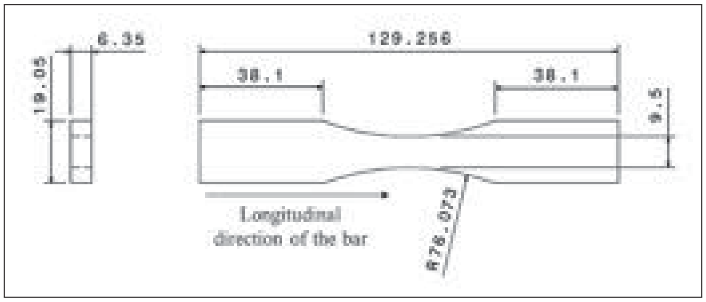

Figure 4.16 Geometry of the fatigue 300M specimen. All dimensions are in mm. Reprinted from Bag *et al.* (2019)

4.3.2 Residual stress and FWHM profiles for two shot peened 300M specimens

The residual stress and FWHM profiles obtained for the CW14 and S230 specimens are presented in Figure 4.17. The values are the average of three measurements. The errorbars, representing the average of the three XRD-measurement errors, are only presented for the residual stress measurements as the standard deviation of the measurements is found to be on average 6 MPa whereas the $FWHM$ one is very small at 0.01°. The two specimens exhibit a similar surface residual stress with -1044 MPa and -1086 MPa for the CW14 and S230 specimens, respectively. Both media allow reaching a maximum compressive residual stress of -1170 MPa at about 30 μm below the surface. The depth affected by residual stresses is found to be smaller for the CW14 specimen (about 134 μm) than for the S230 specimen (about 146 μm). Regarding the FWHM profiles, the two specimens exhibit the same trend: a lower value at the surface than at the center and a minimum value just below the surface. This trend differs from those previously observed for the IN718 and AA7050 specimens. The CW14 specimen exhibits a higher surface $FWHM$ value and a lower minimum $FWHM$ value than the S230 specimen. The two specimens present different $FWHM$ values at the core of the material (5.83° and 5.97° for the CW14 and S230, respectively) but this difference is negligible. An example of the $FWHM$-variations for a given XRD measurement on the CW14 specimen is presented in Appendix VIII.

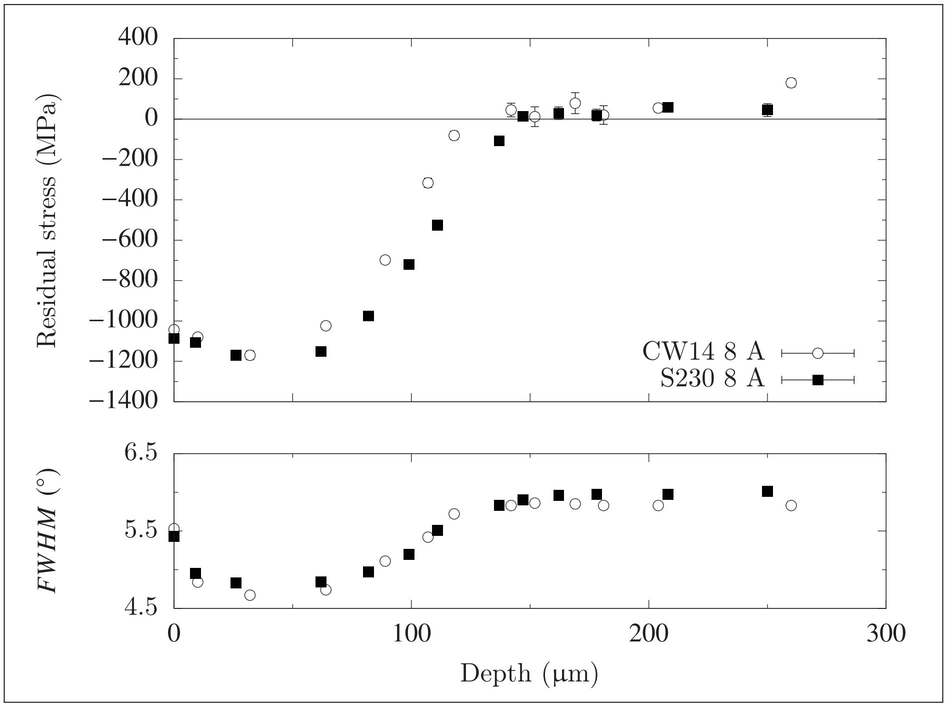

Figure 4.17 Residual stress (top) and FWHM (bottom) profiles for fatigue 300M specimens shot peened at an intensity of 8 A with CW14 and S230 media

4.3.3 Estimation of cold work profiles

The calibration curve for 300M steel is presented, along with the estimated cold work profiles.

4.3.3.1 Calibration curve of 300M: $FWHM$ vs. ε_p

The calibration curve for the 300M steel was obtained at 0 MPa true isostress (unloaded specimen) and following the experiment conditions listed in Section 2.6. The calibration curve ($FWHM$ vs. ε_p) is presented in Figure 4.18. The measurement points are well fitted using Equation (4.1) with $R^2 = 0.99$ but the peak width narrowing during deformation suggests a paradoxical work softening. It is most likely due to the rearrangement of the dislocations present in the material caused by the movement of new dislocations. A reverse trend can be observed compared to the previous materials an exponential decay followed by a linear decay. This means that the diffraction peak narrows with the increase of plastic deformation. It can also be observed that the $FWHM$ variation occurs on a small range (less than 1°, i.e., less than 20% from its initial value).

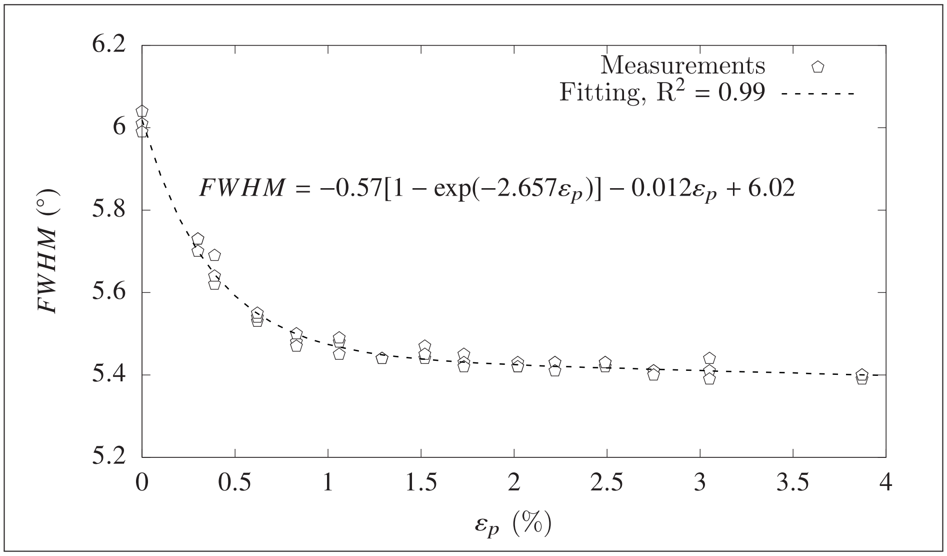

Figure 4.18 Calibration curve for the cold work estimation of 300M at 0 MPa true isostress

4.3.3.2 Cold work profiles of shot peened 300M

The in-depth cold work profiles, computed from the FWHM profiles (Figure 4.17) and the calibration curve (Figure 4.18), are presented in Figure 4.19 for the CW14 and S230 specimens.

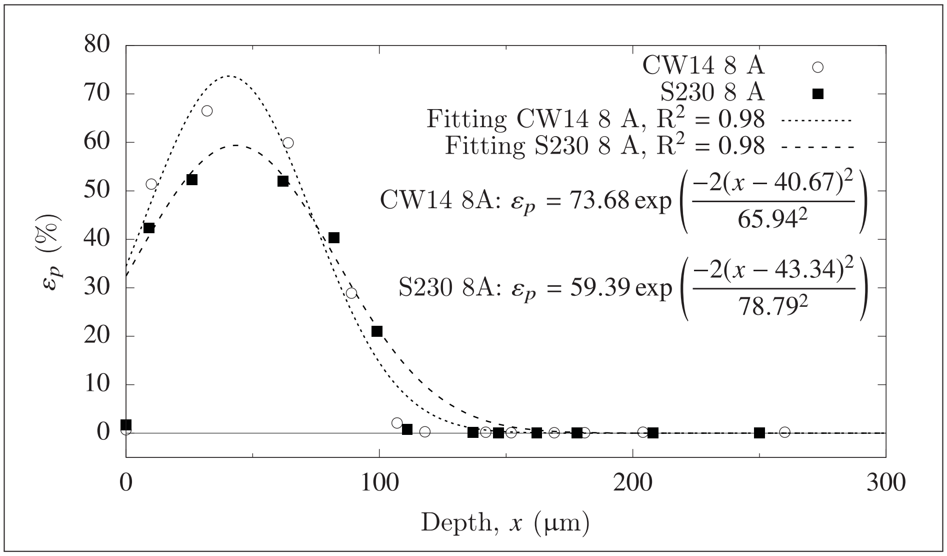

Figure 4.19 In-depth cold work profiles for the 300M specimens shot peened at an intensity of 8 A with CW14 and S230 media

The errorbars are not presented as the widest 95% confidence intervals are ±3% and would not be visible. The two specimens exhibit the same trend but the intensity of cold work differs: values of 0.7% and 1.7% are found at the shot peened surfaces of the CW14 and S230 specimens, respectively, whereas a maximum cold work value is found beneath the shot peened surface (67% and 52%, respectively). The maximum cold work values are found at about 30 μm below the surface and the cold works values reach a plateau of 0.2% plastic deformation, or below, after about 140 μm, but a drastic variation in measured strain amount can be observed at about 110 μm below the surface for both specimens.

The cold work values can be fitted via the following equation

$$\varepsilon_p = a \exp\left(\frac{-2(x-b)^2}{c^2}\right) + d \tag{4.4}$$

where a, b, c, and d are fitting coefficients. a corresponds to the maximum cold work value, b to the depth of the maximum cold work value, c to the width of the peak, and d to the bulk cold work value (taken as 0). The first point of each profile was discarded for fitting and reasons are provided in Section 4.3.6. Equation 4.4 does not allow capturing the drastic variation in cold work amount. The fittings provide the maximum cold work values of 74% and 59% found at 41 μm and 43 μm for the CW14 and the S230 specimens, respectively.

4.3.4 Microhardness profiles

The microhardness profiles were determined for comparison with the cold work profiles. The microhardness profiles were determined on the section of the CW14 and S230 specimens using a Knoop indenter and a 200 gf load. The elongated mark left by the indenter allows measuring the microhardness near the shot peened surface. Microhardness profiles were determined following the measurements conditions given in Section 2.4, and are presented for the CW14 and S230 specimens in Figures 4.20a and 4.20b, respectively. Each figure is composed of ten measurement profiles to fully capture the microhardness trends and shows significant variations from one position to the next. The two profiles exhibit a similar trend: the closer to the surface the lower the microhardness values. The microhardness values reach quasi-constant values of 649 HK_{200gf} and 639 HK_{200gf} at a depth of 120 μm and below for the CW14 and S230 specimens, respectively. The expected hardness value for an untreated 300M steel, corresponding to center values of the shot peened specimens, is 54 HRC or 605-620 HK_{500gf} (Chandler, 1995a). The difference can be partly explained by the use of a lower loading.

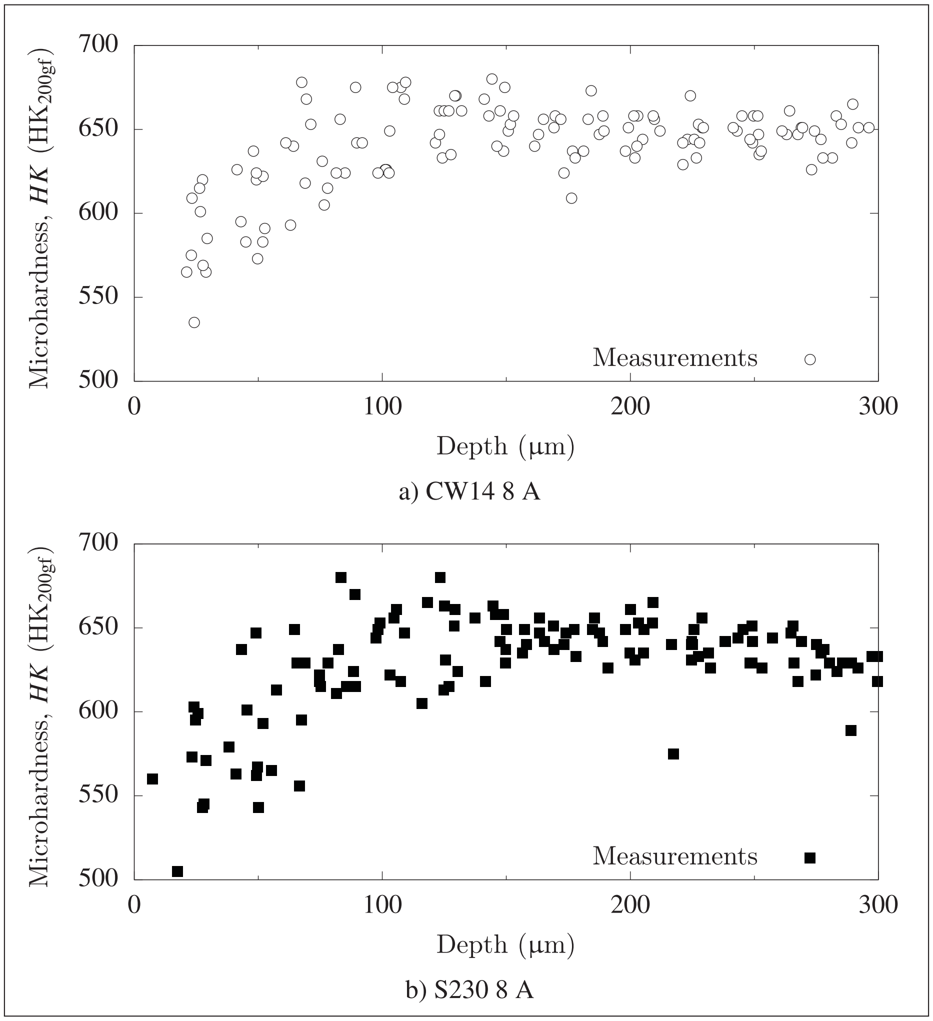

a) CW14 8 A

b) S230 8 A

Figure 4.20 In-depth microhardness profiles for the 300M specimens shot peened at a) CW14 8 A and b) S230 8 A. Ten measurement profiles are presented per specimen

4.3.5 Evolution of the microstructure below the shot peened surface

The evolution of the microstructure below the shot peened surface was investigated for the CW14 specimen to better explain the sub-surface trends observed for the FWHM (Figure 4.17) and ε_p (Figure 4.19) profiles.

The microstructure was first revealed using Vilella's reagent, observed using a confocal microscope, and is presented in Figure 4.21. The sample was mounted to prevent edge rounding

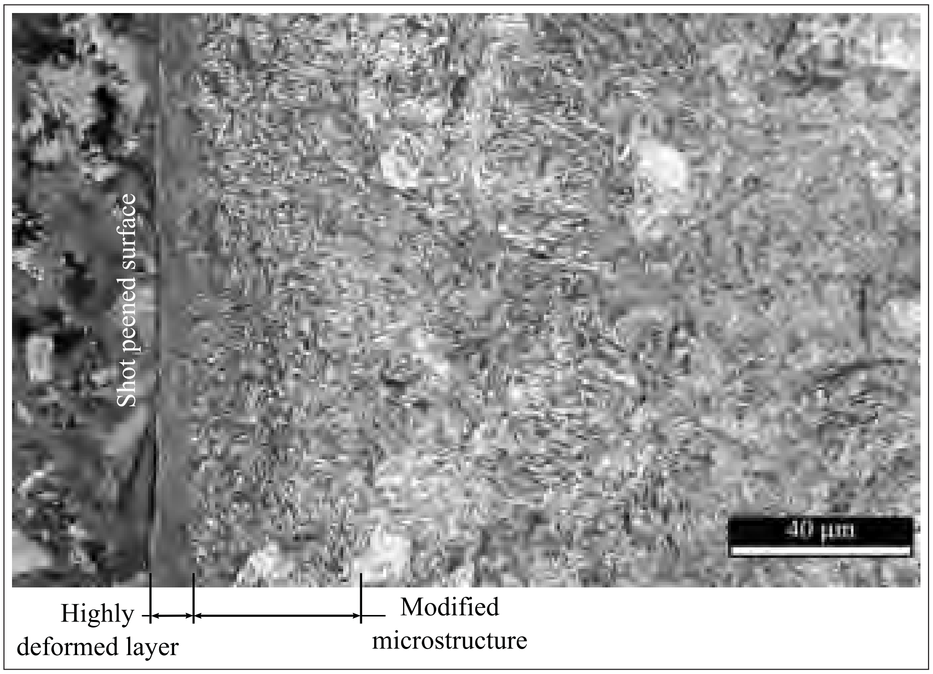

Figure 4.21 Optical micrograph of the CW14 specimen cross-section. Microstructure is revealed using Vilella's reagent. The RD is perpendicular to the micrograph

during the sample preparation. The shot peened surface is visible on the left of the micrograph and the sample RD is perpendicular to the micrograph. A highly deformed layer of 6 to 8 µm can be observed below the shot peened surface, followed by a modified microstructure over a layer of about 40 µm, where the long laths of martensite, typical of the core microstructure, are not present. Deeper (on the right of the micrograph), the observed microstructure is similar to the tempered martensite found in Figure 2.1a for the bulk material.

An EBSD scan was performed on the same sample to characterize the grain size below the shot peened surface and to estimate the local misorientation. The same sample orientation as Figure 4.21 was kept. The scan was performed on a 93×63 μm^2 area using a 0.15 µm step size. Only the martensite phase (BCC structure, a = 2.866 Å) was indexed. The post-treatment was realized using MATLAB and the MTEX open source package (Bachmann *et al.*, 2011). 18830 grains were detected using a grain detection angle of 10°. The orientation map is presented in Figure 4.22 with colors corresponding to the IPF with respect to the RD. Two prior austenite

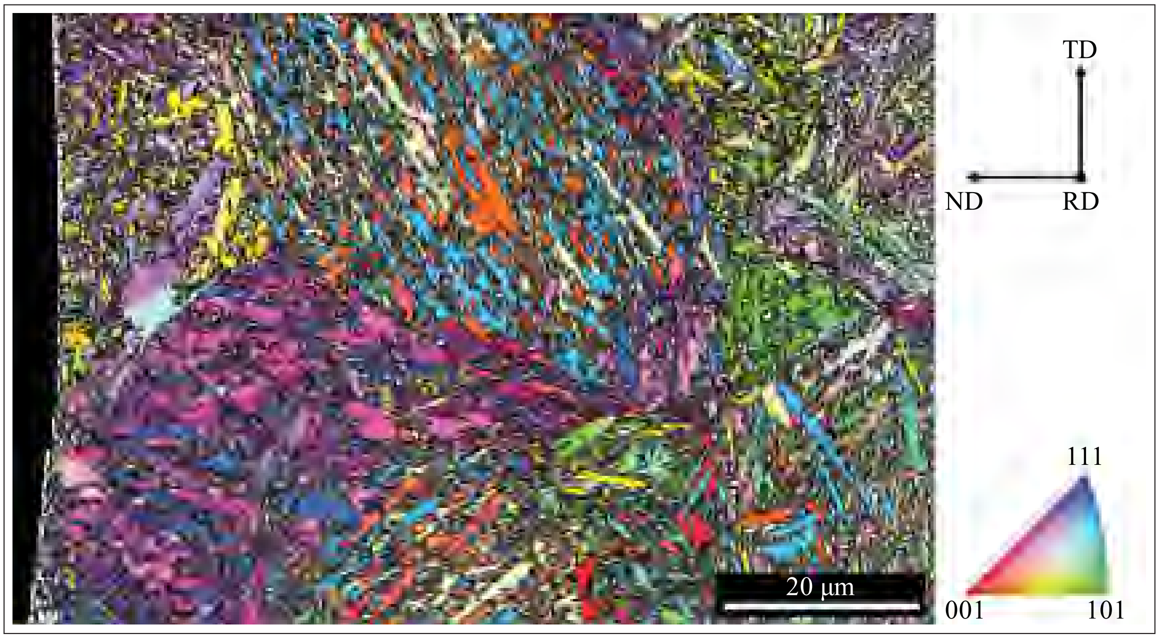

Figure 4.22 Orientation map of the subsurface of the CW14 specimen represented as IPF map with respect to the RD

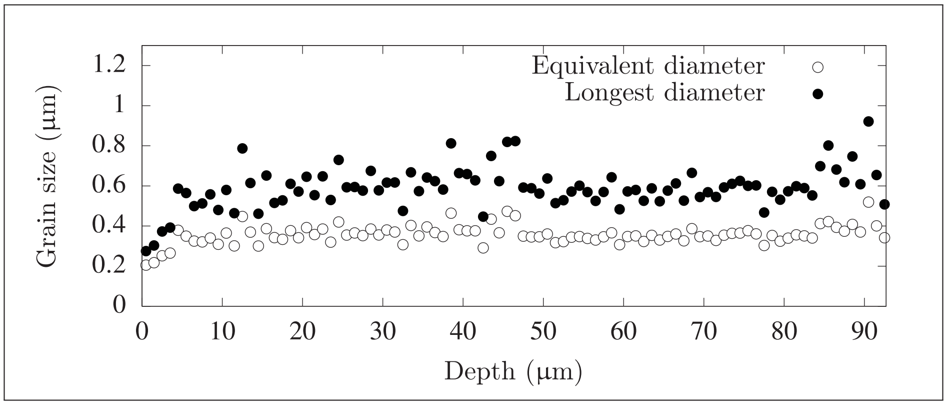

Figure 4.23 Evolution of the average grain size from the shot peened surface. The equivalent diameter is computed from the grain's area, whereas the longest diameter corresponds to the longest distance between any two vertices of the grain boundary

grains can easily be identified with their laths and plates of martensite oriented in the same direction, i.e., similar colors (the first prior austenite grain is composed of dark blue and purple laths and plates, and the second is mainly composed of light blue and orange features). It can be observed that the subsurface layer is different and composed of finer grains than the rest of the map. The average grain size was calculated using two different manners and results are presented in Figure 4.23. The equivalent diameter $\varnothing_{eq}$, which takes into account the scare root of the grain's area, was first considered. The longest distance between any two vertices of a given grain was also considered to better capture the elongated shape of the grains. The average grain size as a function of the depth was calculated for gains whose barycenter was laying in 1 µm thick bands starting from the shot peened surface. Both calculation methods reveal that the first 4 µm exhibit a lower average grain size than the rest of the map, about half the average grain size seen in the rest of the scanned region.

The EBSD data were also used to investigate the cold work affected depth using the kernel average misorientation (KAM), which is the average misorientation angle of a given point with respect to all its neighbors of a given order (Moussa *et al.*, 2015). The values were computed using the MTEX open source package. An upper threshold angle of 10° was considered, meaning that data points with greater KAM values were not considered as they may correspond to regions of another grain. For the same reason, only the first order of neighbors was taken into account in the calculation. The corresponding KAM map is presented in Figure 4.24 along with the graph presenting the average KAM values for a given depth from the shot peened surface. The color bar upper limit was fixed to 5° because despite the 10° threshold angle most of the KAM values are ranged from 0° to 5°. The KAM values were found to be higher near the shot peened surface than deeper in the material (zones I and II). After 35 µm below the surface (zone III), the KAM values decrease toward a quasi constant value of 1.06°. This quasi-constant value was also found for an EBSD map realized at the sample's center (presented in Appendix X), i.e., far from the shot peened surface.

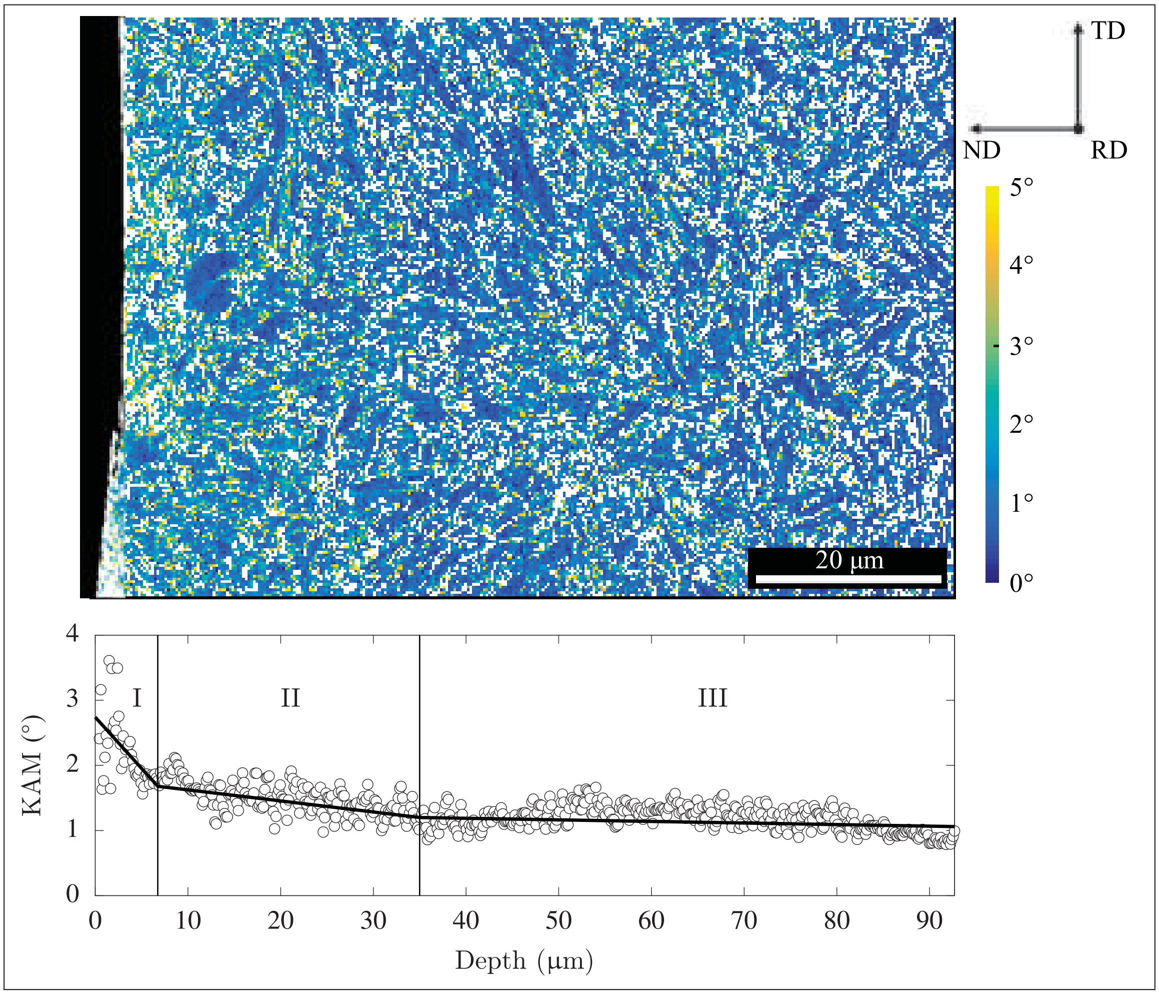

Figure 4.24 Kernel average misorientation (KAM) map computed for the 1^{st} neighbor order and a 10° threshold angle and evolution of the average KAM values for a given depth

4.3.6 Discussion on the cold work affected zone and its measurement

The FWHM profiles obtained for the CW14 and S230 specimens exhibit lower $FWHM$ values at the surface and subsurface than at the center of the specimens, with the lowest value observed at a depth of about 50 μm. The trend obtained in this study is similar to the one obtained by Llaneza & Belzunce (2015) for an AISI 4340 heat treated (quenched and tempered at 200°C, yielding $\sigma_{y0.2\%}$ = 1604 MPa, σ_u = 2057 MPa, and HRC = 52 HRC) and shot peened (14 A to 21 A at 100% coverage) with similar conditions. The peak width narrowing may suggest a work softening near the shot peened surface.

The calibration curve obtained for 300M, which exhibits a different trend than those obtained for IN718 and AA7050, shows that the addition of further plastic deformation narrows the peak width. However, the cold work profiles (Figure 4.18) estimated from the FWHM profiles and the calibration curve are complex and present a subsurface maximum. A zero cold work value was found at the surface for both shot peening conditions, which is not realistic. The optical micrograph (Figure 4.21) and the EBSD map of the CW14 specimen (Figure 4.22) provide an explanation for this unexpected value. In fact, the microstructure of the 4 μm thick highly deformed layer (which is in the range of the effective X-ray penetration depth of a surface measurement) is composed of a majority of nanometric size crystallites (200 nm). The nanometric crystallites are known to increase the peak width (Warren, 1990). The nanostructures generated by intense peening has compensated the reduction of the diffraction peak width due to the work hardening, hence the higher $FWHM$ value found at the peened surface than below. Consequently, the effect of the nanostructures on the peak width should be separated to the contribution to the peak broadening for the XRD surface measurements to be used for the cold work estimation.

The modified microstructure found between 6 μm and 40 μm via the optical micrograph observation (Figure 4.21) can be explained by the KAM map (Figure 4.24), which presents higher KAM values for the first 35 μm. The higher local misorientation reveals the presence of small subgrain structures.

For both shot peening conditions, the cold work was found to increase toward a maximum value at a depth of about 30 μm (about 42 μm considering the measurements fittings) to then decrease toward zero. The cold work profiles follow the Hertz theory with a maximum plastic deformation below the shot peened surface. A similar cold work affected depths is found between the XRD and microhardness measurements: 110 μm and 120 μm, respectively. The KAM values from the EBSD map provide a cold work affected depth of 35 μm. However, the EBSD scan was only performed up to 90 μm below the shot peened surface. This method was used by Soady *et al.* (2013), which obtained a better agreement of the estimated cold work affected depths estimated by XRD and EBSD, for a more intense shot peening treatment (intensity of 13 A and coverage of 200%).

The microhardness profiles exhibit lower microhardness values for the cold work affected layers than for the specimens' cores (Figure 4.20), which implies a work softening of these layers. The initial 300M (quenched and tempered condition) already shows a high density of dislocations, therefore such a work softening can be explained by a re-arrangement of the dislocations toward a lower-energy dislocation walls. To support this hypothesis three non-shot peened samples were heat treated for three different conditions. Two samples were tempered, one for 4 h at 306°C and one for 2 h at 405°C, denoted T1 and T2, respectively. The last sample was austenized for 25 min at 876°C then quenched in oil (denoted Q). The processes of tempering and quenching should provide samples with lower and higher dislocation densities than the base material, respectively. Microhardness and FWHM were measured and are presented in Table 4.2. Measurements were repeated five times. Knoop microhardnesses were measured for 200 gf and 500 gf loads. The measurements at 500 gf are presented as converted Rockwell hardnesses. It can be observed that the T1 condition provides equivalent microhardness and $FWHM$ averages than the base material, whereas the T2 condition exhibits a decrease of the microhardness and the $FWHM$ averages. The T1 conditions was therefore not sufficient to decrease the dislocation density. On

Table 4.2 Microhardness and $FWHM$ values for the base material and the three heat treated conditions: T1: 4 h at 306°C, T2: 2 h at 405°C, and Q: quenched. Measurements were repeated five times, the SD values are presented in parentheses along with the averages

Condition	HK ($\mathrm{HK}_{200\mathrm{gf}}$)	HRC ($\mathrm{HRC}_{500\mathrm{gf}}$)	$FWHM$(°)
Base	621 (±8)	54 (±0.3)	6.01 (±0.2)
T1	634 (±17)	54 (±0.7)	6.04 (±0.4)
T2	603 (±22)	52 (±0.5)	5.19 (±0.3)
Q	722 (±17)	59 (±1.0)	8.09 (±0.7)

the contrary, the Q condition exhibits an increase of the microhardness and the $FWHM$ average due to the increase of the dislocation density. To summarize, the 300M follows a classic change in material properties with the increase of microhardness and $FWHM$ values with the increase of dislocation density, and vice versa. Hence, the microhardness decrease at the subsurface of the shot peened samples can be explained by a re-arrangement of the dislocations toward a lower-energy dislocation walls.

4.4 Chapter conclusions

In this chapter, the residual stress and cold work profiles were assessed by XRD for the IN718, the AA7050, and the 300M steel. For all three materials, the cold work profiles were assessed by XRD via the use of calibration curves and were compared to the respective microhardness profiles. For the three materials the affected depths estimated by XRD or microhardness were found comparable.

Some remarkable points regarding the characterization techniques can be raised. The $FWHM$ values of a single X-ray exposure showed significant $FWHM$ variations in some specific regions of the Debye ring. These variations may be the result of large local heterogeneities due to significant sample's roughness or to inhomogeneous strain distribution in the grains. XRD peaks were found to be narrower (lower $FWHM$ values) for the AA7050 specimens than for the IN718 and 300M specimens. However, the range of $FWHM$ variations was much higher for IN718 than for AA7050 and 300M. The evolution of the $FWHM$ values with depth for the shot peened 300M specimens was found to differ from the shot peened AA7050 and IN718 specimens, which exhibit a similar decrease. The higher $FWHM$ values (broader peaks) found at the surface than subsurface of the shot peened 300M specimens were explained by the observation of nanocrystallites, which tend to broaden XRD peaks. Some difficulties were reported regarding the microhardness measurements due to the low load necessary to capture the microhardness profile below the shot peened surface or the sample preparation. Microhardness measurements reveal subsurface softening of the shot peened 300M steel. The softening was attributable to the re-arrangement of the dislocations toward lower-energy dislocation walls.

An EBSD scan was used to compute the KAM to evaluate the cold work affected depth for one of the 300M specimens. A four time smaller cold work affected depth was found via this technique when compared to the XRD method or to the microhardness testing. However, the EBSD scan was not performed up to the affected depths observed via the XRD method and the microhardness testing, which does not make this EBSD observation sufficient to be compared with the two other techniques.

Different behaviors were observed regarding the calibration curves needed for the estimation of cold work via the XRD method. Contrary to AA7050 and IN718 materials, for the 300M material the increase of plastic deformation was found to decrease the $FWHM$ values (narrow the peak width). The cold work profiles obtained for the three shot peened materials were slightly different. The cold work profiles of the 300M specimens exhibit a maximum value below the surface, whereas the maximum values are found at the surface for the AA7050 and IN718 specimens. This difference can be explained by the competition between the two mechanisms inducing the maximum plastic strain, discussed in Section 1.3.1: the hammering process and the Hertzian pressure. Wohlfahrt (1984) suggested that hard materials (> 600 HV) are more prone to follow the Hertz theory describing a maximum shear stress and thus maximum plastic deformation below the indented surface. With a hardness higher than 600 HV, the quenched and tempered 300M steel was found to follow the Hertz theory, whereas the AA7050 and IN718 materials, which are softer, were found to follow the hammering process, as suggested by Wohlfahrt (1984).

The three materials provide a wide range of material’s hardness allowing drawing some remarks on the effect of shot peening on the generated properties gradients:

- For a given intensity (8 A in this case), the harder the material, the higher is the estimated maximum cold work value,
- Still for a given intensity, the three different materials exhibit a similar cold work affected zone (see Figures 4.7, 4.14, and 4.19),
- And the localization (surface or subsurface) of the maximum plastic deformation is dependent on the material’s hardness.

CONCLUSIONS AND RECOMMENDATIONS

The X-ray diffraction (XRD) technique was used to measure the residual stress and cold work profiles of 300M steel, nickel-based superalloy IN718, and aluminum alloy 7050-T7451 (AA7050) materials for different shot peening conditions. Two main research axes have been considered:

- **The comparison of the $\sin^2\psi$ and $\cos\alpha$ methods for XRD residual stress measurements:**
  For the first time the $\sin^2\psi$ (two linear detectors) and $\cos\alpha$ (2D detector) methods were compared based on the identification of the diffracting grains from EBSD maps by considering the detector geometry and the calculation method of each method. The comparison performed on a homogeneous IN718 microstructure has shown that the 2D detector ($\cos\alpha$ method) allows capturing diffraction data from 1.5 times more unique grains in a single exposure than the linear detectors ($\sin^2\psi$ method) in a multitude of inclinations in the ±25° range. The comparison has also allowed revealing the "artificial" textures induced by two XRD methods. Each type of detectors induces a characteristic texture, which is even more pronounced when plotted for a given inclination β of the linear detectors and a given inclination and angle on the detector α for the 2D detector. The two methods were also compared using the X-ray elastic constant (XEC) $1/2S_2$ computed for the different sets of diffracting grains. The computed XECs vary by 7% and 9% from the average value for the linear detectors and 2D detector, respectively. When comparing the two methods for an inhomogeneous IN718 microstructure, the "artificial" textures were found to be further increased, resulting in a broader confidence interval on the standard deviation of the XECs. The effect of the grain size was also investigated in the case of an homogeneous microstructure. A quasi-constant percentage of diffracting grains was observed for the different grain sizes: 15% and 23% for the linear detectors and 2D detector, respectively. For grain sizes higher

than 60 μm, the initial α-step size (0.72°), used to describe the Debye ring (interception of the diffraction cone with the 2D detector), was found to be not large enough to have diffraction data for each α-step. This can be overcome by changing the α-step size and/or by oscillation of the 2D detector. Finally, it was observed that only a low number of grains are shared between the two methods (representing 20% and 14% of the total identified diffracting grains for the $\sin^2\psi$ and $\cos\alpha$ methods, respectively), explaining the 0.5% and 4% differences between the two methods observed experimentally for the homogeneous and inhomogeneous microstructures, respectively.

- **The use of diffraction peak width for cold work measurements:**
  The diffraction peak width was used to evaluate the cold work introduced by shot peening through the determination of calibration curves for the three materials. The full width at half the maximum (FWHM) was used to describe the diffraction peak widths measured via the 2D detector. Variations of the $FWHM$ values were observed in some regions of the Debye ring for surface X-ray measurements, which can be attributed to significant sample's roughness or to inhomogeneous strain distribution in grains. Default α-step size was used and the 500 $FWHM$ values obtained for a measurement were averaged. AA7050 specimens were exhibiting lower $FWHM$ values (narrower peaks) than the IN718 and 300M specimens. The range of $FWHM$ variations, due to shot peening, was found to be much higher for the IN718 specimens than for the AA7050 and 300M specimens. Typical FWHM profiles (highest $FWHM$ value at the surface followed by an exponential decrease toward a constant value) were observed for the shot peened AA7050 and IN78 specimens. However, a different trend of FWHM profile was observed for the shot peened 300M specimens with a surface value equivalent to the bulk value and subsurface values lower than the bulk value. A different behavior was also observed for the calibration curve of the 300M material, with a decrease of the $FWHM$ values with the increase of plastic deformation, contrary to AA7050 and IN718 materials. Softening below the shot peened surface was also observed

for the 300M specimens via microhardness measurements. The softening was attributed to the re-arrangement of dislocations toward lower-energy dislocation walls with the addition of new dislocations due to shot peening. Using the calibration curves, an increase of the cold work was found below the shot peened surface of all materials, with a maximum found at the surface for the AA7050 and IN718 materials. A thin layer formed of nanocrystallites was found just below the shot peened surface of the 300M specimens. Finally, two general remarks can be drawn: for a given shot peening intensity the three materials exhibit similar cold work affected zone; and the harder the material, the higher is the estimated maximum cold work value.

One article and two conference proceedings published as first author resulted from this Ph.D. thesis, as well as five articles and six conference proceedings published as co-author (all articles are listed in Appendix I).

Recommendations for future studies

The present work has open the way for further investigations. The following lists potential academic studies or industrial use:

- **Extend the comparison of the two XRD methods to textured materials:**

  The comparison of the $\sin^2\psi$ and $\cos\alpha$ methods using the developed script could be performed using more complex microstructures like textured ones (rolled aluminum) to observe the effects on the “artificial” texture and related errors. The computation of the elastic constant should be modified to take into consideration the texture of the material through the use of the X-ray stress factors F_{ij} (Hauk, 1997).

- **Take into consideration second order stress distribution: Part 1 - Numerical computation**

  XRD measurements provide the average residual stresses of the diffracting grains but this value can be affected by the inhomogeneous distribution of the stress in the grains of a polycrystal and differ from the macroscopic value intended to be measured. Macroscopic elastic loads could be applied to a virtual polycrystal and the stress averaged for the grains in condition for diffraction to evaluate the difference between the applied macroscopic stresses and the average of the second order stresses which are experimentally measured. The numerical estimation could be realized using a Cellular Automaton (CA) model. CA models consist of discrete mathematical descriptions of a material where the space is discretized into cells and could be used to calculate the elastic stress in each individual grains of the aggregate. This allows taking into account the neighborhood effect in polycrystal local stress and strain field (Bretin *et al.*, 2019a,b).

- **Take into consideration second order stress distribution: Part 2 - Experimental comparison**

  A comparison of the numerical computations, previously obtained, with experimental XRD measurements could be realized by pairing a diffractometer with a micro-tensile machine as it has been carried out in the present work to measure applied known stresses. However, the numerical computations should be performed for the same microstructure as for the experiments. Consequently, the microstructure of the polycrystal should be characterized in 3D, after the XRD measurements. 2D EBSD maps could be used and eventually a focused ion beam (FIB) for sequential layer ablation, or an electropolishing technique if very well mastered, to describe the 3D microstructure. This provides a method for a better understanding of the role of each diffracting grain on the residual stress value measured by XRD and the actual stress field (first order) in the material. The application to textured materials could lead to the development of new corrections.

- **Use of the variations of the maximum penetration depth along the Debye ring:**

  In case of high stress and cold work gradients below the surfaces and for XRD measurements with the 2D detector, it may exist an opportunity to finely describe the gradient of stress or cold work through the use of the variations of the maximum penetration depth along the Debye ring.

- **Industrial use of the *FWHM* values for the characterization of mechanical processes:** The surface *FWHM* values can be directly related to the corresponding cold work values (if calibration curves are available), which could be used for inline quality control (after any surface manufactured process to ensure the integrity of the part) alone or along residual stress measurements. They can be acquired in few seconds under optimal conditions using a diffractometer equipped with a 2D detector. XRD technique being a non-destructive test (NDT) method, the combination of the surface residual stress and *FWHM* value provides important information on the characterization of a given treatment without altering the inspected component.

APPENDIX I

LIST OF PUBLISHED ARTICLES

The following lists the articles resulting from this Ph.D. thesis:
Peer-reviewed article:

1 Delbergue, D., Texier, D., Lévesque, M., and Bocher, P. (2019). Diffracting- grain identification from electron backscatter diffraction maps during residual stress measurements: a comparison between the $\sin^2\psi$ and $\cos\alpha$ methods. *Journal of Applied Crystallography*, 52 p.828-843. (Delbergue *et al.*, 2019)

Conference proceedings:

1. Delbergue, D., Lévesque, M., and Bocher, P. (2017). About the importance of X-ray elastic constant determination in the precise measurement of residual stress profiles. *Proceedings of the* 13^{th} *International Conference on Shot Peening* (p.237-243). Montreal, Qc, Canada. (Delbergue *et al.*, 2017)
2. Delbergue, D., Texier, D., Lévesque, M., and Bocher, P. (2016). Comparison of Two X-Ray Residual Stress Measurement Methods : $\sin^2\psi$ and $\cos\alpha$, Through the Determination of a Martensitic Steel X-Ray Elastic Constant. *Proceedings of the* 10^{th} *International Conference on Residual Stresses* (p.55-60). Montréal, Qc, Canada. (Delbergue *et al.*, 2016)

The following lists the collaborative activities resulting in six peer-reviewed articles and five conference proceedings:

Peer-reviewed articles:

1. Bag, A., Delbergue, D., Ajaja, J., Bocher, P., Lévesque, M., and Brochu, M. (2020). Effect of different shot peening conditions on the fatigue life of 300M steel submitted to high stress amplitudes. *International Journal of Fatigue*, 130 p.1-12. (Bag *et al.*, 2020)

2. Bag, A., Delbergue, D., Bocher, P., Lévesque, M., and Brochu, M. (2019). Statistical analysis of high cycle fatigue life and inclusion size distribution in shot peened 300M steel. *International Journal of Fatigue*, 118 p.126-138. (Bag *et al.*, 2019)
3. Bianchetti, C., Delbergue, D., Bocher, P., Lévesque, M., and Brochu, M. (2019). Analytical fatigue life prediction of shot peened AA 7050-T7451. *International Journal of Fatigue*, 118 p.271-281. (Bianchetti *et al.*, 2019)
4. Tu, F., Delbergue, D., Klotz, T., Bag, A., Miao, H.Y., Bianchetti, C., Brochu M., Bocher, P. and Lévesque M. (2018). Discrete element-periodic cell coupling model and investigations on shot stream expansion, Almen intensities and target materials. *International Journal of Mechanical Sciences*, 145 p.353-366. (Tu *et al.*, 2018)
5. Klotz, T., Delbergue, D., Bocher, P., Lévesque M. and Brochu M. (2018). Surface characteristics and fatigue behavior of shot peened Inconel 718. *International Journal of Fatigue*, 110 p.10-21. (Klotz *et al.*, 2018a)
6. Tu, F., Delbergue, D., Miao, H.Y., Klotz, T., Brochu, M., Bocher, P. and Lévesque M. (2017). A sequential DEM-FEM coupling method for shot peening simulation. *Surface and Coatings Technology*, 319 p.200-212. (Tu *et al.*, 2017)

Conference proceedings:

1. Bag, A., Delbergue, D., Lévesque, M., Bocher, P., and Brochu, M. (2017). Study of short crack growth in shot peened 300M steel. *Proceedings of the 13th International Conference on Shot Peening* (p.231-236). Montreal, Qc, Canada. (Bag *et al.*, 2017)
2. Klotz, T., Delbergue, D., Miao, H. Y., Castro-Moreno, A., Bocher, P., Lévesque, M., and Brochu, M. (2017). Analytical fatigue life prediction of shot peened Inconel 718. *Proceedings of the 13th International Conference on Shot Peening* (p.244-247). Montreal, Qc, Canada. (Klotz *et al.*, 2017b)

3. Miao, H.Y., Tu, F., Delbergue, D., Bianchetti, C., Klotz, T., Bag, A., and Lévesque, M. (2017). Shot peening DEM-FEM simulation considering shot stream expansion, peening intensity and target materials. *Proceedings of the 13th International Conference on Shot Peening* (p.366-371). Montréal, Qc, Canada. (Miao *et al.*, 2017b)

4. Miao, H. Y., Klotz, T., Delbergue, D., and Lévesque, M. (2017). Finite element simulation of shot peened residual stress relaxation under low and high cycle fatigue loadings. *Proceedings of the 13th International Conference on Shot Peening* (p.384-389). Montreal, Qc, Canada. (Miao *et al.*, 2017a)

5. Lebon, R., Delbergue, D., Miao, H.Y., Lévesque, M., and Bocher, P. (2014). Residual Stress Measurement Correction on Shot Peened AA2024 by Finite Element Analysis. *Proceedings of the 12th International Conference on Shot Peening*. Goslar, Germany. (Lebon *et al.*, 2014)

APPENDIX II

MATHEMATICAL PROOF I: COS α METHOD

Trigonometric identities used in the mathematical proof:

$$\cos(-\theta) = \cos\theta \text{ and } \sin(-\theta) = -\sin\theta \tag{A II-1a}$$

$$\cos(\pi+\theta) = -\cos\theta \text{ and } \sin(\pi+\theta) = -\sin\theta \tag{A II-1b}$$

$$\cos(\pi-\theta) = -\cos\theta \text{ and } \sin(\pi-\theta) = \sin\theta \tag{A II-1c}$$

$$\sin\theta\ \cos\theta = \frac{1}{2}\sin 2\theta \tag{A II-1d}$$

$$\cos^2\theta = \frac{1+\cos 2\theta}{2} \tag{A II-1e}$$

Definition:

ε_{ij}	Strain components
$\varepsilon_{\alpha}^{\{hkl\}}$	Strain measured along the scattering vector $\mathbf{V_{Scat}}$
$\mathbf{V_{Scat}}$	Scattering vector
$E^{\{hkl\}}$	Young’s modulus
$\nu^{\{hkl\}}$	Poisson’s ratio

Reminder of the assumptions:

- Isotropic homogeneous material
- Biaxial stress state

Using the biaxial stress state assumption, the strain $\boldsymbol{\varepsilon_{ij}}$ and stress $\boldsymbol{\sigma_{ij}}$ tensors can be written as

$$\varepsilon_{ij} = \begin{bmatrix} \varepsilon_{11} & \varepsilon_{12} & 0 \\ \varepsilon_{12} & \varepsilon_{22} & 0 \\ 0 & 0 & \varepsilon_{33} \end{bmatrix}, \tag{A II-2}$$

and

$$\sigma_{ij} = \begin{bmatrix} \sigma_{11} & \sigma_{12} & 0 \\ \sigma_{12} & \sigma_{22} & 0 \\ 0 & 0 & 0 \end{bmatrix}. \tag{A II-3}$$

The scattering vector$\mathbf{V_{Scat}}$ expression in the 2D detector coordinates system is found from series of rotations and can be expressed as

$$\mathbf{V_{Scat}}(\eta, \beta, \varphi, \alpha) = \mathbf{R}_z(\varphi).\mathbf{R}_y(\beta).\mathbf{R}_z(\pi - \alpha).\mathbf{R}_y(\eta).\boldsymbol{n} \tag{A II-4}$$

where $\mathbf{R}_y$ and $\mathbf{R}_z$ are the rotation matrices for a given angle around the y and z axes, respectively, and $\boldsymbol{n}$ is the starting vector, parallel to z-axis, expressed in the sample coordinates system. $\mathbf{R}_y$ and $\mathbf{R}_z$ have the form

$$\mathbf{R}_y(\theta) = \begin{bmatrix} \cos(\theta) & 0 & \sin(\theta) \\ 0 & 1 & 0 \\ -\sin(\theta) & 0 & \cos(\theta) \end{bmatrix}, \tag{A II-5a}$$

$$\mathbf{R}_z(\theta) = \begin{bmatrix} \cos(\theta) & -\sin(\theta) & 0 \\ \sin(\theta) & \cos(\theta) & 0 \\ 0 & 0 & 1 \end{bmatrix}, \tag{A II-5b}$$

and **n** has the form

$$\mathbf{n} = \begin{bmatrix} 0 \\ 0 \\ 1 \end{bmatrix}. \tag{A II-6}$$

Performing the four different rotations following the four angles (η, β, φ, and α), $\mathbf{V_{Scat}}$ can be expressed as

$$\begin{aligned} \mathbf{V_{Scat}}(\eta, \beta, \varphi, \alpha) &= \begin{bmatrix} \mathrm{v}_1 \\ \mathrm{v}_2 \\ \mathrm{v}_3 \end{bmatrix} \\ &= \begin{bmatrix} \cos\eta\ \sin\beta\ \cos\varphi - \sin\eta\ \cos\beta\ \cos\varphi\ \cos\alpha - \sin\eta\ \sin\varphi\ \sin\alpha \\ \cos\eta\ \sin\beta\ \sin\varphi - \sin\eta\ \cos\beta\ \sin\varphi\ \cos\alpha + \sin\eta\ \cos\varphi\ \sin\alpha \\ \cos\eta\ \cos\beta + \sin\eta\ \sin\beta\ \cos\alpha \end{bmatrix}. \end{aligned} \tag{A II-7}$$

The strain measured along $\mathbf{V_{Scat}}$ can be expressed in terms of the strain components ε_{ij} in sample coordinates with respect to Einstein's summation convention, assuming a biaxial stress state (Equation (A II-2)), as

$$\begin{aligned} \varepsilon_{\alpha}^{\{hkl\}} &= \mathrm{v}_i \mathrm{v}_j \varepsilon_{ij} \\ &= \mathrm{v}_1^2\ \varepsilon_{11} + \mathrm{v}_2^2\ \varepsilon_{22} + \mathrm{v}_3^2\ \varepsilon_{33} + 2\mathrm{v}_1\mathrm{v}_2\ \varepsilon_{12}. \end{aligned} \tag{A II-8}$$

For isotropic and homogeneous material, Hooke's law takes the form:

$$\varepsilon_{ij} = \frac{1+\nu}{E}\sigma_{ij} - \delta_{ij}\frac{\nu}{E}\sigma_{kk}. \tag{A II-9}$$

Considering the $\{hkl\}$ crystallographic direction for the elastic constants, the measured strain can be expressed in terms of stress combining Equation (A II-8) and Equation (A II-9) as

$$\begin{aligned}\varepsilon_{\alpha}^{\{hkl\}} &= \frac{1+\nu^{\{hkl\}}}{E^{\{hkl\}}}\,\mathrm{v}_i\mathrm{v}_j\,\sigma_{ij} - \delta_{ij}\frac{\nu^{\{hkl\}}}{E^{\{hkl\}}}\,\sigma_{kk} \\ &= \frac{1+\nu^{\{hkl\}}}{E^{\{hkl\}}}\Big[\mathrm{v}_1^2\,\sigma_{11} + \mathrm{v}_2^2\,\sigma_{22} + 2\mathrm{v}_1\mathrm{v}_2\,\sigma_{12}\Big] - \frac{\nu^{\{hkl\}}}{E^{\{hkl\}}}(\sigma_{11}+\sigma_{22}).\end{aligned} \tag{A II-10}$$

In order to compute the residual stress from a linear regression, the cos α method uses the parameter $\overline{\varepsilon}_{\alpha}^{\{hkl\}}$, defined as

$$\overline{\varepsilon}_{\alpha}^{\{hkl\}} = \frac{1}{2}\Big[(\varepsilon_{\alpha}^{\{hkl\}} - \varepsilon_{\pi+\alpha}^{\{hkl\}}) + (\varepsilon_{-\alpha}^{\{hkl\}} - \varepsilon_{\pi-\alpha}^{\{hkl\}})\Big] \tag{A II-11}$$

where $\varepsilon_{\alpha}^{\{hkl\}}$, $\varepsilon_{\pi+\alpha}^{\{hkl\}}$, $\varepsilon_{-\alpha}^{\{hkl\}}$, and $\varepsilon_{\pi-\alpha}^{\{hkl\}}$ are strains determined at four points located at 90° on the Debye ring for a given α angle. By simplification, the combination of Equation (A II-10) and Equation (A II-11) can be written as

$$\begin{aligned}\overline{\varepsilon}_{\alpha}^{\{hkl\}} = \ \frac{1}{2}\ \frac{1+\nu^{\{hkl\}}}{E^{\{hkl\}}}\Bigg[&\sigma_{11}\Big((\mathrm{v}_1^2(\alpha) - \mathrm{v}_1^2(\pi+\alpha) + \mathrm{v}_1^2(-\alpha) - \mathrm{v}_1^2(\pi-\alpha)\Big) \\ &+ \sigma_{22}\Big((\mathrm{v}_2^2(\alpha) - \mathrm{v}_2^2(\pi+\alpha) + \mathrm{v}_2^2(-\alpha) - \mathrm{v}_2^2(\pi-\alpha)\Big) \\ &+ 2\,\sigma_{12}\Big(\mathrm{v}_1(\alpha)\mathrm{v}_2(\alpha) - \mathrm{v}_1(\pi+\alpha)\mathrm{v}_2(\pi+\alpha) \\ &+ \mathrm{v}_1(-\alpha)\mathrm{v}_2(-\alpha) - \mathrm{v}_1(\pi-\alpha)\mathrm{v}_2(\pi-\alpha)\Big)\Bigg].\end{aligned} \tag{A II-12}$$

Let us define

$$A = \Big(\mathrm{v}_1^2(\alpha) - \mathrm{v}_1^2(\pi+\alpha) + \mathrm{v}_1^2(-\alpha) - \mathrm{v}_1^2(\pi-\alpha)\Big), \tag{A II-13a}$$

$$B = \Big((\mathrm{v}_2^2(\alpha) - \mathrm{v}_2^2(\pi+\alpha) + \mathrm{v}_2^2(-\alpha) - \mathrm{v}_2^2(\pi-\alpha)\Big), \tag{A II-13b}$$

$$C = \Big(\mathrm{v}_1(\alpha)\mathrm{v}_2(\alpha) - \mathrm{v}_1(\pi+\alpha)\mathrm{v}_2(\pi+\alpha) + \mathrm{v}_1(-\alpha)\mathrm{v}_2(-\alpha) - \mathrm{v}_1(\pi-\alpha)\mathrm{v}_2(\pi-\alpha)\Big), \tag{A II-13c}$$

such that Equation (A II-12) can be written as

$$\overline{\varepsilon}_{\alpha}^{\{hkl\}} = \frac{1}{2}\,\frac{1+\nu^{\{hkl\}}}{E^{\{hkl\}}}\Big(A\sigma_{11} + B\sigma_{22} + 2C\,\sigma_{12}\Big). \tag{A II-14}$$

The term *A* (Equation (A II-13a)) will be developed first. But, as a starting point the components $\mathrm{v}_1^2(\alpha)$ and $\mathrm{v}_1^2(\pi+\alpha)$ are expanded, using the trigonometric identities, as

$$\begin{aligned}\mathrm{v}_1^2(\alpha) &= \Big(\cos\eta\ \sin\beta\ \cos\varphi\ -\ \sin\eta\ \cos\beta\ \cos\varphi\ \cos\alpha\ -\ \sin\eta\ \sin\varphi\ \sin\alpha\Big)^2\\ &= \cos^2\alpha\ \cos^2\beta\ \sin^2\eta\ \cos^2\varphi\ +\ \sin^2\beta\ \cos^2\eta\ \cos^2\varphi\\ &\quad + \sin^2\alpha\ \sin^2\eta\ \sin^2\varphi\ -\ 2\ \sin\alpha\ \sin\beta\ \cos\eta\ \sin\eta\ \cos\varphi\ \sin\varphi\\ &\quad - 2\ \cos\alpha\ \cos\beta\ \sin\beta\ \cos\eta\ \sin\eta\ \cos^2\varphi\\ &\quad + 2\ \cos\alpha\ \sin\alpha\ \cos\beta\ \sin^2\eta\ \cos\varphi\ \sin\varphi\end{aligned} \tag{A II-15}$$

$$\begin{aligned}\mathrm{v}_1^2(\pi+\alpha) &= \Big(\cos\eta\ \sin\beta\ \cos\varphi\ -\ \sin\eta\ \cos\beta\ \cos\varphi\ \cos(\pi+\alpha)\\ &\qquad - \sin\eta\ \sin\varphi\ \sin(\pi+\alpha)\Big)^2\\ &= \cos^2\alpha\ \cos^2\beta\ \sin^2\eta\ \cos^2\varphi\ +\ \sin^2\beta\ \cos^2\eta\ \cos^2\varphi\\ &\quad + \sin^2\alpha\ \sin^2\eta\ \sin^2\varphi\ +\ 2\ \sin\alpha\ \sin\beta\ \cos\eta\ \sin\eta\ \cos\varphi\ \sin\varphi\\ &\quad - 2\ \cos\alpha\ \cos\beta\ \sin\beta\ \cos\eta\ \sin\eta\ \cos^2\varphi\\ &\quad + 2\ \cos\alpha\ \sin\alpha\ \cos\beta\ \sin^2\eta\ \cos\varphi\ \sin\varphi\end{aligned} \tag{A II-16}$$

Simplifications occur by subtraction of $\mathrm{v}_1^2(\pi + \alpha)$ to $\mathrm{v}_1^2(\alpha)$ and using trigonometric identities such as

$$\begin{aligned} \mathrm{v}_1^2(\alpha) - \mathrm{v}_1^2(\pi + \alpha) = &- 4\ \cos\alpha\ \cos\beta\ \sin\beta\ \cos\eta\ \sin\eta\ \cos^2\varphi \\ &- 4\ \sin\alpha\ \sin\beta\ \cos\eta\ \sin\eta\ \cos\varphi\ \sin\varphi \\ = &- \frac{1}{2}\ \cos\alpha\ \sin 2\beta\ \sin 2\eta\ (1 + \cos 2\varphi) \\ &- \sin\alpha\ \sin\beta\ \sin 2\eta\ \sin 2\varphi \end{aligned} \tag{A II-17}$$

Using the identities of cosine and sine for negative angles, and doing the same expression expansions and simplifications the term $\mathrm{v}_1^2(-\alpha) - \mathrm{v}_1^2(\pi - \alpha)$ takes the following form

$$\begin{aligned} \mathrm{v}_1^2(-\alpha) - \mathrm{v}_1^2(\pi - \alpha) = &- 4\ \cos\alpha\ \cos\beta\ \sin\beta\ \cos\eta\ \sin\eta\ \cos^2\varphi \\ &+ 4\ \sin\alpha\ \sin\beta\ \cos\eta\ \sin\eta\ \cos\varphi\ \sin\varphi \\ = &- \frac{1}{2}\ \cos\alpha\ \sin 2\beta\ \sin 2\eta\ (1 + \cos 2\varphi) \\ &+ \sin\alpha\ \sin\beta\ \sin 2\eta\ \sin 2\varphi \end{aligned} \tag{A II-18}$$

Using the results from Equation (A II-17) and Equation (A II-18), the term A can then be written as

$$A = -\cos\alpha\ \sin 2\beta\ \sin 2\eta\ (1 + \cos 2\varphi) \tag{A II-19}$$

Similarly, the term B (Equation (A II-13b)) can also be divided in two expressions, leading to the following simplifications

$$v_2^2(\alpha) - v_2^2(\pi + \alpha) = 2\ \sin\beta\ \sin 2\eta\ \sin\varphi\ (\sin\alpha\ \cos\varphi\ -\ \cos\alpha\ \cos\beta\ \sin\varphi) \tag{A II-20}$$

and

$$\mathrm{v}_2^2(-\alpha) - \mathrm{v}_2^2(\pi - \alpha) = -2\ \sin\beta\ \sin 2\eta\ \sin\varphi\ (\sin\alpha\ \cos\varphi\ +\ \cos\alpha\ \cos\beta\ \sin\varphi). \tag{A II-21}$$

It then takes the final form

$$\begin{aligned} B &= -2\ \cos\alpha\ \sin 2\beta\ \sin 2\eta\ \sin^2\varphi \\ &= -\cos\alpha\ \sin 2\beta\ \sin 2\eta\ (1-\cos 2\varphi). \end{aligned} \tag{A II-22}$$

Likewise, the term C (Equation (A II-13c)) can be simplified as

$$C = -\cos\alpha\ \sin 2\beta\ \sin 2\eta\ \sin 2\varphi \tag{A II-23}$$

Finally, replacing the different terms by the final forms of Equation (A II-19), Equation (A II-22), and Equation (A II-23), Equation (A II-12) can be written as

$$\begin{aligned} \overline{\varepsilon}_{\alpha}^{\{hkl\}} &= \frac{1}{2}\ \frac{1+\nu^{\{hkl\}}}{E^{\{hkl\}}}\Bigg[\sigma_{11}\Big(-\cos\alpha\ \sin 2\beta\ \sin 2\eta\ (1+\cos 2\varphi)\Big) \\ &\quad + \sigma_{22}\Big(-\cos\alpha\ \sin 2\beta\ \sin 2\eta\ (1-\cos 2\varphi)\Big) \\ &\quad + 2\ \sigma_{12}\Big(-\cos\alpha\ \sin 2\beta\ \sin 2\eta\ \sin 2\varphi\Big)\Bigg] \\ &= -\frac{1}{2}\ \frac{1+\nu^{\{hkl\}}}{E^{\{hkl\}}}\ \cos\alpha\ \sin 2\beta\ \sin 2\eta\Big[\sigma_{11}(1+\cos 2\varphi) \\ &\quad + \sigma_{22}(1-\cos 2\varphi) + 2\ \sigma_{12}\ \sin 2\varphi\Big] \\ &= -\ \frac{1+\nu^{\{hkl\}}}{E^{\{hkl\}}}\ \sin 2\beta\ \sin 2\eta\ \cos\alpha\ \sigma_{\varphi} \end{aligned} \tag{A II-24}$$

where $\sigma_{\varphi} = 1/2\Big(\sigma_{11}(1+\cos 2\varphi)+\sigma_{22}(1-\cos 2\varphi)+2\ \sigma_{12}\ \sin 2\varphi\Big)$ is the stress measured in the φ-direction. The measured stress can be computed by differentiating Equation (A II-24) with respect to $\cos\alpha$ as

$$\sigma_{\varphi} = -\frac{E^{\{hkl\}}}{1+\nu^{\{hkl\}}}\frac{1}{\sin 2\eta\ \sin 2\beta}\frac{\partial\overline{\varepsilon}_{\alpha}^{\{hkl\}}}{\partial\cos\alpha} = -\frac{1}{\frac{1}{2}S_2^{\{hkl\}}}\frac{1}{\sin 2\eta\ \sin 2\beta}\frac{\partial\overline{\varepsilon}_{\alpha}^{\{hkl\}}}{\partial\cos\alpha}. \tag{A II-25}$$

APPENDIX III

MATHEMATICAL PROOF II

To be demonstrated: $-\sin(2\beta)\ \sin(2\eta) = \sin^2(\beta-\eta) - \sin^2(\beta+\eta)$

Trigonometric identity used in this mathematical proof:

$$\sin(\theta) = \frac{\mathrm{e}^{i\theta} - \mathrm{e}^{-i\theta}}{2i}. \tag{A III-1}$$

Let us develop the term $\sin^2(\beta-\eta)$ in terms of exponential functions

$$\begin{aligned}
\sin^2(\beta-\eta) &= \left(\frac{\mathrm{e}^{i(\beta-\eta)} - \mathrm{e}^{-i(\beta-\eta)}}{2i}\right)^2 \\
&= \frac{\mathrm{e}^{2i(\beta-\eta)} - \mathrm{e}^{i(\beta-\eta)}\mathrm{e}^{-i(\beta-\eta)} + \mathrm{e}^{-2i(\beta-\eta)}}{(2i)^2} \\
&= \frac{\mathrm{e}^{2i(\beta-\eta)} - \mathrm{e}^{i[(\beta-\eta)-(\beta-\eta)]} + \mathrm{e}^{-2i(\beta-\eta)}}{(2i)^2} \\
&= \frac{\mathrm{e}^{2i(\beta-\eta)} - \mathrm{e}^{i[(\beta-\eta)-(\beta-\eta)]} + \mathrm{e}^{-2i(\beta-\eta)}}{(2i)^2} \\
&= \frac{\mathrm{e}^{2i\beta}\mathrm{e}^{-2i\eta} - \mathrm{e}^{0} + \mathrm{e}^{-2i\beta}\mathrm{e}^{2i\eta}}{(2i)^2}.
\end{aligned} \tag{A III-2}$$

Similarly, the term $\sin^2(\beta+\eta)$ yields

$$\begin{aligned}\sin^2(\beta+\eta) &= \left(\frac{e^{i(\beta+\eta)} - e^{-i(\beta+\eta)}}{2i}\right)^2 \\ &= \frac{e^{2i\beta}e^{2i\eta} - e^0 + e^{-2i\beta}e^{-2i\eta}}{(2i)^2}.\end{aligned} \tag{A III-3}$$

Finally, the subtraction of the two terms leads to

$$\begin{aligned}\sin^2(\beta-\eta) - \sin^2(\beta+\eta) &= \frac{e^{2i\beta}e^{-2i\eta} + e^{-2i\beta}e^{2i\eta} - e^{2i\beta}e^{2i\eta} - e^{-2i\beta}e^{-2i\eta}}{(2i)^2} \\ &= \frac{e^{2i\beta}(e^{-2i\eta} - e^{2i\eta}) + e^{-2i\beta}(e^{2i\eta} - e^{-2i\eta})}{(2i)^2} \\ &= \frac{e^{2i\beta}(e^{-2i\eta} - e^{2i\eta}) - e^{-2i\beta}(e^{-2i\eta} - e^{2i\eta})}{(2i)^2} \\ &= \frac{(e^{2i\beta} - e^{-2i\beta})(e^{-2i\eta} - e^{2i\eta})}{(2i)^2} \\ &= \frac{(e^{2i\beta} - e^{-2i\beta})}{2i}\frac{(e^{-2i\eta} - e^{2i\eta})}{2i} \\ &= \sin(2\beta)\ \sin(-2\eta) \\ &= -\sin(2\beta)\ \sin(2\eta).\end{aligned} \tag{A III-4}$$

APPENDIX IV

FIRST XEC ASSESSMENT WITH THE SIN$^2\psi$ METHOD

A first XEC $\frac{1}{2}S_2^{\{311\}}$ was experimentally measured using the micro-tensile machine presented in Section 2.6.2 for the ∅89 mm bar, using the Hill limit $\left(\frac{1}{2}S_2^{\{hkl\}}\right)^{\text{Hill}}$ as starting point.

The XRD measurement values plotted versus the applied stresses are presented in Figures-A IV-1. The seven measurements for the nine applied loads are presented in black and red for the loading and unloading conditions, respectively. The linear fitting is presented as the straight blue line and the fitting coefficients are exhibited in the graphs' legends. The dashed black line presents a reference line in the hypothetical case where the XEC $\frac{1}{2}S_2^{\{311\}}$ value can be estimated with the Hill model.

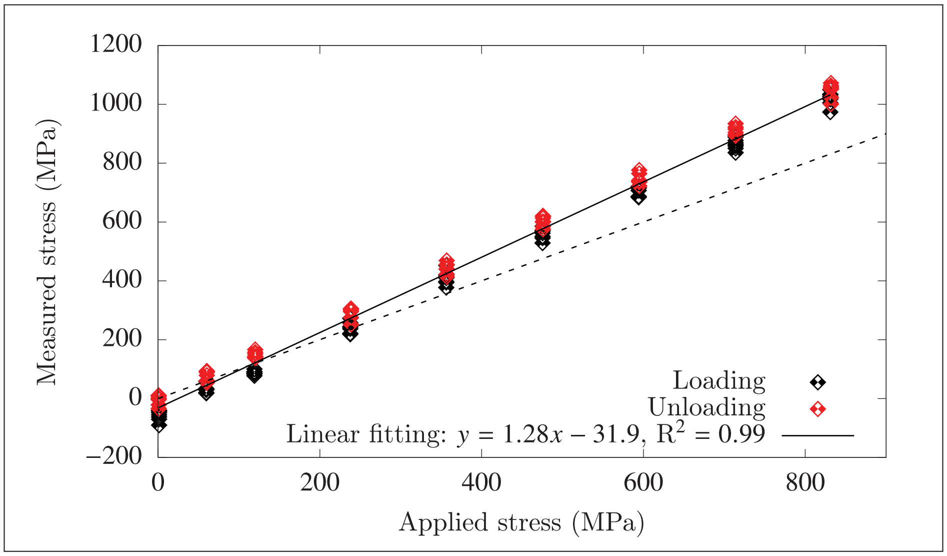

Figure-A IV-1 XRD measured stresses vs. applied stresses for determination of the XEC value using the sin$^2\psi$ method and the Proto iXRD apparatus

The measurements for a given load are less scattered than for the second measurement presented in Section 3.1.2 with an average standard deviation of 18 MPa. The linear regression describes well the data with R^2 a value of 99%. As for the results presented in Section 3.1.2 a negative y-intercept is observed (i.e., suggesting the presence of compressive residual stresses at the surface). Furthermore, it can be observed that, as the results reported in Section 3.1.2, the slope is higher than 1, yielding a XEC value of $\left(\frac{1}{2}S_2^{\{311\}}\right)^{\sin^2\psi} = 8.38 \pm 0.12 \times 10^{-6}$ MPa^{-1}. In this case, using the XEC value computed from the Hill model, the measured stresses would be over estimated by 28%.

Similarly, the shot peening residual stress profile taken as example can be corrected using the measured XEC value. Figure-A IV-2 presents the corrected profile of the shot peening residual stress profiles measured using the $\sin^2\psi$, as well as the corrected profile for the $\cos\alpha$ methods presented in Section 3.1.2. As expected, the residual stress values decrease and differences between the two XRD methods largely increase, especially at the plateau of compressive residual stresses. Using this XEC assessment would lead to inaccurate residual stress measurements.

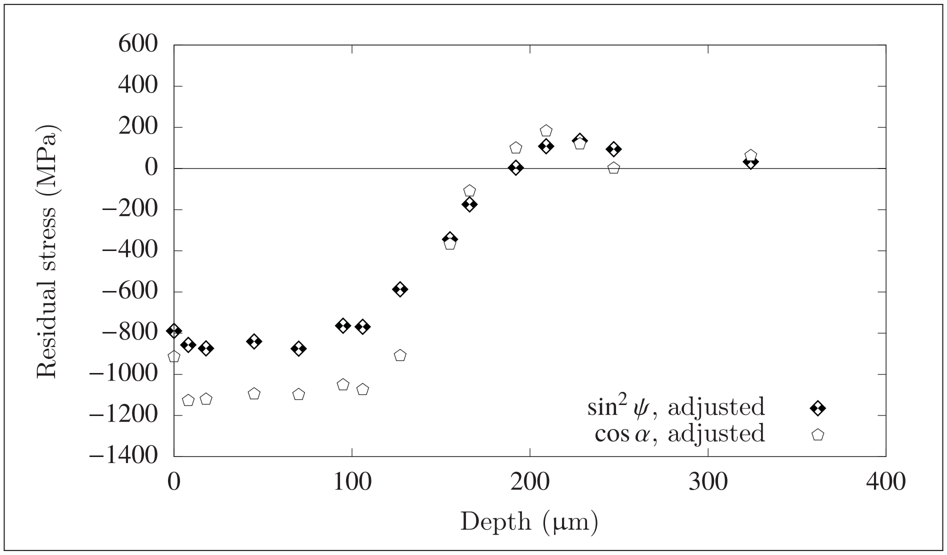

Figure-A IV-2 Corrected profiles using the experimentally determined XEC ($\left(\frac{1}{2}S_2^{\{311\}}\right)^{\sin^2\psi} = 8.38 \pm 0.12 \times 10^{-6}$ MPa^{-1} and $\left(\frac{1}{2}S_2^{\{311\}}\right)^{\cos\alpha} = 7.20 \pm 0.11 \times 10^{-6}$ MPa^{-1}) for the IN718 sample shot peened at an intensity of 8 A

APPENDIX V

DIFFRACTING GRAINS IDENTIFICATION: SCRIPT VALIDATION

The validation of the script diffracting grains was realized by searching the grains having their <001>, <011>, or <111> direction aligned with the RD. Figure-A V-1a presents a closeup of the ∅25 mm sample EBSD map taken as example of the script validation. Figures-A V-1b, V-1c, and V-1d exhibit the EBSD maps plotted using the script to identify the grains their <001>, <011>, or <111> direction aligned with the RD, respectively. It can be observed, for instance, that only the red grains are highlighted in Figure-A V-1b as only the grains having their <001> direction are identified. A tolerance of 2° was used for the identification, leading to slight nuances of a given color, especially visible in Figure-A V-1d.

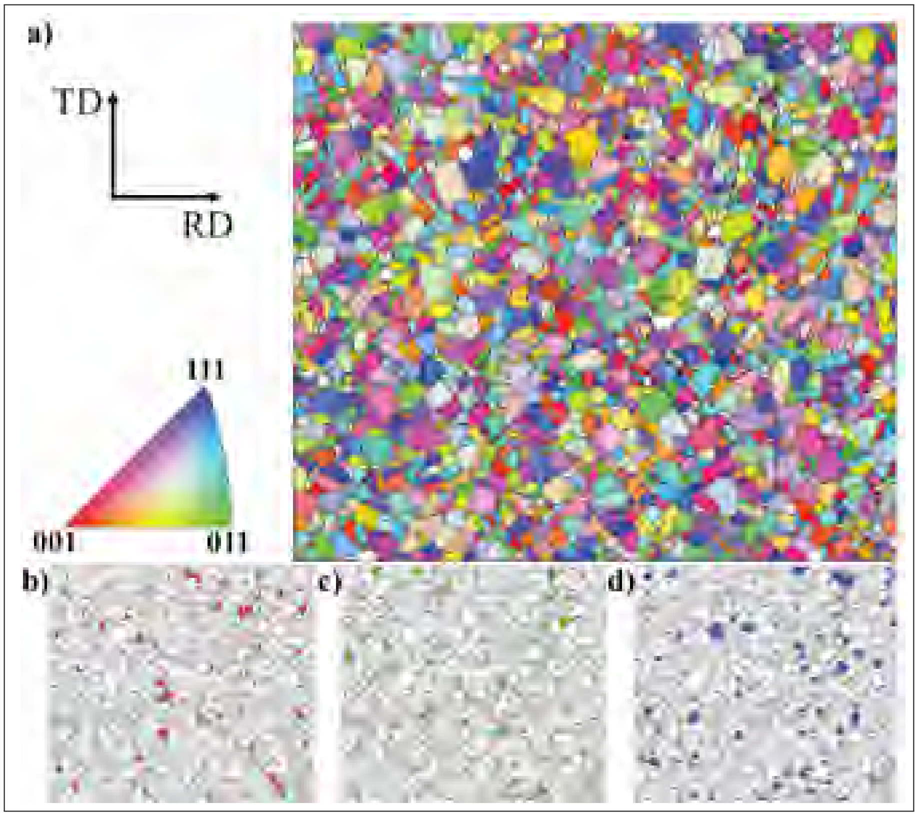

Figure-A V-1 a) Closeup of the ∅25 mm sample EBSD map. Identification of the grains having their b) <001>, c) <011>, and d) <111> direction aligned with the RD

APPENDIX VI

ODF EXAMPLE

Figure-A VI-1 presents, in the Euler space, the ODF of the ∅25 mm sample. Each frame is a section in ($\Phi\varphi_1$) of a given φ_2. No high concentrated zones can be found meaning that the ∅25 mm sample does not present any texture.

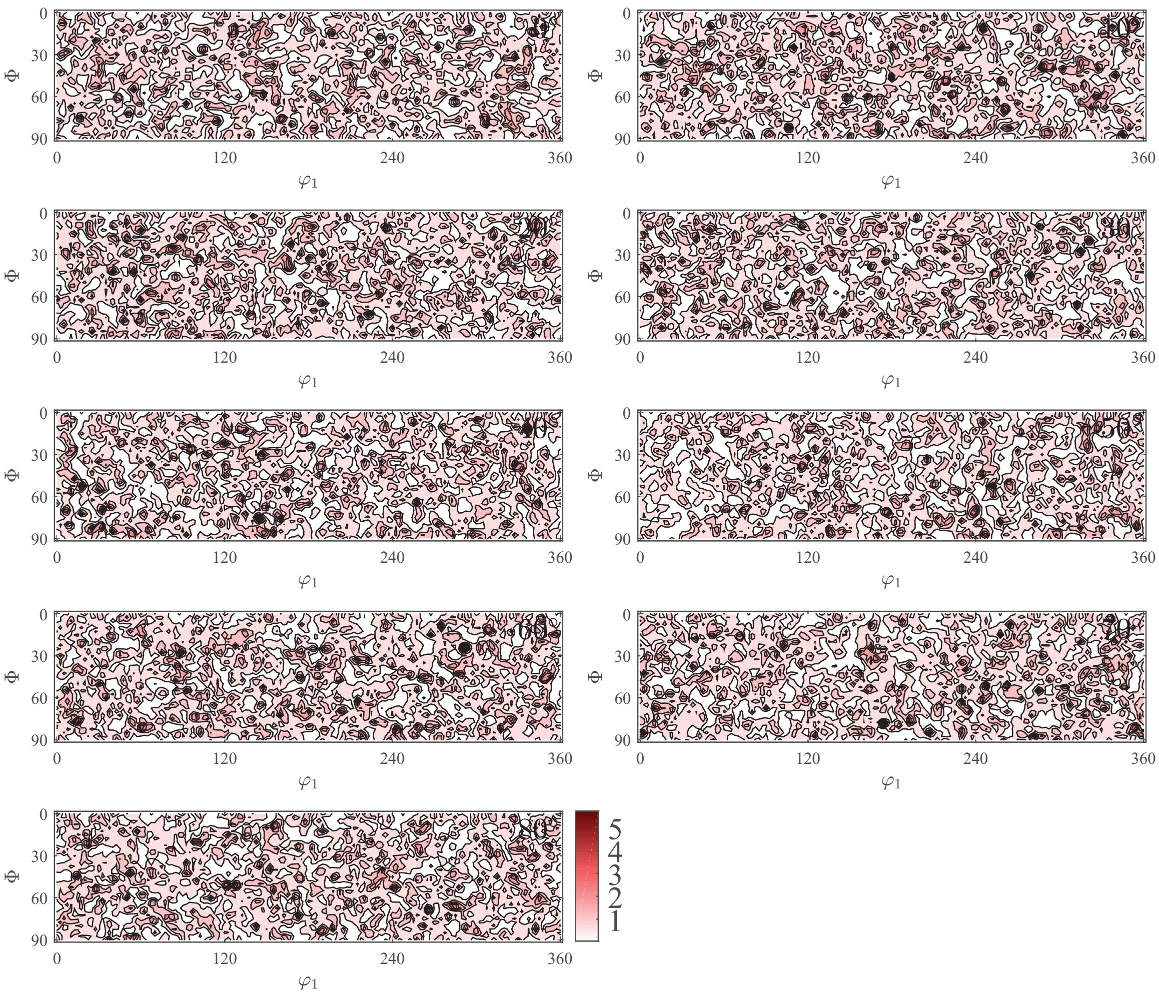

Figure-A VI-1 Visualization of the ODF computed for the ∅25 mm sample. ODF sections: φ_2 = 0°, 10°…80°

APPENDIX VII

SURFACE CHARACTERISTICS AND FATIGUE BEHAVIOR OF SHOT PEENED INCONEL 718

The co-written article entitled "*Surface characteristics and fatigue behavior of shot peened Inconel 718*" (Klotz *et al.*, 2018a) is provided here. The $FWHM$ vs. ε_p, the residual stress, residual stress relaxation, and cold work profiles were measured during this Ph.D. thesis.

International Journal of Fatigue 110 (2018) 10–21

Contents lists available at ScienceDirect

International Journal of Fatigue

journal homepage: www.elsevier.com/locate/ijfatigue

Surface characteristics and fatigue behavior of shot peened Inconel 718

T. Klotz[a,*], D. Delbergue[a,b], P. Bocher[b], M. Lévesque[a], M. Brochu[a]

[a] *Département de génie mécanique, École Polytechnique de Montréal, Qc H3T 1J4 Montréal, Canada*
[b] *Département de génie mécanique, École de Technologie Supérieure, Qc H3C 1K3 Montréal, Canada*

ARTICLE INFO

Keywords:
Inconel 718
Fatigue
Crack initiation
Shot peening
Residual stresses relaxation

ABSTRACT

Shot peening is commonly used in the aerospace industry to improve mechanical components fatigue life. It introduces compressive residual stresses and cold work at the surface which tend to close short fatigue cracks and delay their propagation, respectively. However, shot peening also creates surface irregularities that can be detrimental to fatigue. The effect of different shot peening conditions on Inconel 718 tested in low and high cycle fatigue is presented in this study. An analysis of the fatigue life, crack initiation mechanisms, residual stress relaxation, process induced strain hardening and surface roughness showed that, in high cycle fatigue, shot peening can increase Inconel 718 fatigue life from 2 to 20 times, depending on the shot peening conditions. This observation suggests that careful selection of peening parameters is crucial. In low cycle fatigue the roughness resulting from shot peening is to be considered while in high cycle fatigue, it is the presence of significant residual stresses.

1. Introduction

Inconel 718 is a nickel-based superalloy largely used in aerospace gas turbines components submitted to cyclic loads. Shot peening is a cold work process consisting in impinging hard particles at high velocity onto a ductile metallic surface. The process introduces compressive residual stresses and work hardening on the specimen's surface layer [1], which improves its resistance to fatigue. Compressive residual stresses tend to close short cracks while work hardening improves the material resistance to plastic deformation, which enhances resistance to crack initiation and propagation. However, fatigue life is sensitive to shot peening intensity since deeper dimples are created on the specimen's surface as shot peening intensity increases, resulting in stress concentrating features [2]. It has been reported that there is an optimal shot peening intensity, for each material, that maximizes fatigue life [3,4].

Shot peening is specified by the type of media, the Almen intensity and the surface coverage. The Almen intensity is an indirect measure of the shot peening intensity and is obtained by peening a flat standardized strip, called Almen strip, firmly fixed into an Almen holder by four bolts. Due to the presence of residual stresses, the strips progressively bend as the process progresses. The strip's arc height is measured throughout the process progression and the Almen intensity (A) is defined as the arc height (1 A $= 25.4\,\mu$m) when doubling the peening time increases the arc height by 10%. Coverage is the percentage of the shot peened surface covered by dimples. A coverage beyond 100% corresponds to a multiple of the shot peening time required for reaching 98% coverage. For example, 200% coverage corresponds to twice the shot peening time required to reach 98% coverage.

Compressive residual stresses in Inconel 718 shot peened at an Almen intensity of 8 A, with a coverage of 200% can reach -1000 MPa and the plastic deformation responsible for the hardness increase, commonly called cold work, can be as high as 40% [5] on the part's surface. Nakamura et al. [6] showed that shot peened Inconel 718 can endure a strain range 1.3 times larger than polished specimens for the same 10^4 fatigue cycles at failure under strain controlled axial fatigue at a strain ratio of 0. Other authors [7] have found that cracks initiated beneath the surface and resulted in longer fatigue lives in shot peened Inconel 718 tested at 525 °C under a stress ratio of 0.1. For example, an electropolished specimen lasted 2.7×10^5 cycles for a maximum applied stress of 1240 MPa while it was around 9.0×10^6 cycles for a specimen

---

Abbreviations: E, Young's modulus; ν, Poisson's ratio; $\sigma_{y0.2\%}$, 0.2% offset tensile yield strength; σ_u, ultimate tensile strength; El., elongation at failure; AR., area reduction at failure; Bal., balance; σ_{min}, minimum stress during a fatigue cycle; σ_{max}, maximum stress during a fatigue cycle; R_σ, stress ratio; ε_p, plastic strain; σ_{surf}, surface residual stress; $\sigma_{comp,max}$, maximum compressive residual stress; LB, Lower boundary; Av., Average; $d_{\sigma_{comp,max}}$, maximum compressive residual stress depth; $d_{\sigma_{comp=0}}$, depth at which the residual stresses become tensile; R_t, surface roughness profile height between the deepest valley and the highest peak; *RSm*, mean width of profile elements; N_f, number of cycles to failure; λ, X-ray wavelength; $\frac{1}{2}S_2$, X-ray elastic constant; FWHM, Full width at half-maximum intensity; XRD, X-ray diffraction; β, Weibull distribution's shape factor; λ, Weibull distribution's scale factor

[*] Corresponding author.

E-mail addresses: thierry.klotz@polymtl.ca (T. Klotz), dorian.delbergue.1@ens.etsmtl.ca (D. Delbergue), philippe.bocher@etsmtl.ca (P. Bocher), martin.levesque@polymtl.ca (M. Lévesque), myriam.brochu@polymtl.ca (M. Brochu).

https://doi.org/10.1016/j.ijfatigue.2018.01.005
Received 4 October 2017; Received in revised form 26 December 2017; Accepted 6 January 2018
Available online 10 January 2018
0142-1123/ © 2018 Elsevier Ltd. All rights reserved.

shot peened at 9 A with a coverage of 100%.

Fatigue crack initiations for unpeened Inconel 718 have mainly two sources [8]: (1) initiation at a carbide located at, or beneath, the surface, (2) initiation within a large grain. Initiations from carbides are associated to carbide cracking [9] which occurs during the first cycle [10] or are inherently present in the material [11]. Initiations in large grains are explained by the early formation of persistent slip bands. Slip bands are commonly observed in Inconel 718 following plastic deformation when a grain is favorably oriented in the direction of the maximum shear stress [12,13]. It has been found that, in the nickel-based superalloy René 88DT (similar to Inconel 718), fatigue cracks were formed by localization of cyclic plastic deformation on {111} slip planes near twin boundaries in large grains with high Schmid factors [14]. Stinville et al. [15] showed that local strains at favorably oriented twin boundaries can be 8 times higher than the macroscopically applied strain. In the case of twin boundaries parallel to a slip system, the dislocations can travel throughout the whole grain and their mobility is accentuated by the twin boundary's length [16,17]. Ideal shot peening conditions should prevent crack initiations at carbides and large grains located at the specimen's surface. To the best of our knowledge, fatigue crack initiation mechanism and nucleation depth controlled by shot peening parameters commonly used in the industry is yet to be demonstrated. Making this demonstration would be of considerable interest for companies designing Inconel 718 shot peened parts.

In an attempt to fill this knowledge gap, this study aims to quantify the effects of several shot peening conditions commonly used in the aerospace industry on the fatigue life of Inconel 718 in low and high cycle fatigue (LCF and HCF) at room temperature. The paper is organized as follows: Section 2 presents the studied material, the experimental fatigue procedure, the measurements and observation methods, as well as the equipment used to identify crack initiation features. Experimental results such as surface roughness, residual stress relaxation and cold work redistribution are presented in Section 3, along with the fatigue results and their fractographies. The results are then discussed in Section 4 and Section 5 concludes this work.

2. Material and experimental procedure

2.1. Material

The studied nickel-based superalloy Inconel 718 underwent a solution and precipitation heat treatment as per AMS 5663M [19] to reach an hardness of 45 HRC. The hardness is mainly due to the formation of γ' and γ'' precipitates [20]. The material's tensile properties and chemical composition are listed in Tables 1 and 2, respectively. The austenitic FCC matrix microstructure has a 13 μm average grain size with grains diameters ranging from 5 to 30 μm. The grain size was estimated by manually measuring the perimeter of 115 grains with ImageJ and approximated these as circles perimeters. Fig. 1 shows that the microstructure consists of titanium carbo-nitride (TiCN), δ phase (Ni_3Nb) and NbC carbides. The NbC carbides sizes were measured with the same procedure as for the grain size. The NbC were ranging from 3 to 14 μm with a 9 μm average size. The δ phase is located along the grain and twin boundaries. Aluminum and magnesium oxides were also observed in some TiCN particles. Note that γ' and γ'' particles are not visible on the optical micrograph.

Table 1
Inconel 718 average tensile properties measured on two specimens in agreement with ASTM E8M-13a standard [18]. E: Young's modulus, $\sigma_{y0.2\%}$: 0.2% offset yield strength, σ_u: Ultimate strength, EL.: Elongation at failure and AR.: Area reduction at failure.

E (GPa)	$\sigma_{y0.2\%}$ (MPa)	σ_u (MPa)	El. (%)	AR. (%)
205	1156	1415	23	33

Table 2
Inconel 718 chemical composition obtained by optical spectrometry (weight %).

Elements	Ni	Fe	Cr	Nb	Mo	Ti	Al	Co	Mn	Si
Composition	Bal.	19.53	17.84	5.02	3.07	1.16	0.64	0.35	0.16	0.06

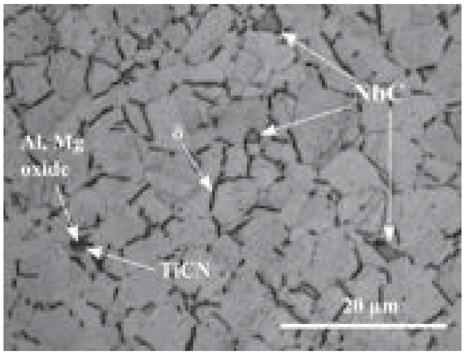

Fig. 1. Inconel 718 optical micrograph. Niobium carbides (NbC) and titanium carbo-nitride (TiCN) are present at the grain boundaries and within the grains. δ phase (Ni_3Nb) can be observed along the grain boundaries. An Al-Mg oxide is present inside a TiCN particle.

2.2. Fatigue tests

Two types of specimens were used to perform fatigue tests: (1) 9.5 mm diameter cylindrical samples designed in agreement with ASTM E466-07 [21] standard to study crack initiation and quantify fatigue life and (2) 3.56 mm × 10.16 mm rectangular cross section samples to study the evolution of residual stresses and cold work during interrupted fatigue tests. The two geometries are presented in Fig. 2(a) and (b). All specimens were extracted in the longitudinal direction of 25.4 mm diameter forged bars.

Tests were performed at room temperature under a 20 Hz constant stress amplitude on an MTS 318.10 hydraulic machine equipped with a 100 kN MTS 661.20e-03 load cell. A stress ratio of $R_\sigma = \frac{\sigma_{min}}{\sigma_{max}} = 0.1$ with $\sigma_{max} = 1390$, 1380, 1370 and 1100 MPa was used under a sinusoidal load history. The stress level where $\sigma_{max} = 1100$ MPa is referred herein as HCF while the higher stress levels are referred as LCF since σ_{max} is above the material's yield strength (1156 MPa). Scanning electron microscope (SEM) observations of the rupture surfaces were performed with a JEOL JSM-7600F microscope. Energy dispersive X-ray (EDX) spectroscopy was achieved with a silicon drift detector Oxford X-Max 80 to identify features present at crack initiation sites.

2.3. Surface conditions

Five different surface conditions were studied: (1) polished (down to 1 μm), (2) as machined, (3) shot peened with cast steel shots ASH 230 (S230) at an intensity of 4 A, (4) shot peened with conditioned carbon steel cut wire shots AWCR 14 (CW14) at an intensity of 4 A and (5) shot peened with CW14 at an intensity of 8 A, as summarized in Table 3. For the sake of clarity, shot peening conditions are designated in this paper by a type of media – Almen intensity couple. For example S230 4 A means a specimen shot peened with S230 media at an Almen intensity of 4 A.

Shot peening was performed with an air-pressured shot peening machine designed by Canablast and Genik. Shot peening was performed in agreement with SAE AMS2430T standard [22] using a 6 axis M-20iA Fanuc robot and a rotating table mounted on a Fanuc 1-axis servo

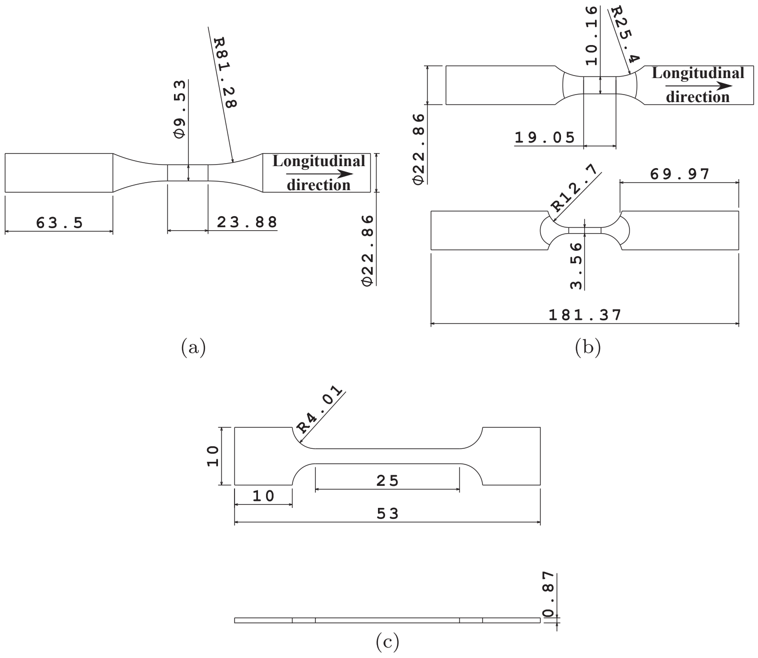

Fig. 2. (a) Cylindrical and (b) rectangular specimens used for the fatigue tests and residual stresses relaxation measurements, respectively. (c) Micro-tensile specimen used for the X-ray elastic constant determination and the FWHM – ε_p relationship. Dimensions are in mm. The longitudinal direction is specified for the fatigue specimens.

Table 3
The five surface conditions studied. The media diameter, velocity and the kinetic energy of a single shot are also presented. The kinetic energy is calculated as 0.5 × media mass × velocity^2. The density of the shots was assumed to be of 7800 kg/m^3.

	Surface	Media	Intensity (A)	Diameter (mm)	Velocity (m/s)	Kinetic energy (J)
1	Polished	–	–	–	–	–
2	As machined	–	–	–	–	–
3	Shot peened	S230	4	0.59	12	6.0×10^{-5}
4	Shot peened	CW14	4	0.36	34	2.2×10^{-4}
5	Shot peened	CW14	8	0.36	76	1.1×10^{-3}

positioner. A 305 mm standoff distance and a 90° peening angle were used. The shots mass flow was controlled by MagnaValves provided by Electronics Inc. The average shots velocities were measured with a ShotMeter G3 from Progressive Technology and are presented in Table 3. 100% coverage was reached for the three peening conditions.

Three longitudinal surface roughness profiles were measured per sample on specimens of each surface condition prior to fatigue testing. The roughness measurements on as machined specimens were performed on samples that were subsequently shot peened. The profiles were obtained using a profilometer Formtrace SV-C 3200 using a 8 mm cut-off wave length.

Micro-hardness measurements were performed on a Akashi MVK-H0 microdurometer at 300 gf with a Vickers indenter, in agreement with ASTM E384-11 standard [23].

2.4. Residual stresses measurements

In-depth residual stress profiles were measured using X-ray diffraction (XRD). XRD measurements were performed on the {3 1 1} family of planes using the Kβ lines on a Pulstec μ-X360n apparatus equipped with a Cr-tube. Diffraction peaks were fit by the Lorentzian method [24]. The cos α method [25] was used to calculate the stresses. The X-ray elastic constant was previously determined for the {3 1 1} family of planes using a specimen, similar to that presented in Fig. 2(c), having the same microstructure as the fatigue specimens and a Kammrath & Weiss GmbH micro-tensile machine, as described in the work of Delbergue et al. [26]. The parameters used for all residual stress measurements are summarized in Table 4. Thin layers of material were removed by electropolishing with a perchloric acid-based solution to extract a subsurface residual stress profile. The thickness of each removed layer was measured using an Olympus LEXT OLS4100 confocal microscope and a Mitutoyo SJ-400 profilometer. The Moore and Evans correction [27] was applied to correct stress redistribution caused by the layer-by-layer removal process, as the sample and electropolished pocket geometry agreed with the correction hypothesis. On average, the errors calculated for XRD measurements are roughly 80 MPa. The error is largely due to a combination of the K line used, the sample surface roughness and the inherent uncertainty associated to the layer removal method. Only the residual stress component parallel to the longitudinal direction (specified in Fig. 2(a) and (b)) was measured as it is the direction in which most of the stress relaxation occurs in axial fatigue.

CW14 8 A rectangular specimens (Fig. 2(b)) were used to measure the residual stress relaxation and/or redistribution that occurred during the cyclic loading. The same XRD settings, electrolytic solution and corrections as those used for the cylindrical specimens, were used.

Table 4
X-ray diffraction parameters used for residual stress measurements.

Detector	Tube target	Aperture size	Diffraction plane
2D	Cr (λ = 2.085 Å)	1 mm	{3 1 1}
Bragg angle (2θ)	XEC ($\frac{1}{2}S_2$)	Nb of inclination	Exposure time
148.2°	7.41×10^{-6} MPa^{-1}	1	90 s

Table 5
Surface roughness prior to test for the studied surface conditions. Three longitudinal measurements were performed per sample.

	As machined	S230 4 A	CW14 4 A	CW14 8 A
Nb of samples	15	6	6	6
R_t (μm) average (standard deviation)	7.15 (3.27)	8.65 (3.34)	11.90 (1.13)	25.38 (3.34)
RSm (μm) average (standard deviation)	246 (15)	362 (66)	328 (17)	405 (34)

2.5. Cold work measurement calibration

The XRD technique was also used to measure the extent of cold work caused by shot peening through diffraction peak broadening since this parameter is proportional to the dislocation dentsity [28]. Prevéy [29] has shown that the peak broadening is independent of the plastic deformation path and can be used as an independent measurement of the local strain in Inconel 718. Calibration was performed using an interrupted tensile test with the Kammrath & Weiss GmbH micro-tensile machine paired up with the Pulstec μ-X360n apparatus used for residual stress measurements. A flat micro-tensile specimen, obtained from the same stock as the fatigue samples and whose geometry is presented in Fig. 2(c), was prepared by grinding. A final layer of 10 μm was removed by electro-polishing to eliminate potential plastic deformation introduced by grinding. XRD measurements were performed up to 19% of true strain, as the striction took place for higher strain values. The diffraction peaks were recorded and fit using the Lorentzian method [24] to extract peak width at half of the diffraction maximum intensity (Full Width at Half the Maximum (FWHM)). X-ray measurements were repeated 3 times.

3. Results

3.1. Surface characteristics prior to fatigue tests

3.1.1. Surface roughness

Surface roughness measurements and SEM observations of specimens surfaces are presented in Table 5 and Fig. 3, respectively. The roughness parameters presented are the maximum peak to valley distance (R_t) and the mean width of roughness profile features (*RSm*) since the stress concentration induced by the dimples on a specimen's surface depends on their depth and width [2].

The average R_t of the as machined samples is 7.15 μm. As can be observed from Fig. 3(b), the dimples created by the S230 media at an intensity of 4 A only partially erased the machining marks created by the turning process and slightly increased R_t to 8.65 μm. CW14 shot peening condition at the same intensity increased the R_t value up to 11.90 μm and the SEM observation (Fig. 3(c)) still shows the presence of remaining machining marks. The surface appears to be more deformed than that obtained from the S230 4 A condition, which is consistent with the higher R_t measurements. The machining marks were totally erased when peening with CW14 at an intensity of 8 A, as seen in

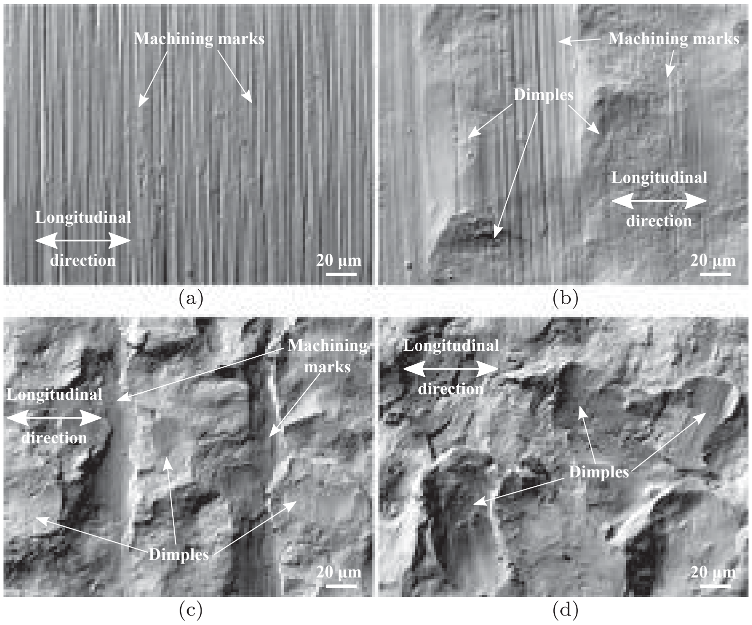

(a) (b)

(c) (d)

Fig. 3. SEM picture of (a) as machined, (b) S230 4 A, (c) CW14 4 A, (d) CW14 8 A samples surface prior to fatigue testing. Machining marks are still present after S230 4 A and CW14 4 A shot peening.

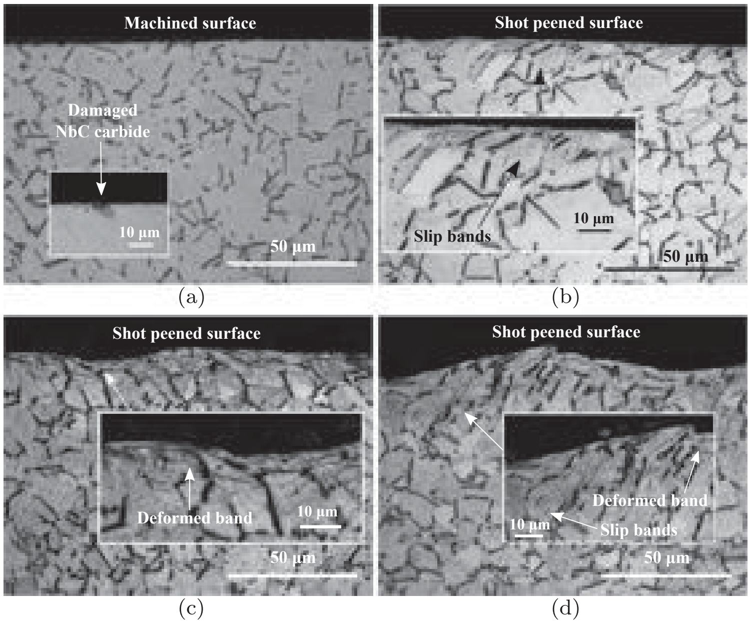

Fig. 4. Pre-testing cross section optical micrographs of samples in the (a) as machined, (b) S230 4 A, (c) CW14 4 A and (d) CW14 8 A conditions. An optical micrograph of a damaged surface carbide taken on a non etched cross section of another as machined specimen is encapsulated in (a) to show that surface NbC carbides damaged by the machining process were found. Encapsulated zoom on persistent slip bands and deformed bands are also present in (b), (c) and (d).

Fig. 3(d). Moreover, the surface's deformation appears to be more significant for this condition than for the others.

These results are consistent with the shot peening media size and the level of kinetic energies calculated in Table 3. In particular, S230 shot peening media is smaller and has less kinetic energy than the CW14 media for the same 4 A peening intensity. This situation results in smaller penetration for the S230 shot peening media, when compared to that of the CW14 media, and a lower average R_t is obtained.

All peening conditions increased the *RSm*. Peening with CW14 at an intensity of 8 A led to the highest *RSm*, in accordance with its higher shots kinetic energy.

3.1.2. Cross sections observations

Cross sections of as machined, S230 4 A, CW14 4 A and CW14 8 A samples were polished and etched to observe the effect of shot peening on the surface and subsurface microstructure. The micrographs are presented in Fig. 4. Damaged NbC carbides were observed on the as machined specimen surfaces, as shown in Fig. 4(a) inset. This observation is consistent with the works of Zhou et al. [11] that showed that machining can damage surface carbides. No evidence of plastic deformation was observed on the as machined cross section (Fig. 4(a)).

S230 4 A and CW14 8 A specimens present persistent slip bands in the first 10 and 25 μm below the surface (Fig. 4(b) and (d)), respectively. Continuous bands of highly deformed material are visible at the surface of CW14 4 A and 8 A specimens, as pointed out by the arrows in Fig. 4(c) and (d). The qualitative amount of plastic deformation visually observed is consistent with the shots kinetic energy (Table 3): higher kinetic energy resulted in more plastic deformation.

Micro-hardness profiles were performed on the cross sections of shot peened specimens. The micro-harness profiles are presented in Fig. 5. The base material had an hardness of 472 HV. Fig. 5 shows that hardening is clearly observable for the CW14 8 A shot peening condition for which the hardness reached the maximum value of 524 HV at the surface and decreased until reaching the base material's hardness at a depth of roughly 125 μm. No evidence of hardening was detected near the surface for the S230 4 A and CW14 4 A shot peening conditions. It might be due to the fact that the measurements could not be performed sufficiently close to the shot peened surface.

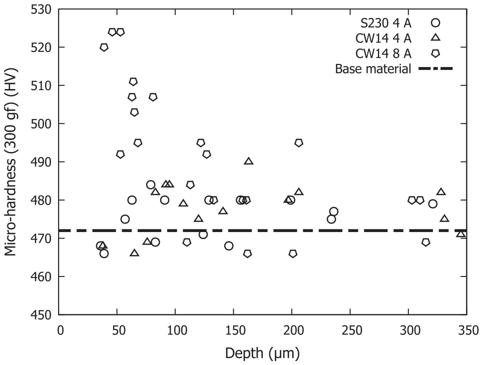

Fig. 5. After shot peening micro-hardness profiles. The 472 HV base material hardness is also represented.

3.1.3. Residual stress and cold work profiles

FWHM versus the plastic strain obtained on the micro-tensile specimen is plotted in Fig. 6. As proposed in the work of Prevéy [29], the relationship between FWHM and the plastic strain, ε_p, was approximated as

$$FWHM = H\,[1-e^{-I\varepsilon_p}] + J\varepsilon_p + K \qquad (1)$$

where H,I,J and K are fitting constants determined by a least square

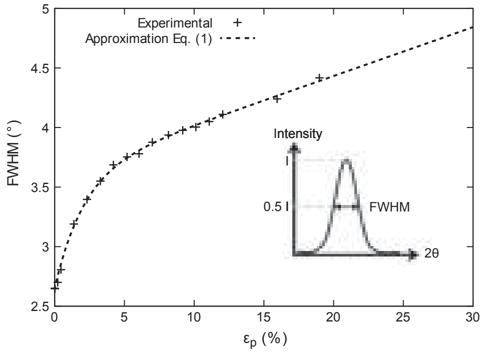

Fig. 6. FWHM as a function of the plastic strain and its approximation by Eq. (1). A schematic of the FWHM determination is encapsulated.

Table 6
Fitting constants obtained for Eq. (1).

H	*I*	*J*	*K*
0.9622	0.4808	0.0410	2.65

Table 7
Summary of the results presented in Fig. 7. σ_{surf}: Residual stress at the surface. $\sigma_{\text{comp,max}}$: maximum compressive residual stress. $d_{\sigma_{\text{comp,max}}}$: depth of the maximum compressive residual stress. $d_{\sigma_{\text{comp}=0}}$: depth at which the residual stresses become tensile.

	Polished	As machined	S230 4 A	CW14 4 A	CW14 8 A
		Residual stress profiles			
σ_{surf} (MPa)	−119	−468	−859	−936	−868
$\sigma_{\text{comp,max}}$ (MPa)	−119	−468	−885	−1020	−1019
$d_{\sigma_{\text{comp,max}}}$ (μm)	0	0	19	19	14
$d_{\sigma_{\text{comp}=0}}$ (μm)	–	38	123	117	210
		Cold work profiles			
ε_p (%)	0.72	5	36	51	56
Profile depth (μm)	11	32	123	123	195

regression. Table 6 lists the best fitting values, whose plot is also shown in Fig. 6. The figure reveals that an excellent agreement was found and we believe that FWHM values for plastic strains above 20% can be extrapolated from Eq. (1). The depth of the cold work profile is defined herein as the depth at which the cold work value becomes lower than 0.2%.

The residual stress and cold work profiles prior to fatigue testing are presented in Fig. 7. Table 7 lists key residual stress measurements for comparison purposes.

The polished sample exhibited a compressive surface residual stress of −119 MPa decreasing to −40 MPa at 10 μm below the surface. The maximum compressive residual stress for the as machined specimen was −468 MPa at the surface and after the depth of 38 μm, the residual stresses are tensile staying in the range of ± 50 MPa.

The residual stresses profiles shapes for the shot peened specimens are similar to those commonly found in the literature. Surface residual stresses (σ_{surf}) and maximum compressive stresses depth ($d_{\sigma_{\text{comp,max}}}$) are not significantly affected by the shot peening intensity, nor by the type of media for the studied conditions. CW14 4 and 8 A shot peening led to comparable maximum compressive residual stresses ($\sigma_{\text{comp,max}}$), while peening with S230 4 A condition resulted in a lower value. The saturation value of maximum compressive residual stress is −1020 MPa, which corresponds to 88% of $\sigma_{y0.2\%}$. Similar values were found by Gao et al. [30] on shot peened 4340 steel samples with a saturation value of roughly 86% of $\sigma_{y0.2\%}$. The depth at which the residual stresses becomes tensile ($d_{\sigma_{\text{comp}=0}}$) is the same for the two 4 A conditions ($\simeq 120$ μm) and is deeper for the CW14 8 A specimen (210 μm). The CW14 8 A specimen exhibits a tensile residual stress peak of 157 MPa at a distance of 230 μm below the surface.

Fig. 7(b) presents the in-depth cold work distribution. The polished specimen shows almost no cold work (0.72% at the surface). The as machined specimen exhibits 5% of cold work at its surface and is free of cold work at a depth of 32 μm. The S230 4 A sample exhibits 36% of cold work at the surface while this value increases to 51% and 57% when peening with CW14 4 A and 8 A, respectively. The shot peened specimens cold work profiles end ($\varepsilon_p < 0.2\%$) at a depth of 123 μm for S230 and CW14 4 A samples while this value is increased to 195 μm for the CW14 8 A specimen.

The surface cold work is consistent with the shots kinetic energy: the higher the shots kinetic energy, the higher the surface cold work. The cold work profiles depths appear to be similar to the depth of the compressive residual stresses.

Note that no comparison between the hardness profiles presented in Fig. 5 and the cold work profiles presented in Fig. 7(b) can be clearly made.

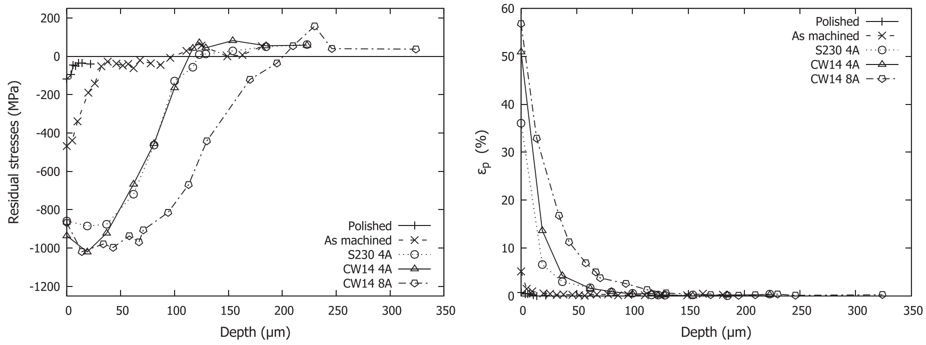

(a) (b)

Fig. 7. Samples in-depth (a) residual stresses and (b) cold work profiles prior to test. Lines are displayed to ease the analysis but are not representative of physical phenomena.

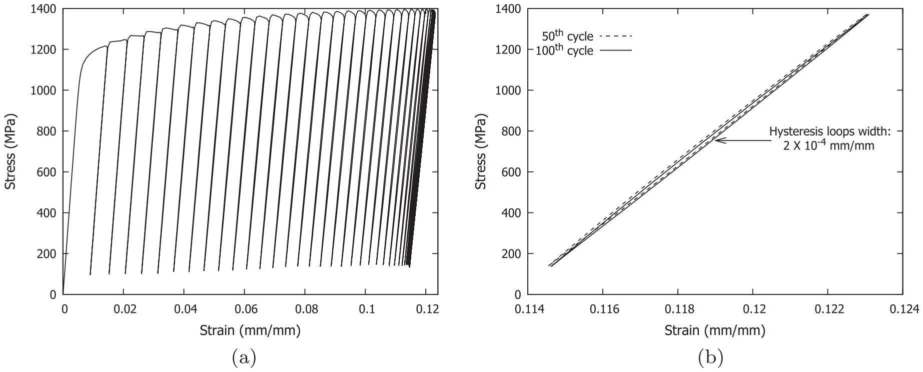

Fig. 8. Deformation versus stress for a sample tested at $\sigma_{max} = 1370$ MPa: (a) from the 1^{st} to the 100^{th} cycle and (b) the 50^{th} and the 100^{th} cycles. Plastic deformations in the form of 2×10^{-4} mm/mm width hysteresis loops are observed during the loading and unloading phases after 50 cycles.

3.2. Fatigue results

3.2.1. LCF results

The stress strain curve of the 100 first loading cycles of a cylindrical specimen tested in LCF are presented in Fig. 8. The material exhibited nearly elastic behavior after 50 cycles since the hysteresis loops have a maximum width of roughly 2×10^{-4} mm/mm for a maximum strain of 0.123 mm/mm.

Fatigue results are presented in Fig. 9. The fatigue results of the surface condition and stress level tested more than 3 times were fitted to a Weibull distribution. The average fatigue lives, the number of cycles leading to a failure probability of 50% and the Weibull distributions shape and scale parameters are presented in Table 8. The lower bounds of the 95% confidence interval for a failure probability of 50% are also provided in Table 8 to inquire on the reliability of the Weibull law predictions. The 95% confidence intervals were computed with a χ^2 test on the logarithm of the likelihood function [31,32]. The linearizations of the Weibull laws are presented in Fig. 10(a) and (b). Typical rupture surfaces and SEM observations of the crack initiation sites are presented in Figs. 11 and 12, respectively.

The fatigue lives obtained at $\sigma_{max} = 1380$ and 1390 MPa for the polished and as machined specimens, and at $\sigma_{max} = 1370$ MPa for the shot peened specimens are shown in Fig. 9(a). The polished specimens present the longest average fatigue life ($\simeq 2 \times 10^4$ cycles) followed by 4

Table 8
Weibull statistical description of the fatigue tests results. Nb: number of specimens. Av. N_f: average fatigue life. Fatigue tests conditions for which the number of tested specimens was inferior to 3 were not considered. The shape (β) and scale (λ) parameters were determined with the linearization of the Weibull laws presented in Fig. 10. The number of cycles for 50% probability (prob.) of failure following the Weibull law are provided. The lower bounds (LB) of 95% confidence (conf.) interval for 50% probability of failure are also listed.

Surface condition	Nb	Av. N_f (cycles)	Scale parameter λ	Shape parameter β	50% prob. failure (cycles)	50% LB 95% conf. (cycles)
			LCF: $\sigma_{max} = 1370$ MPa			
S230 4 A	10	1.65×10^4	1.72×10^4	16.2	1.68×10^4	1.66×10^4
CW14 4 A	10	1.57×10^4	1.61×10^4	18.2	1.58×10^4	1.56×10^4
CW14 8 A	10	1.24×10^4	1.27×10^4	25.8	1.25×10^4	1.23×10^4
			HCF: $\sigma_{max} = 1100$ MPa			
Polished	4	9.91×10^4	1.00×10^5	39.4	9.94×10^4	9.82×10^4
As machined	4	8.56×10^4	9.29×10^4	5.0	8.64×10^4	7.68×10^4
S230 4 A	7	2.02×10^6	2.06×10^6	20.9	2.03×10^6	1.99×10^6
CW14 4 A	9	2.09×10^6	2.14×10^6	22.5	2.10×10^6	2.08×10^6
CW14 8 A	9	4.45×10^5	5.01×10^5	3.0	4.43×10^5	4.03×10^5

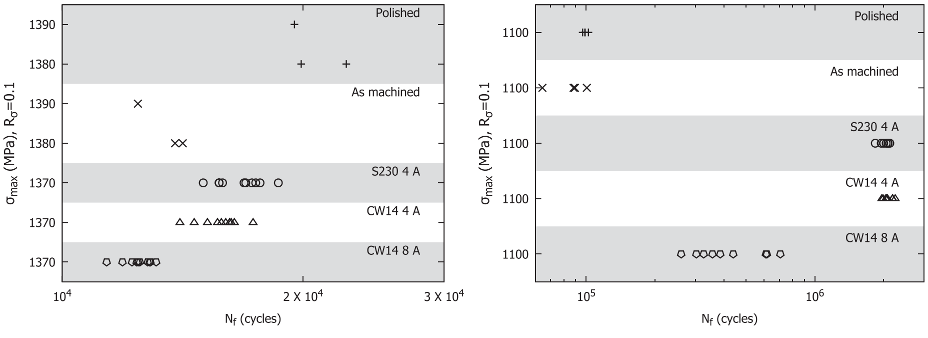

(a) (b)

Fig. 9. SN curve results: (a) Fatigue results under LCF conditions, (b) fatigue results under HCF conditions. Note that the surface conditions have been disposed one upon another for the sake of clarity and to allow for a better comparison. Each horizontal grey/white band represents one surface condition tested at the σ_{max} specified on the vertical axis.

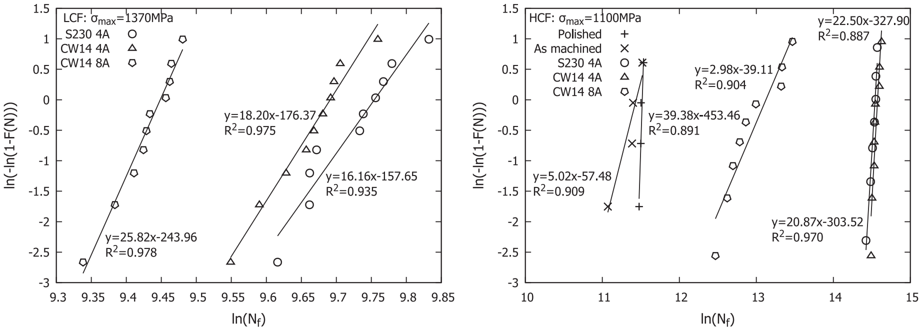

(a) (b)

Fig. 10. Linearization of the Weibull law in (a) LCF and (b) HCF. The median ranks were estimated with the Bernard's approximation: $F(N) = (n°-0.3)/(nb + 0.4)$. n°: number of the specimen. nb: total number of specimens for one condition.

A shot peening conditions (1.59×10^4 and 1.57×10^4 cycles for S230 and CW14, respectively), as machined ($\simeq 1.30 \times 10^4$ cycles) and CW14 8 A (1.24×10^4 cycles). The shot peened specimens average fatigue lives are consistent with the specimens roughness presented in Table 5: The rougher the surface, the lower the fatigue life.

It was not possible to draw statistical conclusion from polished and as machined specimens since too few specimens were tested. However, the number of available data points enabled predicting the number of cycles for a 50% probability of failure (median life) for the shot peened specimens with a Weibull distribution and acceptable regressions were found (Fig. 10). The median lives follow the same trend as the average fatigue lives and provide, with the lower bounds of the 95% confidence intervals, an assessment of fatigue life dispersion. The closer is the lower bound of the 95% interval to the median life, the lower is the dispersion. All the shot peening parameters are robust in LCF since all the 95% confidence interval lower bounds of the 50% probability of failure are very close to the computed median fatigue life, with a difference of less than 2% for each case.

All specimens tested in LCF presented similar rupture surfaces. A typical example is presented in Fig. 11(a). The figure shows the main crack initiation zone containing ratchet marks, sign of several nucleation sites as pointed out by the arrows.

Table 9 summarizes the SEM observations and the corresponding fatigue lives. The fracture surfaces of one polished and one as machined specimens were observed after LCF testing. The shot peened specimen that had the longest fatigue life (1.86×10^4 cycles) and that having the shortest fatigue life (1.14×10^4) were also observed. All rupture surfaces observed under SEM show that cracks initiated either at a surface NbC

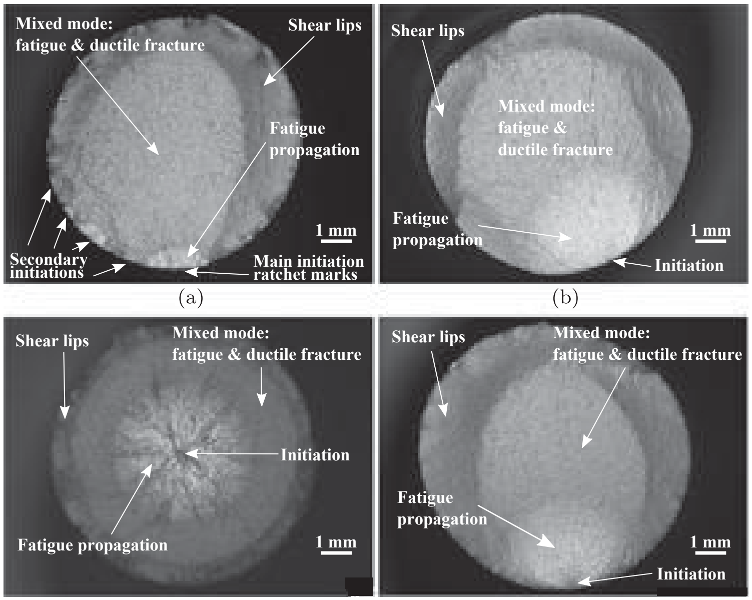
Mixed mode:
fatigue & ductile fracture
Shear lips
Fatigue
propagation
1 mm
Secondary
initiations
Main initiation
ratchet marks
Shear lips
Mixed mode:
fatigue &
ductile fracture
Fatigue
propagation
1 mm
Initiation
Shear lips
Mixed mode:
fatigue & ductile fracture
Initiation
Fatigue propagation
1 mm
Shear lips
Mixed mode:
fatigue & ductile fracture
Fatigue
propagation
1 mm
Initiation

(a) (b) (c) (d)

Fig. 11. Rupture surfaces: (a) All surfaces conditions at $\sigma_{max} \geqslant 1370$ MPa (here a CW14 4 A specimen), (b) Polished and as machined samples at $\sigma_{max} = 1100$ MPa, (c) Shot peened CW14 4 A and S230 4 A at $\sigma_{max} = 1100$ MPa, (d) Shot peened CW14 8 A at $\sigma_{max} = 1100$ MPa.

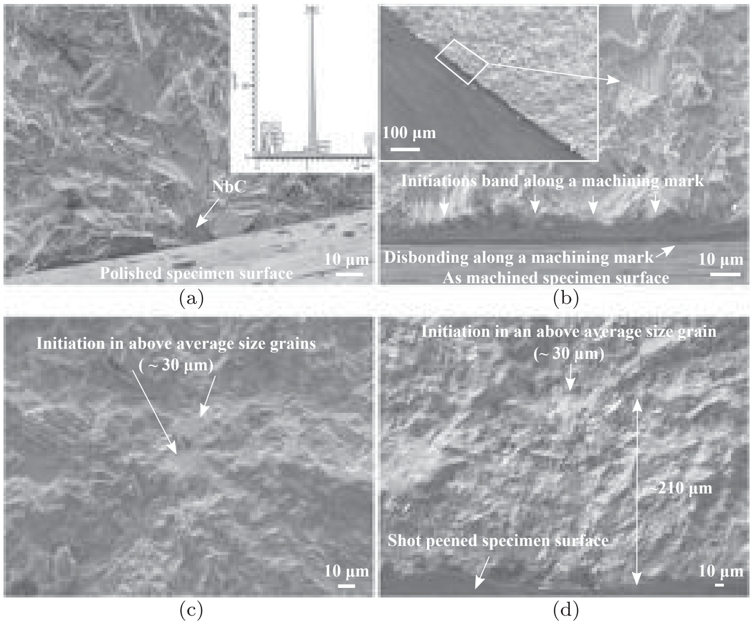
NbC
Polished specimen surface
10 µm
100 µm
Initiations band along a machining mark
Disbonding along a machining mark
As machined specimen surface
10 µm
Initiation in above average size grains
(~ 30 µm)
10 µm
Initiation in an above average size grain
(~ 30 µm)
~210 µm
Shot peened specimen surface
10 µm

(a) (b) (c) (d)

Fig. 12. Various initiations observed under scanning electron microscope: (a) Initiation at a niobium carbide located at a polished specimen surface tested in HCF, the carbide EDX spectrum is inset, (b) Multiple initiations along a surface stress concentration feature on a machining mark. A machining mark disbonding can also be observed in this as machined sample tested in LCF, (c) Crack initiation at an above average size grain in the center of a S230 4 A specimen tested in HCF, (d) Crack initiation in an above average size grain 210 µm underneath the surface in a CW14 8 A specimen tested in HCF.

Table 9
Summary of the initiation features observed under scanning electron microscope. NbC: initiation at a niobium carbide. Surf. conc.: initiation due to stress concentration along a surface defect (machining mark or shot peening dimple). Center: initiation in the center of the specimen. Subsurf.: initiation at roughly 210 µm underneath the surface. The fatigue lives (N_f) of the observed specimens are also presented.

	Polished	As machined	S230 4 A	CW14 4 A	CW14 8 A
		LCF: $\sigma_{max} \geqslant 1370$ MPa			
Initiation	NbC	Surf. conc.	NbC	–	Surf. conc.
N_f (cycles)	2.24×10^4	1.38×10^4	1.86×10^4		1.14×10^4
		HCF: $\sigma_{max} = 1100$ MPa			
Initiation	NbC	NbC	Center	Center	Subsurf.
N_f (cycles)	1.02×10^5	1.01×10^5	1.84×10^6	2.19×10^6	6.17×10^5
Initiation	NbC	Surf. conc.	–	–	Subsurf.
N_f (cycles)	9.65×10^4	6.43×10^4			2.6×10^5

carbide (Fig. 12(a)) or at a stress concentration caused by surface irregularities such as machining marks (Fig. 12(b)).

3.2.2. HCF results

HCF ($\sigma_{max} = 1100$ MPa) fatigue testing results are shown in Fig. 9(b). When compared to as machined specimens average fatigue life (8.56×10^4 cycles), the average fatigue life was increased by a factor of 4.5 for the CW14 8 A specimens (4.45×10^5 cycles) and by up to 20 for the S230 and CW14 4 A shot peening conditions (2.02 and 2.09×10^6 cycles, respectively).

The median fatigue lives follow the same trend as those for the average fatigue lives. Despite the fact that only 4 specimens were tested under the polished conditions, the dispersion in the results is very low since the lower bound of the 95% confidence interval on the median life is only 1.2% lower than the predicted median life. The as machined conditions shows a large dispersion in the results (Fig. 9(a)) and the lower bound of the 95% confidence interval is 11% lower than the median life. S230 and CW14 4 A fatigue lives are highly predictable in HCF since the lower bounds of the 95% confidence interval of the median lives are less than 2% lower than the computed median life. On the other hand, the lower bound of the 95% confidence interval of the CW14 8 A median life is 9% lower than the computed median life, corresponding to a wider dispersion in the results for this loading condition. S230 and CW14 4 A are thus the most robust shot peening conditions and those resulting in the longest fatigue lives in HCF.

Table 9 summarizes the SEM observations. For each surface condition, the specimens that had the longest and the shortest fatigue life were observed. S230 and CW14 4 A were not studied separately because their rupture surfaces and fatigue lives were similar. The experimental data resulting from these two peening conditions were pooled.

In HCF, polished and as machined rupture surfaces were characterized by one or two distinct surface crack initiation sites, as shown in Fig. 11(b). Table 9 shows that all the crack initiations observed under SEM occurred at a surface NbC carbide for polished specimens, as illustrated in Fig. 12(a). The observed crack initiations for the as machined specimens were either located at a surface carbide or at a machining mark, as shown in Fig. 12(b).

All the S230 and CW14 4 A specimens tested in HCF show crack initiations located at depth above 2 mm, as illustrated in Fig. 11(c). SEM observations made on two specimens show that crack initiation occurred in a larger than average (≃ 30 µm) grain, as illustrated in Fig. 12(c). All CW14 8 A specimens show crack initiations just beneath the surface, as shown in Fig. 11(d). For this shot peening condition, the crack initiation occurred in a larger than average (≃ 30 µm) grain at a depth of roughly 210 µm (Fig. 12(d)) for the two specimen observed. This depth corresponds to the depth of the tensile residual stresses peak observed in Fig. 7.

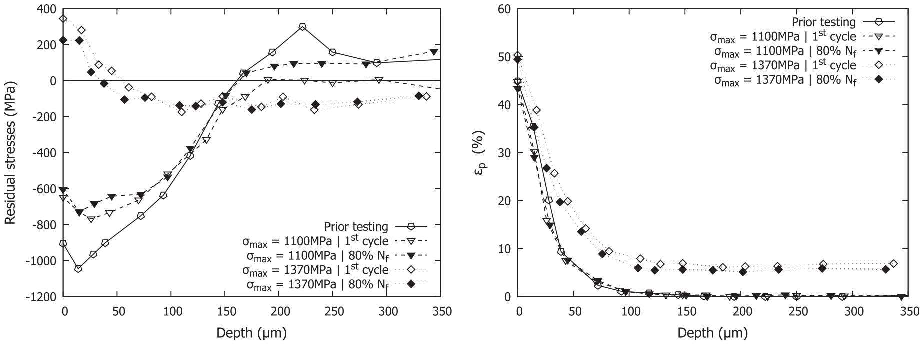

(a) (b)

Fig. 13. (a) Residual stress and (b) cold work relaxation profiles for the CW14 8 A condition. Measurements were realized before testing, after the first cycle and at 80% of the fatigue life (N_f). Lines are displayed to ease the analysis but are not representative of physical phenomena.Recall that the calculated average errors on XRD measurements is 80 MPa.

3.3. Residual stresses redistribution for CW14 8 A

Residual stress and cold work redistribution were measured in LCF ($\sigma_{\max} = 1370$ MPa) and HCF ($\sigma_{\max} = 1100$ MPa) on rectangular cross section specimens shot peened with CW14 8 A only. XRD measurements were performed before and after the first loading cycle, as well as at 80% of the fatigue life previously determined for both fatigue conditions on cylindrical specimens. Each stress profile was obtained from a different specimen. Residual stress and cold work profiles are presented in Fig. 13(a) and (b), respectively.

The initial profiles of residual stress are similar for both the rectangular and cylindrical samples. However, Fig. 13(a) shows higher tensile residual stresses in the rectangular specimen (100 MPa instead of 40 MPa). This is mainly attributable to the difference in thickness between the two geometries and the smaller volume available to balance the compressive residual stresses. Indeed, the surface compressive residual stresses are balanced by nearly constant tensile residual stresses in the core material [33] and thus the thicker the specimen, the lower the tensile residual stresses. The value of the tensile residual stress peak is also higher (300 MPa instead of 157 MPa) but located at the same depth as that of the cylindrical specimen. On the other hand, the surface pre-testing cold work value of the flat specimen for CW14 8 A (45%) is lower than that of the cylindrical samples (57%).

As observed in Fig. 13(a), most of the stress profiles evolution occurred in the first loading cycle as the difference between stresses characterizing the first cycle and 80% of the fatigue life is in the range of the measurement errors (≈ 80 MPa).

In LCF, due to the high level of applied stress, the compressive residual stresses become tensile at the surface (similar results were already reported in the literature [34]). The bulk of the material is plastically deformed. As surface layers have already been hardened by shot peening and are under a bi-axial residual compressive state, they are unlikely to undergo plastic deformation. The bulk material, which undergoes yielding during the first cycle, is permanently deformed and maintains the surface layers in tension when the axial stress is removed. This results in the formation of tensile residual stresses at the surface.

In HCF, after the first loading cycle, the compressive portion of the profile becomes less compressive. The maximum compressive stress value, which is initially at -1044 MPa, relaxes to -767 MPa after the first cycle and -728 MPa at 80% of the fatigue life, which corresponds to a 27 and 30% relaxation, respectively. The tensile residual stress peak vanishes after the first cycles, which suggests that local yielding occurs, leading to the relaxation of the residual stresses. The residual stresses profile depth (150 μm) remains unaltered.

The associated cold work profiles, which are presented in Fig. 13(b), remain stable during HCF. However, in LCF, the overall cold work increases confirming that plasticity occurs during the first loading cycle throughout the material.

4. Discussion

LCF and HCF results are discussed separately to better emphasize the specific effect of shot peening on fatigue life and crack initiation mechanisms.

4.1. LCF

Three distinctive surface characteristics could influence the LCF of the shot peened specimens: roughness, residual stresses and cold work. In order to qualitatively determine the influence of the surface roughness, Fig. 14(a) presents the fatigue life, at $\sigma_{max} = 1370$ MPa, for 14 shot peened samples plotted against the measured roughness parameters R_t. A correlation between the surface roughness and the fatigue life can be made: The higher the R_t, the lower the fatigue life. In this case, all crack initiated at the surface since no compressive residual stress could compensate the roughness induced stress concentration. Recall that the surface layer's residual stresses become tensile after the first loading cycle. Shot peening has a detrimental effect for the LCF conditions tested in this study.

Despite the surface tensile residual stresses and the increase in roughness resulting from shot peening, the average fatigue life of the shot peened specimens is not drastically lower than that of the unpeened specimens. Apparently, the surface cold work can partially counterbalance the negative effects of roughness and tensile residual stresses by increasing the resistance to plastic deformation. Work hardening can delay crack nucleation on one hand, and on the other hand, the crack tip's plastic zone size will be reduced resulting in lower short crack growth rate [1,35]. Fig. 14(b) represents the fatigue life of the same 14 shot peened specimens against the surface cold work value. The figure shows that the cold work surface value did not improve the number of cycles to failure.

4.2. HCF

In HCF, only the compressive residual stresses below -700 MPa have relaxed somehow during the first cycle. The compressive residual stresses introduced by shot peening remain effective so that for all shot peened specimens, crack initiation occurred underneath the surface. The predominant parameters for the site of crack nucleation are the size of grains and the position of an eventual tensile peak in the residual

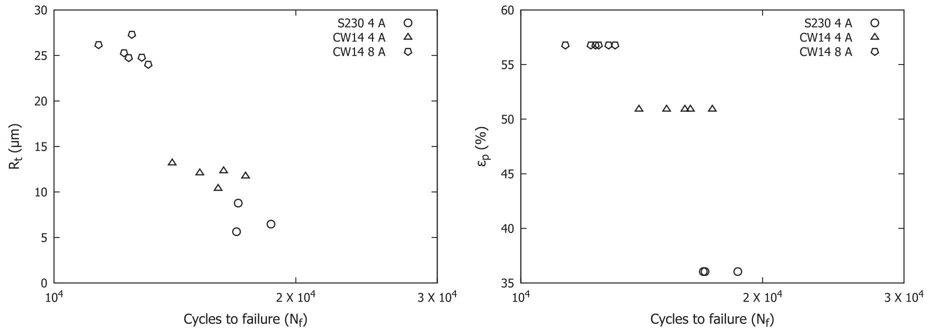

(a) (b)

Fig. 14. Shot peened samples fatigue lives at $\sigma_{max} = 1370$ MPa versus (a) the surface roughness parameters R_t and (b) the surface cold work value. A correlation between R_t and the fatigue life under LCF condition can be observed: the lower the roughness, the better the fatigue life. A relation between the fatigue life and the surface cold work value cannot be clearly drawn.

stress profile introduced by shot peening, even if it seems to disappear after the first loading cycle. Recall that the uncertainty on our residual stresses measurements was of ± 80 MPa and that a tensile region must be present to balance the compressive residual stresses. Surface cold work and compressive residual stresses, which are the two benificial effects of shot peening, push the site of crack initiation underneath the surface, counterbalancing the detrimental effect of surface roughness.

In the case of S230 and CW14 4 A shot peening conditions, cracks initiated deep inside the material, in a large grain. Cracks initiated at depth above 2 mm where the residual stresses are negligible. The fatigue life dispersion of these samples is very low as the initial cracks are arising from a large volume of potential sites. The small scatter in the results suggests robust manufacturing parameters. Moreover, the average fatigue life is improved by a factor of 20, when compared to the polished specimens. With such improvement, 4 A shot peening conditions (S230 or CW14) illustrate the full potential of the material since the initiation occurred in a microstructural weakness regardless of surface defects (roughness, NbC carbides) and tensile residual stresses. The microstructural weakness becomes an above the average size grain and most likely a grain with twin boundaries, as suggested by Stinville et al. [15]. The local high strains are due to the resistance in slip transmission from a border of the twin boundary to the other one, resulting in slip bands parallel to the twin boundary where crack will nucleate preferentially. The size of the grain is controlling the free distance of the dislocations and thus larger grains will also promote early crack nucleation. Miao et al. [16] reported, in René 88DT, that initiation along twin boundary appeared in grains 3 times larger than average, as in this study. Stinville et al. [17], as well as Miao et al. [14], demonstrated that a large grain having a high Schmid factor and a twin boundary aligned with the slip systems are the criteria for crack initiations in plain materials.

The compressive residual stresses at the surface and beneath it for the CW14 8 A peening condition improved the fatigue life average by a factor of 4.5, when compared to polished specimens. When compared to the 4 A peening conditions, the samples seem to be "over peened" as the full potential of the process is not reached. As in the previous cases, cracks systematically initiated in grains significantly larger than the average grain size. These crack initiations were found in a narrow region at roughly 210 µm beneath the surface. This position, 210 µm beneath the surface, corresponds to the tensile residual stress peak after peening. However, the tensile residual stress peak seems to disappear after the first cycle due to local yielding. This local yielding will lead to high strains along favorably oriented coherent twin boundaries in large grains [15] and thus will accelerate the accumulation of dislocations leading to early crack nucleation, when compared to randomly oriented grains. At this 210 µm depth, a relatively small number of grains are potential nucleation sites when compared to the S230 4 A and CW14 4 A conditions for which crack initiation occured at depths higher than 2 mm. This situation favors a wider results dispersion for the CW14 8 A condition. Shot peening parameters should thus be chosen in order to avoid a subsurface tensile residual stress peak after peening.

5. Conclusions

Force controlled fatigue tests at $R_\sigma = 0.1$ were performed in HCF and LCF on polished, as machined, S230 4 A, CW14 4 and 8 A shot peened Inconel 718 samples. The initial surface roughness, surface microstructure alteration, initial and redistributed residual stresses profiles, cold work profiles and rupture surfaces were presented and analyzed. The analysis of the results led to 3 important conclusions:

1. Shot peening effects on fatigue life are different in LCF and HCF. In LCF, roughness seems to be the dominant parameter that controls fatigue life improvement while the presence of significant residual stresses is the controlling factor in HCF.
2. In LCF, residual stresses redistribute during the first loading cycle to become tensile and are detrimental to the fatigue life. Under this condition, a negative relation between surface roughness and the logarithm of the fatigue life was shown. These two drawbacks are partially counterbalanced by the surface cold work introduced by shot peening as the tensile residual stresses do not significantly reduce the fatigue life.
3. In HCF, all nucleation sites were located in subsurface grains three times larger than the average grain size. CW14 8 A shot peening led to an improvement of the average fatigue life by a factor of 4.5, but with a large scatter, and crack initiated systematically at the depth corresponding to the presence of the tensile peak in the residual stress profile after shot peening. Even if the tensile residual stress peak seemed to disappear from the first cycle due to local yielding, the accumulation of strain (dislocations) in the larger grains, in the yield region, seems to promote early crack initiation. S230 and CW14 4 A are optimal and robust shot peening parameters since no tensile residual stress peak is present in the surface layer and the fatigue lives were improved by a factor of 20 with low dispersion. Crack initiated in the material at microstructural weakness (large grains), regardless of the surface defects and residual stresses profile.

All in all, a too high shot peening intensity (8 A in this work) resulted in deeper compressive residual stress profiles but the resulting increased surface roughness and the presence of a tensile peak in the residual stress profile were found to be drawbacks in LCF and HCF, respectively. Larger media (S230 instead of CW14) and lower intensity (4 A instead of 8 A) will thus be preferred for the studied material in the range of tested cases.

Acknowledgements

This work was financially supported by the Consortium of Research and Innovation in Aerospace in Quebec, the Natural Sciences and Engineering Research Council of Canada, Pratt & Whitney Canada, Bell Helicopter Textron, L3-Communications MAS, Heroux Devtek and Mathematics of Information Technology and Complex Systems (Grant No.: RDC 435539-12).

References

[1] De Los Rios ER, Walley A, Milan MT, Hammersley G. Fatigue crack initiation and propagation on shot-peened surfaces in A316 stainless steel. Int J Fatigue 1995;17(7):493–9.

[2] Li JK, Mei Y, Duo W, Renzhi W. An analysis of stress concentrations caused by shot peening and its application in predicting fatigue strength. Fatigue Fract Eng Mater Struct 1992;15(12):1271–9.

[3] Novovic D, Dewes RC, Aspinwall DK, Voice W, Bowen P. The effect of machined topography and integrity on fatigue life. Int J Mach Tools Manuf 2004;44(2):125–34.

[4] Wagner L. Mechanical surface treatments on titanium, aluminum and magnesium alloys. Mater Sci Eng: A 1999;263(2):210–6.

[5] Prevéy P. The effect of cold work on the thermal stability of residual compression in surface enhanced IN718. Tech Rep, DTIC Document; 2000.

[6] Nakamura H, Takanashi M, Itabashi Y, Kuroki H, Ueda Y. Shot peening effect on low cycle fatigue properties of Ti-6Al-4V and Inconel 718. In: ASME 2011 Turbo Expo: turbine technical conference and exposition, American Society of Mechanical Engineers; 2011. p. 791–7.

[7] Cammett JT, Prevéy PS, Jayaraman N. The effect of shot peening coverage on residual stress, cold work, and fatigue in a nickel-base superalloy. Tech Rep, DTIC Document; 2005.

[8] Maderbacher H, Oberwinkler B, Gänser H-P, Tan W, Rollett M, Stoschka M. The influence of microstructure and operating temperature on the fatigue endurance of hot forged *Inconel®* 718 components. Mater Sci Eng: A 2013;585:123–31.

[9] Ono Y, Yuri T, Sumiyoshi H, Takeuchi E, Matsuoka S, Ogata T. High-cycle fatigue properties at cryogenic temperatures in INCONEL 718 nickel-based superalloy. Mater Trans 2004;45(2):342–5.

[10] Alexandre F, Deyber S, Pineau A. Modelling the optimum grain size on the low cycle fatigue life of a Ni based superalloy in the presence of two possible crack initiation sites. Scripta Mater 2004;50(1):25–30.

[11] Zhou J, Bushlya V, Stahl J. An investigation of surface damage in the high speed turning of Inconel 718 with use of whisker reinforced ceramic tools. J Mater Process Technol 2012;212(2):372–84.

[12] Fournier D, Pineau A. Low cycle fatigue behavior of Inconel 718 at 298 K and 823 K. Metall Trans A 1977;8(7):1095–105.

[13] Klotz T, Blas S, Lévesque M, Brochu M. 1D cyclic yield model independent of load spectrum characteristics and its application to Inconel 718. Mech Mater 2017;109:34–41.

[14] Miao J, Pollock TM, Jones JW. Crystallographic fatigue crack initiation in nickel-based superalloy rené 88DT at elevated temperature. Acta Mater 2009;57(20):5964–74.

[15] Stinville JC, Vanderesse N, Bridier F, Bocher P, Pollock TM. High resolution mapping of strain localization near twin boundaries in a nickel-based superalloy. Acta Mater 2015;98:29–42.

[16] Miao J, Pollock TM, Jones JW. Microstructural extremes and the transition from fatigue crack initiation to small crack growth in a polycrystalline nickel-base superalloy. Acta Mater 2012;60(6):2840–54.

[17] Stinville J, Lenthe W, Miao J, Pollock T. A combined grain scale elastic–plastic criterion for identification of fatigue crack initiation sites in a twin containing polycrystalline nickel-base superalloy. Acta Mater 2016;103:461–73.

[18] ASTM Standard E8M-13a. Standard test methods for tension testing of metallic materials; 2013.

[19] SAE AMS5663M. Nickel alloy, corrosion and heat-resistant, bars, forgings, and rings 52.5Ni–19Cr–3.0Mo–5.1Cb (Nb)–0.90Ti–0.5Al–18Fe consumable electrode or vacuum induction melted 1775 °F (968 °C) solution and precipitation heat treated; 2009.

[20] Xiao L, Chen D, Chaturvedi M. Cyclic deformation mechanisms of precipitation-hardened Inconel 718 superalloy. Mater Sci Eng: A 2008;483:369–72.

[21] ASTM Standard E466-07. Standard practice for conducting force controlled constant amplitude axial fatigue tests of metallic materials; 2007.

[22] SAE AMS2430T. Shot peening, automatic; 2015.

[23] ASTM Standard E384-11. Standard test method for Knoop and vickers hardness of materials; 2011.

[24] Noyan IC, Cohen JB. Residual stress: measurement by diffraction and interpretation. Springer; 2013.

[25] Sasaki T, Hirose Y, Sasaki K, Yasukawa S. Influence of image processing conditions of debye Scherrer ring images in x-ray stress measurement using an imaging plate. Adv X-ray Anal 1997;40:588–94.

[26] Delbergue D, Texier D, Lévesque M, Bocher P. Comparison of two X-ray residual stress measurement methods: Sin2 ψ and cos α, through the determination of a martensitic steel X-ray elastic constant. Materials Res Proc 2016;2.

[27] Moore MG, Evans WP. Mathematical correction for stress in removed layers in X-ray diffraction residual stress analysis. Tech Rep, SAE technical paper; 1958.

[28] Warren B. X-ray diffraction; courier corporation: 1969.

[29] Prevéy PS. The measurement of subsurface residual stress and cold work distributions in nickel base alloys. In: Young WB, editor. Residual stress in design, process and materials selection. Metals Park, OH: ASME; 1987. p. 11–9.

[30] Gao Y, Yao M, Li J. An analysis of residual stress fields caused by shot peening. Metall Mater Trans A 2002;33(6):1775–8.

[31] Bianchetti C, Lévesque M, Brochu M. Probabilistic analysis of the effect of shot peening on the high and low cycle fatigue behaviors of AA 7050-T7451. Sub Int J Fatigue. November 2017.

[32] Abramovich F, Ritov Y. Statistical theory: a concise introduction. CRC Press; 2013.

[33] Menig R, Pintschovius L, Schulze V, Vöhringer O. Depth profiles of macro residual stresses in thin shot peened steel plates determined by X-ray and neutron diffraction. Scripta Mater 2001;45(8):977–83.

[34] Kirk D. Effects of plastic straining on residual stresses induced by shot-peening. (retroactive coverage). Shot Peening: Sci, Technol 1987:213–20.

[35] Miller K. Materials science perspective of metal fatigue resistance. Mater Sci Technol 1993;9(6):453–62.

APPENDIX VIII

EXAMPLE OF *FWHM* VALUES FOR AA7050 AND 300M

Figures-A VIII-1 and VIII-2 present the variation of the *FWHM* values for a given XRD measurement for the AA7050 and 300M, respectively. The AA7050 specimen (Figure-A VIII-1) presents variations over large α range. Whereas the 300M specimen (Figure-A VIII-2) exhibits similar point-to-point variations than the IN718 (Figure 4.4) but with less amplitude.

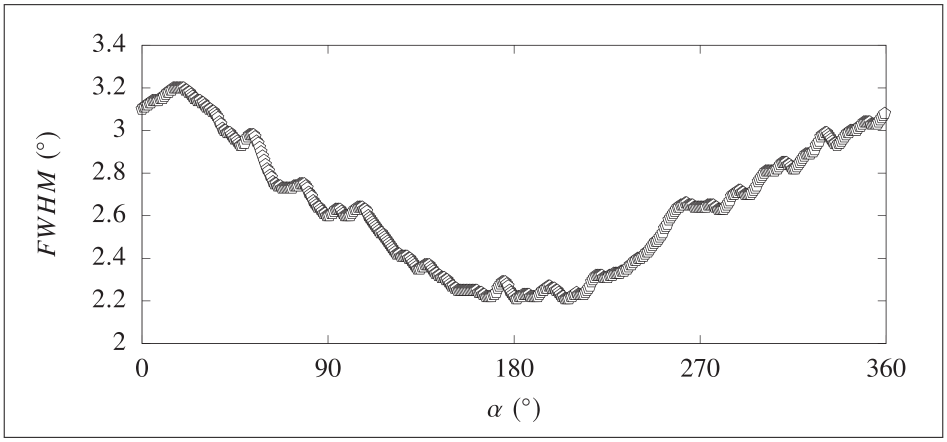

Figure-A VIII-1 *FWHM*-values variation for the α angle describing the Debye ring, for the AA7050 specimen shot peened with S230 at 8 A

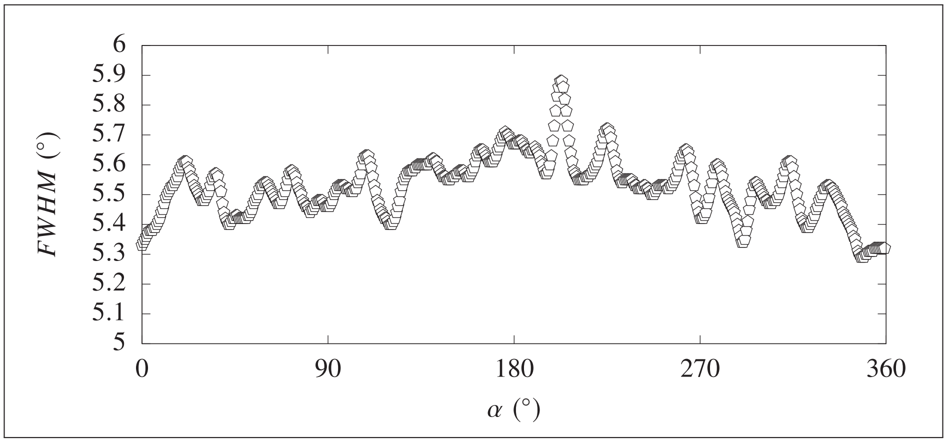

Figure-A VIII-2 *FWHM*-values variation for the α angle describing the Debye ring, for the 300M specimen shot peened with CW14 at 8 A

APPENDIX IX

IN718 - CALIBRATION CURVE OBTAINED AT 700 MPA TRUE ISOSTRESS

The calibration curve obtained for an unloaded specimen (0 MPa true stress) and presented in Figure 4.6 is compared here to a calibration curve obtained for a specimen under a controlled elastic load to show that $FWHM$ values are independent of elastic strains. A 700 MPa true isostress (65% of the initial yield stress) was chosen as elastic loading, as it should not add further plastic deformations. The calibration curve obtained for the XRD measurements performed at 700 MPa true isostress is presented in Figure-A IX-1. The three XRD measurements for each increment of plastic deformation exhibit an identical trend to that obtained in Figure 4.6. The $FWHM$ values obtained at 700 MPa true isostress are found slightly higher that the ones measured at 0 MPa true isostress (unloaded specimen), especially for high cold work values. The custom fitting using Equation (4.1) is also presented. The fitting coefficients for the two calibration curves and their 95% confidence intervals are listed in Table-A IX-1.

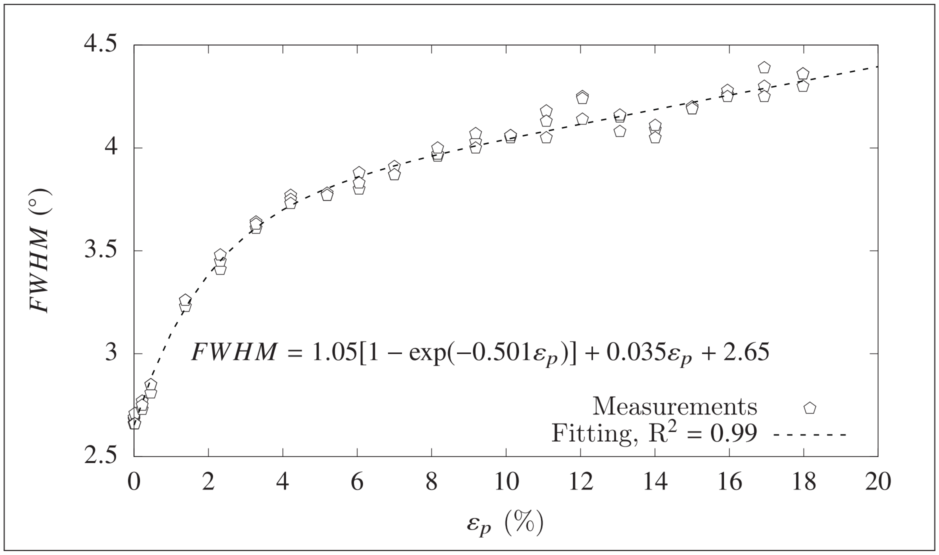

Figure-A IX-1 Calibration curve for the cold work estimation of IN718 obtained for XRD measurements performed at 700 MPa true isostresses

Table-A IX-1 Fitting coefficients obtained for Equation (4.1) and their corresponding 95% confidence intervals $CI_{95\%}$. Coefficients are obtained at 700 MPa and 0 MPa true isostresses

Fitting coefficients	iso 700 MPa		iso 0 MPa	
	Value	$CI_{95\%}$	Value	$CI_{95\%}$
H	1.049	(0.983 , 1.115)	1.075	(1.017 , 1.132)
I	0.5009	(0.4287 , 0.5730)	0.4515	(0.3996 , 0.5034)
J	0.0347	(0.0298 , 0.0395)	0.0313	(0.0271 , 0.0355)
K	2.653	(2.622 , 2.684)	2.623	(2.599 , 2.647)

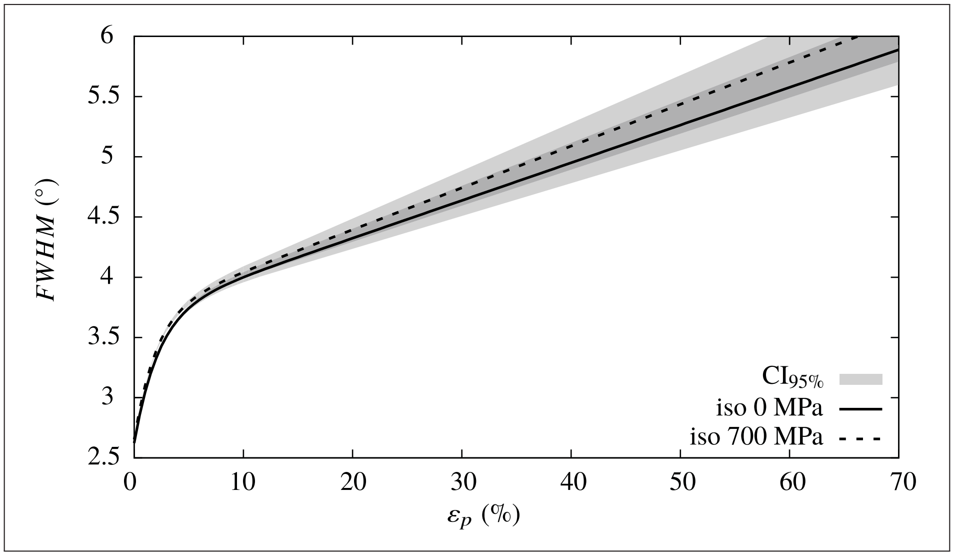

Figure-A IX-2 Comparison of the calibration curves fitting with the 95% confidence interval $CI_{95\%}$ plotted for the slope coefficient J

A better comparison of the two fitting curves is provided in Figure-A IX-2. The curves are extrapolated for cold work values up to 70%. It can be observed that the main difference between the curves is found for the linear portion of the fittings at high cold work values. The y-intercept coefficient K being similar for the two fittings, the 95% confidence interval of the slope coefficient, J, is also presented in grey in Figure-A IX-2 to visualize the effects of the slope value. The two fittings do not appear statistically different when considering the 95% confidence intervals, as they largely superimpose, which proves that the *FWHM* values are independent of elastic strains.

APPENDIX X

EBSD CENTER MAP OF 300M STEEL

An EBSD scan was performed at the center of the CW14 specimen using the same parameters. The final map size is $47\times63\,\mu m^2$ using a step size of 0.15μm. Grains were detected using a grain detection angle of 10°. Figure-A X-1 presents the orientation distribution with respect to the RD. A similar microstructure than the one found far from the shot peened surface (Figure 4.22) can be observed.

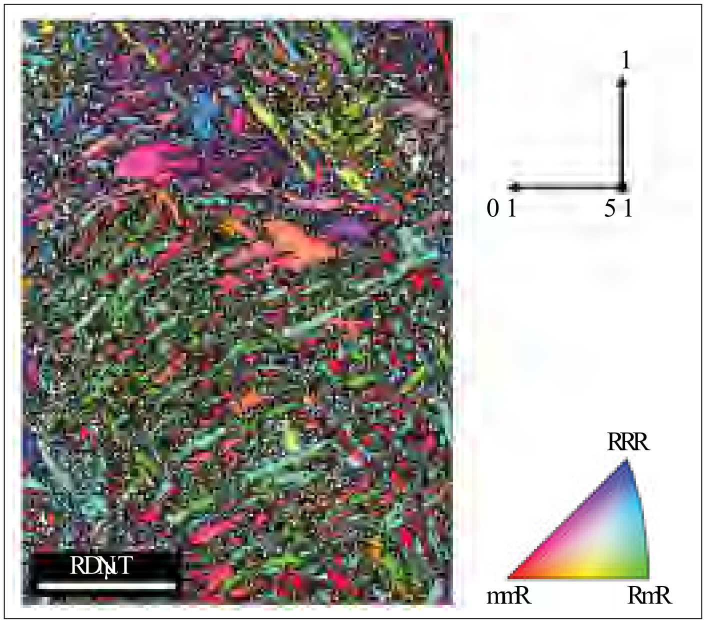

Figure-A X-1 Orientation map of the CW14 specimen's center represented as IPF map with respect to the RD

The kernel average misorientation (KAM) values were computed using a upper threshold angle of 10° and for the 1^{st} neighbor order. Figure-A X-2 presents the KAM map obtained for the CW14 specimen's center. The average of the KAM values for a given depth (lines perpendicular to the ND) are also exhibited in the graph below the KAM map. Contrary to the subsurface EBSD scan (Figure 4.24) the KAM values are found quasi-constant. The average and SD of the KAM values are 1.06° and 0.14°, respectively.

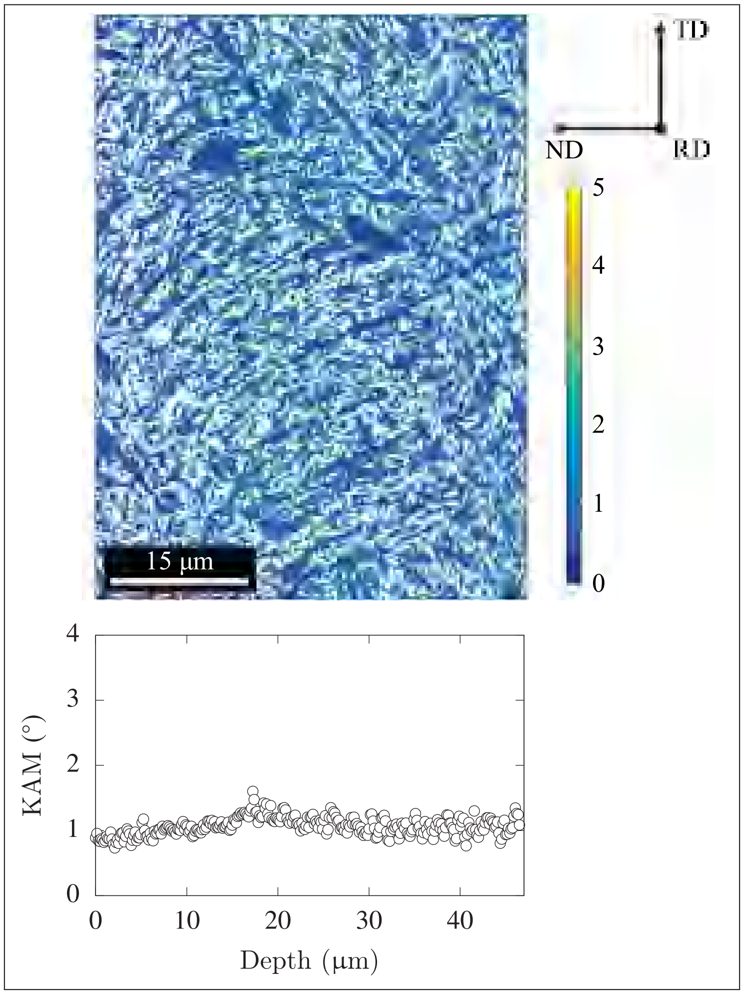

Figure-A X-2 Kernal average misorientation (KAM) map, for the CW14 specimen's center, computed for the 1st neighbor order and a 10° threshold angle and evolution of the average KAM values for a given depth

BIBLIOGRAPHY

Aba-Perea, P. E., Pirling, T., Withers, P. J., Kelleher, J., Kabra, S. & Preuss, M. (2016). Determination of the high temperature elastic properties and diffraction elastic constants of Ni-base superalloys. *Materials & Design*, 89, 856–863. doi: 10.1016/j.matdes.2015.09.152.

Al-Hassani, S. T. S. (1981). Mechanical aspect of residual stress development in shot peening. *In proceedings of the 1st International Conference on Shot Peening (ICSP-1)*, pp. 583–602.

Al-Obaid, Y. F. (1995). Shot peening mechanics: experimental and theoretical analysis. *Mechanics of Materials*, 19(2-3), 251–260. doi: 10.1016/0167-6636(94)00036-g.

AMS 2430T. (2015). *Shot Peening, Automatic*. Warrendate, PA, USA: SAE International.

AMS 2431/2E. (2010). *Peening Media (ASH) Cast Steel Shot, High Hardness (55 to 62 HRC)*. Warrendate, PA, USA: SAE International.

AMS 2431/3D. (2007). *Peening Media (AWCR) Conditioned Carbon Steel Cut Wire Shot, Regular Hardness (45 to 52 HRC)*. Warrendate, PA, USA: SAE International.

AMS 2431/7B. (2013). *Peening Media Ceramic Shot*. Warrendate, PA, USA: SAE International.

AMS 4050J. (2014). *Aluminum Alloy, Plate 6.2zn 2.3cu 2.2mg 0.12zr (7050-T7451) Solution Heat Treated, Stress Relieved, and Overaged*. Warrendate, PA, USA: SAE International.

AMS 5663M. (2009). *Nickel Alloy, Corrosion and Heat-Resistant, Bars, Forgings, and Rings 52.5Ni - 19Cr - 3.0Mo - 5.1Cb (Nb) - 0.90Ti - 0.50Al - 18Fe Consumable Electrode or Vacuum Induction Melted 1775 °F (968 °C) Solution and Precipitation Heat Treated*. Warrendate, PA, USA: SAE International.

AMS 6257F. (2016). *Steel Bars, Forgings, and Tubing 1.6SI - 0.82Cr - 1.8Ni - 0.40Mo - 0.08V (0.40 - 0.44C) Consumable Electrode Vacuum Remelted Normalized and Tempered*. Warrendate, PA, USA: SAE International.

ASM Aerospace Specification Metals, I. (2019). Aluminum 7050-T7451 datasheet. Consulted at http://asm.matweb.com/search/SpecificMaterial.asp?bassnum=MA7050T745.

ASTM E112-13. (2013). *Standard Test Methods for Determining Average Grain Size*. West Conshohocken, PA, USA: ASTM International.

ASTM E1426-98. (2009). *Standard Test Method for Determining the Effective Elastic Parameter for X-Ray Diffraction Measurements of Residual Stress*. West Conshohocken, PA, USA: ASTM International.

ASTM E2860-12. (2012). *Standard Test Method for Residual Stress Measurement by X-Ray Diffraction for Bearing Steels*. West Conshohocken, PA, USA: ASTM International.

ASTM E384-17. (2017). *Standard Test Method for Microindentation Hardness of Materials*. West Conshohocken, PA, USA: ASTM International.

ASTM E837-13a. (2013). *Standard Test Method for Determining Residual Stresses by the Hole-Drilling Strain-Gage Method*. West Conshohocken, PA, USA: ASTM International.

Averbach, B. L. & Warren, B. E. (1949). The Effect of Cold Work in Metals on Powder Pattern Intensities. 20, 1066–1069. doi: 10.1063/1.1698276.

Ayad, A., Allain-Bonasso, N., Rouag, N. & Wagner, F. (2012, 1). Grain Orientation Spread Values in if Steels after Plastic Deformation and Recrystallization. *Textures of Materials - ICOTOM 16*, 702(Materials Science Forum), 269–272. doi: 10.4028/www.scientific.net/MSF.702-703.269.

Bachmann, F., Hielscher, R. & Schaeben, H. (2011). Grain detection from 2d and 3d EBSD data-Specification of the MTEX algorithm. *Ultramicroscopy*, 111(12), 1720–1733. doi: 10.1016/j.ultramic.2011.08.002.

Bag, A., Delbergue, D., Lévesque, M., Bocher, P. & Brochu, M. (2017). Study of short crack growth in shot peened 300M steel. *In proceedings of the 13th International Conference on Shot Peening (ICSP-13)*, pp. 231–236.

Bag, A., Delbergue, D., Bocher, P., Lévesque, M. & Brochu, M. (2019). Statistical analysis of high cycle fatigue life and inclusion size distribution in shot peened 300M steel. *International Journal of Fatigue*, 118, 126–138. doi: 10.1016/j.ijfatigue.2018.08.009.

Bag, A., Delbergue, D., Ajaja, J., Bocher, P., Lévesque, M. & Brochu, M. (2020). Effect of different shot peening conditions on the fatigue life of 300M steel submitted to high stress amplitudes. *International Journal of Fatigue*, 130, 105274. doi: 10.1016/j.ijfatigue.2019.105274.

Bagherifard, S. & Guagliano, M. (2012). Fatigue behavior of a low-alloy steel with nanostructured surface obtained by severe shot peening. *Engineering Fracture Mechanics*, 81, 56–68. doi: 10.1016/j.engfracmech.2011.06.011.

Beaney, E. M. (1976). Accurate measurement of residual stress on any steel using the centre hole method. *Strain*, 12(3), 99-106. doi: 10.1111/j.1475-1305.1976.tb00194.x.

Beaney, E. M. & Procter, E. (1974). A critical evaluation of the centre hole technique for the measurement of residual stresses. *Strain*, 10(1), 7–14. doi: 10.1111/j.1475-1305.1974.tb00074.x.

Beghini, M., Bertini, L. & Santus, C. (2010). A procedure for evaluating high residual stresses using the blind hole drilling method , including the effect of plasticity. *Journal of Strain Analysis for Engineering Design*, 45(4), 301–318.

Belassel, M., Pineault, J. & Brauss, M. E. (2006). Comparison and evaluation of residual stress measurement techniques, a technical and economical study. *In proceedings of the SEM Annual Conference and Exposition on Experimental and Applied Mechanics*, 2, 756–762.

Benedetti, M., Fontanari, V., Scardi, P., Ricardo, C. L. A. & Bandini, M. (2009). Reverse bending fatigue of shot peened 7075-T651 aluminium alloy: The role of residual stress relaxation. *International Journal of Fatigue*, 31(8-9), 1225–1236. doi: 10.1016/j.ijfatigue.2008.11.017.

Benedetti, M., Fontanari, V. & Monelli, B. D. (2010). Numerical Simulation of Residual Stress Relaxation in Shot Peened High-Strength Aluminum Alloys Under Reverse Bending Fatigue. *Journal of Engineering Materials and Technology*, 132(1), 11012. doi: 10.1115/1.3184083.

Bever, M. B., Holt, D. L. & Titchener, A. L. (1973). The stored energy of cold work. *Progress in materials science*, 17, 5–177.

Bianchetti, C., Lévesque, M. & Brochu, M. (2018). Probabilistic analysis of the e ff ect of shot peening on the high and low cycle fatigue behaviors of AA 7050-T7451. *International Journal of Fatigue*, 111(February), 289–298. doi: 10.1016/j.ijfatigue.2018.02.029.

Bianchetti, C., Delbergue, D., Bocher, P., Lévesque, M. & Brochu, M. (2019). Analytical fatigue life prediction of shot peened AA 7050-T7451. *International Journal of Fatigue*, 118(April 2018), 271–281. doi: 10.1016/j.ijfatigue.2018.07.007.

Bravais, A. (1848). Mémoire sur les systèmes formés par des points distribués régulièrement sur un plan ou dans l'espace. *Journal de l'École Polytechnique*, 32.

Bray, D. E. (2013). Ultrasonics. In Schajer, G. S. (Ed.), *Practical Residual Stress Measurements Methods* (pp. 259–277). John Wiley & Sons.

Bretin, R., Lévesque, M. & Bocher, P. (2019a). Neighborhood effect on the strain distribution in linearly elastic polycrystals: Part 1 – Finite element study of the interaction between grains. *International Journal of Solids and Structures*, 176-177, 36–48. doi: 10.1016/j.ijsolstr.2019.05.015.

Bretin, R., Lévesque, M. & Bocher, P. (2019b). Neighborhood effect on the strain distribution in linearly elastic polycrystals: Part 2 – Cellular Automaton. *International Journal of Solids and Structures*, 176-177, 49–67. doi: 10.1016/j.ijsolstr.2019.07.005.

Buttle, D. J. (2013). Magnetic Methods. In Schajer, G. S. (Ed.), *Practical Residual Stress Measurements Methods* (pp. 225–258). John Wiley & Sons.

Cahoon, J., Broughton, W. & Kutzak, A. (1971). The determination of yield strength from hardness measurements. *Metallurgical transactions*, 2(7), 1979–1983.

Cammett, J., Prevéy, P. S. & Jayaraman, N. (2005). The effect of shot peening coverage on residual stress, cold work, and fatigue in a nickel-base superalloy. Lambda Research, Cincinnati, OH.

Carvalho, A. L. M. & Voorwald, H. J. C. (2007). Influence of shot peening and hard chromium electroplating on the fatigue strength of 7050-T7451 aluminum alloy. *International Journal of Fatigue*, 29(7), 1282–1291. doi: 10.1016/j.ijfatigue.2006.10.003.

Chaboche, J. & Rousselier, G. (1983). On the plastic and viscoplastic constitutive equations—Part I: Rules developed with internal variable concept. *Journal of Pressure Vessel Technology*, 105(2), 153–158.

Champaigne, J. (1993). Shot peening intensity measurement. *The shot peener*, 6, 1–6.

Chan, K. S. (2003). A microstructure-based fatigue-crack-initiation model. *Metallurgical and Materials Transactions A*, 34(1), 43–58.

Chandler, H. (1995a). 19.5 300M. In *Heat Treater's Guide - Practices and Procedures for Irons and Steels* (ed. 2nd, pp. 700–701). ASM International.

Chandler, H. (1995b). 19.3 4140, 4140H, 4140RH. In *Heat Treater's Guide - Practices and Procedures for Irons and Steels* (ed. 2nd, pp. 680–689). ASM International.

Chandler, H. (1995c). 19.4 4340, 4340H. In *Heat Treater's Guide - Practices and Procedures for Irons and Steels* (ed. 2nd, pp. 690–700). ASM International.

Chantler, C., Olsen, K., Dragoset, R., Chang, J., Kishore, A., Kotochigova, S. & Zucker, D. (2005). Detailed Tabulation of Atomic Form Factors, Photoelectric Absorption and Scattering Cross Section, and Mass Attenuation Coefficients for Z= 1–92 from E= 1–10 eV to E= 0.4–1.0 MeV. Consulted at https://physics.nist.gov/PhysRefData/FFast/html/form.html.

Cheng, W. & Finnie, I. (1985). A Method for Measurement of Axisymmetric Axial Residual Stresses In Ciroumferentially Welded Thin-Wailed Cylinders. *Journal of Engineering Materials and Technology*, 107(3), 181–185.

Cheng, W. & Finnie, I. (2007). *Residual stress measurement and the slitting method*. Springer Science & Business Media.

Christien, F., Telling, M. T. F. & Knight, K. S. (2013). Neutron diffraction in situ monitoring of the dislocation density during martensitic transformation in a stainless steel. *Scripta Materialia*, 68(7), 506–509. doi: 10.1016/j.scriptamat.2012.11.031.

Crecraft, D. I. (1967). The measurement of applied and residual stresses in metals using ultrasonic waves. *Journal of Sound and Vibration*, 5(1), 173–192.

Cullity, B. D. (1956a). Chap.1 Properties of X-rays. In *Elements of X-ray diffraction* (ed. 1st, pp. 1–28). Addison-Wesley.

Cullity, B. D. (1956b). Chap.2 The geometry of crystals. In *Elements of X-ray diffraction* (ed. 1^{st}, pp. 29–77). Addison-Wesley.

Cullity, B. D. (1956c). Chap.3 Diffraction I: The directions of diffracted beams. In *Elements of X-ray diffraction* (ed. 1^{st}, pp. 78–103). Addison-Wesley.

Cullity, B. D. (1956d). Chap.9 The structure of polycrystalline aggregates. In *Elements of X-ray diffraction* (ed. 1^{st}, pp. 259–296). Addison-Wesley.

Cullity, B. D. (1956e). App.3 Wavelengths of some characteristic emission lines and absorption edges. In *Elements of X-ray diffraction* (ed. 1^{st}, pp. 464–465). Addison-Wesley.

de Los Rios, E. R., Walley, A., Milan, M. T. & Hammersley, G. (1995). Fatigue crack initiation and propagation on shot-peened surfaces in A316 stainless steel. *International Journal of Fatigue*, 17(7), 493–499. doi: 10.1016/0142-1123(95)00044-T.

De Los Rios, E. R., Trooll, M. & Levers, A. (1999). Improving the fatigue crack resistance of 2024-t351 aluminum alloy by shot peening. *Life Extension-Aerospace Technology Opportunities, The Royal Aeronautical Society Publication*, 26.1–26.8.

Delbergue, D., Texier, D., Lévesque, M. & Bocher, P. (2016). Comparison of Two X-Ray Residual Stress Measurement Methods : $\sin^2\psi$ and $\cos\alpha$, Through the Determination of a Martensitic Steel X-Ray Elastic Constant. *In proceedings of the* 10^{th} *Internal Conference on Residual Stresses (ICRS-10)*, 2, 55–60. doi: 10.21741/9781945291173-10.

Delbergue, D., Lévesque, M. & Bocher, P. (2017). About the importance of X-ray elastic constant determination in the precise measurement of residual stress profiles. *In proceedings of the* 13^{th} *International Conference on Shot Peening (ICSP-13)*, pp. 237–243.

Delbergue, D., Texier, D., Lévesque, M. & Bocher, P. (2019). Diffracting-grain identification from electron backscatter diffraction maps during residual stress measurements: a comparison between the $\sin^2\psi$ and $\cos\alpha$ methods. *Journal of Applied Crystallography*, 52(4), 828–843. doi: 10.1107/S1600576719008744.

Dingley, D. J. (2012). Un regard sur l'EBSD, procédures passées et nouvelles. In Lodini, A. & Baudin, T. (Eds.), *Rayonnement synchrotron, rayons X et neutrons au service des matériaux: Analyse des contraintes et des textures*. Les Ulis, France: EDP sciences.

Egle, D. M. & Bray, D. E. (1976). Measurement of acoustoelastic and third-order elastic constants for rail steel. *The journal of the Acoustical Society of America*, 60(3), 741–744.

Etter, A. L. & Baudin, T. (2013). Représentation des orientations cristallines -Quelques exemples de texture. In Lodini, A. & Baudin, T. (Eds.), *Rayonnement syncrotron, rayons X et neutrons au service des matériaux* (ch. 6, pp. 278–321). EDP Sciences.

Farrahi, G. H., Lebrun, J. L. & Couratin, D. (1995). Effect of Shot Peening on Residual Stress and Fatigue Life of a Spring Steel. *Fatigue & Fracture of Engineering Materials and Structures*, 18(2), 211–220. doi: 10.1111/j.1460-2695.1995.tb00156.x.

Fathallah, R., Laamouri, A., Sidhom, H. & Braham, C. (2004). High cycle fatigue behavior prediction of shot-peened parts. *Elsevier International Journal of Fatigue*, 26(10), 1053–1067. doi: 10.1016/j.ijfatigue.2004.03.007.

Faucheux, P. A., Gosselin, F. P. & Lévesque, M. (2018). Simulating shot peen forming with eigenstrains. *Journal of Materials Processing Tech.*, 254, 135–144. doi: 10.1016/j.jmatprotec.2017.11.036.

Fischer-Cripps, A. C. (2011). *Nanoindentation* (ed. 3rd). Springer.

Fitzpatrick, M., Fry, A., Holdway, P., Kandil, F., Shackleton, J. & Suominen, L. (2005). Determination of residual stresses by X-ray diffraction. Teddington, UK: National Physical Laboratory.

Fournier, D. & Pineau, A. (1977). Low cycle fatigue behavior of Inconel 718 at 298 K and 823 K. *Metallurgical Transactions A*, 8(7), 1095–1105.

Fujita, T., Kamura, N., Maruyama, Y. & Sasaki, T. (2016). Evaluation of Rolling Contact Fatigue Using X-Ray Diffraction Ring. *Materials Performance and Characterization*, 5(1), 23–37. doi: 10.1520/MPC20150027.

Gariépy, A., Bridier, F., Hoseini, M., Bocher, P., Perron, C. & Lévesque, M. (2013). Experimental and numerical investigation of material heterogeneity in shot peened aluminium alloy AA2024-T351. *Surface and Coatings Technology*, 219, 15–30. doi: 10.1016/j.surfcoat.2012.12.046.

Gariépy, A. (2012). *Finite Element Modelling of Shot Peening and Peen Forming Processes and Characterisation of Peened AA2024-T351 Aluminium Alloy*. (Ph.D. thesis, École Polytechnique de Montréal).

Garikepati, P., Chang, T. T. & Jiles, D. C. (1988). Theory of ferromagnetic hysteresis: evaluation of stress from hysteresis curves. *IEEE Transactions on Magnetics*, 24(6), 2922–2924.

Gauthier, J., Krause, T. W. & Atherton, D. L. (1998). Measurement of residual stress in steel using the magnetic Barkhausen noise technique. *NDT & E International*, 31(1), 23–31.

Gnäupel-Herold, T., Brand, P. C. & Prask, H. J. (1998). Calculation of Single-Crystal Elastic Constants for Cubic Crystal Symmetry from Powder Diffraction Data. *Journal of Applied Crystallography*, 31(6), 929–935. doi: 10.1107/S002188989800898X.

Haldipur, P. (2006). Material characterization of nickel-based super alloys through ultrasonic inspection. Iowa State University.

Hall, M., Veeraraghavan, V., Rubin, H. & Winchell, P. (1977). The approximation of symmetric X-ray peaks by Pearson type VII distributions. *Journal of Applied Crystallography*, 10(1), 66–68.

Hauk, V. (1997). *Structural and Residual Stress Analysis by Nondestructive Methods: Evaluation-Application-Assessment*. Amsterdam, The Netherlands: Elsevier.

He, B. B. (2009). *Two-dimensional X-ray diffraction*. New Jersey, USA: J. Wiley & Sons, Inc. doi: 10.1002/9780470502648.

He, B. B., Preckwinkel, U. & Smith, K. L. (1998). Advantages of using 2D detectors for residual stress measurements. *Advances in X-ray Analysis*, 42(2000), 429–438.

He, B., Soady, K., Mellor, B., Morris, A. & Reed, P. (2013). Effects of shot peening on short crack growth rate and resulting low cycle fatigue behaviour in low pressure turbine blade material. *Materials Science and Technology*, 29(7), 788–796.

Hertzberg, R. W., Vinci, R. P. & Hertzberg, J. L. (2012). Chapter 2, Yielding and Plastic Flow. In *Deformation and fracture mechanics of engineering materials* (ed. 5^{th}). Wiley New York.

Heydari Astaraee, A., Miresmaeili, R., Bagherifard, S., Guagliano, M. & Aliofkhazraei, M. (2017). Incorporating the principles of shot peening for a better understanding of surface mechanical attrition treatment (SMAT) by simulations and experiments. *Materials and Design*, 116, 365–373. doi: 10.1016/j.matdes.2016.12.045.

Hielscher, R. (2013). Kernel density estimation on the rotation group and its application to crystallographic texture analysis. *Journal of Multivariate Analysis*, 119, 119–143. doi: 10.1016/j.jmva.2013.03.014.

Hill, M. R. (2013). The Slitting Method. In Schajer, G. S. (Ed.), *Practical Residual Stress Measurements Methods* (pp. 89–108). John Wiley & Sons.

Hill, R. (1952). The Elastic Behaviour of a Crystalline Aggregate. *Proceedings of the Physical Society. Section A*, 65(5), 350–354. doi: https://doi.org/10.1088/0370-1298/65/5/307.

Hill, R., Storåkers, B. & Zdunek, A. (1989). A theoretical study of the Brinell hardness test. *Proceedings of the Royal Society of London. A. Mathematical and Physical Sciences*, 423(1865), 301–330.

Hines, W. W., Montgomery, D. C., Goldsman, D. M. & Borror, C. M. (2008). *Probability and statistics in engineering* (ed. 4^{th}). John Wiley & Sons.

Hiratsuka, K., Sasaki, T., Seki, K. & Hirose, Y. (2003). Development of measuring system for stress by means of image plate for laboratory X-ray experiment. *Advances in X-ray Analysis*, 46, 61–67.

Hoffmeister, J., Schulze, V., Wanner, A., Hessert, R. & Koenig, G. (2008). Thermal Relaxation of residual Stresses induced by Shot Peening in IN718. *In proceedings of the 10th International Conference on Shot Peening (ICSP-10)*, pp. 1–6.

Hornbach, D. J., Prevéy, P. S. & Mason, P. W. (1995). X-ray diffraction characterization of the residual stress and hardness distributions in induction hardened gears. *In Proceedings of the 1st International Conference on Induction Hardened Gears and Critical Components*, pp. 69–76.

Hutchings, M. T., Withers, P. J., Holden, T. M. & Lorentzen, T. (2005). *Introduction to the characterization of residual stress by neutron diffraction*. CRC press.

ISO 643. (2003). *Steels—micrographic determination of the apparent grain size*. International Organization for Standardization.

Jiles, D. C. (1988). Review of magnetic methods for nondestructive evaluation. *NDT International*, 21(5), 311–319. doi: https://doi.org/10.1016/0308-9126(88)90189-7.

Jun, T.-s. & Korsunsky, A. M. (2010). International Journal of Solids and Structures Evaluation of residual stresses and strains using the Eigenstrain Reconstruction Method. *International Journal of Solids and Structures*, 47(13), 1678–1686. doi: 10.1016/j.ijsolstr.2010.03.002.

Kaufman, J. (2000). Aluminum Alloy and Temper Designation Systems of the Aluminum Association. In *Introduction to Aluminum Alloys and Tempers*. ASM International.

Kim, T., Lee, H., Jung, S. & Lee, J. H. (2012). A 3D FE model with plastic shot for evaluation of equi-biaxial peening residual stress due to multi-impacts. *Surface & Coatings Technology*, 206(13), 3125–3136. doi: 10.1016/j.surfcoat.2011.12.042.

Kirk, D. (1999). Shot peening. *Aircraft Engineering and Aerospace Technology*, 71(4), 349–361. doi: Doi 10.1108/00022669910270727.

Kirk, D. (2016). Peening Intensity: True Meaning and Measurement Strategy. *The Shot Peener*, (Summer), 349–361.

Klotz, T., Blas, S., Lévesque, M. & Brochu, M. (2017a). 1D cyclic yield model independent of load spectrum characteristics and its application to Inconel 718. *Mechanics of Materials*, 109, 34–41. doi: 10.1016/j.mechmat.2017.03.011.

Klotz, T., Delbergue, D., Miao, H. Y., Castro-Moreno, A., Bocher, P., Lévesque, M. & Brochu, M. (2017b). Analytical fatigue life prediction of shot peened Inconel 718. *In proceedings of the 13th International Conference on Shot Peening (ICSP-13)*, pp. 244–247.

Klotz, T., Delbergue, D., Bocher, P., Lévesque, M. & Brochu, M. (2018a). Surface characteristics and fatigue behavior of shot peened Inconel 718. *International Journal of Fatigue*, 110, 10–21. doi: 10.1016/j.ijfatigue.2018.01.005.

Klotz, T., Miao, H. Y., Bianchetti, C., Lévesque, M. & Brochu, M. (2018b). Analytical fatigue life prediction of shot peened Inconel 718. *International Journal of Fatigue*, 113, 204–221. doi: 10.1016/j.ijfatigue.2018.04.011.

Kocks, U. F. (1976). Laws for Work-Hardening and Low-Temperature Creep. *Journal of Engineering Materials and Technology*, 98(1).

Kocks, U. F., Tomé, C. N. & Wenk, H. R. (1998). *Texture & Anisotropy: preferred orientations in polycrystals and their effect on materials properties*. Cambridge University Press.

Kohri, A., Takaku, Y. & Nakashiro, M. (2016). Comparison of X-Ray Residual Stress Measurement Values by Cos α Method and Sin$^2\Psi$ Method. *In proceedings of the 10th International Conference on Residual Stresses (ICRS-10)*, pp. 103–108. doi: 10.21741/9781945291173-18.

Korsunsky, A. M. (2005). On the modelling of residual stresses due to surface peening using eigenstrain distributions. *Journal of strain analysis*, 40(8), 817–824. doi: 10.1243/030932405X30984.

Kröner, E. (1958). Berechnung der elastischen Konstanten des Vielkristalls aus den Konstanten des Einkristalls. *Zeitschrift für Physik*, 151(4), 504–518.

Lambda Research. (1996). *Finite element correction for stress relaxation in complex geometries* (Report n°17). Consulted at https://www.lambdatechs.com/wp-content/uploads/dif17.pdf.

Lebon, R., Delbergue, D., Miao, H. Y., Lévesque, M. & Bocher, P. (2014). Residual Stress Measurement Correction on Shot Peened AA2024 by Finite Element Analysis. *In proceedings of the 12th International Conference on Shot Peening (ICSP-12)*.

Ledbetter, H. M. & Reed, R. P. (1973). Elastic Properties of Metals and Alloys, I. Iron, Nickel, and Iron-Nickel Alloys. *Journal of Physical and Chemical Reference Data*, 2(3), 531–618.

Lee, S. Y., Ling, J., Wang, S. & Ramirez-Rico, J. (2017). Precision and accuracy of stress measurement with a portable X-ray machine using an area detector. *Journal of Applied Crystallography*, 50(1), 131–144. doi: 10.1107/S1600576716018914.

Ling, J. J. & Lee, S.-Y. (2015). Characterization of a portable x-ray device for residual stress measurements. *Adv. in X-ray Analysis*, 59, 153–162.

Liu, J. L., Umemoto, M., Todaka, Y. & Tsuchiya, K. (2007). Formation of a nanocrystalline surface layer on steels by air blast shot peening. *Journal of Materials Science*, 42(18), 7716–7720. doi: 10.1007/s10853-007-1659-x.

Llaneza, V. & Belzunce, F. J. (2015). Study of the effects produced by shot peening on the surface of quenched and tempered steels: Roughness, residual stresses and work hardening. *Applied Surface Science*, 356, 475–485. doi: 10.1016/j.apsusc.2015.08.110.

Löhe, D. & Vöhringer, O. (2002). Stability of Residual Stresses. In Totten, G., Howes, M. & Inoue, T. (Eds.), *Handbook of Residual Stress and Deformation of Steel* (pp. 54–69). ASM International.

Löhe, D., Lang, K.-H. & Vöhringer, O. (2002). Residual stresses and fatigue behavior. In Totten, G., Howes, M. & Inoue, T. (Eds.), *Handbook of Residual Stress and Deformation of Steel* (pp. 27–53). ASM International.

Lu, J. (1996). *Handbook of measurement of residual stresses*. Fairmont Press.

Mainprice, D., Hielscher, R. & Schaeben, H. (2011). Calculating anisotropic physical properties from texture data using the MTEX open-source package. *Geological Society, London, Special Publications*, 360(1), 175–192. doi: 10.1144/SP360.10.

Maitland, T. & Sitzman, S. (2007). Electron backscatter diffraction (EBSD) technique and materials characterization examples. In Zhou, W. & Wang, Z. L. (Eds.), *Scanning Microscopy for Nanotechnology: Techniques and Applications*. Berlin, Germany: Springer.

Maiya, P. S. & Busch, D. E. (1975). Effect of Surface Roughness on Low-Cycle Fatigue Behavior of Type 304 Stainless Steel. *Metallurgical Transactions A*, 6, 1761–1766. doi: https://doi.org/10.1007/BF02642305.

Margetan, F., Nieters, E., Haldipur, P., Brasche, L., Chiou, T., Keller, M., Degtyar, A., Umbach, J., Hassan, W., Patton, T. & Smith, K. (2005). *Fundamental studies of nickel billet materials–Engine Titanium Consortium II*.

Maruyama, Y. (2014). *International patent application n° WO 2014/010260*. Genève, Suisse: World Intellectual Property Organization.

Maslen, E. N. (2006). X-ray absorption. In Prince, E. (Ed.), *International Tables for Crystallography* (ed. 3$^{\mathrm{rd}}$, vol. C: Mathematical, physical and chemical tables, pp. 599–608). Springer, Dordrecht. doi: 10.1107/97809553602060000602.

Mathar, J. (1934). Determination of initial stresses by measuring the deformation around drilled holes. *Trans. ASME*, 56(4), 249–254.

Meyers, M. A. & Chawla, K. K. (2009). Creep and superplasticity. In *Mechanical Behavior of Materials* (ed. 2$^{\mathrm{nd}}$, pp. 653–712). Cambridge University Press.

Miao, H. Y., Klotz, T., Delbergue, D. & Levesque, M. (2017a). Finite element simulation of shot peened residual stress relaxation under low and high cycle fatigue loadings. *In proceedings of the 13th International Conference on Shot Peening (ICSP-13)*, pp. 384–389.

Miao, H. Y., Tu, F., Delbergue, D., Bianchetti, C., Klotz, T., Bag, A. & Levesque, M. (2017b). Shot peening DEM-FEM simulation considering shot stream expansion, peening intensity and target materials. *In proceedings of the 13th International Conference on Shot Peening (ICSP-13)*, pp. 366–371.

Milbradt, K. P. (1951). Ring Method Determination of Residual Stresses. *Proceedings SESA*, 9, 63–74.

Miyazaki, T. & Sasaki, T. (2014). X-ray stress measurement with two-dimensional detector based on Fourier analysis. *International Journal of Materials Research*, 105(9), 922–927. doi: Doi 10.3139/146.111101.

Miyazaki, T. & Sasaki, T. (2015). X-ray stress measurement from an imperfect Debye–Scherrer ring. *International Journal of Materials Research*, 106(3), 237–241. doi: 10.3139/146.111179.

Miyazaki, T. & Sasaki, T. (2016). A comparison of X-ray stress measurement methods based on the fundamental equation. *Journal of Applied Crystallography*, 49(2014), 426–432. doi: 10.1107/S1600576716000492.

Moore, M. G. & Evans, W. P. (1958). Mathematical correction for stress in removed layers in X-ray diffraction residual stress analysis. *SAE Trans*, 66, 340–345. doi: 10.4271/580035.

Moussa, C., Bernacki, M., Besnard, R. & Bozzolo, N. (2015). About quantitative EBSD analysis of deformation and recovery substructures in pure Tantalum. *IOP Conf. Ser.: Mater. Sci. Eng.*, 89, 012038. doi: 10.1088/1757-899X/89/1/012038.

Müller, P. & Macherauch, E. (1961). Das Sin2ψ Verfahren der röntgenographischen Spannungsmessung. *Z. angew. Phys*, 13, 305–312.

Munsi, A. S. M. Y., Waddell, A. J. & Walker, C. A. (2003). A Method for Determining X-ray Elastic Constants for the Measurement of Residual Stress. *Strain*, 39(1), 3–10. doi: 10.1046/j.1475-1305.2003.00044.x.

Murray, C. E. (2013). Equivalence of Kröner and weighted Voigt-Reuss models for x-ray stress determination. *Journal of Applied Physics*, 113(15), 1–12. doi: 10.1063/1.4801917.

NASA. (2010). Tour of the electromagnetic spectrum: Visible light. Consulted at https://science.nasa.gov/ems/09_visiblelight.

Navarro, A. & de los Rios, E. R. (1988). Short and long fatigue crack growth: A unified model. *Philosophical Magazine A*, 57(1), 15–36. doi: 10.1080/01418618808204496.

Navarro, A. & de Los Rios, E. (1988). A microstructurally-short fatigue crack growth equation. *Fatigue & Fracture of Engineering Materials & Structures*, 11(5), 383–396.

Nobre, J. P., Kornmeier, M., Dias, A. M. & Scholtes, B. (1999). Comparative analysis of shot-peening residual stresses using hole-drilling and X-ray diffraction methods. *In proceedings of the 5th European Conference on Residual Stresses (ECRS-5)*, 347-349, 138–143. doi: 0.4028/www.scientific.net/MSF.347-349.138.

Noyan, I. C. & Cohen, J. B. (1987). Determination of strain and stress fields by diffraction methods. In *Residual stress measurement by diffraction and interpretation* (pp. 276). New York: Springer-Verlag.

Oblak, M., Paulonis, D. F. & Duvall, D. S. (1974). Precipitation of the δ-Ni3Nb phase in two nickel base superalloys. *Metallurgical Transactions*, 16, 555–561.

Pangborn, R. N., Weissmann, S. & Kramer, I. R. (1981). Dislocation distribution and prediction of fatigue damage. *Metallurgical Transactions A*, 12(1), 109–120. doi: 10.1007/bf02648515.

Pawade, R. S., Joshi, S. S. & Brahmankar, P. K. (2008). Effect of machining parameters and cutting edge geometry on surface integrity of high-speed turned Inconel 718. *International Journal of Machine Tools and Manufacture*, 48(1), 15–28. doi: 10.1016/j.ijmachtools.2007.08.004.

Peterson, N., Kobayashi, Y. & Sanders, P. (2017). Assessment and Validation of Cosα Method for Residual Stress Measurement. *In proceedings of the 13th International Conference on Shot Peening (ICSP-13)*, pp. 80–86.

Prevéy, P. S. (1986). The Use of Pearson Vii Distribution Functions in X-Ray Diffraction Residual Stress Measurement. *Advances in X-Ray Analysis,*, 29, 103–111.

Prevéy, P. S. (1987). The measurement of subsurface residual stress and cold work distributions in nickel base alloys. *In proceedings of the ASM's conference on residual stress in design, process and materials selection*, pp. 11–20.

Prevéy, P. S. (2000). The effect of cold work on the thermal stability of residual compression in surface enhanced Inconel 718. *In proceedings of the 20th ASM Materials Solution Conference & Exposition*.

Prevéy, P. S., Jayaraman, N., Ontko, N., Shepard, M., Ware, R. & Coate, J. (2005). Comparison of mechanical suppression by shot peening and low plasticity burnishing to mitigate SCC and corrosion fatigue failures in 300M landing gear steel. *In proceedings of the 9th International Conference on Shot Peening (ICSP-9)*, pp. 247–251.

Prime, M. B. (1999). Residual Stress Measurement by Successive Extension of a Slot: The Crack Compliance Method. *Applied Mechanics Reviews*, 52(2), 75. doi: 10.1115/1.3098926.

Prime, M. B. (2001). Cross-Sectional Mapping of Residual Stresses by Measuring the Surface Contour After a Cut. *Journal of Engineering Materials and Technology-Transactions of the Asme*, 123(2), 162. doi: 10.1115/1.1345526.

Prime, M. B. & DeWald, A. T. (2013). The contour method, in Practical Residual Stress Measurement Methods. In Schajer, G. S. (Ed.), *Practical Residual Stress Measurements Methods* (pp. 109–138). John Wiley & Sons.

Ramirez-Rico, J., Lee, S.-Y., Ling, J. J. & Noyan, I. C. (2016). Stress measurement using area detectors: a theoretical and experimental comparison of different methods in ferritic steel using a portable X-ray apparatus. *Journal of Materials Science*, 51(11), 5343–5355. doi: 10.1007/s10853-016-9837-3.

Read, W. T. (1953). *Dislocations in Crystals* (ed. McGrawHill). New York.

Reuss, A. (1929). Berechnung der fließgrenze von mischkristallen auf grund der plastizitätsbedingung für einkristalle. *Zeitschrift für Angewandte Mathematik und Mechanik*, 9(1), 49–58.

Ruud, C. (2002). Measurement of Residual Stresses. In Totten, G., Howes, M. & Inoue, T. (Eds.), *Handbook of Residual Stress and Deformation of Steel* (pp. 99–117). ASM International. doi: 10.1361/hrsd2002p099.

SAE HS784. (2003). *Residual stress measurement by X-ray diffraction*. Warrendate, PA, USA: SAE International.

SAE J2277. (2013). *Shot Peening Coverage Determination*. Warrendate, PA, USA: Surface Enhancement Committee.

SAE J442. (2008). *Test Strip, Holder, and gae for shot peening*. Warrendate, PA, USA: Surface Enhancement Committee.

SAE J443. (2017). *Procedures for Using Standard Shot Peening Test Strip*. Warrendate, PA, USA: Surface Enhancement Committee.

Sasaki, T. (2006). Application of the $\cos\alpha$ Method to Area Detector Type Neutron Stress Measurement. *In proceedings of the 7^{th} European Conference on Residual Stresses (ECRS-7)*, pp. 247–252. doi: 10.4028/www.scientific.net/MSF.524-525.247.

Sasaki, T., Hirose, Y., Sasaki, K. & Yasukawa, S. (1997). Influence of image processing conditions of Debye Scherrer ring images in X-ray stress measurement using an imaging plate. *Adv X-ray Anal*, 40, 588–594.

Sasaki, T., Yaguchi, O. & Suzuki, H. (2010). Neutron Residual Stress Measurement of Railway Rails Using Image Plate. *Mechanical Stress Evaluation by Neutrons and Synchrotron Radiation*, 652, 260–265. doi: 10.4028/www.scientific.net/MSF.652.260.

Sato, M., Tsuji, N., Minamino, Y. & Koizumi, Y. (2004). Formation of nanocrystalline surface layers in various metallic materials by near surface severe plastic deformation. *Science and Technology of Advanced Materials*, 5(1-2), 145–152. doi: 10.1016/j.stam.2003.10.015.

Savaria, V., Bridier, F. & Bocher, P. (2012). Computational quantification and correction of the errors induced by layer removal for subsurface residual stress measurements. *International Journal of Mechanical Sciences*, 64(1), 184–195. doi: 10.1016/j.ijmecsci.2012.07.003.

Schajer, G. S. & Ruud, C. O. (2013). Overview of residual stresses and their measurement. In Schajer, G. S. (Ed.), *Practical Residual Stress Measurements Methods* (pp. 1–27). John Wiley & Sons.

Seeger, A., Diehl, J., Mader, S. & Rebstock, H. (1956). Work-hardening and work-softening of face- centred cubic metal crystals. *The Philosophical Magazine: A Journal of Theoretical Experimental and Applied Physics*, 2(8), 323–350. doi: 10.1080/14786435708243823.

Soady, K. A., Mellor, B. G., West, G. D., Harrison, G., Morris, A. & Reed, P. A. S. (2013). Evaluating surface deformation and near surface strain hardening resulting from shot peening a tempered martensitic steel and application to low cycle fatigue. *International Journal of Fatigue*, 54, 106–117. doi: 10.1016/j.ijfatigue.2013.03.019.

Spolenak, R., Brown, W. L., Tamura, N., MacDowell, A. A., Celestre, R. S., Padmore, H. A., Valek, B. C., Bravman, J. C., Marieb, T. & Fujimoto, H. (2003). Local plasticity of Al thin films as revealed by X-ray microdiffraction. *Physical review letters*, 90(9), 1–4.

Struers. (2019). Electrolytic preparation. Consulted at https://www.struers.com/en/Knowledge/Electrolytic-preparation.

Sundararaman, M., Mukhopadhyay, P. & Banerjee, S. (1988). Precipitation of the δ-Ni3Nb phase in two nickel base superalloys. *Metallurgical Transactions A*, 19(3), 453–465. doi: 10.1007/BF02649259.

Taira, S., Tanaka, K. & Yamasaki, T. (1978). A method of X-ray microbeam measurement of local stress and its application to fatigue crack growth problems. *Journal of the Society of Materials Science, Japan*, 27(294), 251–256.

Tanaka, K. (2018). X-ray measurement of triaxial residual stress on machined surfaces by the cosα method using a two-dimensional detector. *Journal of Applied Crystallography*, 51(5), 1329–1338. doi: 10.1107/S1600576718011056.

Tanaka, K. & Akiniwa, Y. (2004). Diffraction Measurements of Residual Macrostress and Microstress Using X-Rays, Synchrotron and Neutrons. *JSME International Journal Series A*, 47(3), 252–263. doi: 10.1299/jsmea.47.252.

Torres, M. A. S. & Voorwald, H. J. C. (2002). An evaluation of shot peening, residual stress and stress relaxation on the fatigue life of AISI 4340 steel. *International Journal of Fatigue*, 24(8), 877–886. doi: 10.1016/S0142-1123(01)00205-5.

Totten, G., Howes, M. & Inoue, T. (2002). *Handbook of residual stress and deformation of steel*. ASM international.

Tu, F., Delbergue, D., Miao, H. Y., Klotz, T., Brochu, M., Bocher, P. & Lévesque, M. (2017). A sequential DEM-FEM coupling method for shot peening simulation. *Surface & Coatings Technology*, 319, 200–212. doi: 10.1016/j.surfcoat.2017.03.035.

Tu, F., Delbergue, D., Klotz, T., Bag, A., Miao, H. Y., Bianchetti, C., Brochu, M., Bocher, P. & Levesque, M. (2018). Discrete element-periodic cell coupling model and investigations on shot stream expansion , Almen intensities and target materials. 145, 353–366. doi: 10.1016/j.ijmecsci.2018.06.023.

Van Acker, K., De Buyser, L., Celis, J. P. & Van Houtte, P. (1994). Characterization of thin nickel electrocoatings by the low-incident-beam-angle diffraction method. *Journal of Applied Crystallography*, 27(1), 56–66. doi: doi:10.1107/S002188989300651X.

Van Houtte, P. (1993). Stress Measurements in Textured Materials. *In the proceedings of the 2^{nd} European Powder Diffraction conference*, 133-136, 97–110.

Van Houtte, P. & De Buyser, L. (1993). The influence of crystallographic texture on diffraction measurements of residual stress. *Acta metallurgica et materialia*, 41(2), 323–336.

Vermeulen, A. C., Delhez, R., de Keijser, T. H. & Mittemeijer, E. J. (1997). X-ray diffraction analysis of simultaneous changes in stress and dislocation densities in thin films. *Advances in X-ray Analysis*, 39, 195–208.

Voigt, W. (1928). *Lehrbuch der kristallphysik*. Leipzig Teubner.

Wagner, L. (1999). Mechanical surface treatments on titanium, aluminum and magnesium alloys. *Materials Science and Engineering: A*, 263(2), 210–216.

Wang, Z. B., Tao, N. R., Li, S., Wang, W., Liu, G., Lu, J. & Lu, K. (2003). Effect of surface nanocrystallization on friction and wear properties in low carbon steel. *Materials Science and Engineering: A*, 352(1-2), 144–149. doi: https://doi.org/10.1016/S0921-5093(02)00870-5.

Warren, B. E. (1990). *X-ray Diffraction*. Courier Corporation.

Welzel, U., Ligot, J., Lamparter, P., Vermeulen, A. C. & Mittemeijer, E. J. (2005). Stress analysis of polycrystalline thin films and surface regions by X-ray diffraction. *Journal of Applied Crystallography*, 38(1), 1–29. doi: 10.1107/S0021889804029516.

Withers, P. J. (2013). Synchrotron X-ray Diffraction. In Schajer, G. S. (Ed.), *Practical Residual Stress Measurements Methods* (pp. 163–194). John Wiley & Sons.

Withers, P. J. & Bhadeshia, H. K. D. H. (2001). Residual stress Part 1 - Measurement techniques. *Materials Science and Technology*, 17(4), 355–365.

Wohlfahrt, H. (1984). The influence of peening conditions on the resulting distribution of residual stress. *In proceedings of the 2^{nd} International Conference on Shot Peening (ICSP-2)*, pp. 316–331.

Wright, S. I., Nowell, M. M. & Field, D. P. (2011). A review of strain analysis using electron backscatter diffraction. *Microscopy and Microanalysis*, 17(3), 316–329. doi: 10.1017/S1431927611000055.

Yelbay, H. I., Cam, I. & Gür, C. H. (2010). Non-destructive determination of residual stress state in steel weldments by Magnetic Barkhausen Noise technique. *NDT & E International*, 43(1), 29–33.

Yoshioka, Y. & Ohya, S. (1994). X-ray Measurement of Residual Stress in a Localized Area by Use of Imaging Plate. *In the proceedings of the 4th International Conference on Residual Stresses (ICRS-4)*, pp. 263–268.

Youngblood, J. L. & Raghavan, M. (1977). Correlation of Microstructure with Mechanical Properties of 300M Steel. *Metallurgical Transactions A*, 8A, 1439–1448. doi: 10.1007/BF02642857.

Zaleski, K., Skoczylas, A. & Brzozowska, M. (2017). The Effect of the Conditions of Shot Peening the Inconel 718 Nickel Alloy on the Geometrical Structure of the Surface. *Advances in Science and Technology Research Journal*, 11(2), 205–211. doi: 10.12913/22998624/74180.

Zinn, W. & Scholtes, B. (2005). Influence of shot velocity and shot size on almen intensity and residual stress depth distributions. *In proceedings of the 9th International Conference on Shot Peening (ICSP-9)*, pp. 379–384.

Zinn, W., Schulz, J., Kopp, R. & Scholtes, B. (2002). The Influence of the Velocity of a Peening Medium on the Almen Intensities and Residual Stress States of Shot Peened Specimens. *In proceedings of the 8th International Conference on Shot Peening (ICSP-8)*, pp. 161–166. doi: 10.1002/3527606580.ch21.